Elastic Wave Propagation and Scattering in Anisotropic Fractured Media

by

Richard Lloyd Gibson, Jr.

B.S. Geology
Baylor University (1985)

Submitted to the Department of Earth, Atmospheric, and Planetary Sciences
in partial fulfillment of the requirements for the degree of

Doctor of Philosophy

at the

MASSACHUSETTS INSTITUTE OF TECHNOLOGY

May 1991

Signature of Author .....
Department of Earth, Atmospheric, and Planetary Sciences
May 16, 1991

Certified by .....
M. Nafi Toksöz
Professor of Geophysics
Thesis Advisor

Accepted by .....
Thomas H. Jordan
Chairman, Department of Earth, Atmospheric and Planetary Sciences

Elastic Wave Propagation and Scattering in Anisotropic Fractured Media

by

Richard Lloyd Gibson, Jr.

Submitted to the Department of Earth, Atmospheric, and Planetary Sciences
on May 16, 1991, in partial fulfillment of the
requirements for the degree of
Doctor of Philosophy

Abstract

In this thesis, we develop several methods for the delineation and analysis of anisotropic fractures in the subsurface. Our principal goal is to develop methods to use seismic data to infer fracture properties. In turn, we relate this information to the fluid flow properties of anisotropically fractured media.

The first problem is to examine media with cracks oriented over a range of directions rather than begin perfectly aligned. We use this model of crack distributions to examine both velocity and permeability variations in an anisotropically fractured rock. The analysis begins by considering a material under a uniaxial stress, as cracks in a rock mass subjected to a uniaxial stress will be preferentially closed depending on the angle between the fracture normal vectors and the direction of the applied stress. If the prestress fracture orientation distribution is isotropic, the effective elastic properties of such a material after application of the stress are then transversely isotropic due to the overall alignment of the cracks still open. Velocity measurements in multiple directions are used to invert for the probability density function describing orientations of crack normals in such a rock. The information on fracture distribution obtained from the velocity inversion allows an estimation of the anisotropic permeability of the fractured rock system. Permeability estimates are based on the number of cracks open in each direction. This approach yields a prediction of permeability as a function of the angle from the uniaxial stress axis. The inversion for crack orientation is applied to ultrasonic velocity measurements on Barre granite, and permeability predictions for this sample are presented. The inversion results are good and reproduce velocity measurements well, and the permeability predictions show some of the expected trends. Initial comparisons of the predictions with available permeability data, however, show deviations suggesting that further information on partial crack closure and connectivity of cracks should be included into the permeability model.

After considering the more general range of crack orientations considered in the

inversion procedure, we analyze the behavior of elastic waves on encountering a fractured region which is too small for velocity variations to become apparent, and therefore too small for observations of shear wave splitting. This new problem is solved through the study of the scattering of elastic waves from isolated fracture zones. When the scattering zone is much smaller than the wavelength of an incident plane wave and has a relatively small difference in elastic properties from the surrounding background medium, the Born approximation allows an estimate of the radiation pattern of elastic wave Rayleigh scattering of both compressional and shear waves due to a perturbation of any combination of the 21 independent elastic constants. Examination of radiation patterns for incident shear and compressional waves shows that the shear waves are the most sensitive to the alignment of fractures in anisotropic zones. As the polarization of the incident S-wave ranges from perpendicular to parallel to the fractures, the amplitude of the scattered waves goes to zero.

The calculation of scattered wavefields is extended to larger regions of inhomogeneity by application of a Ray-Born technique. This approach applies ray methods to the computation of Green's tensors for the background medium and uses the Born approximation to determine the scattered wavefield from each volume element within a discretized model of heterogeneity. Comparisons of Ray-Born results to the complete solution for scattering from an elastic sphere show that that method works fairly well for wavelengths on the order of five times larger than the scale lengths typical of the heterogeneity, but then breaks down to the failure of the Born approximation. With this restriction in mind, the method is applied to a hypothetical layered earth model containing a thin, laterally extensive fracture zone. The results confirm that scattering from shear waves will give unique information on fracture orientation even for this extended zone. On the other hand, compressional waves are more useful in inference of nature of the fluid filling the cracks. Modeling of scattered waves in VSP data from the Lardarello geothermal field in Italy demonstrates the applicability of the method and suggests that at least in this locality, anisotropic fracturing is not responsible for the observations. Analysis of the Fresnel zones affecting reflections from the thin fracture zones responsible for the scattering allows a delineation of regions of more intense fracturing, information of importance for the development of geothermal resources.

Thesis Advisor: M. Nafi Toksöz
Title: Professor of Geophysics

Acknowledgements

This thesis has benefited from the influence of a number of people. My advisor, Nafi Toksöz, has provided a research environment at the Earth Resources Laboratory with support and direction encouraging me to take my research interests into a variety of areas while contributing his own insights into the nature of rock physics and seismic data. In addition, his prodding helped me to gain the confidence to publish my work. Close work with Ari Ben-Menahem has also been an invaluable aspect of my education. His enthusiasm for and understanding of mathematical geophysics has thoroughly strengthened my understanding of wave propagation. I also learned from him the joy of truly beginning to understand subtle aspects of this field, not to mention the insights of his analyses of World Cup soccer matches! Many conversations with Arthur Cheng have guided my study of the physics of fractured rock and other aspects of the strategy of science at ERL. Roger Turpening has always been supportive and, as usual, has pushed all students in an effort to drive us into examining "real data". Of course, the opportunity he provided for me to visit the Michigan reef experimental site was also very valuable in helping me to understand how unrealiable the collection of this "real data" can be! Wafik Beydoun has always been encouraging and helpful in regard to the implementation and use of Ray-Born methods, while Fausto Batini and Gildes Omnes both provided data and helpful suggestions in the study of the VSP data from the Badia 1A well in Lardarello. Interaction with a number of other staff and faculty members in the Department of Earth, Atmospheric and Planetary Sciences has also been very beneficial. Some of these are Greg Duckworth and Ted Madden, who served as advisors in my early years, Vernon Cormier, and Batakrishna Mandal. ERL administrative and computer staff have also provided a great deal of help in the practical side of getting through MIT. I appreciate the help of Sara Brydges, Naida Buckingham, Liz Henderson, Jane Maloof, Al Taylor and Sue Turbak.

One of the most important sides of an education is the interaction with other students. My officemates Lisa Block and Delaine Thompsen have been friendly and encouraging through my time here, although they didn't always appreciate my efforts at air conditioning the office in winter. Arcangelo Sena has always been eager to help with mathematical problems and discussions of some very difficult problems in our various collaborations, and he was a great traveling companion on our trips to Venezuela and to Israel. Ted Charrette was very helpful in his capacity as an nCUBE employee at helping me implement my computer codes on the nCUBE parallel computer, which made the efficient development of the Ray-Born code possible. I have also benefited greatly from working with and enjoying the company of a number of other students, including Chris Bradley, Bob Cicerone, Karl Ellefsen, Jack Foley, Joe Matarese, Jeff Meredith, Michael Prange, Ed Reiter, and Craig Schultz.

On a more personal note, I am indebted to my parents and brother for their support and encouragement throughout my education. Even when things were most difficult and stressful, they continued to be a very positive influence. Many friends

from the MIT Baptist Student Fellowship and Metropolitan Baptist Church have helped me to maintain a balanced perspective on life as a whole during my stay at MIT. I am especially grateful for the positive spirit of chaplain Betsy Draper and Rev. David Draper ("No P.N.!"), who helped me see how to pursue an understanding of the truly important things in life. Missy Tackett has also been supportive and encouraging as I struggled with this thesis, as were Keith Eady and Steve Walker.

This work has been supported by the Reservoir Delineation and Full Waveform Acoustic Logging Consortia at the Earth Resources Laboratory, a National Science Foundation Graduate Fellowship, an nCUBE Fellowship, and the Defense Advanced Research Project Agency through contract #F 19628-90-K-0057 administered by the Air Force Geophysics Laboratory.

Contents

1 INTRODUCTION **9**

1.1 Objectives 9

1.2 Background 12

1.3 Outline 17

2 Fracture Orientation and Permeability Estimation From Velocity Anisotropy in Fractured Rock **21**

2.1 Introduction 21

2.2 Theory 23

2.2.1 Inversion for Crack Orientations 23

2.2.2 Permeability Prediction 30

2.3 Application To Ultrasonic Data 33

2.3.1 Velocity Inversions 34

2.3.2 Permeability Predictions 38

2.4 Discussion And Conclusions 40

3 Elastic Wave Scattering by Anisotropic Obstacles: Application to Fractured Zones **63**

3.1 Introduction 63

3.2 Estimation of the General Scattered Field 67

3.2.1 The Born Approximation 67

3.2.2 The Moment Tensor Source 70
3.2.3 Radiation Patterns for Rayleigh Scattering 72
3.3 Scattering Due to Fracturing 73
3.3.1 Perturbations to Elastic Constants 74
3.3.2 Radiation Patterns for the Fractured Scatterers 81
3.4 Discussion and Conclusions 86

4 Ray-Born Synthetic Seismograms for Anisotropic, Fractured Media 100
4.1 Introduction 100
4.2 Computation of the Born Scattered Field 103
4.2.1 The Born Integral Equation 103
4.2.2 Evaluation of the Integral 105
4.3 Comparison of Ray-Born Results to a Known Analytic Solution . . . 110
4.4 Synthetic Seismograms from a Fracture Zone Model 116
4.4.1 Isotropic, gas-filled fractures 118
4.4.2 Anisotropic, gas-filled fractures perpendicular to the receiver array 120
4.4.3 Anisotropic, gas-filled fractures parallel to the receiver array . 121
4.4.4 Anisotropic, gas-filled fractures at 45 degrees to the receiver array 121
4.4.5 Isotropic, water-filled fractures 122
4.5 Application to Field Data 123
4.5.1 Background Model 124
4.5.2 Data 124
4.5.3 Modeling results 125
4.6 Discussion and Conclusions 130

5 Summary and Conclusions 181
5.1 Implications for Fracture Analysis with Seismic Data 185
5.2 Future Work 187

A Effective Elastic Constants for Fractured Media **189**

B Derivations of Radiation Patterns for Rayleigh Scattering **193**

B.1 Single dipole 193

B.2 Two dipoles 196

B.3 Double couple 198

B.4 Double couple and a dipole 200

B.5 Two double couples. 202

C Spherical Coordinates in the Development of Radiation Pattern Equations **204**

D Radiation Patterns for Perturbations to the Elastic Constants **206**

E Density Contributions to Scattering by Fractured Volumes **215**

F Overview of Dynamic Ray Tracing **219**

References **224**

Chapter 1

INTRODUCTION

It is always hazardous to attempt the quantitative discussion of geological problems, for the reason that the conditions are apt to be complex and imperfectly known; and in this case an uncertainty attaches to the law of relation, as well as to the quantities to which it is applied.

—Grove Karl Gilbert (1880)

1.1 Objectives

Elastic wave propagation in the earth is affected by many forms of heterogeneity. While layered earth models, along with the well developed theory of wave propagation in plane or radially layered media, can account for a large portion of seismic data from both local and teleseismic recordings, there are many observations which clearly reflect more complicated features. Much of this complication results simply from two or three-dimensional geologic structure along the propagation path. However, it is becoming increasingly clear that anisotropy also can have a significant influence on seismic observations. The most concrete evidence for the presence of anisotropic earth materials arises from the phenomenon of shear-wave splitting or birefringence, the separation of a shear wave into two quasi-shear waves with different velocity

and perpendicular polarizations as the wave propagates in an anisotropic region. Definitive identification of this splitting allows the inference of an anisotropic material.

Many studies have used this property, or the general variation of travel time with direction, to determine the presence of anisotropy in a variety of settings. The oceanic crust and upper mantle can display a significant degree of anisotropy (Hess, 1964; Raitt et al., 1968; Bachman, 1979, 1983; White and Whitmarsh, 1984; Stephen, 1981, 1985; Kuo et al., 1987; Berge et al., 1991). Earthquake source regions are also often anisotropic (Crampin et al., 1985; Peacock et al., 1988; Kaneshima et al., 1988, 1989; Iannaccone and Deschamps, 1989; Booth et al., 1990; Savage et al., 1990; Shih and Meyer, 1990), as are other regions of crystalline crust (Hurich et al., 1985; Chroston and Max, 1988; Christensen and Szymanski, 1988; Wang et al., 1989; Leary, 1990). It is also clear that anisotropy is a property of importance in sedimentary basins where hydrocarbon exploration is common (Podio et al., 1968; Kaarsberg, 1968; Jones and Wang, 1981; Robertson and Corrigan, 1983; White et al., 1983; Helbig, 1984; Banik, 1984; Winterstein, 1986; Thomsen, 1986; Kerner et al. 1989). It is well known that an elastic medium containing a set of aligned ellipsoidal inclusions will be effectively anisotropic for wavelengths greater than the dimension of an individual ellipsoid (Hudson, 1980, 1981). A fractured medium can be modeled as a homogeneous matrix containing a set of such inclusions with a low aspect ratio, and, if the fractures are aligned, it follows that the resulting material will be anisotropic. Observations of shear-wave birefringence in areas where other explanations are not geologically realistic have led to the suggestion that many portions of the earth's crust contain fractures or microcracks which are aligned in a parallel, vertical orientation by the influence of regional tectonic stresses (e.g., Bamford and Nunn, 1979; Crampin, 1981; Leary and Henyey, 1985; Crampin et al., 1985; Crampin et al., 1986; Martin and Davis, 1987; Leary et al., 1987; Peacock et al., 1988; Leary et al., 1990).

This particular form of anisotropy is of significant economic and academic interest. For example, it is possible that the seismic anisotropy can be used to gain a knowledge

of the *in situ* state of stress in the subsurface by relating anisotropic velocities to fracture orientation. Knowledge of fracture orientation is also of great value in a rock where the matrix has a background permeability which is very low, as the fractures can provide the most important conduits for fluid flow and can cause a relatively significant permeability. Therefore, any information on subsurface fracture properties which can be obtained from seismic data has many possible uses, and a number of studies have been conducted to model such media. The majority of these works have considered layered earth materials with a constant degree of fracturing of identical orientation. Due to the inherent complexities of the earth, however, a model with large regions of the crust containing equal densities of fractures perfectly aligned is clearly a simplification. Like all layered earth models, it will probably allow the explanation of many data sets, but will fall short in cases where the earth is simply too complicated to be represented by this idealized structure.

The purpose of this thesis is to propose and test several models for elastic wave propagation and scattering in fractured media and utilize the results to develop an understanding of the effects of anisotropic fracture distributions on fluid flow in the subsurface. These techniques are designed to allow remote inference of the fracture properties in the crust. In turn, this knowledge will aid in the determination of the *in situ* state of stress and permeability, which are important for an understanding of current tectonic influences and for analysis of hydrothermal and hydrocarbon production.

We examine first the properties of a granite which is subjected to uniaxial stress in the laboratory. In this case where only a comparatively small laboratory rock sample is considered, the microcracks create the anisotropy. Our analysis allows an investigation of the effects on elastic wave velocities of cracks distributed over a range of orientations. Subsequently, we view the problem from a more regional scale to consider instead the influence of complex zones of locally intense, parallel fracturing on elastic wave propagation. To this end, we apply the Born approximation to scattering

in anisotropic media in Chapter 3. Consideration of the Rayleigh scattering from a single, small fractured volume provides some simple guidelines for the generation of scattered wavefields which can be extended to more realistic and involved models of fracture zones. We do this in Chapter 4 by computing the Green's tensors for wave propagation in the background medium with ray theoretical methods. The asymptotic Green's tensors, in combination with the Born scattering theory from Chapter 3, provide a means for modeling the seismic waves reflected from three-dimensional fracture zones such as those commonly found in geothermal fields. In the remainder of this chapter, we describe in more detail the background leading to the material described in the following chapters and then provide a summary of the contents of the thesis.

1.2 Background

The problem of determining the effective elastic properties of two-phase mixtures has frequently been investigated in order to better understand the seismic properties of rocks under *in situ* conditions. It has long been suggested that the closing of microcracks explains the rapid increases of elastic wave velocities with applied pressure in laboratory measurements (e.g., Nur and Simmons, 1969; Nur, 1971). With this evidence for the presence of microcracks in rocks which form the earth's crust, several models were developed for the seismic velocities of a homogeneous medium containing voids or inclusions representing cracks with different advantages and various degrees of accuracy. Isotropic models for the effects of randomly aligned ellipsoidal cracks include those by Kuster and Toksöz (1974) and O'Connell and Budiansky (1974). The latter has the advantage of allowing the introduction of larger quantities of fractures through the application of a self-consistent approximation which accounts for multiple scattering.

However, to investigate the seismic effects of aligned cracks, different models must

be sought. Because of the symmetry in the problem, a material containing parallel cracks is transversely isotropic with five independent elastic constants and an axis of symmetry perpendicular to the cracks. Anderson et al. (1974) presented a numerical scheme for the evaluation of the anisotropic velocities in such media which can include arbitrary ellipsoidal voids. Nishizawa (1982) extended this approach by adding only a small amount of the total fracture volume and calculating the effective properties of the resulting anisotropic material before adding another subset of fractures. This iterative procedure should allow the application of the theory to large crack densities. In contrast to these numerical schemes, Hudson (1980, 1981; see also Crampin, 1984) developed an analytic solution for the effective elastic constants of the transversely isotropic medium containing aligned cracks. This solution was obtained by consideration of the wavefields scattered by a set of ellipsoidal cracks with three important assumptions: 1) the incident wavelength is longer than the size of individual cracks, 2) the cracks have small aspect ratio, and 3) the overall crack density is low. With these assumptions, a set of equations for the five independent elastic constants in the effective medium was derived. It is an expansion of the total scattered wavefield in powers of crack density ξ up to second order terms. This crack density is equal to na^3, where n is the number density of cracks and a is the radius of an individual ellipsoidal crack. For simplicity the crack is assumed to be "penny-shaped", an ellipsoid with two equal semi-axes much larger than the third. Various possibilities for pore-fluid are considered in the derivation. This solution, though subject to certain limitations due to the assumptions, is versatile and flexible due to the explicit equations for the elastic constants. These expressions can easily be used in theoretical applications other than the calculation of velocities.

The utility of the Hudson solution is obtained by the use of an idealized representation of the structure of crack distributions in true earth materials, however. True rock microcrack distributions can be observed to have a wide variety of shapes and interconnections which can strongly affect the elastic behavior of the sample (Hadley,

1976; Batzle et al., 1980). In particular, the two surfaces of a crack are not simple and smooth, but instead have roughness and asperities which come into contact as a crack closes with increasing applied pressure. Gangi (1978) developed a "bed of nails" model which applied a statistical distribution of crack surface roughness to examine in detail the pressure dependence of crack closure and permeability of rough cracks. Walsh and Grosenbaugh (1979) modeled the compressibility of a material containing an isotropic distribution of rough cracks with isolated asperities, while more recently Brown and Scholz (1985) presented a model for closure of a single crack or joint with two rough surfaces. An inversion scheme developed by Zhao and Toksöz (1991a) based on a modified version of this theory allows an estimation of the distribution of roughness of the crack surfaces. For the purposes of this thesis, we will utilize the penny-shaped crack model following Hudson (1980) in order to make theoretical developments and calculations feasible.

One means of making the penny-shaped crack model more realistic for the study of anisotropic media is to allow for cracks with a range of orientations distributed around a preferred direction rather than a single, parallel set of cracks. Sayers (1988a, 1988b) developed a scheme for averaging the Hudson (1980) expressions for the effective moduli over a crack orientation distribution function, and, through a curve fitting procedure, for obtaining an estimate of crack density. This algorithm was applied to a set of ultrasonic measurements of velocity in a granite sample which was subjected to a uniaxial stress. As the uniaxial stress was applied, the velocities which were initially isotropic became distinctly anisotropic, with two unique quasi-shear waves. The behavior results from crack closure with increasing stress which is dependent on the crack orientation with respect to the uniaxial stress axis. Such a medium displays transverse isotropy even though the cracks are not parallel, as there is still a unique axis of symmetry, the stress axis. In Chapter 2, we take this idea of averaging over crack orientation and develop a true inversion scheme which helps to gain an understanding of the unique parameters relating the mathematics to the observable velocity

variations in the rock. One of the principal conclusions is that it is very difficult to develop a unique set of parameters describing the true microcrack properties of the rock which also allows a calculation or prediction of the elastic properties.

These detailed studies of the microcrack structure of rocks make clear some of the difficulties involved in obtaining a thorough understanding of the relationship between nature of cracks and elastic wave propagation. At the same time, it is possible to use a simple representative model of the rock, such as that employed by the Hudson theory, to account for many aspects of seismic observations. There have been many observations of anisotropic velocity variations in a variety of geological environments (Bamford and Nunn, 1979; Leary and Henyey, 1985; Crampin et al., 1986; Leary et al., 1987; Martin and Davis, 1987). Modeling of seismic waves in such media generally applies models which contain homogeneous layers of fractured rock, with effective elastic constants from the Hudson theory or a similar approach (Liu et al., 1989; Mandal and Toksöz, 1990). The results make it clear that such media will yield distinctive evidence for anisotropy and therefore of the aligned fracturing, chiefly through analysis of polarization anomalies.

However, it is also clear from field observations that in many regions the fracture zones cannot be represented by simple, homogeneous layered structures. For example, in many regions of interest for geothermal field development or for nuclear waste disposal, the problem is to find relatively localized zones of fractured rock which may or may not be laterally continuous and are certainly not simple layers (Green and Mair, 1983; Carswell and Moon, 1985; Batini et al., 1985a; Batini et al., 1990.; Juhlin et al., 1991). Such media cannot be modeled by the reflectivity or discrete wavenumber algorithms, which are limited to plane layered media (Booth and Crampin, 1983; Mandal and Toksöz, 1990). Even ray theoretical methods may not be applicable if the zone of fracturing is on the order of a wavelength in dimension. Fracture zones in the Lardarello geothermal field in Italy fit this description (Batini et al., 1990). These thin fracture zones have significant seismic signatures (Batini et al., 1983; Batini et

al., 1985a), and an important area of research is to gain an understanding of the effects of such zones on seismic data in order to better locate suitable drilling sites for development of the geothermal field.

For these problems, a different modeling algorithm must be developed. In Chapter 4, we present a Ray-Born algorithm to solve this problem. Beydoun and Mendes (1989) developed a Ray-Born method for modeling and inversion in isotropic media which combines two very general approximations. The Born approximation is used to account for the effects of short wavelength heterogeneities in a background medium. This approach expresses the heterogeneity as a perturbation to the elastic properties of the background which in turn leads to an expression for the scattered wavefield as a perturbation to the displacements resulting from propagation in the background medium. The effect of the heterogeneity can be expressed as a secondary source radiating energy as the incident wave passes by. A version of this solution was derived as early as 1896 to derive the scattering of acoustic waves from objects much smaller than a wavelength in dimension (Rayleigh, 1945). This phenomenon is known as *Rayleigh scattering.* Since then, there have been numerous applications of this general type of theory to elastic, isotropic media for both modeling the scattered field and as a basis for inversion (e.g., Miles, 1960; Chernov, 1960; Gubernatis et al., 1977b; Clayton and Stolt, 1981; Cohen et al., 1986; Boyse and Keller, 1986; Beydoun and Mendes, 1989). More recently, expressions for Rayleigh scattering due to transversely isotropic obstacles in an isotropic medium have been developed by Ben-Menahem and Gibson (1990), and the theory is extended to the case of the most general anisotropic obstacle in Chapter 3.

The second fundamental approximation involved in the Ray-Born method is the application of asymptotic ray theory for the calculation of wave propagation in the background medium. This step imposes the constraint of a smoothly varying background on the procedure, as the high frequency assumption involved in the development of the ray equations requires that the wavelength of the propagation signal be

much less than the scale length typical of the medium (Červený et al., 1977; Ben-Menahem and Beydoun, 1985). Therefore, the Ray-Born approach in full implies that the wavelength must be *greater* than the scale length of the heterogeneous zone of interest, but *less* than the scale length of the background earth model.

Implementation of the Ray-Born computations has two basic steps. First the Green's tensors for wave propagation from the energy source to the scattering region and from the scattering region to the receivers are calculated by paraxial ray tracing (Červený et al., 1984; Červený, 1985; Beydoun and Keho, 1987). Secondly, the Born approximation is used to compute the properties of the secondary sources which represent the heterogeneity. The incident wavefield controls the properties of the secondary source, and propagation from this source is controlled by the rays from the scatterer to receiver. An integration over the total region of heterogeneity is required. Whereas previous applications of this approach have been only to isotropic media, in Chapter 4 we also include the effects of anisotropy due to fractures.

1.3 Outline

The background provided above gives the motivation behind our investigations of the complex models of fractured media. This material will be covered in the following chapters as follows.

In Chapter 2 we consider the behavior of an isotropically fractured medium subjected to uniaxial stress. Following the method suggested by Sayers (1988a, 1988b), it is assumed that the unstressed rock contains only a random orientation of cracks, and a model for the closure of cracks with applied uniaxial stress can be obtained. By expanding the resulting orientation distribution function in generalized spherical harmonics, the effective elastic constants from the Hudson (1980, 1981) theory are averaged over all orientations yielding the effective properties of the rock sample under uniaxial stress. The resulting equations for phase velocities in such a material are

nonlinear functions of crack density ξ and a parameter α_m which describes the aspect ratio distribution. An inversion for these two parameters is implemented by linearizing the equations for phase velocity about starting estimates of ξ and α_m. An estimate of permeability variation with direction in the resulting transversely isotropic medium is obtained from a model which assumes that the anisotropic permeability will be related to the density of cracks open in a given direction. The inversion is applied to ultrasonic measurements of velocity in a Barre granite sample (Nur and Simmons, 1969), and permeability predictions are presented. We discuss the implications for the inference of both crack structure and permeability from velocity measurements.

Chapter 3 extends the theory of Born scattering to include a general anisotropic perturbation to an isotropic background medium. The perturbation can therefore have up to 21 independent elastic constants. After deriving the general expressions for the radiation patterns, the specific example of Born scattering from a localized region of fracturing within an isotropic medium is considered. This is a canonical problem which can be used to gain some intuitive guidelines for both forward and back scattering from more complicated regions of fracturing, anisotropic or isotropic. The problem is solved by using as perturbations to the elastic constants the results of the Hudson (1980, 1981) theory. By substituting these analytic expressions for the perturbations into the appropriate equations for Rayleigh scattering from the Born approximation, we can write explicit results for Rayleigh scattering from the fractured region due to an incident plane wave. We show that the scattered shear-wave energy from an anisotropic region will be distinctly different from that generated by an isotropically perturbed zone. In particular, when the cracks are aligned rather than randomly oriented, the shear wave scattering in this approximation will vanish for directions of incidence where the shear wave polarization is parallel to the plane of the fracture orientation. This implies that some experiments might be possible which could use observations of seismic wave scattering to obtain some knowledge of the orientation of aligned fractures in the subsurface.

The solution to the canonical problem of Rayleigh scattering from an anisotropic obstacle derived in Chapter 3 forms a fundamental part of the Ray-Born algorithm presented in Chapter 4. We begin by outlining how the algorithm can be used for a fully general anisotropic medium with anisotropic perturbations using ray theoretical solutions for the Green's tensors in an anisotropic or isotropic medium along with the Born approximation. Our implementation includes only isotropic earth models with anisotropic perturbations due to aligned fractures. The computation of Green's tensors in the background is accomplished by using dynamic ray tracing in ray-centered coordinates, which allows the simple application of paraxial ray tracing methods. After describing the algorithm, we first test its accuracy by comparison with a complete discrete wavenumber solution for scattering from an elastic sphere due to an incident plane compressional wave. The results suggest that the wavelength of interest must be on the order of five times longer than the length scale of the heterogeneous zone to be modeled with the Ray-Born method. Using this guideline, we next apply the method to a hypothetical layered model containing a thin but laterally extensive fracture zone. By considering both isotropic and anisotropic fracture zones, we show that the P to P-wave reflections from the fracture zone can be expected to yield almost no information on fracture orientation, though S to S-wave reflections are highly sensitive to the orientation of the incident wave polarization with respect to the aligned fractures. In contrast, the P-wave reflections can be used in some cases to allow an inference of the nature of the fluid filling the fractures. Finally, after considering this hypothetical model, we apply the Ray-Born calculations to the modeling of VSP data from the Lardarello geothermal field in Italy. As only vertical component P-wave data is available from the field experiment, we would expect it would not be possible to determine the presence or absence of fracture alignment in the thin fracture zones below the depth of the well. However, it was possible to develop a realistic model for these fracture zones which was entirely isotropic, and it was not possible to find an vertical fracture model of realistic fracture density which could explain the large

amplitude reflected waves found in some of the data. This suggests that anisotropic fracturing is not causing these reflections.

In Chapter 5, we summarize the results of the thesis. The different models we have derived allow different ways of developing more realistic depictions of the propagation of elastic waves in fractured media. We discuss the insights gained from these studies as well as some of the limitations which became apparent. Possible extensions of this work for future research applications are suggested.

Chapter 2

Fracture Orientation and Permeability Estimation From Velocity Anisotropy in Fractured Rock

With every new answer unfolded, science has consistently discovered at least three new questions.

—Wernher von Braun

2.1 Introduction

A common goal of seismic field experiments is to estimate rock properties such as permeability from the information contained in the seismic waveforms. Fractured media provide a particularly interesting example of a permeable medium, since a material containing an aligned system of cracks will be effectively anisotropic for elastic wavelengths much greater than the crack dimensions (Hudson, 1980, 1981; Crampin, 1984). While a particular rock may have a randomly oriented distribution

of cracks, application of a uniaxial stress will preferentially close fractures depending on orientation with respect to the stress axis (Walsh, 1965; Nur, 1971). It has been suggested that the prevailing tectonic stress regimes in the Earth frequently include a maximum compressive stress which is horizontal, resulting in such an alignment of vertically oriented cracks (Crampin, 1981). A uniaxial stress is easily produced in laboratory experiments as well (Nur and Simmons, 1969).

Analysis of the elastic anisotropy produced by crack alignment can be used to investigate fracture properties. Sayers (1988a, b) suggested a means of inverting for the orientations of crack normals using these velocity measurements. This method involves an expansion of the fracture orientation distribution function in terms of harmonics related to the system of Euler angles describing the orientations. The coefficients in the expansion are subsequently related to perturbations in elastic moduli predicted by the Hudson (1981) theory for the properties of a cracked medium, and an inversion was performed based on an approximate expression for elastic wave velocity derived from a variational approach (Sayers, 1988a, b).

In this chapter, we apply an alternative form of an inversion for crack orientations. A nonlinear inversion is performed by linearizing the phase velocity expressions about an initial estimate of crack density and a parameter describing the distribution of crack aspect ratios. The resulting estimates of crack orientations and the distribution of aspect ratios with respect to direction are used to predict permeability as a function of direction with respect to the uniaxial stress axis. These permeability predictions are calculated based on a model for permeability in the fractured medium which accounts for crack closure effects by multiplication by the fraction of cracks open in a given direction. The method is applied to ultrasonic velocity data for Barre granite (Nur and Simmons, 1969), and the implications of the results for permeability prediction are discussed.

2.2 Theory

2.2.1 Inversion for Crack Orientations

The rock medium is assumed to contain an isotropic distribution of cracks in the unstressed state so that the effective elastic parameters of the material are also isotropic in this case. When a uniaxial stress is applied to such a material, some of the cracks will close depending on the angle of the crack normal with respect to the stress axis (Walsh, 1965) (Figure 2-1). This angle γ_0 is given by

$$\cos\gamma_0 = \sqrt{\frac{\alpha E_0}{\sigma}} \tag{2.1}$$

where α is the crack aspect ratio, E_0 is the Young's modulus of the uncracked material, and σ is the applied uniaxial stress. The initially isotropic material will become anisotropic after application of the stress with rotational symmetry about the stress axis (Nur, 1971). The effective elastic properties of the stressed, cracked material will then have a transversely isotropic symmetry.

The effective elastic moduli of the medium can be estimated by averaging the elastic constants of the fractured material over a crack orientation distribution function $N(\theta, \psi, \phi)$, where θ, ψ, and ϕ are Euler angles of rotation specified in Figure 2-2. These angles define the set of rotations necessary to obtain the orientation of the crack Cartesian coordinate system x, y, z for each crack with respect to the composite medium reference Cartesian coordinate system denoted by X, Y, Z. We specify the initial orientation of the fracture prior to rotation such that the crack normal (parallel to z) is parallel to Z, and the other two axes x and y are therefore in the plane of the fracture. Note that for a circular crack, only θ and ψ are necessary to fully specify crack orientations, and ϕ can freely range from 0 to 2π. The crack orientation distribution function $N(\theta, \psi, \phi)$ is defined so that integration over the full domain is one:

$$\int_0^{2\pi}\int_0^{2\pi}\int_0^{\pi} N(\theta,\psi,\phi)\, d\theta\, d\psi\, d\phi = 1 \tag{2.2}$$

This function can be expanded in generalized spherical harmonics

$$N(\theta,\psi,\phi) = \sum_{l=0}^{\infty} \sum_{m=-l}^{l} \sum_{n=-l}^{l} W_{lmn} Z_{lmn}(\zeta) e^{-im\psi} e^{-in\phi} \tag{2.3}$$

Here $\zeta = \cos\theta$. The derivation of the generalized Legendre functions $Z_{lmn}(\zeta)$ and some of their properties are described by Ben-Menahem and Singh (1981). Each coefficient W_{lmn} in the expansion of the orientation distribution function $N(\zeta,\psi,\phi)$ is obtained by integrations of the following form:

$$W_{lmn} = \frac{1}{4\pi^2} \int_0^{2\pi} \int_0^{2\pi} \int_{-1}^{1} N(\zeta,\psi,\phi) Z_{lmn}(\zeta) e^{im\psi} e^{in\phi}\, d\zeta\, d\psi\, d\phi \tag{2.4}$$

With this expansion, the orientation distribution function can be decomposed into harmonic components.

If a polycrystalline aggregate were considered, an estimate of the elastic properties of the aggregate could be obtained by simply averaging the elastic constants of the individual crystals with respect to the orientation distribution. This method, the Voigt approach, is known to yield an upper bound on the elastic constants (Hearmon, 1961). The same procedure can be applied to the fractured medium by averaging the effective elastic constants of fractured material over all sets of fracture orientations in the rock (Sayers, 1988a). Since this is an upper bound, and it is not clear how far removed from the true solution this bound is, there will be some limitations on the accuracy of the results which are not well defined. Application of similar techniques to other problems involving cracks has shown that resulting errors are generally not too large for smaller crack concentrations, however (Walsh, 1965). The averaged constants can be written (Morris, 1969)

$$\begin{aligned} \overline{c}_{ijkl} &= c_{mnpq} \int_0^{2\pi} \int_0^{2\pi} \int_{-1}^{1} T_{ijklmnpq}(\zeta,\psi,\phi)\, N(\theta,\psi,\phi)\, d\zeta\, d\psi\, d\phi \\ &= c_{mnpq} \overline{T}_{ijklmnpq} \\ T_{ijklmnpq} &= \frac{\partial x_i}{\partial X_m} \frac{\partial x_j}{\partial X_n} \frac{\partial x_k}{\partial X_p} \frac{\partial x_l}{\partial X_q} \end{aligned} \tag{2.5}$$

The Einstein summation convention is applied. The matrix $\overline{T}_{ijklmnpq}$ essentially defines an average rotation of the elastic constants of the individual components c_{mnpq},

which for the polycrystalline case are the elastic constants of a single crystal and for the fractured material case are the constants corresponding to a single set of parallel fractures. Morris (1969) has calculated a table of values for the matrix elements $\overline{T}_{ijklmnpq}$ in terms of the coefficients of the expansion of the distribution function up to order $l = m = n = 4$ for composites of materials with orthorhombic symmetry which can also be applied to material with hexagonal symmetry. The orthogonality properties of the harmonics cause terms for indices greater than 4 to disappear, since the fourth-order elastic tensor c_{mnpq} will only have coefficients for $l = m = n = 4$. The Morris (1969) table can easily be used in equation (2.5) to find the overall properties.

The theory of Hudson (1980, 1981) for the stiffness constants of a fractured medium can be used to obtain values for c_{ijkl} to use on the right-hand side of equation (2.5). This theory provides an expression for the effective elastic tensor c_{ijkl} of a homogeneous medium containing a single set of parallel penny-shaped cracks with dimensions much less than a wavelength. This expression is in terms of a first-order correction c^1_{ijkl} to the elastic tensor of the unfractured material c^0_{ijkl}:

$$c_{ijkl} = c^0_{ijkl} + \xi\, c^1_{ijkl} \tag{2.6}$$

Here ξ is the crack density defined by $\xi = na^3$, n is the number of cracks per unit volume, and a is the crack radius. The explicit forms of the correction terms is given in Appendix A. Hudson (1980) also derived a second-order term which results in values of the stiffnesses which are quadratic functions of the concentration of cracks, and hence the second-order theory actually displays divergent behavior for large crack concentrations. In order to match the observed data discussed below, the second-order correction was therefore not applied.

If we apply a stress along the z axis, the only nonzero coefficients in the expansion of the resulting crack distribution will be W_{000}, W_{200}, and W_{400} due to the symmetry around the z axis and the circular symmetry of the cracks. For purposes of the inversion, we follow Nur (1971) and Sayers (1988b) and take as a model for the crack

aspect ratio distribution in the unstressed state a simple linear function

$$N^l(\alpha) = N_0^l(1 - \frac{\alpha}{\alpha_m}) \qquad 0 < \alpha < \alpha_m \tag{2.7}$$

The parameter α_m sets the maximum aspect ratio present in the rock sample and is given by $\alpha_m = \sigma_0/E_0$, where σ_0 is the hydrostatic pressure required to close all cracks. To serve as a density function, equation (2.7) is normalized by the total number of cracks present n_σ^l at stress σ:

$$n_\sigma^l = N_0^l \left[\frac{\alpha_m}{2} + \frac{\sigma^2}{E_0^2} \frac{1}{10\alpha_m} - \frac{\sigma}{3E_0} \right] \tag{2.8}$$

Given this distribution of cracks, the crack orientation distribution function after application of a uniaxial stress can be obtained using the closure model given by equation (2.1). At any given angle θ from the stress axis, all fractures with aspect ratio $\alpha > \sigma \cos^2\theta/E_0$ are open. The resulting coefficients in the expansion of the orientation distribution function are

$$\begin{aligned}
W_{000} &= \frac{1}{8\pi^2} \\
W_{200} &= -\frac{1}{5n_\sigma^{l\prime}2\pi^2}\sqrt{\frac{5}{2}}\frac{\sigma}{E_0}\left(\frac{1}{3} + \frac{1}{7}\frac{\sigma}{E_0\alpha_m}\right) \\
W_{400} &= \frac{1}{315}\frac{1}{n_\sigma^{l\prime}\pi^2}\sqrt{\frac{9}{2}}\frac{\sigma^2}{E_0^2\alpha_m} \\
n_\sigma^{l\prime} &= \frac{n_\sigma^l}{N_0^l}
\end{aligned} \tag{2.9}$$

One important aspect of this particular distribution model is that the expansion up to terms $l = 4$ is exact, and there is therefore no truncation error from termination of the series. If, however, only a single crack aspect ratio were considered, the poststress distribution of cracks resulting from the closure model governed by equation (2.1) would be a box car function with respect to the θ (or η) variable, and strong Gibbs phenomena effects would result since accurate representation of this discontinuous function will require a large number of terms in the expansion. Truncation of the expansion series in this case would yield unrealistic results due to strong oscillations of the predicted distribution function.

The choice of aspect ratio in equation (2.7) is rather arbitrary and may not be truly representative of the cracks within a rock sample, though accuracy of results using the distribution will give some indication of its validity. For purposes of comparison in applications, we also consider a flat aspect ratio distribution

$$N^f(\alpha) = N_0^f \qquad 0 < \alpha < \alpha_m \tag{2.7'}$$

For this aspect ratio distribution, the normalization constant is

$$n_\sigma^f = N_0^f \left[\alpha_m - \frac{1}{3}\frac{\sigma}{E_0}\right] \tag{2.8'}$$

and the coefficients in the generalized spherical harmonic representation are

$$\begin{aligned} W_{000} &= \frac{1}{8\pi^2} \\ W_{200} &= -\frac{1}{n_\sigma^{f\prime} 30\pi^2}\sqrt{\frac{5}{2}}\frac{\sigma}{E_0} \\ W_{400} &= 0 \\ n_\sigma^{f\prime} &= \frac{n_\sigma^f}{N_0^f} \end{aligned} \tag{2.9'}$$

The results for this hypothetical distribution of cracks may be compared to those obtained using the distribution given in equation (2.7).

Given the values of the elastic constants resulting from the averaging process, velocities can be computed for the stressed, cracked material. The quasi-compressional wave phase velocity v_{qP}, vertically polarized quasi-shear wave velocity v_{qSV}, and horizontally polarized shear wave velocity v_{SH} in a general transversely isotropic medium are given by (Musgrave, 1970)

$$\rho v_{qP}^2 = \overline{C}_{44} + \frac{1}{2}\left(h\cos^2\beta + a\sin^2\beta\right) \tag{2.10}$$
$$+ \frac{1}{2}\left[(h\cos^2\beta + a\sin^2\beta)^2 - 4(ah - d^2)\cos^2\beta\sin^2\beta\right]^{1/2}$$

$$\rho v_{qSV}^2 = \overline{C}_{44} + \frac{1}{2}\left(h\cos^2\beta + a\sin^2\beta\right) \tag{2.11}$$
$$- \frac{1}{2}\left[(h\cos^2\beta + a\sin^2\beta)^2 - 4(ah - d^2)\cos^2\beta\sin^2\beta\right]^{1/2}$$

$$\rho v_{SH}^2 = \overline{C}_{44}\cos^2\beta + \overline{C}_{66}\sin^2\beta \tag{2.12}$$

$$\begin{aligned} a &= \overline{C}_{11} - \overline{C}_{44} \\ h &= \overline{C}_{33} - \overline{C}_{44} \\ d &= \overline{C}_{13} + \overline{C}_{44} \end{aligned}$$

Here β is the angle measured from the symmetry axis, in this case the z axis, and the standard 6 by 6 form for the tensor of elastic constants has been utilized. This expression uses the averaged elastic constants to predict the phase velocity value in a given direction.

For a given uniaxial stress σ and intrinsic Young's modulus E_0, the only unknown parameters necessary to compute velocity from equation (2.10) are crack density ξ and maximum crack size α_m. Therefore, these are the natural quantities to determine through inversion procedures. Since equation (2.10) is a nonlinear function of ξ and α_m (through the dependence of the elastic constants on the orientation function), an inversion is performed by linearizing the problem about an initial estimate of model parameters (Tarantola, 1987; Hatton et al., 1986):

$$\mathbf{d} \cong \mathbf{G}\mathbf{m_0} + \mathbf{A}\boldsymbol{\Delta}\mathbf{m} \tag{2.13}$$

Here $\mathbf{d}$ is the data vector containing observed velocity values, $\mathbf{G}$ is the forward model operator yielding velocity predictions for a given set of model parameters in starting model vector $\mathbf{m_0}$, $\mathbf{A}$ is a matrix of partial derivatives of velocity with respect to model parameters, and $\boldsymbol{\Delta}\mathbf{m}$ is a perturbation to the starting estimate of model values. The partial derivatives are somewhat complicated algebraically but can be computed analytically with no approximations. We then perform an iterative least squares inversion for the model parameters α_m and ξ, which allows an estimate of the crack normal orientation distribution.

The forward modeling part of this inversion procedure is similar to that proposed by Sayers (1988a, b), but there are several significant differences. For example, Sayers

(1988b) considers a stress applied along the x axis, which results in a more complicated expansion of the crack orientation distribution function since the orientation is in that case a function of angle ψ as well as θ. The approach described in this paper uses the exact expression for phase velocity, while Sayers (1988b, see also Sayers 1986) uses an approximate expression derived from a variational method.

More important than these considerations, however, are the differences in inversion algorithms. Sayers (1988b) proposes what is essentially a curve fitting methodology where v_{qSV} is approximated by a constant and v_{qP} and v_{SH} are approximated as the sum of a constant and a $\cos 2\theta$ term. The coefficients of these functions are then determined using a least squares procedure, and crack density is obtained from the values of the coefficients. Since there are at most two coefficients in any one of the velocity expressions, only two-parameter values can be obtained in this way, though Sayers (1988b) chooses only to attempt to estimate crack density ξ. In contrast, the procedure suggested here uses the complete expressions for the velocities and for the partial derivatives in the inversion. As many parameters as there are data points can be estimated by this approach, and data types from different experiments can easily be combined in a single inversion. For example, velocity measurements from different stress values can be used to invert for crack density at each stress and for a single value of α_m, which should remain constant for a given rock sample. On the other hand, the curve fitting approach will only allow a determination of the coefficients for each data curve at each stress and does not truly allow a combination of the data sets.

Perhaps the most important advantage of the more complex inversion scheme in seeking to understand the properties of the physical model and of the effects of the cracks on the propagation of elastic waves is that consideration of the partial derivatives allows insights into the sensitivity of the inversion to each of the various parameters. In turn, this gives more information on the validity of inversion results and on the factors which are important in controlling velocity variations within the

fractured medium. A disadvantage of this more complicated inversion algorithm is that it is potentially more susceptible to problems such as nonuniqueness and local minima, whereas as the curve fitting approach will tend to be more robust.

2.2.2 Permeability Prediction

The crack orientation distribution function resulting from the inversion can be used to predict permeability values. The permeability of a single fracture of aperture L_0 is simply

$$k_1 = \frac{L_0^3}{12} \tag{2.14}$$

This cubic law permeability results from the analysis of flow through a single parallel plane walled fracture (Snow, 1969) and gives the flow rate per unit length along the fracture. Conventional permeability values are defined from Darcy's law relative to flow across a unit surface element area. To make this conversion, consider as a model a block volume containing a set of cracks which extend through the length of the block. The permeability of the volume relative to the surface area of the block is obtained by simply adding the contribution of each fracture, which amounts to multiplying equation (2.14) by the number of cracks in the volume. The number of cracks of interest is the number with normals perpendicular to the direction in which permeability is to be estimated, which requires a knowledge of the crack normal distribution function $P^l(\chi, \eta)$, $\chi = \cos\delta$ (Figure 2-3). The superscript l refers to the linear aspect ratio distribution in equation (2.7), and a superscript f would refer to the flat distribution. Due to the circular symmetry of the cracks, this function is equal to $2\pi N^l(\zeta, \psi, \phi)$ so that $\chi = \zeta$ and $\eta = \psi$. Remembering that $\xi = na^3$, a set of cracks of density ξ_0 with aspect ratio α yields a permeability k_α

$$k_\alpha = \frac{\xi_0 \alpha^3}{12} \tag{2.15}$$

where the product in the numerator gives nL_0^3. Since the model considers a unit volume, the dimensions of k_α in equation (2.15) are length squared, where the length

unit will be the same as that of the unit volume under consideration.

Integrating over the range of crack aspect ratios for cracks still open in a given direction, from $\alpha_{cl} = \cos^2\gamma_0\sigma/E_0$ to α_m, using the linear aspect ratio distribution from equation (2.7), gives permeability as a function of angle θ measured from the stress axis for all of the cracks in this direction:

$$k'(\theta-\pi/2) = \frac{\xi}{96\pi^2\left(\frac{\alpha_m^2}{2}\frac{\sigma^2}{E_0^2}\frac{1}{10} - \frac{\alpha_m}{3}\frac{\sigma}{E_0}\right)}\left[\frac{\alpha_m^5}{20} - \frac{\alpha_m}{4}\frac{\sigma^4}{E_0^4}\cos^8\theta + \frac{1}{5}\frac{\sigma^5}{E_0^5}\cos^{10}\theta\right] \quad (2.16)$$

Cracks oriented in directions other than parallel to the applied pressure gradient will also have a contribution to the permeability. The effects of these cracks can be partially included by adding their permeability, multiplied by the cosine of the angle between each fracture set and the direction of the pressure gradient. Restricting attention to crack normals within a single vertical plane, such as the $x-z$ plane, we can integrate the result of equation (2.16) multiplied by the appropriate cosine function:

$$\int_{\gamma-\frac{\pi}{2}}^{\gamma+\frac{\pi}{2}} k'(\theta-\pi/2)\cos(\gamma-\theta)d\theta \quad (2.17)$$

Here $\gamma-\pi/2$ is the direction of interest for the permeability estimation. In principle, cracks with normals outside of the vertical plane could be considered, but it turns out that the resulting integral is very complicated and does not add significant insight to the resulting permeability model. Carrying out the integration in equation (2.17), we have for the linear aspect ratio distribution

$$k^l(\gamma-\pi/2) = \frac{\xi}{48\pi^2\left(\frac{\alpha_m^2}{2}\frac{\sigma^2}{E_0^2}\frac{1}{10} - \frac{\alpha_m}{3}\frac{\sigma}{E_0}\right)}X^l \quad (2.18)$$

$$\begin{aligned} X^l = {} & \frac{\alpha_m^5}{20} \\ & -\frac{\alpha_m}{4}\frac{\sigma^4}{E_0^4}\frac{1}{9}\left[\frac{\cos^2\gamma}{35}\left(128+128\sin^2\gamma+48\sin^4\gamma+40\sin^6\gamma+35\sin^6\gamma\right)+\sin^{10}\gamma\right] \\ & +\frac{1}{55}\frac{\sigma^5}{E_0^5}\left[\frac{\cos^2\gamma}{63}\left(256+256\sin^2\gamma+96\sin^4\gamma\right.\right. \\ & \left.\left.+80\sin^6\gamma+70\sin^8\gamma+63\sin^{10}\gamma\right)+\sin^{12}\gamma\right] \end{aligned}$$

The same procedure can be performed for the flat aspect ratio case (equation (2.7')), and the resulting permeability expression is

$$k^f(\gamma - \pi/2) = \frac{\xi}{192\pi^2} \frac{1}{\alpha_m - \frac{1}{3}\frac{\sigma}{E_0}} X^f \tag{2.19}$$

$$X^f = \alpha_m^4$$
$$-\frac{\sigma^4}{E_0^4}\frac{1}{9}\left[\frac{\cos^2\gamma}{35}\left(128 + 128\sin^2\gamma + 48\sin^4\gamma + +40\sin^6\gamma + 35\sin^6\gamma\right) + \sin^{10}\gamma\right]$$

These two results may be used to provide an estimate to permeability within the fractured rock as uniaxial stress is applied. If the uniaxial stress is sufficiently large to close off all cracks present in a given direction, then the integration limits in equation (2.17) must be changed to account for the range of angles where no cracks are present. This results in expressions of very similar form to the permeability results in equations (2.18) and (2.19).

While this appears to be a simple approach to permeability estimation, it is related to other studies of fluid flow through crystalline rock. Bernabe (1986) examines in detail the applicability of the equivalent channel concept to permeability modeling for several granites and concludes that it is a valid approach. Our case is analogous to an equivalent channel model in that we replace the complicated fracture network by a simplified representation of sets of plane walled fractures extending through the medium, though we do not base our "channel" on some of the conventional concepts of the surface area and volume of the porous structure. However, the model does include the effects of crack closure as a function of direction. Some of the effects which are neglected are the diminished aperture of cracks due to asperities and the complicated flow paths within the rock. The effect of surface roughness of cracks is probably not too important over relatively low pressure ranges, since fractures with asperities still display a cubic law permeability behavior with an effective, mean crack width (Tsang and Witherspoon, 1981, 1983). Numerical studies of fluid flow through cracks with asperities confirm this conclusion (Brown, 1987). Therefore, the tortuosity effect is

of much greater concern. The most direct way to include the tortuosity is to simply normalize the permeability predictions by some constant so that the values are of the correct order of magnitude. This can be done easily if permeability for one direction is known or if the permeability of the unstressed rock is known.

It is important that we have only included a fracture contribution to permeability in this model. If the medium under consideration has a significant amount of a different type of interconnected pores and tubular fluid conduits, such as is the case in some sandstones, the effects of the crack closure must be added to the permeability due to other porosity types. Since the equidimensional pores of a sandstone will only be minimally affected by the applied stress, the effects of the cracks may not be so important for overall permeability values. This crack model is most important for low porosity rocks such as fractured limestones or granites and other crystalline and metamorphic which would be essentially impermeable except for the cracks.

The permeability model also essentially assumes a prestress isotropicity of the fracture network creating the permeability of the rock medium. It is conceivable that some particular arrangements of cracks and their intersections might show strong variations in effective permeability depending on the direction of the applied stress, but the model assumes that this effect will not occur and that the behavior of the medium is independent of the direction of the stress axis. Therefore the cracks in the medium must on average have an isotropic distribution in both orientation and in intersection properties.

2.3 Application To Ultrasonic Data

The inversion procedure together with the permeability models equations (2.18) and (2.19) provide a method for predicting permeability values given observations of elastic wave velocities which could be obtained from either laboratory samples or field data. Nur and Simmons (1969) made velocity measurements on samples of Barre

granite as a function of direction for several magnitudes of applied uniaxial stress. Measurements were presented for both quasi-compressional wave signals and quasi-transverse waves, SV and SH. The Barre granite sample used by Nur and Simmons (1969) was dry, so the Hudson (1981) formulation for dry cracks is appropriate. A value of 2.7 g/cm^3 was used for density in the equations required for the inversion, and the Lamé parameters used to compute the Young's modulus were $\lambda_0 = 22.05$ GPa and $\mu_0 = 35.97$ GPa (Nur, 1971).

2.3.1 Velocity Inversions

Velocity data for qP waves at uniaxial stress values of 0, 10, 20, and 30 MPa were jointly inverted for the crack density ξ at each stress value and for a single value of maximum aspect ratio α_m. The results for these parameters are given in Table 2.1 for both the linear and the flat aspect ratio distribution function (equations (2.7) and (2.7′)). Corresponding quasi-compressional wave velocity predictions and observations are compared in Figures 2-4 and 2-5. The theory is able to match the data fairly well, with a fit approximately the same as that obtained by Sayers (1988b). In general, the linear distribution gives a slightly better fit to the observed velocity values. The trends in crack density shown by the inversion results in Table 2.1 are reasonable. As stress increases, more cracks will close reducing the overall crack density, as occurs for these results. In addition, the two aspect ratio distributions give essentially the same ξ at each pressure (Table 2.1). However, the maximum aspect ratio given by the constant distribution function, 3.99×10^{-4}, is about 60% of the value resulting from the linear case, 6.34×10^{-4}. This occurs because with the Walsh (1965) crack closure model, many cracks of small aspect ratio are required to close at low pressures such as 10 or 20 MPa. For example, at 10 MPa, the largest crack which closes, with a normal in the direction of the applied stress, has an aspect ratio of approximately 1.17×10^{-4} for a material with the Lamé parameters used for this inversion. The flat distribution will contain proportionately fewer small aspect

ratio cracks for a given total crack density and so will require a smaller α_m to achieve the same degree of predicted velocity increase for a given applied uniaxial stress.

Analogous results for the SH data are presented in Table 2.2, and velocity predictions are shown in Figures 2-6 and 2-7. While the SH data are similar to those in Figures 2-4 and 2-5 for the quasi-compressional waves, the qSV results are relatively poor and are given in Table 2.3 and Figures 2-8 and 2-9. A non-attenuative transversely isotropic medium always has equal qSV velocities parallel and perpendicular to the symmetry axis (see equation (2.11)), but it is clear from the data in Figure 2-8 that this condition is not quite true for these observations. It is clear that there is a trend to the qSV velocity with direction that is not reproduced in the variations predicted by the crack model. It is possible that the Barre granite has some slight intrinsic anisotropy which would cause the stressed system to have some overall symmetry other than transversely isotropic. A likely cause of SV velocity variation is preferred grain orientation in the granite. Lo et al. (1986) clearly demonstrate such a residual anisotropy after crack closure in measurements of velocity in Chelmsford granite. If the residual anisotropy is the cause of most of the velocity variation for the SV data, the inversion results are not significant for inference of crack orientation since the forward model involved in the inversion includes only anisotropy due to cracks.

The effects of this residual anisotropy seem to be evident to a smaller degree at high pressures for the quasi-compressional and SH wave data also (Figures 2-4, 2-5, 2-6 and 2-7). Since the total velocity anisotropy is greater for the quasi-compressional and SH data, however, the fractures have more effect on observed velocities and the inversion results are more significant for these cases. The values of crack density ξ obtained from the two quasi-shear wave data sets are very similar, but the quasi-compressional wave data consistently yielded a somewhat lower estimate of crack density. The results for all data sets are also essentially the same as those obtained by Sayers (1988b). In order to examine these differences in estimated crack density,

a joint inversion of both SH and qP wave data from experiments at a single uniaxial stress was attempted, but it was found that the value of ξ obtained was between the values resulting from the individual inversions and predicted velocities too large to match the qP data well, but too small for the SH velocity measurements. The cause of the difference in results for quasi-compressional and quasi-shear wave data is difficult to explain but may be caused by remnant water within the granite sample. Liquid within the cracks would tend to raise the qP wave velocity for a given crack density, while having a much more negligible effect on quasi-shear wave velocities. Therefore a single value of ξ would be able to yield velocity predictions matching both sets of data. It would be desirable to repeat the velocity experiment with uniaxial stress taking great care to maintain the dryness of the rock sample in order to confirm this hypothesis.

It is possible that both the qP and SH estimates for crack density are high due to the use of the Voigt approximation in calculating elastic constants (equation (2.5)). Since the Voigt approach gives an upper bound, the averaged constants could be "stiffer" than those of the fractured medium, and a higher density of cracks would then be necessary to reduce the velocities to the observed values. If, however, the qP estimated crack density is reduced by the presence of liquids as suggested above, this will offset the error and the solution will not be too far off. It is likely that the true crack density is near the values we estimate.

Unlike the crack density, the estimates for α_m from qP and SH data are comparable for each aspect ratio distribution. For the flat distribution, the values differ by about 12%, and the variation is about 6% for the linear function. In both cases, the qP inversion yields the smaller estimate for α_m. This difference likely stems from effects similar to those suggested as causing the decrease in crack density estimates.

Although there is some consistency of these inversion results for crack density and for the maximum aspect ratio parameter, it remains to establish the validity of the inversion results and the accuracy of the resulting description of crack geometry

within the rock. Several studies involving direct examination of rock samples for crack geometry have been conducted. Sprunt and Brace (1974) examined Westerly granite using SEM techniques and estimated an aspect ratio distribution which showed a large number of cracks with aspect ratio greater than 10^{-2}. A similar, but more detailed, study by Hadley (1976) revealed a much larger proportion of aspect ratios of the order of 10^{-4} but also showed that the distribution depends on the stress history of the rock sample with prestressed samples containing a larger fraction of small aspect ratio cracks. Hadley (1976) concluded that a typical mean aspect ratio was of the order of 1×10^{-3}. Due to resolution limitations of the SEM technique, the smallest aspect ratio which was observable was estimated to be about 5×10^{-5}, but it is also clear that some limitations on the validity of the observations will result from the limited, two-dimensional sampling of three-dimensional cracks. Therefore, many small aspect ratio cracks in the rock could have been missed using the SEM imaging. Wong et al. (1989) also conclude that SEM images failed to detect a significant segment of the small aspect ratio population in a Westerly granite.

Direct observation of crack closure under uniaxial stress reveals other potential difficulties of the crack closure model used in this study. Batzle et al. (1980) showed that crack closure in Westerly granite can be incomplete due to the influence of roughness of the crack surfaces. In addition, the effects of crack intersections can be important in altering crack behavior as stress is applied. The crack roughness and intersections combined will clearly result in departures from the simple crack model locally, but it is not obvious how significant this effect will be on the macroscopic scale.

Other, indirect, investigations of crack dimensions have been conducted using differential strain analysis (DSA) techniques (Siegfried and Simmons, 1978). In principle, the DSA approach can produce information on crack aspect ratios by monitoring linear strain of a rock sample subjected to hydrostatic pressure. However, this method is subject to relatively large error due to numerical differentiation (Cheng

and Toksöz, 1979). It is worth noting that Feves and Simmons (1976) found that the majority of cracks in a Westerly granite close at hydrostatic pressures of about 20 to 30 MPA, corresponding to an aspect ratio of about $5. \times 10^{-4}$ to 7.5×10^{-4} using the Walsh (1965) theory, a range which includes the results of our inversion. Cheng and Toksöz (1979) applied a velocity inversion technique for isotropic, hydrostatic pressure cases to Westerly granite and found an aspect ratio distribution in general agreement with this result. It seems that our inversion results are corroborated by other indirect techniques using elastic properties in finding a significant amount of small aspect ratios for cracks within igneous rocks, while direct observations using SEM reveal porosity of larger aspect ratio. The larger aspect ratio porosity is a much less important source of variation in elastic behavior than the cracks under the pressure changes we consider here.

2.3.2 Permeability Predictions

Permeability predictions using the qP and SH results from both aspect ratio distribution functions are shown in Figure 2-10, and they all compare favorably, though there is some variation for uniaxial stresses of 30 and 40 MPa. The curves for 10 MPa were normalized in the direction perpendicular to the applied stress to match a permeability measurement for Barre granite under 10 MPa hydrostatic pressure (Bernabe, 1986). This normalization assumes that the permeability in the direction perpendicular to the stress shows the same behavior as does isotropic permeability in the hydrostatic case. The other permeability curves were normalized to have the same permeability in the stress direction since the physical model for crack behavior includes no change in the crack distribution in this direction. In principle, the closure of cracks in other directions is also included in equations (2.18) and (2.19), but the arbitrary normalization is still necessary. Without this scaling, the permeability predictions would actually rise in the stress direction as stress increases due to the lack of tortuosity effects in the permeability theory.

Laboratory experiments (Zoback and Byerlee, 1975) show that there is in fact a decrease in permeability in the direction parallel to the applied uniaxial stress, but this effect is not very large. Figure 2-11 compares the permeability measurements by Zoback and Byerlee (1975) to the constant values we would predict for permeability in the stress direction. The three data points in Figure 2-11 were measured by Zoback and Byerlee (1975) while increasing uniaxial stress on a sample of Westerly granite under 50 MPa confining pressure and 11 MPa pore pressure, and the curve between the two data is the trend inferred for permeability between these points. The Zoback and Byerlee (1975) data were made at very high uniaxial pressures to investigate dilatancy effects, and our theory is based on linear behavior which cannot be extrapolated to high stress.

While measurements of anisotropic permeability as a function of direction are not available to confirm the permeability predictions, the comparison to measurements parallel to the stress axis provide one check on the model, and a second check can be made by comparison with permeability measurements as a function of hydrostatic pressure. The permeability values perpendicular to the stress axis from both the qP and SH results are compared to the measurements by Bernabe (1986) for Barre granite in Figure 2-12. The predicted permeability decreases are too small, and, in addition, the measurements show a tendency to decrease the most rapidly at the lower pressures, while the predictions have the opposite tendency. Within the limitations of the fact that we are comparing hydrostatic pressure and uniaxial stress cases, this suggests that some effects of crack closure are missing from our model. Other examples of permeability measurements reported in the literature for granites show a wide variation both in the absolute value of permeabilities under pressure and in the magnitude of change in isotropic permeability with increasing pressure (e.g., Brace et al. 1968; Bernabe, 1986), so a perfect correlation would not necessarily be expected.

Although these comparisons of theory and data are limited, alternative numerical schemes for analysis of permeability anisotropy in fractured media have been recently

developed. Zhao and Toksöz (1991b) apply finite difference methods to the modeling of steady state fluid flow in statistical models of fractured media. The results show that the numerically estimated permeability has a highly variable degree of anisotropy, 87% to 184%, which depends on the nature of the synthetic fracture network. This numerical permeability anisotropy is higher than we estimate here since the fracture description applied by Zhao and Toksöz (1991b) is much more strongly aligned than our distributions of orientations, but it is encouraging that the variation of permeability with respect to the symmetry direction of the model has similar trends in both cases.

2.4 Discussion And Conclusions

The results of the velocity inversion suggest that the physical model for the fracture behavior under uniaxial stress is capable of describing most of the effects of the cracks on the elastic properties of the medium and that the model is able to match observations of velocity in the Barre granite. The aspect ratio of the dry fractures does not affect the elastic wave velocities in the Hudson formulation. Only the density of cracks ξ is important in this case, and so the inversion results suggest that we are modeling this aspect of the system fairly well. On the other hand, permeability critically depends on the aspect ratio due to the cubic dependence on crack width in equation (2.14). The permeability predictions are highly sensitive to this parameter, and it is important to have an understanding of the aspect ratio distribution obtained by inversion.

Some insight into the roles of α_m and ξ in the model of cracks and their effect on elastic behavior is obtained by independently inverting velocity data from different uniaxial stresses for crack density and α_m at each stress. Parameter results for the independent inversion procedure applied to the SH data are given in Table 2.4, and the theoretical velocities are compared to the data in Figure 2-13. Because α_m is

though the joint inversion solutions are still preferred, since α_m should not be a function of pressure. Note that the velocity at 0 MPa is independent of aspect ratio and α_m cannot be determined for this case. The crack density values are almost identical to those obtained by the joint inversion (Table 2.2), but the results for α_m vary around the value 6.75×10^{-4}. Independent inversions of the qP data result in similar comparisons. From this and other properties of the inversion behavior, it is clear that the crack density is uniquely determined for each data set and serves to provide an overall shift upward of the velocity curve as density reduces so that the mean velocity matches the mean of velocity observations. It can even be determined independently of the aspect ratio distribution. In contrast, the aspect ratio parameter α_m gives fine control of the shape of the velocity curve so that it may match the details of the data trends. It does this by governing the amount of fine cracks present for a given aspect ratio distribution which close at the pressure of interest.

Further understanding of the behavior of the inversion procedure is given by the similarity of the predictive capability of the flat and linear aspect ratio distributions in the velocity inversions (Figures 2-4, 2-5, 2-6, 2-7, 2-8 and 2-9). This indicates a nonuniqueness of inversion results arising from the fact that enough cracks of aspect ratios which will close with the appropriate magnitudes of uniaxial stress are present in both distributions. Some constraints on this type of nonuniqueness can be made based on the accuracy of the velocity predictions resulting from the aspect ratio distributions. For example, an inversion based on a parabolic aspect ratio distribution proportional to $(\alpha - \alpha_m)^2$ was attempted. This parabolic distribution will have an even large proportion of small aspect ratio cracks than the linear model in equation (2.7). However, the inversion based on this distribution failed to converge to parameter values which could reproduce velocity data. This provides indirect evidence that the parabolic distribution is not realistic and that more larger aspect ratio cracks are required. On the other hand, the results of the two distributions presented above both reproduce data fairly well. Although the differences tend to be subtle in the plots of

velocity predictions and data, the linear model is consistently somewhat better and also gives a smaller root mean square error, about 30% for the qP inversion and 17% for the SH case. This suggests that the linear model is in fact a better representation of the real crack distribution and that there are many fine cracks which cannot be resolved with SEM techniques. In addition, the larger value of maximum aspect ratio is encouraging since it is closer to the results of other studies (Feves and Simmons, 1976; Cheng and Toksöz, 1979), though in any case, the rock may contain porosity of even larger aspect ratio.

Nonuniqueness in the inversion also results from the assumption of noninteractive, penny-shaped cracks. Mavko and Nur (1978) consider a tapered crack model instead of ellipsoidal cracks and show that the two crack models can produce the same effects on elastic behavior, indicating an inherent lack of uniqueness. They also demonstrate that ellipsoidal crack models achieve these results with smaller values of aspect ratio. A theory accounting for the interactions of cracks will also give a larger estimate for aspect ratio than the noninteractive theories such as the Walsh (1965) model (Doyen, 1987). It is clear then that our results are dependent on the crack model, which assumes penny-shaped, noninteracting cracks. In summary, it seems that our results for crack density are well defined and reliable but that the estimation of α_m must be considered more carefully in order to confirm its validity. This confirmation can be based on the accuracy of the inversion and on comparison to observation of aspect ratio distributions in rocks.

The ambiguity in the aspect ratio does not seem to have too large of an impact on permeability predictions, however (Figure 2-10). Instead, the dissimilarity between the hydrostatic data of Bernabe (1986) and the predictions for the direction perpendicular to the stress axis (Figure 2-12) is caused by other effects. There are two likely principal causes of this failure.

First, the permeability model fails to include the effects of interconnecting cracks. It is clear that intersections can affect crack closure (Batzle et al., 1980). Numerical

studies in two-dimensional models of fractured materials show that connectivity is also very important for fluid flow (Long and Witherspoon, 1985). It is difficult to model these effects in the true three-dimensional medium. Snow (1969) presents an approach similar to our model of continuous planar fractures which is appropriate for several discrete sets of fractures but also neglects the effects of interconnection. Long et al. (1985) and Andersson and Dverstorp (1987) present numerical techniques for modeling the permeability of sets of penny-shaped cracks suspended in a three-dimensional volume. An application of our inversion technique could be to develop crack aspect ratio and orientation models for procedures like this.

A second source of error in our permeability calculations is that the present version of this theory does not include any change in aspect ratio for the cracks which remain open. In actuality, the aspect ratio of the open cracks will decrease as the uniaxial stress is applied (Toksöz et al., 1976). This effect will tend to decrease the permeability values in directions away from the stress axis. This is one major reason that permeability predictions for 10 MPa show an almost imperceptible drop from the constant 0 MPa case. The largest crack which will completely close in the Barre granite at this pressure, the crack with a normal parallel to the stress axis, has an aspect ratio 1.1×10^{-4}. With the cubic law behavior of the crack permeability, the cracks with aspect ratios smaller than this value have minimal contribution to fluid flow even in the zero stress case. The permeability predition would drop further and be more realistic if the partial closure of cracks with initial aspect ratios larger than 1.1×10^{-4} was incorporated into the modeling scheme.

The change in aspect ratio with stress will affect only the permeability predictions as long as the cracks are dry. If, however, the cracks are assumed to be filled with a fluid, the aspect ratio also affects the elastic constant values. The forward modeling of velocities would then have to include the variation of aspect ratio with direction in order to compute the velocity values. However, a relatively small amount of gas mixed with the fluid will still cause the the effective properties of the medium to be

essentially that of a gas, since the effective bulk modulus k^* of a two-phase medium is given by

$$(k^*)^{-1} = Vk_f^{-1} + (1 - V)k_g^{-1} \tag{2.20}$$

where k_f and k_g are fluid and gas bulk moduli, respectively, and V is the volume fraction of fluid (Kuster and Toksöz, 1974). The large compressibility of the gas will tend to dominate the overall properties of the crack-filling material, and it will tend to behave as though the cracks are filled with a gas. As long as the shear modulus and bulk modulus of the crack-filling material are small, the aspect ratio of the cracks has little impact on the elastic constants in the Hudson (1981) approach, and the present approach will be sufficient.

This approach should at least provide a means of obtaining an initial estimate of permeabilities for use in modeling of fluid flow in subsurface fractured media. Potential areas of application include both hydrological studies and petroleum reservoir modeling. Perhaps the most important aspect of the theory is that it represents an attempt to extend knowledge of the permeability of a subsurface feature to regions beyond the borehole using seismic data.

	Aspect Ratio Distribution Function	
Parameter	Flat	Linear
α_m	3.99×10^{-4}	6.34×10^{-4}
ξ_0	0.275	0.275
ξ_{10}	0.253	0.254
ξ_{20}	0.235	0.235
ξ_{30}	0.221	0.221

Table 2.1. Inversion results using qP velocity measurements of Nur and Simmons (1969). The subscript P on ξ_P indicates the uniaxial stress value for each crack density.

	Aspect Ratio Distribution Function	
Parameter	Flat	Linear
α_m	4.48×10^{-4}	6.75×10^{-4}
ξ_0	0.315	0.315
ξ_{10}	0.286	0.285
ξ_{20}	0.257	0.256
ξ_{30}	0.235	0.234
ξ_{40}	0.214	0.215

Table 2.2. Inversion results using SH velocity measurements of Nur and Simmons (1969). The subscript P on ξ_P indicates the uniaxial stress value for each crack density.

	Aspect Ratio Distribution Function	
Parameter	Flat	Linear
α_m	7.34×10^{-4}	13.1×10^{-4}
ξ_0	0.314	0.314
ξ_{10}	0.286	0.285
ξ_{20}	0.252	0.252
ξ_{30}	0.227	0.227
ξ_{40}	0.206	0.206

Table 2.3. Inversion results using qSV velocity measurements of Nur and Simmons (1969). The subscript P on ξ_P indicates the uniaxial stress value for each crack density.

Uniaxial Stress, MPa	ξ	α_m
0	0.315	
10	0.283	4.98×10^{-4}
20	0.255	5.94×10^{-4}
30	0.234	6.78×10^{-4}
40	0.217	5.61×10^{-4}

Table 2.4. Results of independent inversion of SH velocity measurements of Nur and Simmons (1969) for crack density ξ and maximum aspect ratio α_m at each stress. The inversion cannot determine information on aspect ratio at 0 MPa.

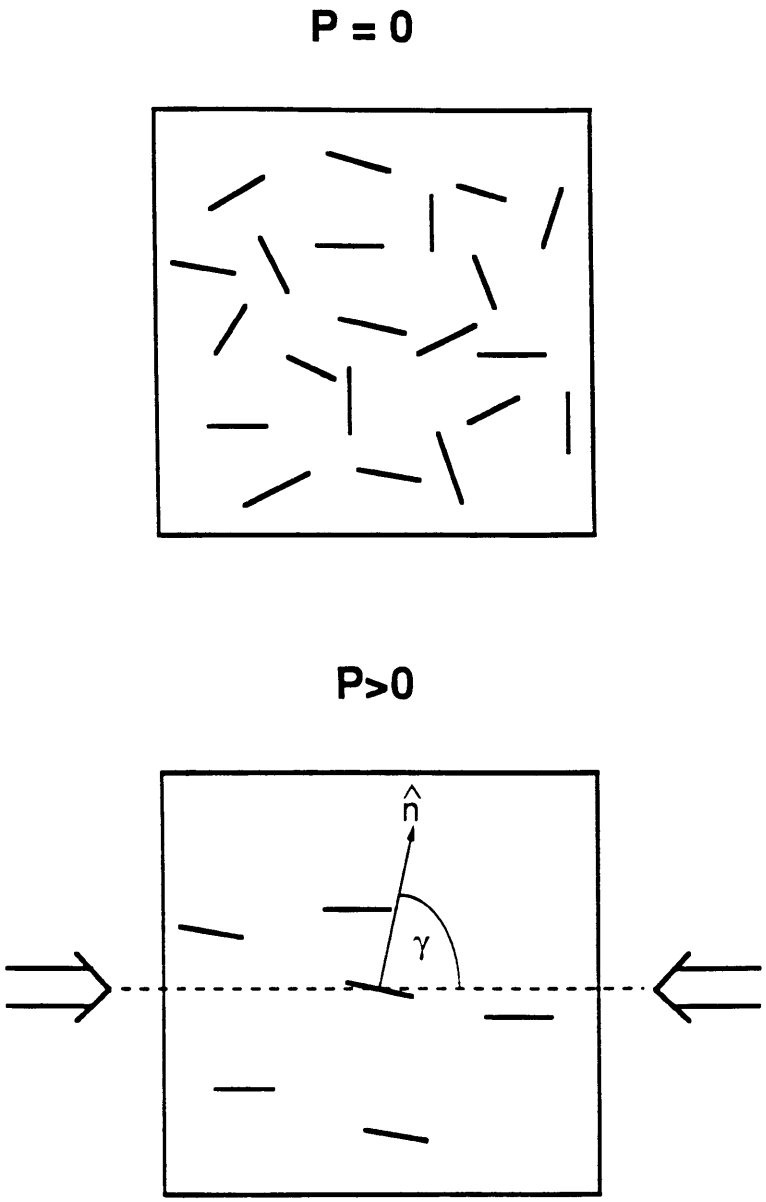

Figure 2-1: Schematic diagram illustrating the behavior of a randomly fractured medium under an applied uniaxial stress. (Top) A possible random crack system with no stress applied. (Bottom) The same system after application of the uniaxial stress, where cracks have closed depending on their orientation with respect to the stress. If the angle γ indicated on the figure is equal to or smaller than the angle γ_0 defined in the text, the crack will close under the applied uniaxial stress.

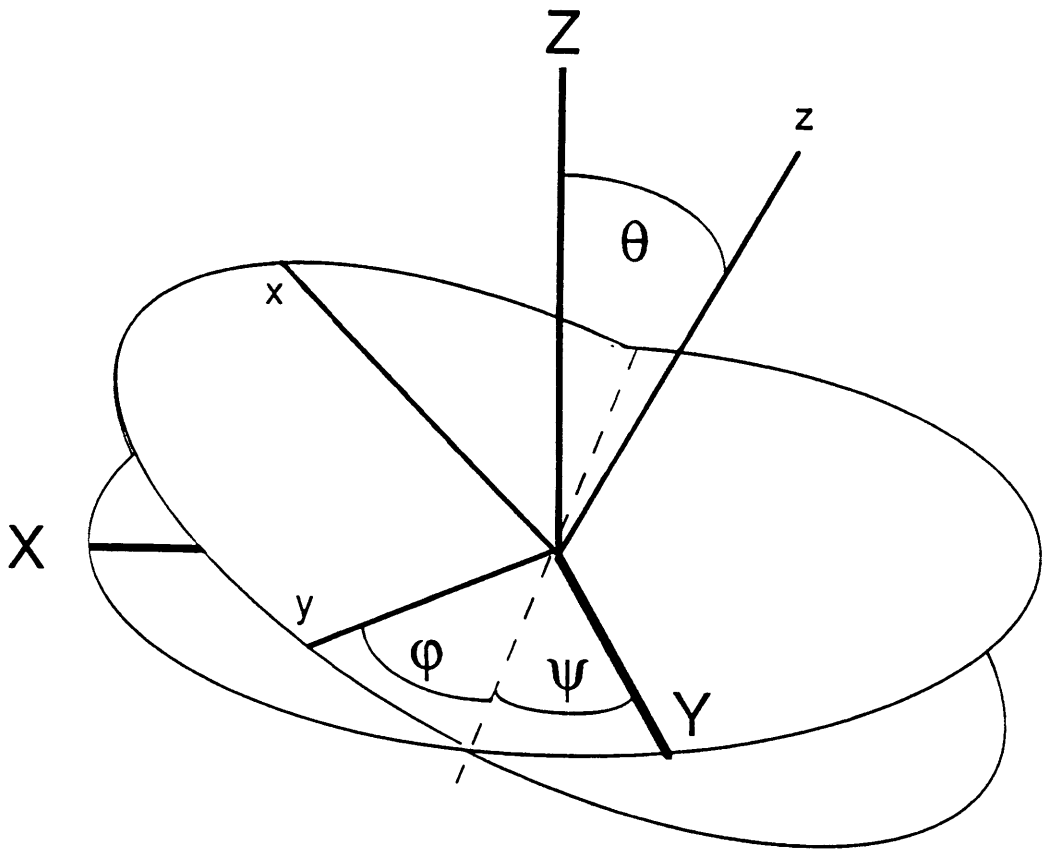

Figure 2-2: Euler angles of rotation θ, ψ, ϕ describing orientation of a given crack coordinate system x, y, z (fine lines) with respect to the composite medium coordinate system X, Y, Z (heavy lines). The dashed line indicates the intermediate position of the y axis, and the two disks represent the $X - Y$ planes before and after rotation, which are also the crack planes. The set of rotations is defined as follows: (1) rotate by ψ about Z (the same as z initially), (2) rotate by θ about the new y axis, (3) rotate by ϕ about the new z axis. Since the cracks are assumed to have circular symmetry, the first two rotations actually uniquely specify the orientation of a single crack.

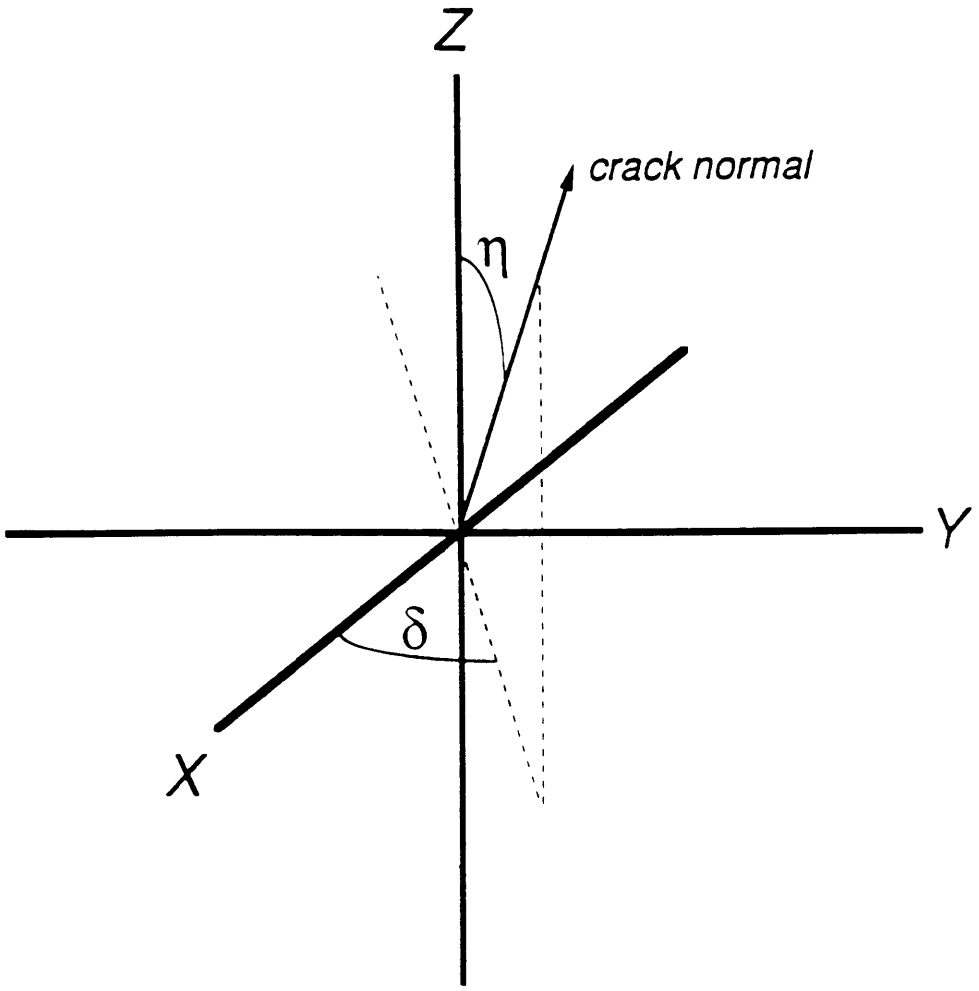

Figure 2-3: The angles δ and η necessary to specify the orientation of a crack normal.

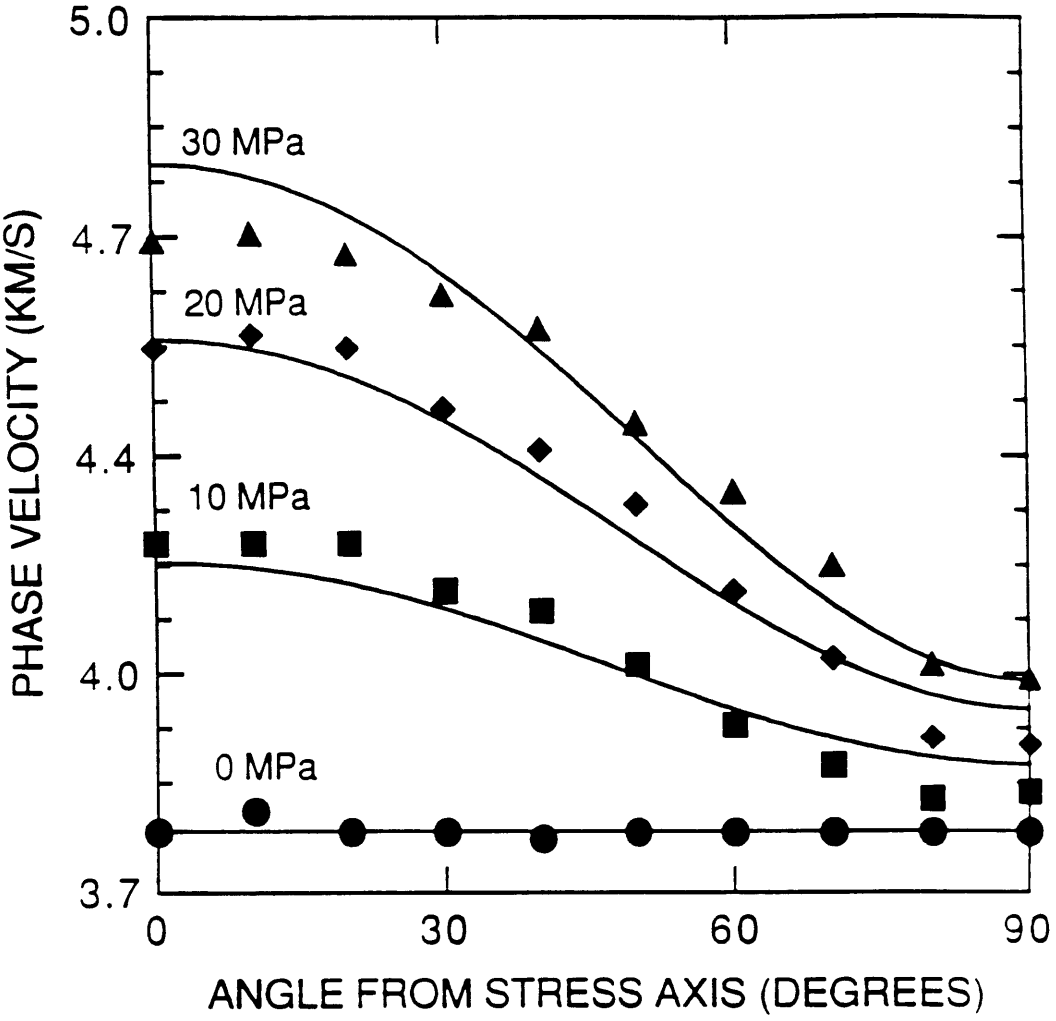

Figure 2-4: Results of inversion for crack density ξ and maximum aspect ratio α_m using Barre granite quasi-compressional wave velocity data and the linear aspect ratio distribution function (equation (2.7)). The points are data collected by Nur and Simmons (1969), and the lines indicate the results of a joint inversion of all of the data in this figure. The value of the applied uniaxial stress is indicated for each curve.

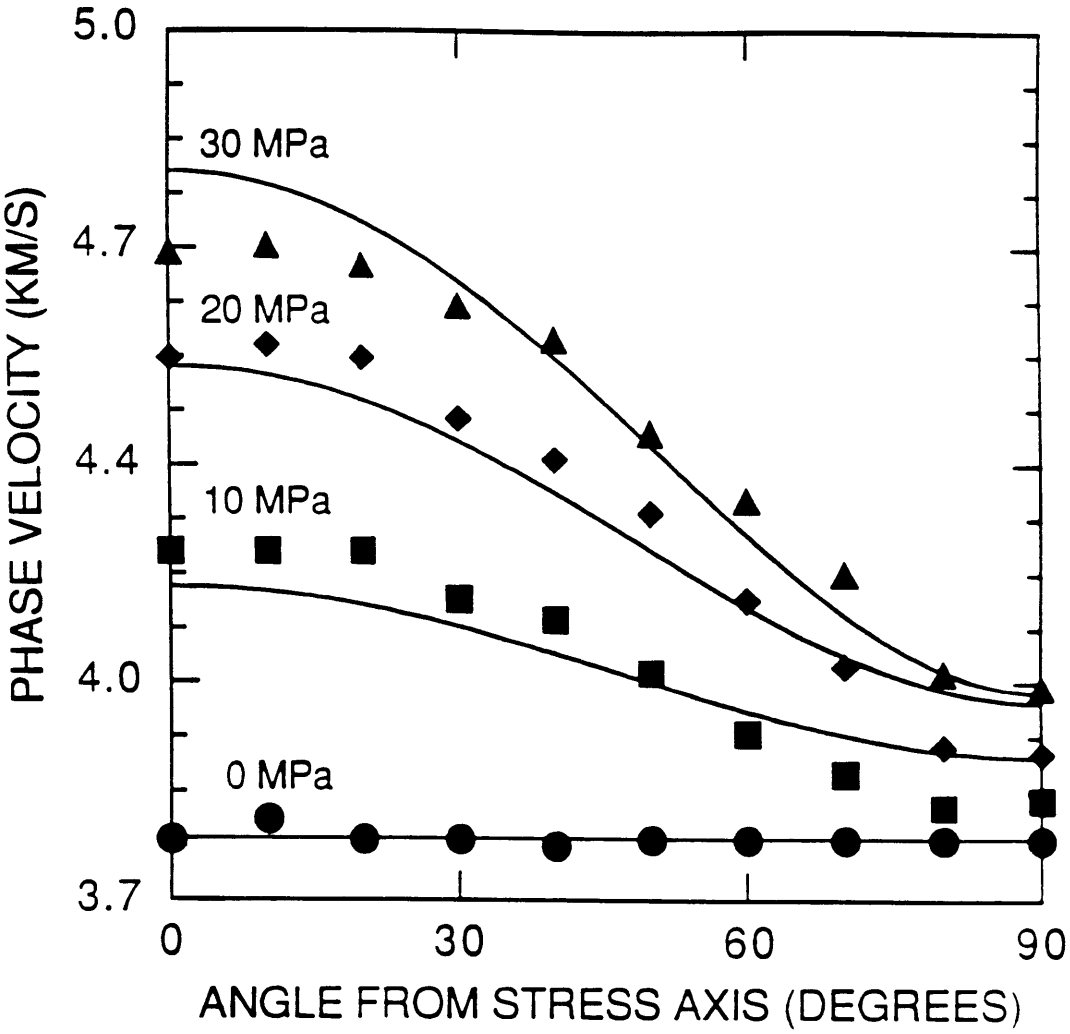

Figure 2-5: Results of inversion for crack density ξ and maximum aspect ratio α_m using Barre granite quasi-compressional wave velocity data and the flat aspect ratio distribution function (equation (2.7′)). The points are data collected by Nur and Simmons (1969), and the lines indicate the results of a joint inversion of all of the data in this figure. The value of the applied uniaxial stress is indicated for each curve.

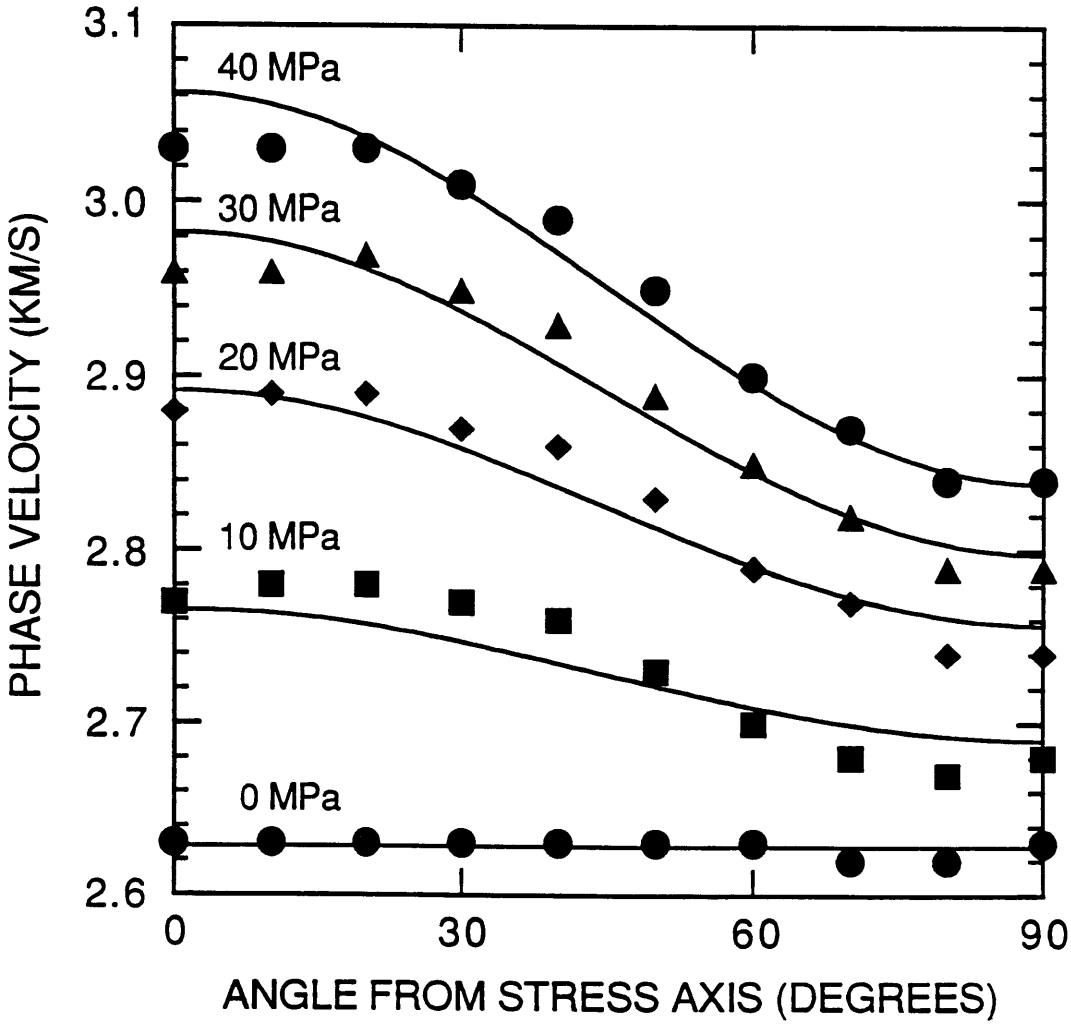

Figure 2-6: Results of inversion for crack density ξ and maximum aspect ratio α_m using Barre granite SH velocity data and the linear aspect ratio distribution (equation (2.7)). The points are data collected by Nur and Simmons (1969), and the lines indicate the results of a joint inversion of all of the data in this figure. The value of the applied uniaxial stress is indicated for each curve.

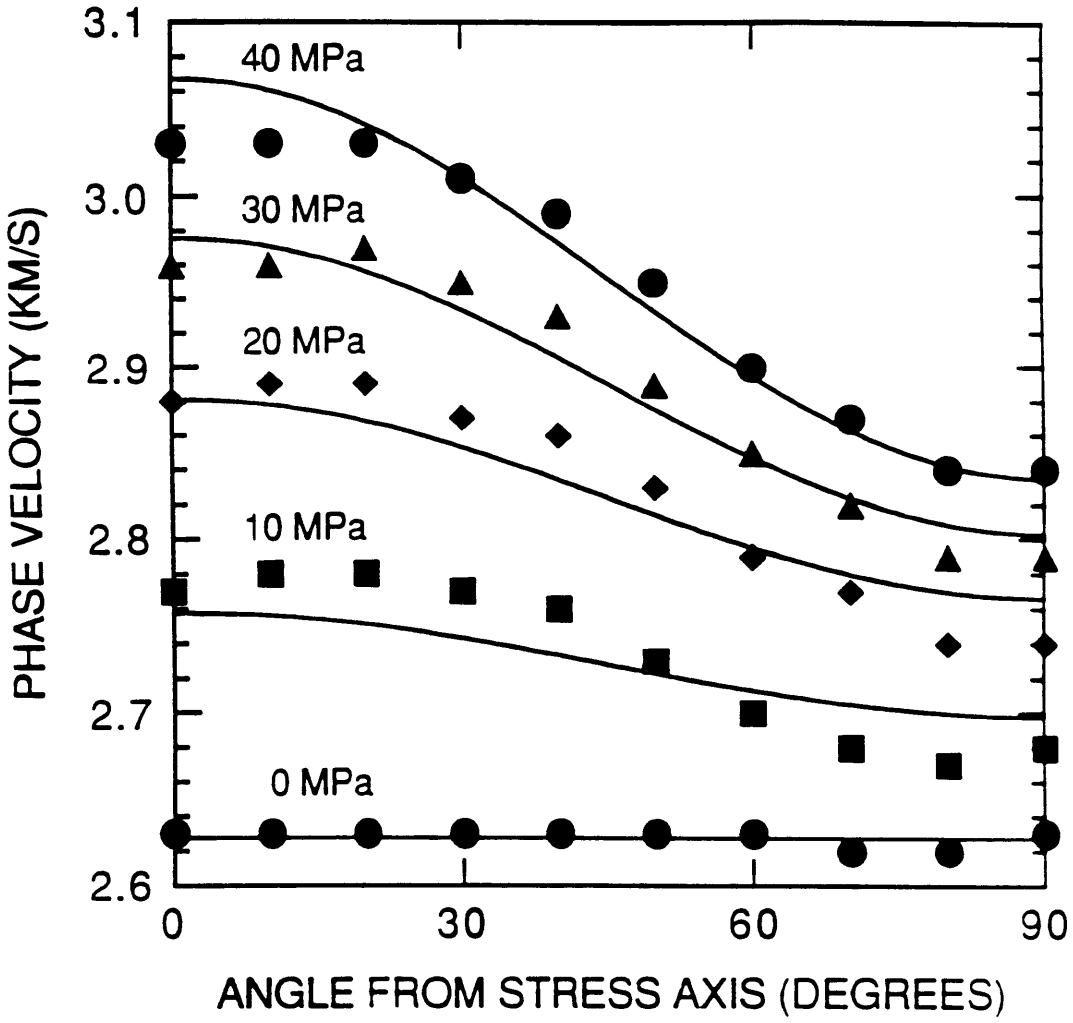

Figure 2-7: Results of inversion for crack density ξ and maximum aspect ratio α_m using Barre granite SH velocity data and the flat aspect ratio distribution (equation (2.7')). The points are data collected by Nur and Simmons (1969), and the lines indicate the results of a joint inversion of all of the data in this figure. The value of the applied uniaxial stress is indicated for each curve.

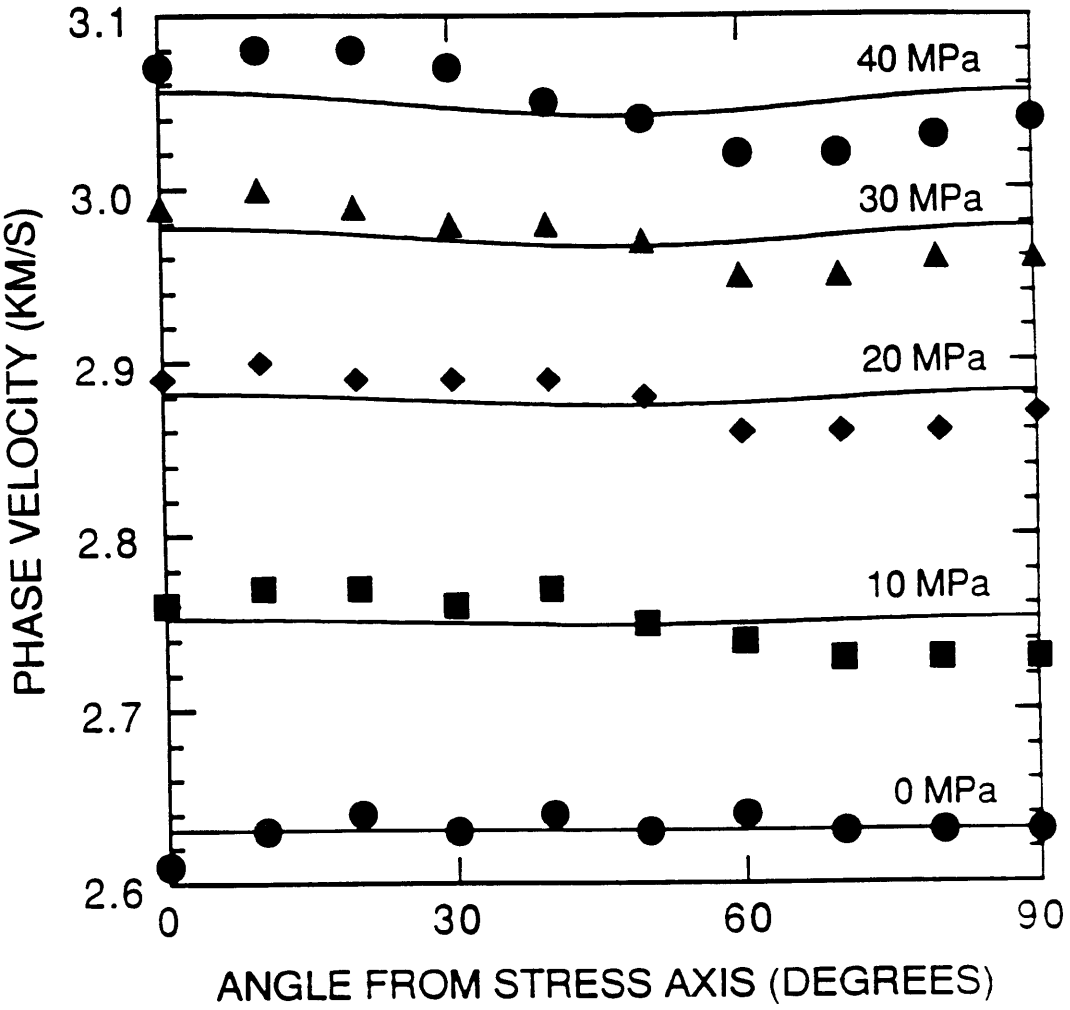

Figure 2-8: Results of inversion for crack density ξ and maximum aspect ratio α_m using Barre granite qSV velocity data and the linear aspect ratio distribution (equation (2.7)). The points are data collected by Nur and Simmons (1969), and the lines indicate the results of a joint inversion of all of the data in this figure. The value of the applied uniaxial stress is indicated for each curve.

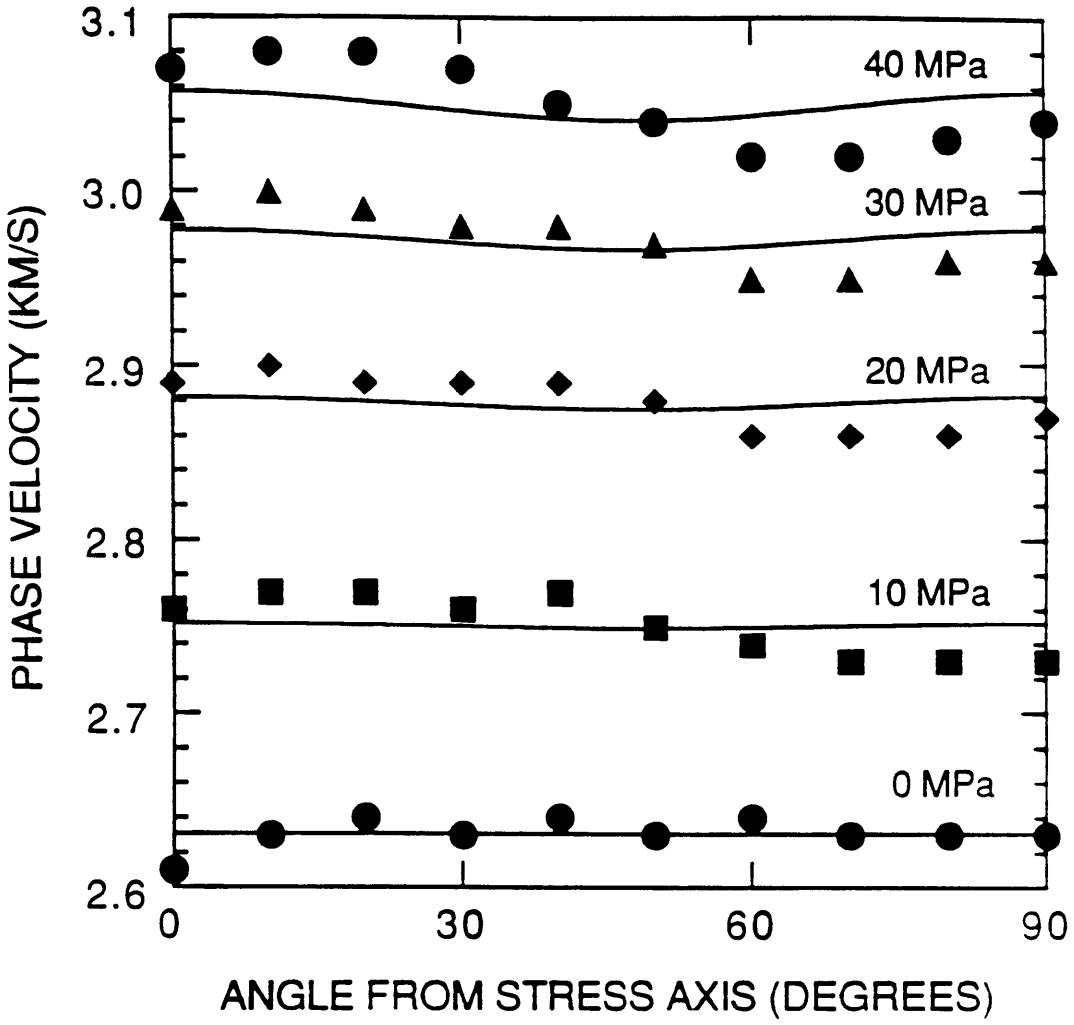

Figure 2-9: Results of inversion for crack density ξ and maximum crack size α_m using Barre granite qSV velocity data and the flat aspect ratio distribution (equation (2.7')). The points are data collected by Nur and Simmons (1969), and the lines indicate the results of a joint inversion of all of the data in this figure. The value of the applied uniaxial stress is indicated for each curve.

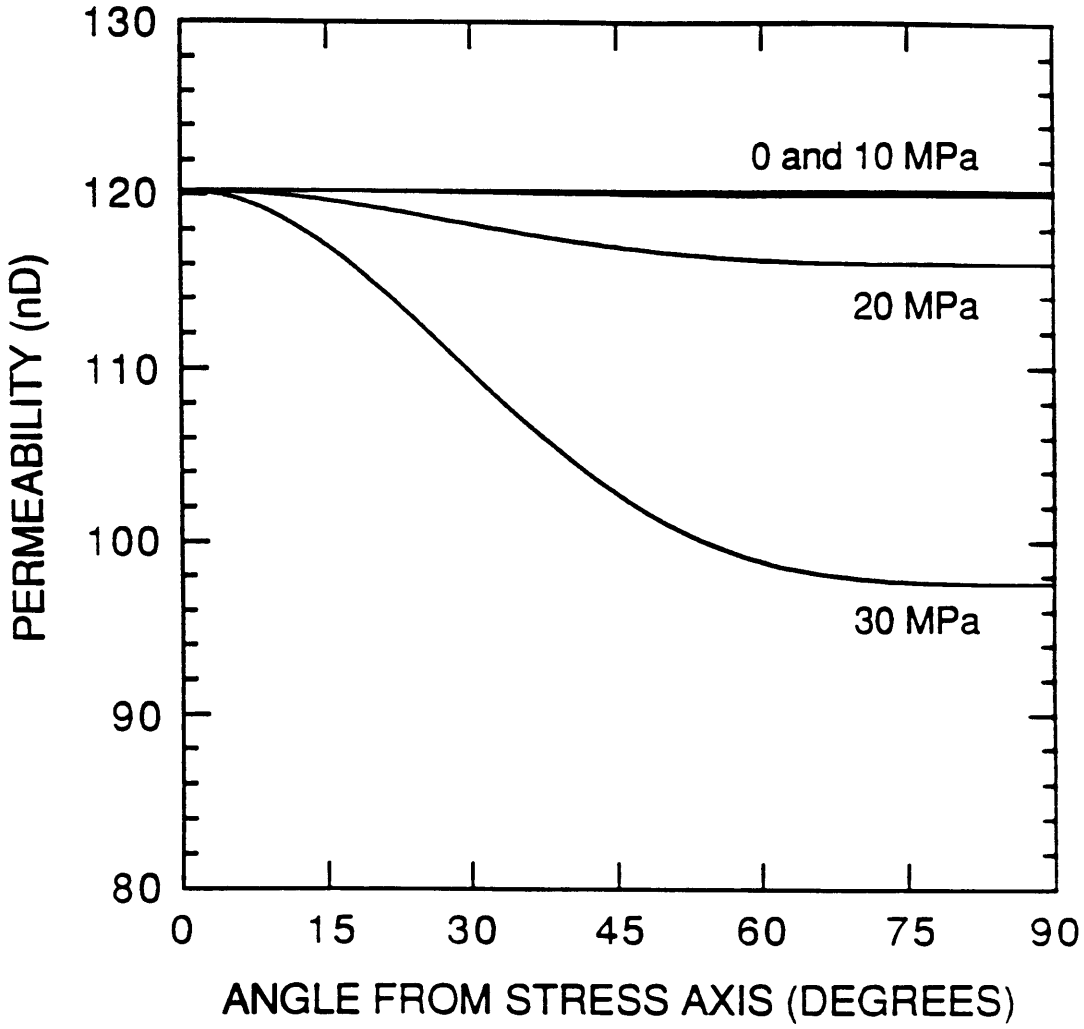

Figure 2-10: A) Permeability predictions as a function angle from the applied uniaxial stress axis. The predictions use the results from the inversion of qP data and the flat aspect ratio distribution. The uniaxial stress is indicated for each curve.

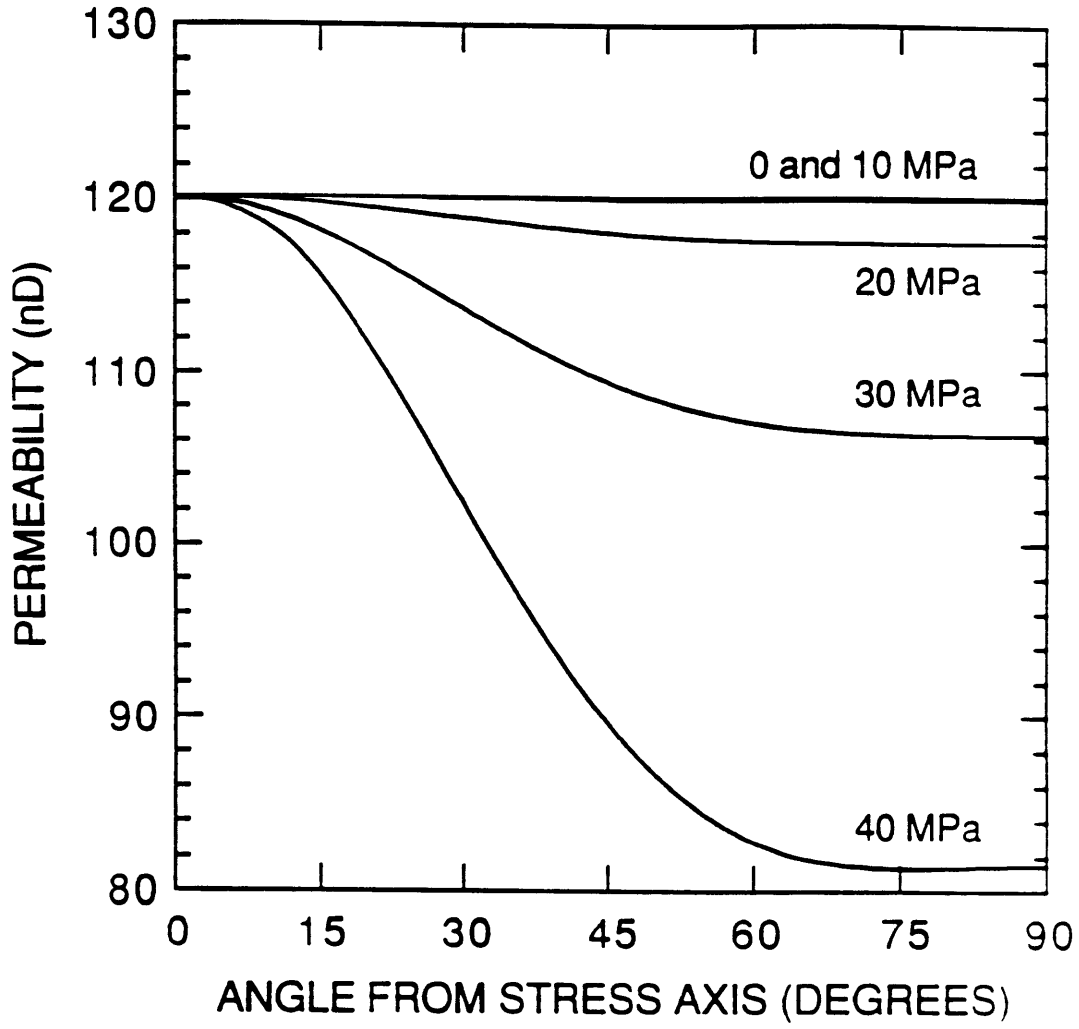

Figure 2-10: B) Permeability predictions as a function angle from the applied uniaxial stress axis. The predictions use the results from the inversion of SH data and the flat aspect ratio distribution. The uniaxial stress is indicated for each curve.

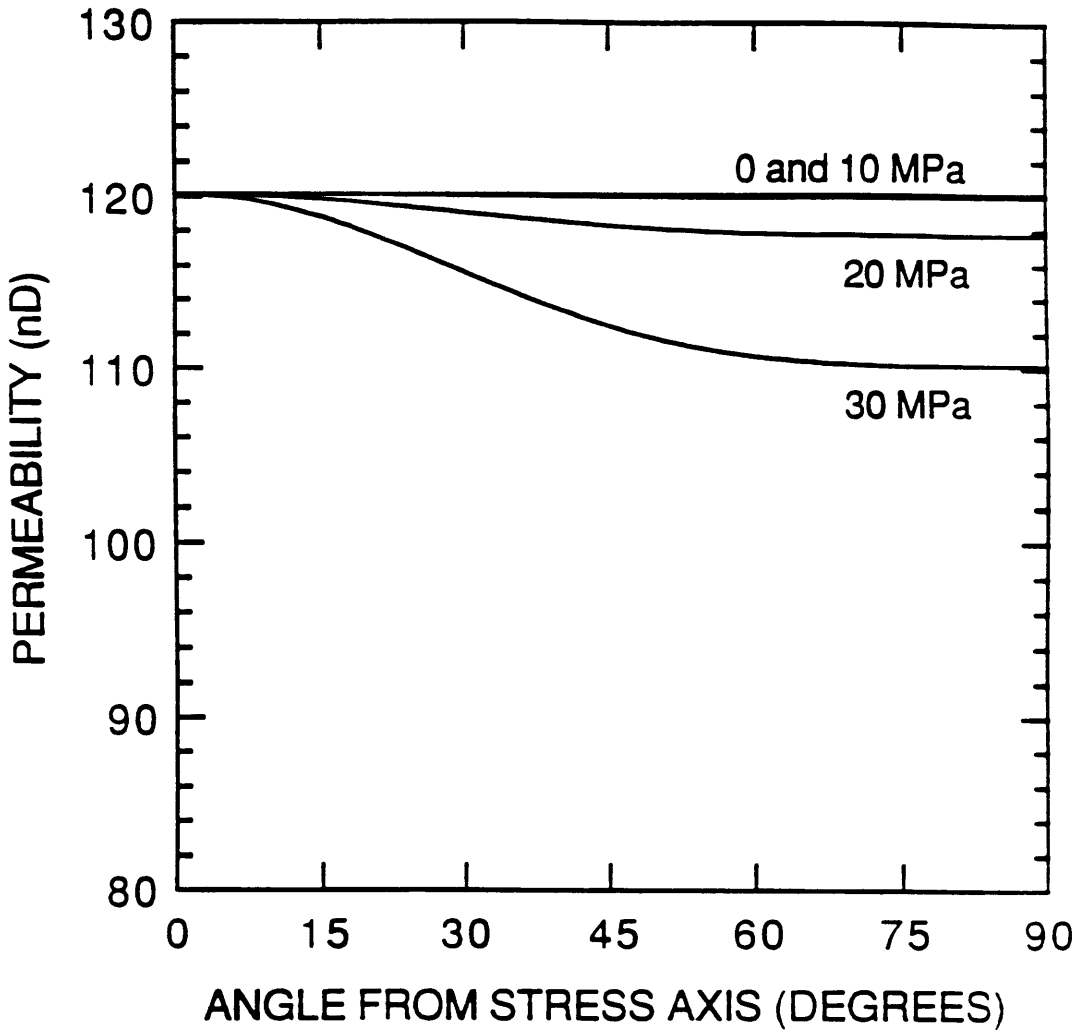

Figure 2-10: C) Permeability predictions as a function angle from the applied uniaxial stress axis. The predictions use the results from the inversion of qP data and the linear aspect ratio distribution. The uniaxial stress is indicated for each curve.

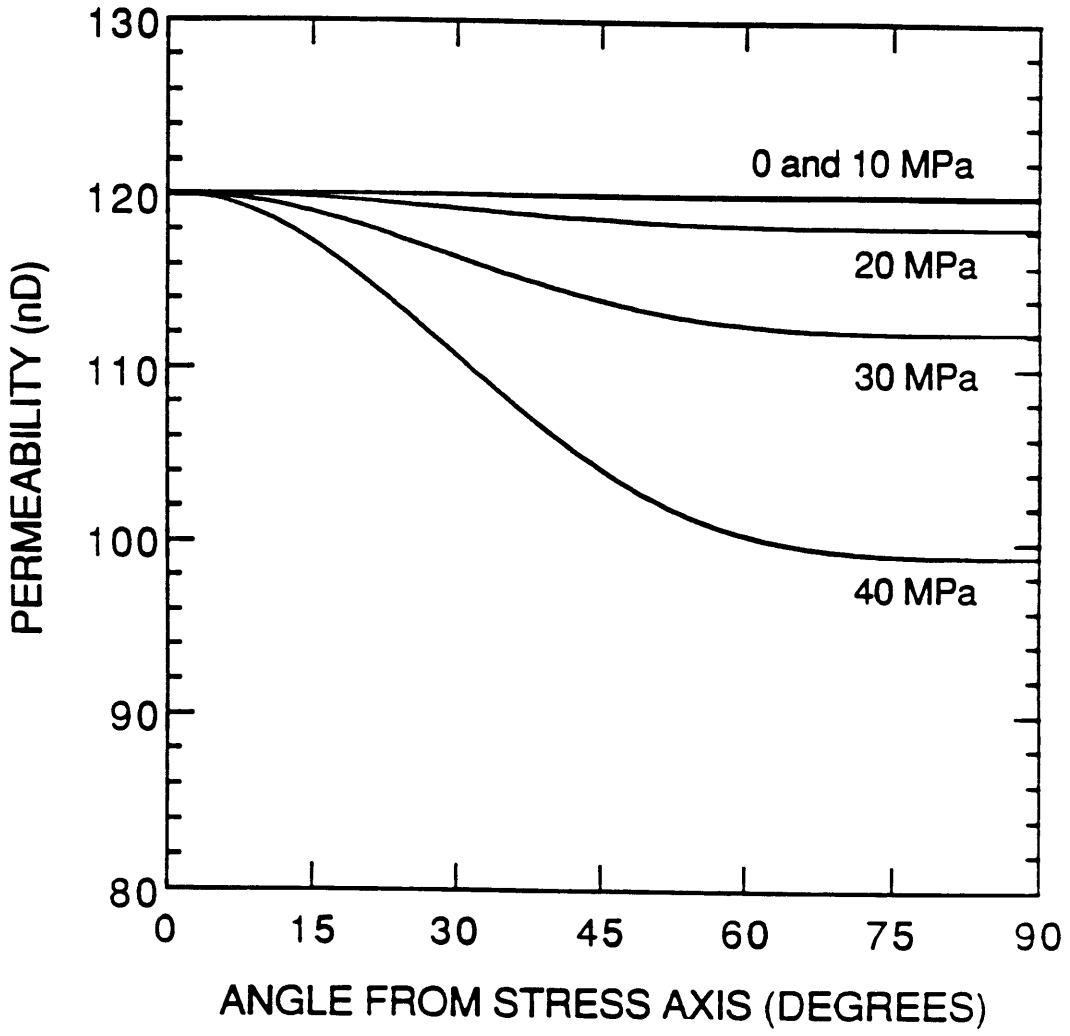

Figure 2-10: D) Permeability predictions as a function angle from the applied uniaxial stress axis. The predictions use the results from the inversion of SH data and the linear aspect ratio distribution. The uniaxial stress is indicated for each curve.

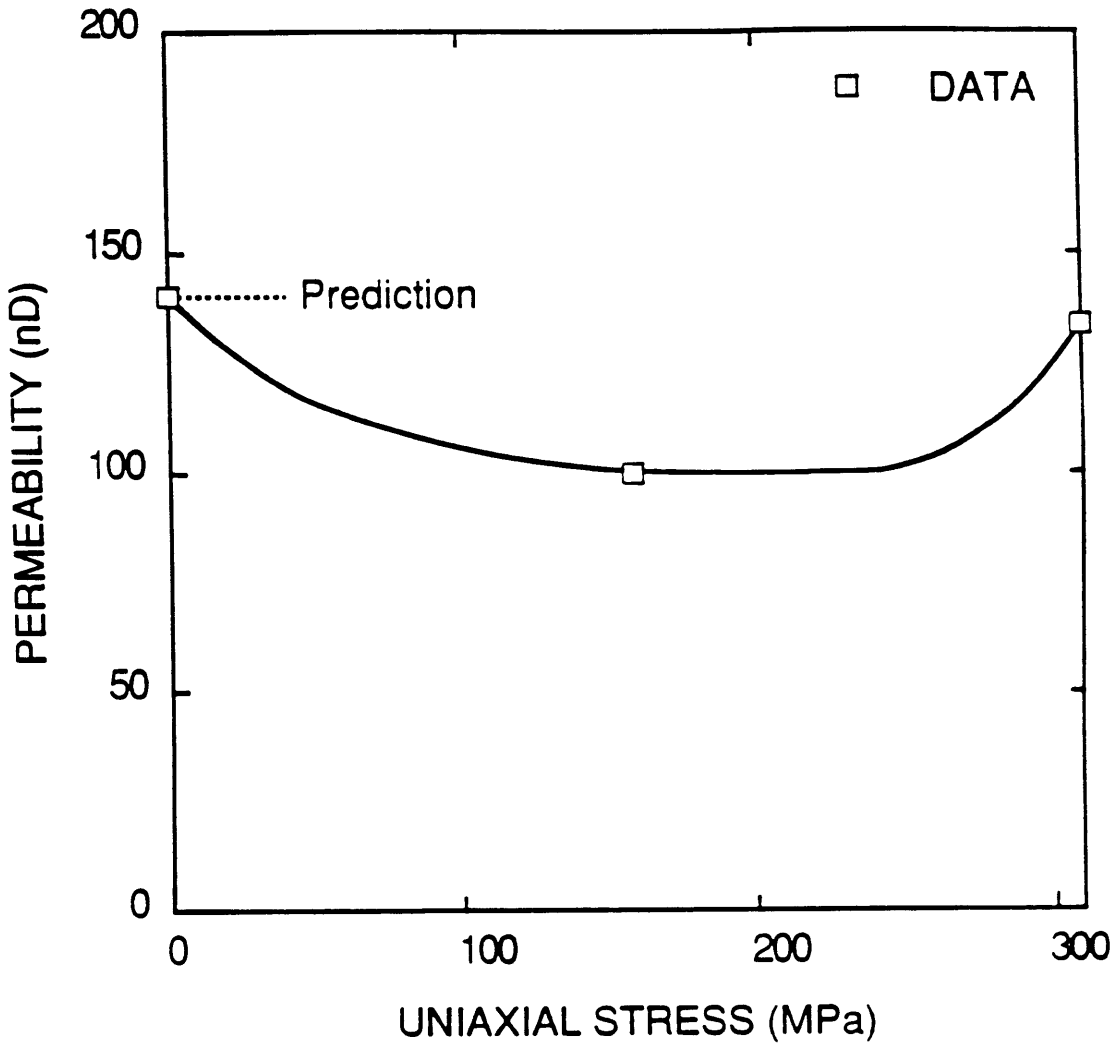

Figure 2-11: Comparison of permeability predictions parallel to the stress axis with measurements by Zoback and Byerlee [1975] of permeability parallel to the stress axis in an experiment performed on Westerly granite. The curve inferred by Zoback and Byerlee [1975] to represent permeability behavior between data points at 0 and 310 MPa is given by the solid line. The constant permeability which would be predicted by the theoretical model over the pressure range investigated by Nur and Simmons (1969) is indicated.

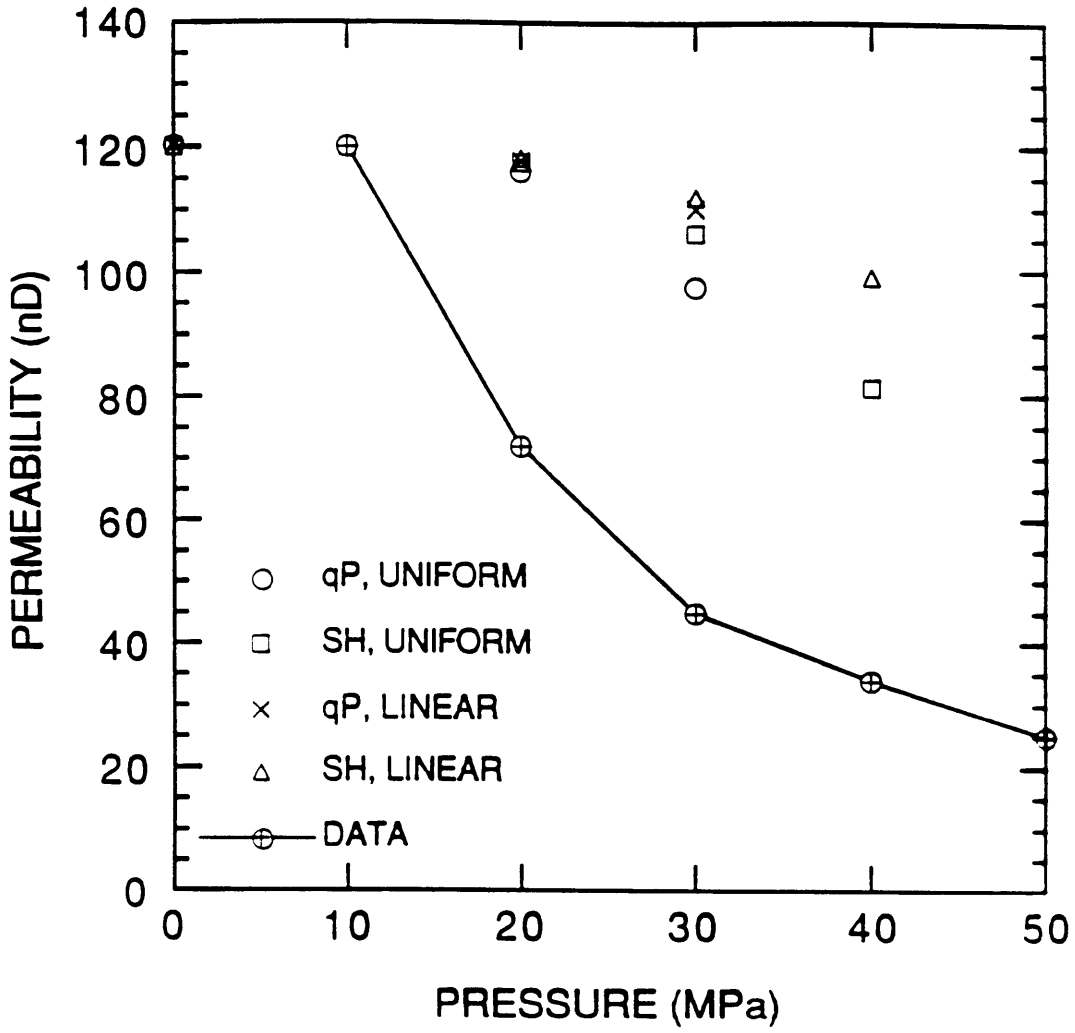

Figure 2-12: Comparison of hydrostatic permeability measurements with theoretical permeabilities perpendicular to the stress axis. The data, measurements on Barre granite [Bernabe, 1986], are indicated by the line and the points are calculated from equations (2.18) and (2.19). Since the permeabilities are normalized to have the same value at 10 MPa, the data and theoretical points overlap at this value of stress. The velocity data types used to calculate the permeability predictions are indicated in the figure.

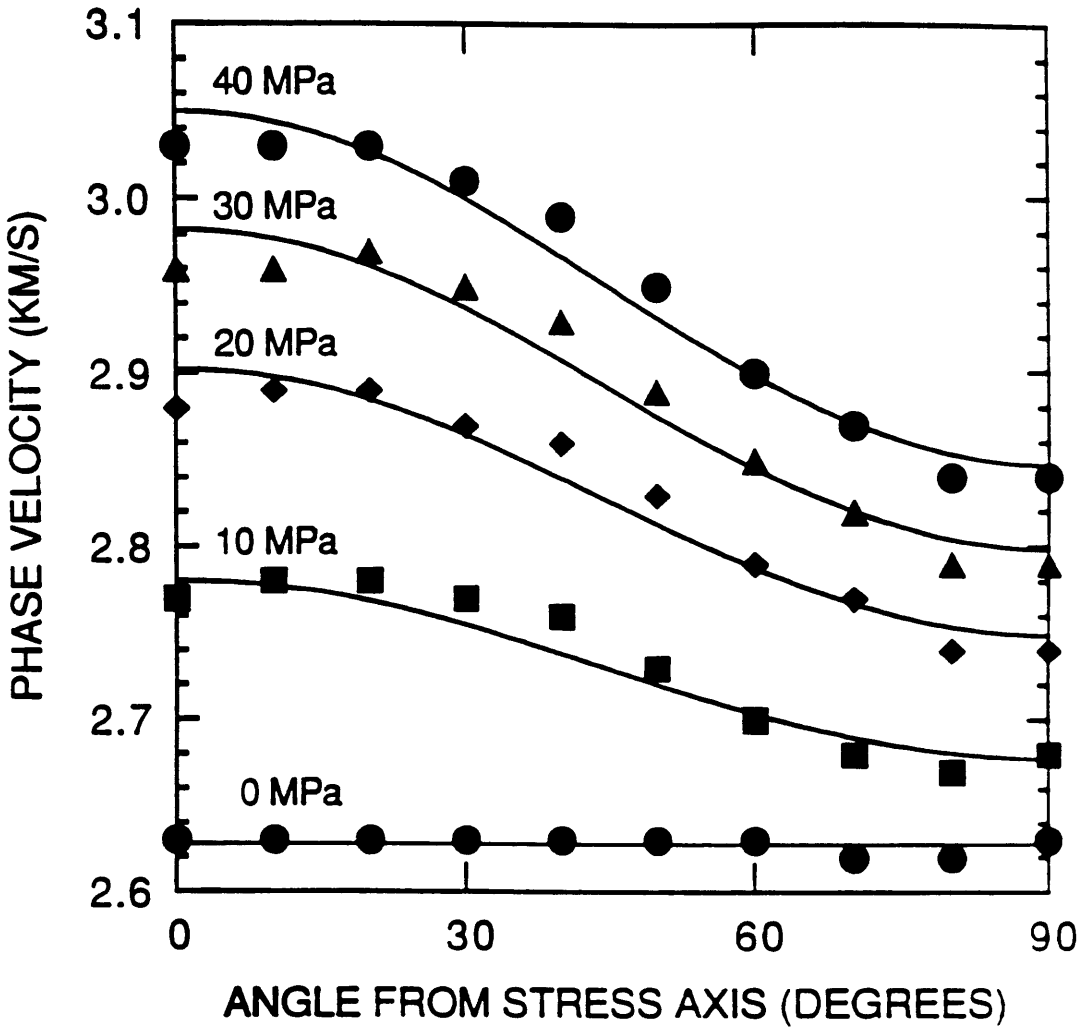

Figure 2-13: Results of independent inversions for crack density ξ and maximum crack size α_m of Barre granite SH velocity data. The points are data collected by Nur and Simmons (1969), and the lines indicate the inversion results. The value of the applied uniaxial stress is indicated for each curve.

Chapter 3

Elastic Wave Scattering by Anisotropic Obstacles: Application to Fractured Zones

All mathematicians would therefore be intuitive if they had good sight, because they do not draw false conclusions from principles that they know. And intuitive minds would be mathematical if they could adapt their sight to the unfamiliar principles of mathematics.

–Blaise Pascal

3.1 Introduction

Scattering of elastic waves by variations of the elastic properties of the earth is a fundamental problem with significant applications in several areas. As early as 1896, the effects of localized variations in bulk modulus and density on propagation of the acoustic waves were considered with what was essentially the first Born approximation (Rayleigh, 1945). More recently, Miles (1960) outlined the extension of the Born approximation to a fully elastic scattering obstacle. Chernov (1960) applied the same

approach, under the name of the method of small perturbations, to the acoustic case in order to examine propagation in random media. The application of the Born approximation essentially consists of the insertion of a perturbation solution into the equation of motion, and the perturbations to the elastic properties of the medium then appear as source terms for waves which propagate in the unperturbed, background medium. This method only accounts for single scattering, but nonetheless can be very useful.

In seismology, the scattering due to random variations of velocity is often considered as an explanation for features of elastic wave propagation which are difficult to account for as deterministic body or surface wave propagation. Aki (1969) suggested surface wave single scattering by heterogeneities concentrated along the earth's surface as a source for the coda energy following deterministic arrivals of local earthquakes and attempted to infer typical scatterer size and density. Subsequent work continued to explore this hypothesis, considering the effects of body wave scattering as well (e.g., Aki and Chouet, 1975). The application of the Born approximation to a single scattering model for P-wave coda was described by Hudson (1977), outlining some suggestions for application to statistical distributions of fluctuations of the elastic properties of a given medium and the resulting stochastic variations of the wavefield. Subsequently, Hudson and Heritage (1981) thoroughly analyzed the application of the Born approximation to the elastodynamic scattering in an effort to estimate the applicability of the method to various scattering problems in earthquake seismology. Gao et al. (1983a, 1983b) presented some simple models for the effects of multiple scattering on observed coda signals, while Wu and Aki (1985a) applied a single scattering model, including the Born approximation, for a volume distribution of scatterers and inferred mean amplitude deviations of seismograms for given distributions of scatterers. The influence of scattering on the observed attenuation of various waves is also important (e.g., Aki and Chouet, 1975; Dainty and Toksöz, 1977; Dainty, 1981; Aki, 1980). A recent general model for the attenuation of elas-

tic waves within the earth includes a significant contribution from scattering due to inhomogeneity in the uppermost crust (Toksöz et al., 1988).

In addition to these studies of the effects of scattering on forward modeling of wave propagation, both stochastic and deterministic, scattering theory has important implications for various inversion algorithms. The application of the Born approximation allows a linearization of the inversion procedure which is often utilized in very general inversion schemes in exploration seismology (e.g., Beydoun and Mendes, 1989; Cohen et al., 1986; Boyse and Keller, 1986; Clayton and Stolt, 1981). A fundamental aspect of these approaches to inversion is that a relatively accurate *background* model must be available which accounts for the smoothly varying properties of the medium. The Born scattering theory then can account for sharp, localized variations of the velocity, impedance or density (Beydoun and Mendes, 1989). These methodologies applied to exploration seismology are developed with the intent of estimating the properties of large regions of the subsurface. Another significant area of use for the Born approximation is the field of nondestructive evaluation. In this case, the task is generally to examine the scattering due to a single flaw or inhomogeneity within an otherwise homogeneous material (Gubernatis et al, 1977a). For spherical obstacles, the size of the inhomogeneity enters the expressions for the scattered field only through the product of volume and elastic parameters and hence cannot be determined uniquely without assumptions regarding obstacle properties (Gubernatis et al., 1979; Kohn and Rice, 1979). A technique to determine the radius of a spherical obstacle fairly robustly is described by Bond et al. (1988) with an application to data for a polystyrene sphere embedded in thermoplastic.

The studies discussed above generally consider only the effects of isotropic variations of elastic moduli, though Kohn and Rice (1979) discuss briefly the generality of the scattering results for anisotropic materials. It is clear that the earth is in many areas anisotropic, motivating the extension of these Born scattering techniques to more general media. Anisotropy of oceanic crust has been clearly observed (Hess, 1964;

Stephen, 1985), and shales and other materials in sedimentary basins are frequently observed to exhibit relatively strong anisotropy (Winterstein, 1986; Thomsen, 1986). It is also often suggested that much of the earth's crust is fractured and that the cracks which remain open tend to be aligned by prevailing tectonic stress regimes (Crampin, 1981). An isotropic material containing an aligned system of cracks will be effectively anisotropic for wavelengths larger than the crack size (Hudson, 1980, 1981; Crampin, 1984). Various observations of shear wave splitting and travel time anomalies in several areas help to confirm the existence of anisotropy due to aligned crack systems (Peacock et al., 1988; Leary et al., 1987; Crampin et al., 1986; Bamford and Nunn, 1979).

An initial investigation of the effects of anisotropy on Rayleigh scattering was made by Ben-Menahem and Gibson (1990) by looking at the simple, special case of a transversely isotropic inclusion in an isotropic background medium without application. We generalize this investigation of the effects of anisotropy on scattering theory by considering the Rayleigh scattering due to the most general anisotropic inclusion and apply it to the realistic example of variations in elastic properties caused by fracturing. A general inclusion can have up to 21 independent elastic constants, although there will generally be fewer due to symmetry considerations. In order to estimate the scattered wavefields, the values of the elastic constants and density are expressed as an average background value plus a small variation. The first Born approximation is applied to the subsequent perturbed wave equation, which yields an expression for the scattered field which is linear in the perturbations of the elastic constants. Expressions for the radiation patterns due to perturbations of each of the 21 independent elastic constants are derived.

In order to present a concrete example of the application of this method, we examine the effects of a small volume of fracturing within a homogeneous background medium. The effective elastic moduli in the presence of the aligned crack system can be estimated using the theory of Hudson (1980, 1981), which gives approximate values

for perturbations to elastic constants as functions of second order in crack density for both the isotropic case of randomly oriented cracks and for the anisotropic case of parallel cracks. These expressions for the perturbations provide realistic values to use in the scattering theory. The parallel crack model has 5 independent elastic constants, and therefore the medium is transversely isotropic with a horizontal axis of symmetry when the cracks are vertical. Consideration of the radiation patterns for the random and aligned crack volumes with equal crack density show that there are some distinct differences in the scattered displacement fields. Scattering from the parallel crack volume is significantly larger than from a random crack volume in some directions and much smaller in others. In particular, scattering completely vanishes for shear waves incident from certain directions with polarization parallel to the crack orientations. Some hypothetical seismic experiments which could be used to determine whether or not a fractured volume consists of aligned cracks are described, based on these differences.

3.2 Estimation of the General Scattered Field

3.2.1 The Born Approximation

The equation of motion in an anisotropic medium is

$$\rho\ddot{\mathbf{u}} - \nabla \cdot \mathbf{S} = \mathbf{f} \tag{3.1}$$

where $\mathbf{f}$ is the single force source vector, and

$$\begin{aligned} \mathbf{S} &= \mathbf{T} - \mathbf{M} \\ \mathbf{T} &= \mathbf{c} : \mathbf{E}. \end{aligned} \tag{3.2}$$

Here $\mathbf{S}$ is the physical stress field, $\mathbf{T}$ is the stress given by Hooke's law, $\mathbf{E}$ being the strain tensor, and $\mathbf{M}$ is a moment tensor density source (Ben-Menahem and Singh, 1981; Backus and Mulcahy, 1977a). The components of the tensor $\mathbf{S}, \mathbf{T}$ and $\mathbf{E}$ are

denoted by σ_{ij}, τ_{ij} and ϵ_{ij}, respectively. The solution of equation (3.1) can be obtained in integral form using the Green's tensor solution, where the component $G_{ij}(\mathbf{x}, t; \mathbf{x}', t')$ of the Green's tensor represents the i'th component of displacement at $\mathbf{x}$ and time t due to the a point force in the j direction applied at $\mathbf{x}'$ at time t'. The solution is written (Ben-Menahem and Singh, 1981)

$$\begin{aligned} \mathbf{u}(\mathbf{x}, t) &= \int dV(\mathbf{x}') \int dt' \ \mathbf{G}(\mathbf{x}, t; \mathbf{x}', t') \cdot \mathbf{f}(\mathbf{x}', t') \\ &\quad + \int dV(\mathbf{x}') \int dt' \ \mathbf{M}(\mathbf{x}', t') : \nabla \widetilde{\mathbf{G}}(\mathbf{x}, t; \mathbf{x}', t'), \end{aligned} \tag{3.3}$$

where the $\tilde{}$ symbol indicates transpose. This formulation can be used to find the displacement due to any combination of single force or moment tensor type sources distributed in space and time.

Now suppose that the values of density and elastic constants vary slightly from given background values ρ_0 and c^0_{ijkl}, so that the new values are given by:

$$\begin{aligned} \rho &= \rho^0 + \delta\rho \\ \mathbf{c} &= \mathbf{c}^0 + \delta\mathbf{c}. \end{aligned} \tag{3.4}$$

The deviations of the density and elastic constants result in deviations of the displacement field as well. We proceed by assuming a perturbed field of the form

$$\mathbf{u}(\mathbf{x}, t) = \mathbf{u}^0(\mathbf{x}, t) + \delta\mathbf{u}(\mathbf{x}, t), \tag{3.5}$$

where again the superscript 0 indicates a background field which is the field which would be obtained if in fact the true medium properties were ρ_0 and c^0_{ijkl}. Substitution of the perturbed field (3.5) and the perturbed medium properties (3.4) into equation (3.1), neglecting terms of second order, gives the following result:

$$\rho^0\ddot{\mathbf{u}}^0 + \rho^0\delta\ddot{\mathbf{u}} + \delta\rho\ddot{\mathbf{u}}^0 - \nabla \cdot (\mathbf{c}^0 : \mathbf{E}^0 + \delta\mathbf{c} : \mathbf{E}^0 + \mathbf{c}^0 : \delta\mathbf{E} - \mathbf{M}) = \mathbf{f}. \tag{3.6}$$

Upon inspection, we see that equation (3.6) is the sum of two equations, one of which is equation (3.1), the equation of motion for the background displacement field $\mathbf{u}^0$

propagating in a material with the background properties. The other equation can be obtained by subtracting equation (3.1) from equation (3.6):

$$\rho^0 \delta\ddot{\mathbf{u}} - \nabla \cdot (\mathbf{c} : \delta\mathbf{E} + \delta\mathbf{c} : \mathbf{E}) = -\delta\rho\ddot{\mathbf{u}}^0. \tag{3.7}$$

Comparing this result with equation (3.1), it is evident that this provides an equation of motion describing propagation of the scattered field $\delta\mathbf{u}$, where the source terms are a single force arising from density perturbations, and a moment tensor or double force type source due to the elastic constant perturbations. This source representation is an example of a *stress glut* due to the excess of the actual physical stress field $\mathbf{S}$ in comparison to the stress field modeling the propagation of the elastic waves, $\mathbf{T}$ (Backus and Mulcahy, 1977a, 1977b; Kennett, 1983). Wu and Aki (1985b) have described a similar moment tensor source representation to estimation of the scattered field for perturbations to the Lamé parameters λ and μ. The components of the moment tensor

$$\delta\mathbf{M} = \delta\mathbf{c} : \mathbf{E^0} \tag{3.8}$$

for a general perturbation to any one of the elastic constants are simply

$$\delta M_{ij} = \delta c_{ijkl} \epsilon^0_{kl}. \tag{3.9}$$

The time dependence of this source is governed only by the displacement due to the background field $\mathbf{u^0}$, which can be simply calculated since in this approximation it propagates with the properties of the background medium. The propagation of the perturbed field $\delta\mathbf{u}$ is also governed only by the background properties of the medium, and the perturbations enter only in the source terms. This allows a relatively straightforward estimation of the scattered field, and in a sense, the problem is completely solved at this point, since the displacement due to both single force and moment tensor sources is given by equation (3.3). We can write this solution as

$$\begin{aligned} \delta\mathbf{u}(\mathbf{x}, t) \;=\; & \int dV(\mathbf{x}') \int dt' \;\; \mathbf{G}^0(\mathbf{x}, t; \mathbf{x}', t') \cdot (\delta\rho\ddot{\mathbf{u}}^0(\mathbf{x}', t')) \\ & + \int dV(\mathbf{x}') \int dt' \;\; [(\delta\mathbf{c}(\mathbf{x}', t') : \mathbf{E}^0(\mathbf{x}', t'))] : [\nabla\widetilde{\mathbf{G}}^{\mathbf{0}}(\mathbf{x}, t; \mathbf{x}', t')]. \end{aligned} \tag{3.10}$$

Here $\mathbf{G}^0$ denotes the Green's tensor in the background medium. All that remains is to actually write out the solutions due to various perturbations of material properties. It is important to note that in addition to the simplification resulting from waves propagating only in the background medium, certain advantages result from the fact that the approximation is linear in perturbations to material parameters. Doubling the amount of a perturbation will double the amplitude of the scattered waves, for example. Inversions for medium velocities or densities are also facilitated by this linearization (e.g., Beydoun and Mendes, 1989). The term $\delta\mathbf{u}(\mathbf{x}, t)$ is known as the *Frechet derivative*, a quantity often utilized in inversion schemes (Tarantola, 1987).

This estimate of the scattered field is variously known as the method of small perturbations (Chernov, 1960) or the first Born approximation (Hudson and Heritage, 1981; Gubernatis et al., 1977b; Wu and Aki, 1985b). Since all second order terms are neglected in the derivation, it is clear that the applicability of the results will be limited by any departures from these assumptions. The stronger the contrast in material properties between the obstacle and the surrounding background material, the worse the results will be. Likewise, as the dimensions of the obstacle increase, the validity of the Rayleigh scattering approach will decrease. Because the scattered field is assumed to propagate in a medium with the properties of the background, that if there is a slight departure from the background properties over a large volume, the approximation will be poor as even estimates of travel times of the scattered field will not be accurate due to the integration of an error in velocity over the propagation path of the scattered signal.

3.2.2 The Moment Tensor Source

If we consider only perturbations to the elastic constants, the radiation due to the scattering obstacles will be given entirely by the moment tensor source in equations (3.9). The relationship between the strains due to an incident wave $\mathbf{u}^0$ and the moment tensor components δM_{ij} can be concisely expressed in the standard six by six form

of the elastic tensor (Musgrave, 1970). This expression is

$$\begin{bmatrix} \delta M_{11} \\ \delta M_{22} \\ \delta M_{33} \\ \delta M_{23} \\ \delta M_{13} \\ \delta M_{12} \end{bmatrix} = \begin{bmatrix} \delta C_{11} & \delta C_{12} & \delta C_{13} & \delta C_{14} & \delta C_{15} & \delta C_{16} \\ & \delta C_{22} & \delta C_{23} & \delta C_{24} & \delta C_{25} & \delta C_{26} \\ & & \delta C_{33} & \delta C_{34} & \delta C_{35} & \delta C_{36} \\ & & & \delta C_{44} & \delta C_{45} & \delta C_{46} \\ & & & & \delta C_{55} & \delta C_{56} \\ & & & & & \delta C_{66} \end{bmatrix} \begin{bmatrix} \epsilon^0_{11} \\ \epsilon^0_{22} \\ \epsilon^0_{33} \\ 2\epsilon^0_{23} \\ 2\epsilon^0_{13} \\ 2\epsilon^0_{12} \end{bmatrix}. \quad (3.11)$$

Since the elastic constant matrix δC_{IJ} is symmetric, only the upper half is shown for clarity. This representation of the scattered field moment tensor obviates the relationships of the incident field and the various moment tensor components. For example, any element of the elastic constant matrix in the first row, δC_{1J}, will contribute to δM_{11}, the dipole source oriented along the $x-$axis. A general perturbation δC_{IJ} with $I \neq J$ will contribute to the I'th and J'th moment tensor components in the column vector on the left hand side of equation (3.11), though the diagonal elements with $I = J$ will only contribute to one source type. Likewise, any element C_{IJ} in the J'th column of the matrix will only contribute to scattering if the incident wave has a non-zero strain in the J'th component of the strain vector. This demonstrates important restrictions on the information contained in the scattered wavefield generated by a given incident wave. If it is desired to determine information on a number of perturbations δC_{IJ} from the scattered waves, then a large variety of incidence directions and wave types will be required.

The significance of different elastic constants can also be categorized according to the double force representation of the scattering due to the constants to summarize their effects on scattering:

1. Single dipole.

   $\delta C_{11}, \delta C_{22}$, and δC_{33}.

2. Two dipoles.

$\delta C_{12}, \delta C_{13}$, and δC_{23}.

3. Double couple.

   $\delta C_{44}, \delta C_{55}$, and δC_{66}.

4. Double couple and a dipole.

   $\delta C_{14}, \delta C_{15}, \delta C_{16}, \delta C_{24}, \delta C_{25}, \delta C_{26}, \delta C_{34}, \delta C_{35}$, and δC_{36}.

5. Two double couples.

   $\delta C_{45}, \delta C_{46}$, and δC_{56}.

A representative example of each of these double force systems is illustrated in Figure 3-1, showing the different degrees of complexity in the sources.

3.2.3 Radiation Patterns for Rayleigh Scattering

In order to derive far-field radiation patterns for the scattered field due to the perturbation of one of the elastic constants, we assume that the perturbation is located within a small volume centered on the origin of the spherical coordinate system (Figure 3-2). When this volume is much less than a wavelength in size, the amplitude and phase of the incident field $\mathbf{u}^0(\mathbf{x}, t)$ can be assumed constant throughout the volume of the obstacle at a given time, and the spatial distribution of the obstacle in equation (3.10) can be expressed as a Dirac delta located at the origin with amplitude equal to the volume δV of the perturbed zone. Therefore, the integration in equation (3.10) reduces to

$$\delta\mathbf{u}(\mathbf{x}, t) \;=\; \delta V \int dt' \;\; (\delta\mathbf{c}(\mathbf{0}, t') : \mathbf{E}^0(\mathbf{0}, t')) : \nabla\widetilde{\mathbf{G}}^{\mathbf{0}}(\mathbf{x}, t; \mathbf{0}, t'). \qquad (3.12)$$

As the algebra is cumbersome and extensive, presentation of a representative example of each of the five source groups is relegated to Appendix B to demonstrate the application of this method, and radiation patterns for all of the elastic constants are given in Appendix D. Along with the derivations of radiation patterns, we summarize

the unique aspects of scattering due to each perturbation example to illustrate the information contained in observations of scattered fields and how this will affect estimates of elastic properties from scattered displacements. A similar methodology for calculation of radiation patterns was employed by Ben-Menahem and Gibson (1990) for the case of a transversely isotropic inclusion.

3.3 Scattering Due to Fracturing

While in principle the scattering results shown above and in Appendix D can be applied to any combination of one or more of the 21 independent elastic constants, in general far fewer independent coefficients will likely be required to examine scattering due to symmetry considerations for realistic earth materials. For example, some of the most common causes of anisotropy in the earth's crust are periodic fine layering and aligned fracture systems, both of which create an effective anisotropy (Crampin, 1981). These effects lead to a transversely isotropic symmetry with 5 independent elastic constants. In addition, some lithologies, particularly shales, have significant anisotropies on a large scale (Winterstein, 1986).

In order to restrict the analysis to cases of scattering with some degree of realism, we can consider the scattering due to a small fractured region within an otherwise isotropic rock layer. Effective anisotropy due to aligned systems of vertical cracks appears to be widespread (Crampin, 1981; Crampin et al., 1986; Peacock et al., 1988). However, it seems likely that the earth's crust is not uniformly fractured to a constant degree. If the fracturing is not uniform, then the effects on elastic wave propagation would not always be simply the propagation of elastic waves in an effectively anisotropic medium with resultant shear wave splitting. When the wavelength of the propagating wave is larger than the fractured zone, the effects of the cracks would be scattering phenomena, and shear wave splitting would not be observed, although the polarizations of propagating waves would be altered due to

the scattered waves.

The Born scattering approach can be used to gain some understanding of the expected effects in this case. We consider the case of aligned vertical fractures with 5 independent elastic constants. If the cracks were inclined at some angle less than 90° with respect to vertical, several additional elastic constants would become non-zero due to the rotation of the reference coordinate system, but there still are only 5 independent constants. Therefore, the subsequent analysis is still fairly general for systems of aligned cracks, since a rotation of the cracks is equivalent to a change in direction of the incident wave.

3.3.1 Perturbations to Elastic Constants

We can analyze the effects of fractured zones on scattering by applying the theory of Hudson (1980, 1981) for perturbations to elastic constants due to the cracks. This theory has also been applied by Crampin (1984). If we consider first the case where the cracks are randomly oriented, we have the following approximations for the effects of the cracks on the Lamé parameters of the medium (Hudson, 1980):

$$\begin{aligned}\mu &\cong \mu_0 + \mu_0[-\xi\frac{2}{15}(3U_{33}+2U_{11}) + \xi^2\left(\frac{2}{15}\right)^3\left(\frac{3\lambda_0+8\mu_0}{\lambda_0+\mu_0}\right)(3U_{33}+2U_{11})^2] \quad (3.13)\\ &= \mu_0 + \delta\mu\end{aligned}$$

$$\begin{aligned}\lambda &\cong \lambda_0 - \xi\left[\frac{(3\lambda_0+2\mu_0)^2}{9\mu_0} + \frac{2}{3}\frac{2\mu_0}{15}(3U_{33}+2U_{11})\right]\\ &\quad + \xi^2\left[\frac{(3\lambda_0+2\mu_0)^4}{81\mu_0^2(\lambda_0+2\mu_0)}U_{11}^2 - \frac{2}{3}\mu_0\left(\frac{2}{15}\right)^3\frac{3\lambda_0+8\mu_0}{\lambda_0+2\mu_0}(3U_{33}+2U_{11})^2\right] \quad (3.14)\\ &= \lambda_0 + \delta\lambda.\end{aligned}$$

Here λ_0 and μ_0 are the Lamé parameters of the unfractured background material, and ξ is the crack density defined as

$$\xi = na^3. \quad (3.15)$$

The number density of cracks is n, and a is the radius of the low aperture ratio, penny-shaped cracks. Perturbations of the Lamé parameters given by equations (3.13) and (3.14) are therefore expansions to second order in crack density ξ, which is assumed to be relatively small. The two quantities U_{11} and U_{33} are functions of the Lamé parameters of the uncracked medium and the crack filling material, and in this paper, we will apply the definitions given by Crampin (1984). If the cracks are empty (dry) then these two quantities are

$$U_{11} = \frac{4}{3}\frac{\lambda_0 + 2\mu_0}{\lambda_0 + \mu_0} \tag{3.16}$$

$$U_{33} = \frac{16}{3}\frac{\lambda_0 + 2\mu_0}{3\lambda_0 + 4\mu_0}. \tag{3.17}$$

If the cracks are filled with a gas, the effective Lamé parameters will still be essentially the same as those in equations (3.13) and (3.14), since the low bulk modulus of a gas will yield effectively the same values of U_{11} and U_{33} as those given in (3.16).

The Voigt form of the elastic tensor for an isotropic material is

$$\begin{bmatrix} \lambda+2\mu & \lambda & \lambda & & & \\ \lambda & \lambda+2\mu & \lambda & & & \\ \lambda & \lambda & \lambda+2\mu & & & \\ & & & \mu & & \\ & & & & \mu & \\ & & & & & \mu \end{bmatrix}, \tag{3.18}$$

where zero values have been omitted for clarity. Therefore, the non-zero perturbations to the elastic constants are $\delta C_{11} = \delta C_{22} = \delta C_{33} = \delta\lambda + 2\delta\mu$, $\delta C_{12} = \delta C_{13} = \delta C_{23} = \delta\lambda$, and $\delta C_{44} = \delta C_{55} = \delta C_{66} = \delta\mu$. The moment tensor source is

$$\delta\mathbf{M} = \begin{bmatrix} \delta\lambda\epsilon^0_{ii} + 2\delta\mu\epsilon^0_{11} & 2\delta\mu\epsilon^0_{12} & 2\delta\mu\epsilon^0_{13} \\ 2\delta\mu\epsilon^0_{12} & \delta\lambda\epsilon^0_{ii} + 2\delta\mu\epsilon^0_{22} & 2\delta\mu\epsilon^0_{23} \\ 2\delta\mu\epsilon^0_{13} & 2\delta\mu\epsilon^0_{23} & \delta\lambda\epsilon^0_{ii} + 2\delta\mu\epsilon^0_{33} \end{bmatrix}, \tag{3.19}$$

and we see that $\delta\lambda$ leads to an explosion-like source consisting of a sum of 3 equal and mutually perpendicular dipoles proportional to the divergence of the wavefield ϵ^0_{ii},

whereas $\delta\mu$ leads to a more complicated radiation pattern depending on the strains associated with the incident wave. These results reproduce those of Wu and Aki (1985b), except for differences due to the generalization of the directions of propagation and polarization of the incident waves. Since the $\delta\lambda$ perturbation multiplies the divergence of the wavefield, it will never generate scattered wavefields for shear wave incidence and even for compressional wave incidence, will only radiate compressional waves since it is an explosion-like source.

The scattered displacement fields due to the fractured material can be simply computed by adding the contributions due to the perturbations to the Lamé parameters, noting the relationship to the elastic constants δC_{IJ} (Appendix D). Carrying out this addition, the resulting expressions for the scattered fields for compressional wave incidence are

$$\begin{aligned}
\delta u_r^P(\mathbf{x},t) &= -(\delta VA)\frac{\omega^2}{4\pi\rho\alpha^4}\frac{e^{i(\omega t-r/\alpha)}}{r}\mathcal{F}^i_{rP}(\theta,\phi;\theta_0,\phi_0) \\
\delta u_\theta^P(\mathbf{x},t) &= -(\delta VA)\frac{\omega^2}{4\pi\rho\alpha\beta^3}\frac{e^{i(\omega t-r/\beta)}}{r}\mathcal{F}^i_{\theta P}(\theta,\phi;\theta_0,\phi_0) \qquad (3.20)\\
\delta u_\phi^P(\mathbf{x},t) &= -(\delta VA)\frac{\omega^2}{4\pi\rho\alpha\beta^3}\frac{e^{i(\omega t-r/\beta)}}{r}\mathcal{F}^i_{\phi P}(\theta,\phi;\theta_0,\phi_0),
\end{aligned}$$

with the scattering coefficients $\mathcal{F}^i_{rP}, \mathcal{F}^i_{\theta P}$, and $\mathcal{F}^i_{\phi P}$:

$$\begin{aligned}
\mathcal{F}^i_{rP}(\theta,\phi;\theta_0,\phi_0) &= \delta\lambda + \delta\mu[\sin^2\theta_0\sin^2\theta(2\cos^2\phi_0\cos^2\phi + 2\sin^2\phi_0\sin^2\phi \\
&\quad + \sin 2\phi_0 \sin 2\phi) \\
&\quad + \sin 2\theta_0 \sin 2\theta \cos(\phi_0-\phi) + 2\cos^2\theta_0\cos^2\theta] \\
\mathcal{F}^i_{\theta P}(\theta,\phi;\theta_0,\phi_0) &= \delta\mu[\sin^2\theta_0\sin\theta\cos\theta(2\cos^2\phi_0\cos^2\phi + 2\sin^2\phi_0\sin^2\phi \\
&\quad + \sin 2\phi_0 \sin 2\phi) \\
&\quad + \sin 2\theta_0 \cos 2\theta \cos(\phi_0-\phi) - 2\cos^2\theta_0\sin\theta\cos\theta] \qquad (3.21)\\
\mathcal{F}^i_{\phi P}(\theta,\phi;\theta_0,\phi_0) &= \delta\mu[\sin^2\theta_0(-\cos 2\phi_0\sin\theta\sin 2\phi + \sin 2\phi_0\sin\theta\cos 2\phi) \\
&\quad + \sin 2\theta_0\cos\theta\sin(\phi_0-\phi)].
\end{aligned}$$

The total scattered field for either SV or SH-wave incidence can also be computed by

the same approach, yielding expressions of the form

$$\begin{aligned}
\delta u_r^{SH}(\mathbf{x},t) &= -(\delta VA)\frac{\omega^2}{4\pi\rho\beta\alpha^3}\frac{e^{i(\omega t-r/\alpha)}}{r}\mathcal{F}^i_{rS}(\theta,\phi;\theta_0,\phi_0) \\
\delta u_\theta^{SH}(\mathbf{x},t) &= -(\delta VA)\frac{\omega^2}{4\pi\rho\beta^4}\frac{e^{i(\omega t-r/\beta)}}{r}\mathcal{F}^i_{\theta S}(\theta,\phi;\theta_0,\phi_0) \qquad (3.22)\\
\delta u_\phi^{SH}(\mathbf{x},t) &= -(\delta VA)\frac{\omega^2}{4\pi\rho\beta^4}\frac{e^{i(\omega t-r/\beta)}}{r}\mathcal{F}^i_{\phi S}(\theta,\phi;\theta_0,\phi_0),
\end{aligned}$$

where $\mathcal{F}^i_{rS}$ is the scattering coefficient $\mathcal{F}^i_{rSV}$ or $\mathcal{F}^i_{rSH}$ for SV or SH-wave incidence, respectively. The same system of notation holds true for the other spherical coordinates of the displacement for the scattered fields. These scattering coefficients are

$$\begin{aligned}
\mathcal{F}^i_{rSV}(\theta,\phi;\theta_0,\phi_0) &= \delta\mu[\sin\theta_0\cos\theta_0\sin^2\theta(2\cos^2\phi_0\cos^2\phi+2\sin^2\phi_0\sin^2\phi \\
&\quad +\sin 2\phi_0\sin 2\phi)+\cos 2\theta_0\sin 2\theta\cos(\phi_0-\phi)-\sin 2\theta_0\cos^2\theta] \\
\mathcal{F}^i_{\theta SV}(\theta,\phi;\theta_0,\phi_0) &= \delta\mu[\sin\theta_0\cos\theta_0\sin\theta\cos\theta(2\cos^2\phi_0\cos^2\phi+2\sin^2\phi_0\sin^2\phi+ \\
&\quad \sin 2\phi_0\sin 2\phi+2)+\cos 2\theta_0\cos 2\theta\cos(\phi_0-\phi)] \qquad (3.23)\\
\mathcal{F}^i_{\phi SV}(\theta,\phi;\theta_0,\phi_0) &= \delta\mu[\sin\theta_0\cos\theta_0\sin\theta\sin(2\phi_0-2\phi) \\
&\quad +\cos 2\theta_0\cos\theta\sin(\phi_0-\phi)]
\end{aligned}$$

and

$$\begin{aligned}
\mathcal{F}^i_{rSH}(\theta,\phi;\theta_0,\phi_0) &= \delta\mu[\sin\theta_0\sin^2\theta\sin(2\phi_0-2\phi)+\cos\theta_0\sin 2\theta\sin(\phi_0-\phi)] \\
\mathcal{F}^i_{\theta SH}(\theta,\phi;\theta_0,\phi_0) &= \delta\mu[\sin\theta_0\sin\theta\cos\theta\sin(2\phi_0-2\phi) \qquad (3.24)\\
&\quad +\cos\theta_0\cos 2\theta\sin(\phi_0-\phi)] \\
\mathcal{F}^i_{\phi SH}(\theta,\phi;\theta_0,\phi_0) &= \delta\mu[\sin\theta_0\sin\theta\cos(2\phi_0-2\phi)+\cos\theta_0\cos\theta\cos(\phi_0-\phi)].
\end{aligned}$$

These expressions for the isotropic coefficients obviate the simple role of $\delta\lambda$ in the scattering process, since it occurs only in $\mathcal{F}^i_{rP}$ for P to P mode scattering.

In contrast to the isotropic scattering obstacle defined by the randomly oriented fractures, we can consider the case of aligned, vertical fractures. When the orientation of the cracks is defined to be perpendicular to the x-axis of the Cartesian coordinate

system, the resulting perturbations to the elastic constants to second order in ξ are (Crampin, 1984):

$$\mathbf{C} \cong \mathbf{C^0} \tag{3.25}$$

$$-\frac{\xi}{\mu}\begin{bmatrix} (\lambda_0+2\mu_0)^2U_{11} & \lambda_0(\lambda_0+2\mu_0)U_{11} & \lambda_0(\lambda_0+2\mu_0)U_{11} & & & \\ \lambda_0(\lambda_0+2\mu_0)U_{11} & \lambda_0^2U_{11} & \lambda_0^2U_{11} & & & \\ \lambda_0(\lambda_0+2\mu_0)U_{11} & \lambda_0^2U_{11} & \lambda_0^2U_{11} & & & \\ & & & 0 & & \\ & & & & \mu_0^2U_{33} & \\ & & & & & \mu_0^2U_{33} \end{bmatrix}$$

$$+\frac{\xi^2}{15}\begin{bmatrix} (\lambda_0+2\mu_0)qU_{11}^2 & \lambda_0qU_{11}^2 & \lambda_0qU_{11}^2 & & & \\ \lambda_0qU_{11}^2 & \frac{\lambda_0^2qU_{11}^2}{\lambda_0+2\mu_0} & \frac{\lambda_0^2qU_{11}^2}{\lambda_0+2\mu_0} & & & \\ \lambda_0qU_{11}^2 & \frac{\lambda_0^2qU_{11}^2}{\lambda_0+2\mu_0} & \frac{\lambda_0^2qU_{11}^2}{\lambda_0+2\mu_0} & & & \\ & & & 0 & & \\ & & & & XU_{33}^2 & \\ & & & & & XU_{33}^2 \end{bmatrix},$$

where

$$\begin{aligned} q &= 15\frac{\lambda_0^2}{\mu_0^2}+28\frac{\lambda_0}{\mu_0}+28 \\ X &= 2\mu_0\frac{3\lambda_0+8\mu_0}{\lambda_0+2\mu_0}. \end{aligned}$$

For the aligned fractures the non-zero perturbations are then δC_{11}, $\delta C_{22} = \delta C_{33} = \delta C_{23}$, $\delta C_{12} = \delta C_{13}$, and $\delta C_{55} = \delta C_{66}$, a total of four independent variations. The moment tensor source for this obstacle is

$$\delta\mathbf{M} = \tag{3.26}$$

$$\begin{bmatrix} \delta C_{11}\epsilon_{11}^0+\delta C_{12}(\epsilon_{22}^0+\epsilon_{33}^0) & 2\delta C_{55}\epsilon_{12}^0 & 2\delta C_{55}\epsilon_{13}^0 \\ 2\delta C_{55}\epsilon_{12}^0 & \delta C_{12}\epsilon_{11}^0+\delta C_{22}(\epsilon_{22}^0+\epsilon_{33}^0) & 0 \\ 2\delta C_{55}\epsilon_{13}^0 & 0 & \delta C_{12}\epsilon_{11}^0+\delta C_{22}(\epsilon_{22}^0+\epsilon_{33}^0) \end{bmatrix}.$$

The radiation pattern is due to a superposition of three dipoles, in general unequal, and two double couples, again not necessarily of equal magnitude.

The scattered fields due to the aligned fractured material are computed by adding the contributions due to each of the five independent perturbations (Appendix D). Application of this procedure yields expressions for the scattered fields which have the same form as those in equations (3.20) and (3.22), with the following scattering coefficients:

$$\begin{aligned}
\mathcal{F}_{rP}(\theta,\phi;\theta_0,\phi_0) &= \delta C_{11}\sin^2\theta_0\cos^2\phi_0\sin^2\theta\cos^2\phi \\
&\quad + \delta C_{22}(\cos^2\theta+\sin^2\theta\sin^2\phi)(\cos^2\theta_0+\sin^2\theta_0\sin^2\phi_0) \\
&\quad + \delta C_{12}[(\sin^2\theta_0\sin^2\phi_0+\cos^2\theta_0)\sin^2\theta\cos^2\phi \\
&\quad + \sin^2\theta_0\cos^2\phi_0(\sin^2\theta\sin^2\phi+\cos^2\theta)] \\
&\quad + \delta C_{55}(\sin 2\theta_0\cos\phi_0\sin 2\theta\cos\phi+\sin^2\theta_0\sin 2\phi_0\sin^2\theta\sin 2\phi) \\
\mathcal{F}_{\theta P}(\theta,\phi;\theta_0,\phi_0) &= \delta C_{11}\sin^2\theta_0\cos^2\phi_0\sin\theta\cos\theta\cos^2\phi \\
&\quad - \delta C_{22}\sin\theta\cos\theta\cos^2\phi(\sin^2\theta_0\sin^2\phi_0+\cos^2\theta_0) \\
&\quad + \delta C_{12}\sin\theta\cos\theta[(\sin^2\theta_0\sin^2\phi_0+\cos^2\theta_0)\cos^2\phi \\
&\qquad + \sin^2\theta_0\cos^2\phi_0(\sin^2\phi-1)] \qquad (3.27) \\
&\quad + \delta C_{55}(\sin 2\theta_0\cos\phi_0\cos 2\theta\cos\phi \\
&\qquad + \sin^2\theta_0\sin 2\phi_0\sin\theta\cos\theta\sin 2\phi) \\
\mathcal{F}_{\phi P}(\theta,\phi;\theta_0,\phi_0) &= -\delta C_{11}\sin^2\theta_0\cos^2\phi_0\sin\theta\sin\phi\cos\phi \\
&\quad + \delta C_{22}\sin\theta\sin\phi\cos\phi(\sin^2\theta_0\sin^2\phi_0+\cos^2\theta_0) \\
&\quad + \delta C_{12}\sin\theta\sin\phi\cos\phi(\sin^2\theta_0\cos 2\phi_0-\cos^2\theta_0) \\
&\quad + \delta C_{55}(-\sin 2\theta_0\cos\phi_0\cos\theta\sin\phi+\sin^2\theta_0\sin 2\phi_0\sin\theta\cos 2\phi).
\end{aligned}$$

$$\begin{aligned}
\mathcal{F}_{rSV}(\theta,\phi;\theta_0,\phi_0) &= \delta C_{11}\sin\theta_0\cos\theta_0\cos^2\phi_0\sin^2\theta\cos^2\phi \\
&\quad + \delta C_{22}\sin\theta_0\cos\theta_0(\sin^2\phi_0-1)(\sin^2\theta\sin^2\phi+\cos^2\theta) \\
&\quad + \delta C_{12}\sin\theta_0\cos\theta_0\cos^2\phi_0(-\sin^2\theta\cos 2\phi+\cos^2\theta)
\end{aligned}$$

$$
\begin{aligned}
&+ \delta C_{55}(\cos 2\theta_0 \cos\phi_0 \sin 2\theta \cos\phi \\
&\qquad \sin\theta_0 \cos\theta_0 \sin 2\phi_0 \sin^2\theta \sin 2\phi)
\end{aligned}
$$

$$
\begin{aligned}
\mathcal{F}_{\theta SV}(\theta,\phi;\theta_0,\phi_0) &= \delta C_{11} \sin\theta_0 \cos\theta_0 \sin\theta \cos\theta(\cos^2\phi_0 \cos^2\phi) \\
&+ \delta C_{22} \sin\theta_0 \cos\theta_0 \sin\theta \cos\theta(\sin^2\phi_0 - 1)(\sin^2\phi - 1) \\
&+ \delta C_{12} \sin\theta_0 \cos\theta_0 \sin\theta \cos\theta(-2\cos^2\phi_0 \cos^2\phi) \qquad (3.28) \\
&+ \delta C_{55}(\cos 2\theta_0 \cos\phi_0 \cos 2\theta \cos\phi \\
&+ \sin\theta_0 \cos\theta_0 \sin 2\phi_0 \sin\theta \cos\theta \sin 2\phi)
\end{aligned}
$$

$$
\begin{aligned}
\mathcal{F}_{\phi SV}(\theta,\phi;\theta_0,\phi_0) &= -\delta C_{11} \sin\theta_0 \cos\theta_0 \cos^2\phi_0 \sin\theta \sin\phi \cos\phi \\
&+ \delta C_{22} \sin\theta_0 \cos\theta_0 \sin\theta \sin\phi \cos\phi(\sin^2\phi_0 - 1) \\
&+ \delta C_{12} \sin\theta_0 \cos\theta \sin\theta \sin\phi \cos\phi(\cos 2\phi_0 + 1) \\
&+ \delta C_{55}(-\cos 2\theta_0 \cos\phi_0 \cos\theta \sin\phi \\
&\qquad + \sin\theta_0 \cos\theta_0 \sin 2\phi_0 \sin\theta \cos 2\phi).
\end{aligned}
$$

$$
\begin{aligned}
\mathcal{F}_{rSH}(\theta,\phi;\theta_0,\phi_0) &= \delta C_{11} \sin\theta_0 \sin\phi_0 \cos\phi_0 \sin^2\theta \cos^2\phi \\
&+ \delta C_{22} \sin\theta_0 \sin\phi_0 \cos\phi_0(\sin^2\theta \sin^2\phi + \cos^2\theta) \\
&+ \delta C_{12} \sin\theta_0 \sin\phi_0 \cos\phi_0(\sin^2\theta \cos 2\phi - \cos^2\theta) \\
&+ \delta C_{55}(-\cos\theta_0 \sin\phi_0 \sin 2\theta \cos\phi + \sin\theta_0 \cos 2\phi_0 \sin^2\theta \sin 2\phi)
\end{aligned}
$$

$$
\begin{aligned}
\mathcal{F}_{\theta SH}(\theta,\phi;\theta_0,\phi_0) &= -\delta C_{11} \sin\theta_0 \sin\phi_0 \cos\phi_0 \sin\theta \cos\theta \cos^2\phi \\
&+ \delta C_{22} \sin\theta_0 \sin\phi_0 \cos\phi_0 \sin\theta \cos\theta(\sin^2\phi - 1) \\
&+ \delta C_{12} \sin\theta_0 \sin\phi_0 \cos\phi_0 \sin\theta \cos\theta(\cos 2\phi + 1) \qquad (3.29) \\
&+ \delta C_{55}(-\cos\theta_0 \sin\phi_0 \cos 2\theta \cos\phi \\
&+ \sin\theta_0 \cos 2\phi_0 \sin\theta \cos\theta \sin 2\phi)
\end{aligned}
$$

$$
\begin{aligned}
\mathcal{F}_{\phi SH}(\theta,\phi;\theta_0,\phi_0) &= (\delta C_{11} + \delta C_{22}) \sin\theta_0 \sin\phi_0 \cos\phi_0 \sin\theta \sin\phi \cos\phi \\
&- \delta C_{12} \sin\theta_0 \sin\phi_0 \cos\phi_0 \sin\theta \sin 2\phi \\
&+ \delta C_{55}(\cos\theta_0 \sin\phi_0 \cos\theta \sin\phi + \sin\theta_0 \cos 2\phi_0 \sin\theta \cos 2\phi).
\end{aligned}
$$

The unique values of the four scattering coefficients lead to more complicated radia-

tion than for the isotropic obstacle.

Radiation patterns for these fracture zones also include a contribution from density variations as well. Since the presence of the cracks introduces a certain degree of void space into the rock matrix, the resulting composite material will have a reduced density. However, since the overall volume of pore space due to low aspect ratio fractures is very low, the density change is very small and will have a minimal contribution to scattered wave amplitudes. This point is discussed in more detail in Appendix E.

3.3.2 Radiation Patterns for the Fractured Scatterers

The perturbations to the elastic constants for the isotropic and anisotropic cases are calculated using the background Lamé parameters $\lambda_0 = 43.93$ GPa and $\mu_0 = 28.80$ GPa. This corresponds to isotropic velocities of $\alpha_0 = 6.13$ km/s and $\beta_0 = 3.27$ km/s when the density is 2.70 g/cm^3. The factor $A\delta V\omega^2$ appearing in the expressions for radiation patterns was arbitrarily set to 1×10^{10} for plotting purposes in all radiation patterns shown below. Assuming a crack density of 0.05, the perturbations to the isotropic and anisotropic elastic constants are given in Table 3.1. Comparing values of the perturbations, the effects of crack alignment is clear. While both δC_{11} and δC_{22} are analogous to the isotropic $\delta\lambda + 2\delta\mu$, δC_{11} is about twice as large as $\delta\lambda + 2\delta\mu$, and δC_{22} is about half the size of the isotropic quantity. This can be understood by considering that δC_{11} relates to ϵ^0_{11}, a strain acting to distort the medium perpendicular to all cracks, but δC_{22} relates to ϵ^0_{22} and ϵ^0_{33}, strains affecting dilatation parallel to all cracks. When the cracks are randomly oriented, the affects on strains are averaged over direction, and the elastic parameter perturbations are also intermediate to the anisotropic extremes.

The isotropic velocities of the randomly cracked medium are $\alpha = 5.68$ km/s and $\beta = 3.16$ km/s, defining velocity perturbations of 7.4% and 3.3%, respectively. Phase velocities for the parallel crack case are shown in Figure 3-3 for the three coordinate

planes. The overall quasi-compressional wave anisotropy is about 12%, and the quasi-shear wave anisotropy is 5.3%. This degree of quasi-compressional wave anisotropy is about half that observed by Bamford and Nunn (1979) in a shallow limestone formation.

Vertical incidence ($\theta_0 = \phi_0 = 0$).

For vertically incident plane waves, the anisotropic scattering coefficients defined in equations (3.27) through (3.29) reduce to

$$\begin{aligned}
\mathcal{F}_{rP}(\theta,\phi;0,0) &= \delta C_{22}\cos^2\theta + \delta C_{12}\sin^2\theta\cos^2\phi + \delta C_{23}\sin^2\theta\sin^2\phi \\
\mathcal{F}_{\theta P}(\theta,\phi;0,0) &= -\delta C_{22}\sin\theta\cos\theta + \delta C_{12}\sin\theta\cos\theta\cos^2\phi \\
&\quad + \delta C_{23}\sin\theta\cos\theta\sin^2\phi \\
\mathcal{F}_{\phi P}(\theta,\phi;0,0) &= -\delta C_{12}\sin\theta\sin\phi\cos\phi + \delta C_{23}\sin\theta\sin\phi\cos\phi
\end{aligned} \tag{3.30}$$

$$\begin{aligned}
\mathcal{F}_{rSV}(\theta,\phi;0,0) &= \delta C_{55}\sin 2\theta\cos\phi \\
\mathcal{F}_{\theta SV}(\theta,\phi;0,0) &= \delta C_{55}\cos 2\theta\cos\phi \\
\mathcal{F}_{\phi SV}(\theta,\phi;0,0) &= -\delta C_{55}\cos\theta\sin\phi
\end{aligned} \tag{3.31}$$

$$\begin{aligned}
\mathcal{F}_{rSH}(\theta,\phi;0,0) &= 0 \\
\mathcal{F}_{\theta SH}(\theta,\phi;0,0) &= 0 \\
\mathcal{F}_{\phi SH}(\theta,\phi;0,0) &= 0.
\end{aligned} \tag{3.32}$$

Likewise, the isotropic coefficients (equations (3.21) through (3.24)) are

$$\begin{aligned}
\mathcal{F}^i_{rP}(\theta,\phi;0,0) &= \delta\lambda + 2\delta\mu\cos^2\theta \\
\mathcal{F}^i_{\theta P}(\theta,\phi;0,0) &= -2\delta\mu\sin\theta\cos\theta \\
\mathcal{F}^i_{\phi P}(\theta,\phi;0,0) &= 0
\end{aligned} \tag{3.33}$$

$$
\begin{aligned}
\mathcal{F}^i_{rSV}(\theta,\phi;0,0) &= \delta\mu \sin 2\theta \cos\phi \\
\mathcal{F}^i_{\theta SV}(\theta,\phi;0,0) &= \delta\mu \cos 2\theta \cos\phi \\
\mathcal{F}^i_{\phi SV}(\theta,\phi;0,0) &= -\delta\mu \cos\theta \sin\phi
\end{aligned} \tag{3.34}
$$

$$
\begin{aligned}
\mathcal{F}^i_{rSH}(\theta,\phi;0,0) &= \delta\mu \sin 2\theta \sin\phi \\
\mathcal{F}^i_{\theta SH}(\theta,\phi;0,0) &= \delta\mu \cos 2\theta \sin\phi \\
\mathcal{F}^i_{\phi SH}(\theta,\phi;0,0) &= \delta\mu \cos\theta \cos\phi.
\end{aligned} \tag{3.35}
$$

Since $\phi_0 = 0$, the incident "SV" signal is polarized in the x direction, while the "SH" is polarized parallel to the $y-$axis and causes no scattered field to be generated from the anisotropic obstacle. Radiation patterns for vertically incident plane waves are presented in Figures 3-4 and 3-5 for the randomly oriented and aligned crack models, respectively. Note that the range of the coordinate axes in each of the plots is indicated in the pattern for the P to P (P-P) scattering in the upper left corner of each figure. Considering first the incident P-wave, the back scattered P-wave field ($\theta = 0$) for the isotropic obstacle is larger than back scattering in the anisotropic case. The amplitudes of back scattering are proportional to $\delta\lambda + \delta\mu$ and δC_{22}. Noting the values in Table 3.1 for the perturbations, it is seen that back scattering in the isotropic case is more than twice that for the aligned fractures. Also of importance, for incident P-waves, no SH field is generated for the isotropic obstacle, while there in fact is a considerable SH radiation from the aligned fracture perturbations due to the difference in values of δC_{23} and δC_{12} in $\mathcal{F}_{\phi P}(\theta,\phi;0,0)$ (equation (3.30)). However, the shapes of the radiation patterns for SV incidence are the same, since the only perturbation affected by the vertically propagating SV signal is δC_{55}, which plays the same role as $\delta\mu$ in the isotropic case. Therefore, the shapes of the patterns are the same with a scaling factor due to the relative magnitudes of $\delta\mu$ and δC_{55}. The most significant difference between the isotropic scattering and the aligned fractured scatterer is for the incident SH-wave, polarized parallel to the crack plane in the anisotropic case.

The isotropic patterns in this case are the same as for an incident SV-wave rotated by 90°. However, no scattered field at all is generated for the anisotropic perturbation since $\delta C_{44} = 0$.

Horizontal incidence along $x-$axis ($\theta_0 = 90°, \phi_0 = 0$).

The anisotropic scattering coefficients for waves propagating perpendicular to the crack plane reduce to

$$\begin{aligned}
\mathcal{F}_{rP}(\theta,\phi;90,0) &= \delta C_{11}\sin^2\theta\cos^2\phi + \delta C_{12}(\sin^2\theta\sin^2\phi + \cos^2\theta) \\
\mathcal{F}_{\theta P}(\theta,\phi;90,0) &= \delta C_{11}\sin\theta\cos\theta\cos^2\phi + \delta C_{12}\sin\theta\cos\theta(\sin^2\phi - 1) \\
\mathcal{F}_{\phi P}(\theta,\phi;90,0) &= (\delta C_{12} - \delta C_{11})\sin\theta\sin\phi\cos\phi
\end{aligned} \tag{3.36}$$

$$\begin{aligned}
\mathcal{F}_{rSV}(\theta,\phi;90,0) &= -\delta C_{55}\sin 2\theta\cos\phi \\
\mathcal{F}_{\theta SV}(\theta,\phi;90,0) &= -\delta C_{55}\cos 2\theta\cos\phi \\
\mathcal{F}_{\phi SV}(\theta,\phi;90,0) &= \delta C_{55}\cos\theta\sin\phi
\end{aligned} \tag{3.37}$$

$$\begin{aligned}
\mathcal{F}_{rSH}(\theta,\phi;90,0) &= \delta C_{55}\sin^2\theta\sin 2\phi \\
\mathcal{F}_{\theta SH}(\theta,\phi;90,0) &= \delta C_{55}\sin\theta\cos\theta\sin 2\phi \\
\mathcal{F}_{\phi SH}(\theta,\phi;90,0) &= \delta C_{55}\sin\theta\cos 2\phi,
\end{aligned} \tag{3.38}$$

and the isotropic versions are

$$\begin{aligned}
\mathcal{F}^i_{rP}(\theta,\phi;90,0) &= \delta\lambda + 2\delta\mu\sin^2\theta\cos^2\phi \\
\mathcal{F}^i_{\theta P}(\theta,\phi;90,0) &= 2\delta\mu\sin\theta\cos\theta\cos^2\phi \\
\mathcal{F}^i_{\phi P}(\theta,\phi;90,0) &= -\delta\mu\sin\theta\sin 2\phi
\end{aligned} \tag{3.39}$$

$$\begin{aligned}
\mathcal{F}^i_{rSV}(\theta,\phi;90,0) &= -\delta\mu\sin 2\theta\cos\phi \\
\mathcal{F}^i_{\theta SV}(\theta,\phi;90,0) &= -\delta\mu\cos 2\theta\cos\phi
\end{aligned} \tag{3.40}$$

$$\mathcal{F}^i_{\phi SV}(\theta,\phi;90,0) = \delta\mu\cos\theta\sin\phi$$

$$\begin{aligned}
\mathcal{F}^i_{rSH}(\theta,\phi;90,0) &= -\delta\mu\sin^2\theta\sin 2\phi \\
\mathcal{F}^i_{\theta SH}(\theta,\phi;90,0) &= -\delta\mu\sin\theta\cos\theta\sin 2\phi \\
\mathcal{F}^i_{\phi SH}(\theta,\phi;90,0) &= \delta\mu\sin\theta\cos 2\phi.
\end{aligned} \tag{3.41}$$

The patterns for the incident SV wave have the same directional variation as those for vertical incidence, with the polarity of the radiated field reversed. A significant difference in this case is that the incident SH-wave also generates a scattered field proportional to δC_{55}.

Three-dimensional plots of the radiation patterns for all three incident signals are presented in Figures 3-6 and 3-7, for the isotropic and anisotropic scatterers, respectively. The isotropic patterns for P-wave incidence are equivalent to those for vertical incidence (Figure 3-4) with some interchange between SV and SH displacements due to the change in direction of propagation. Total shear wave scattering is the same as for the earlier case. The back scattered P-wave displacement field ($\theta = 90°, \phi = 0$) is significantly larger than for vertically propagating incident fields since it is proportional to δC_{11} rather than δC_{22} (Table 3.1). In addition, the P-SV and P-SH scattered fields are both proportionately larger than for the randomly fractured scatterer, since the magnitude of these fields includes δC_{11} and δC_{12}. The isotropic scattering will be multiplied by $\delta\lambda$, which is close to the value of δC_{12}, but δC_{11} is much larger than the isotropic equivalent, $\delta\lambda + 2\delta\mu = -14.45$ GPa. Physically, these perturbation values imply that the anisotropic rock is much more compliant to a traction applied in the x direction than the isotropic rock is to a traction applied in any direction. Since δC_{55} is of the same order of magnitude as $\delta\mu$, the radiation patterns for shear wave incidence are similar for both the aligned and randomly oriented fractured scattering obstacles.

Incidence out of symmetry planes ($\theta_0 = 45°, \phi_0 = 45°$).

The scattering coefficients for this incidence direction do not simplify significantly from the forms given in equations (3.27) through (3.29), and all four of the elastic constant perturbations contribute to the scattered displacement field. Plots of the radiation patterns for the isotropic and anisotropic obstacles are compared in Figures 3-8 and 3-9. With the exception of the SV-wave incidence, the patterns are highly distorted for the aligned fracture inclusion. The amplitude of the scattered SV-waves are somewhat reduced for SV incidence, though the radiated SH field is larger. In comparison, the radiation patterns for the incident P-wave are skewed toward the $x-$axis in the anisotropic case by the large perturbation to δC_{11}, and, as for the other incidence directions, the P-SV and P-SH fields are comparatively larger than for the isotropic scatterer. The patterns for an incident SH-wave are also twisted toward the $x-z$ plane by the high value of δC_{11}. This effect will change the observed polarizations of forward and back scattered displacement fields.

3.4 Discussion and Conclusions

The analysis of Rayleigh scattering using the Born approximation shows that perturbations to any of the 21 independent elastic constants can be simply related to a scattered field through a moment tensor type source proportional to a strain tensor component generated by the incident wave (equation (3.12)). Though the algebra may be cumbersome, the total radiation pattern created by an anisotropic obstacle of any symmetry can be calculated by summing the effects of all perturbations. Application of this approach to an obstacle consisting of a vertically fractured region of an otherwise homogeneous, isotropic background medium shows some distinct variations from the scattering due to a volume of material which contains an equal density of randomly oriented cracks. Probably the most significant difference is that for some directions of incidence on the anisotropic obstacle, a shear wave will not generate any

scattered waves.

The variations of the radiated displacement field with the propagation direction of the incident wave can be used to infer some properties of the medium. At least in principle, the back and forward scattered fields in the Rayleigh scattering limit could be used to obtain information about a vertically fractured region within an elastic material. The most definitive experiment would be to use a shear wave seismic source to examine the scattered field. By rotating the orientation of the shear wave source polarization through at least 90°, the crack plane is determined by finding the source polarization yielding the smallest scattered field, which ideally would actually vanish. If instead the cracks are randomly oriented throughout the scattering volume, the back scattered shear wave displacements will remain constant in amplitude. To further confirm the alignment of cracks, a P-wave source could be employed. For isotropic scatterers, the back and forward scattered P-wave fields have the same amplitude independent of incident direction (note Figures 3-4, 3-6, and 3-8). An aligned crack volume would again yield a variation of the amplitudes of the scattered displacements as source orientation with respect to the scattering region is varied.

It is important to note that the effect of vanishing scattering for certain S-wave incidence directions will hold true even as the scattering region becomes large with respect to a wavelength as long as the Born approximation is valid. Assuming a vertical crack orientation with cracks perpendicular to the $x-$axis, δC_{44} will always be zero (equation (3.25)). For an SV-wave propagating in the $y-z$ plane, $\phi_0 = 90°$,

$$\begin{aligned} \epsilon^0_{22} &= -ik_\beta \sin\theta_0 \cos\theta_0 A e^{-i\psi_\beta} \\ \epsilon^0_{33} &= +ik_\beta \sin\theta_0 \cos\theta_0 A e^{-i\psi_\beta}, \end{aligned}$$

and so the contributions of these strains to the anisotropic fracturing moment tensor in equation (3.26) vanishes independently of the value of θ_0. Since the only other non-zero strain is ϵ^0_{23}, which multiplies δC_{44}, the moment tensor vanishes for any SV-wave incident in the plane defined by $\phi_0 = 90°$. The integral equation for the scattered field in equation (3.10) includes no assumption regarding size of the scattering region, and

so the scattered field vanishes even as the dimension of the fractured volume increases.

A more appropriate problem regarding the accuracy of the predicted scattering amplitude variations is the accuracy of the Born approximation itself. This is a question which is still not completely answered (Beydoun and Mendes, 1989). Hudson and Heritage (1981) undertook a detailed study of the validity of the Born approximation, checking conclusions in part by comparison to analytical results for the complete scattered field from a spherical object. One of the principal conclusions is that rigorously speaking it is not sufficient for the amplitude of the scattered field to be small compared to the incident wave. Instead, the field obtained by substituting the scattered field $\delta\mathbf{u}(\mathbf{x},t)$ in place of $\delta\mathbf{u}^0(\mathbf{x},t)$ into equation (3.10) must generate a secondary field which is much smaller than the field $\delta\mathbf{u}(\mathbf{x},t)$. This is difficult to check in a general case. Another critical point is that the Born approximation is expected to break down as the volume occupied by the perturbations δC_{IJ} increases due to the increasingly significant multiple scattering effects. Naturally, if the perturbations are small enough, this breakdown in the approximation will occur more slowly with increasing size. Therefore, there is a trade-off between the size of the scattering volume and the magnitude of perturbations to the elastic constants. If fracturing is sufficiently weak, extension of the approximation to larger rock volumes containing cracks should be possible due to small variation in δC_{IJ}.

The implications of these results for inversion problems is also of importance. Tarantola (1986) uses the Rayleigh scattering results for isotropic materials to infer adequate medium parameterizations for traditional seismic data configurations. The most significant consideration was to determine a parameterization yielding large back scattered fields for all medium parameters under consideration, such as λ, μ and ρ, since for seismic reflection experiments, energy generally tends to propagate vertically downwards and to reflect back up to observing points. Assuming similar geometries for the anisotropic obstacles (Figures 3-4 and 3-5), we see that the shear wave sources would be expected to yield the most information regarding crack orientations and

that the use of P-wave sources and back scattered data would make it more difficult to distinguish crack orientations. A Born inversion scheme would ideally employ S-wave sources and multiple source polarizations to invert for anisotropic perturbations to an isotropic background model in order to estimate locations of fracturing.

Another important question regarding the properties of the scattered fields is whether the effects of anisotropic scattering obstacles can be mimiced by some combination of isotropic perturbations. Specifically, is there some arrangement of isotropic scatterers which can cause scattering to completely vanish for some directions of incidence? It is difficult to imagine such a configuration in the Rayleigh scattering limit, since the shapes of individual obstacles are not taken into account. The scattering coefficients presented for isotropic perturbations in equations (3.21) through (3.24) show that there is no plane of incidence where scattering will vanish. Therefore, within limitations of the Born and Rayleigh scattering theory, it would seem that the aligned fracture obstacle defines a case where the presence of anisotropy can be uniquely determined by the properties of the scattered fields. This evidence is distinctly different from shear wave splitting, which generally defines the best evidence for elastic wave propagation within an anisotropic region larger than a wavelength (Crampin, 1981).

The Rayleigh scattering results provide a good insight into the effects of slight inhomogeneity upon the propagation of elastic waves, and it is clear from the results for the fractured obstacle that there are significant differences between isotropic and anisotropic scattering. These results outline a basis for data analysis to examine the fractured nature of crustal material. Future extensions of imaging algorithms may also be able to apply this scattering theory to better determine slight anisotropy in a more generally isotropic portion of the earth as well.

PARAMETER	PERTURBATION (GPa)
λ_0	43.93
μ_0	28.80
$\delta\lambda$	-10.63
$\delta\mu$	-1.91
δC_{11}	-27.12
δC_{22}	-5.08
δC_{12}	-11.73
δC_{23}	-5.08
δC_{55}	-2.99

Table 3.1. Background Lamé parameters λ_0 and μ_0 and perturbations to elastic constants used to compute radiation patterns.

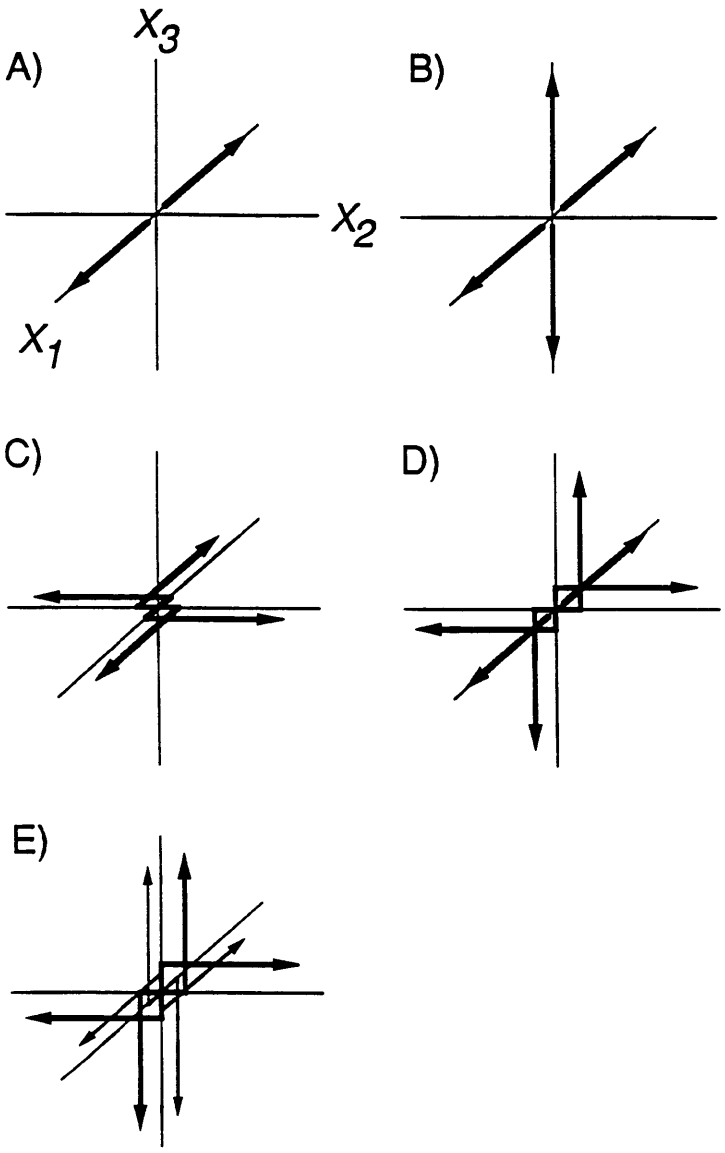

Figure 3-1: Double force systems for each of the five types of sources resulting from perturbations to elastic constants. Equations for the radiation patterns for each of the sources depicted here are presented in Appendix B. A) Single dipole, 11, corresponding to δC_{11}. B) Two dipoles, 11 and 33, corresponding to δC_{13}) C) Double couple, 12, corresponding to δC_{66}. D) Double couple, 23, and a dipole, 11, corresponding to δC_{14}. E) Two double couples, 13 and 23, corresponding to δC_{45}.

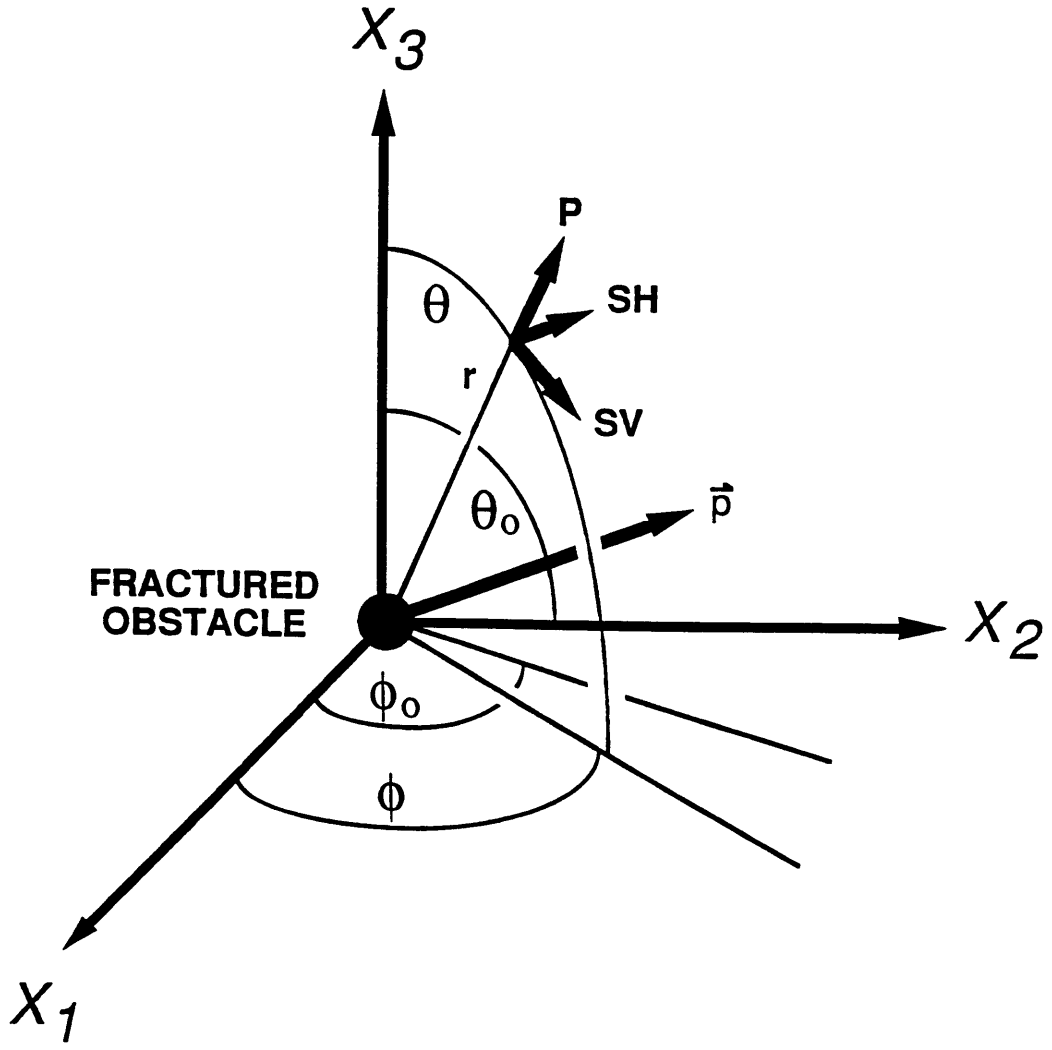

Figure 3-2: Coordinate system used for the radiation patterns. The direction of propagation of the incident plane wave with wavefront normal vector $\vec{p}$ is given by the two spherical angle coordinates ϕ_0 and θ_0. Likewise, the propagation direction of the scattered wave is specified by ϕ and θ.

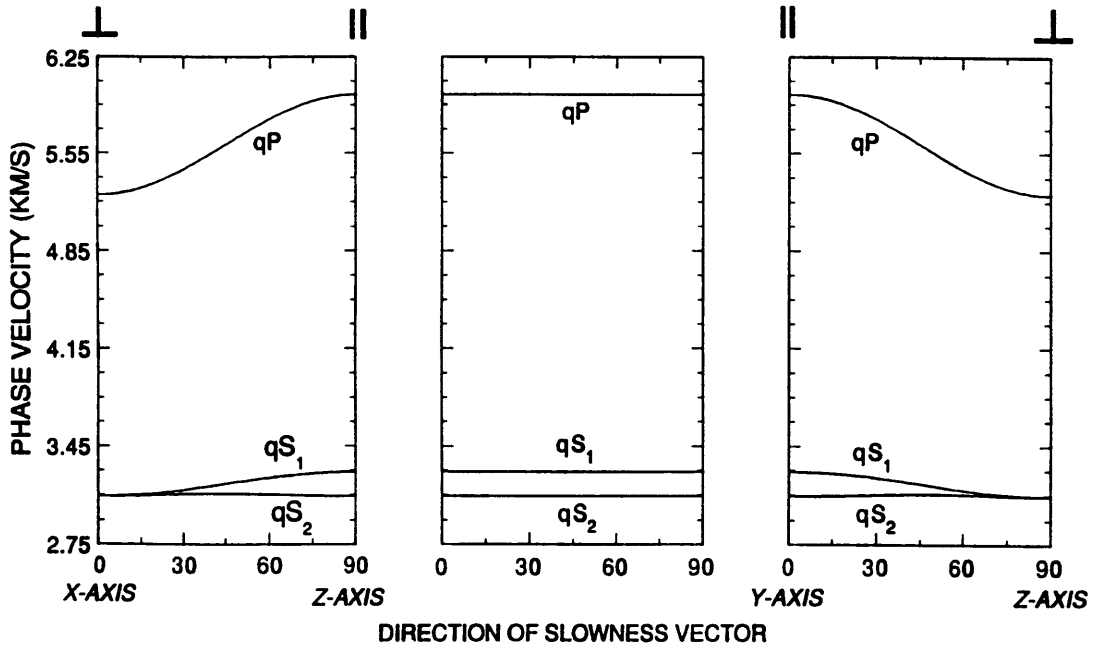

Figure 3-3: Phase velocities for the anisotropic fractured material. The phase velocities for each of the three wave types which would propagate within the anisotropic rock are shown as a function of the direction of the corresponding slowness vector (Musgrave, 1970). The velocities are shown in each of the three coordinate planes, with the directions of Cartesian coordinate axes at the bottom of the plots and the symbols indicating propagation parallel and perpendicular to the cracks at the top. Because the cracks are oriented perpendicular to the $x-$axis, this is the direction of slowest propagation.

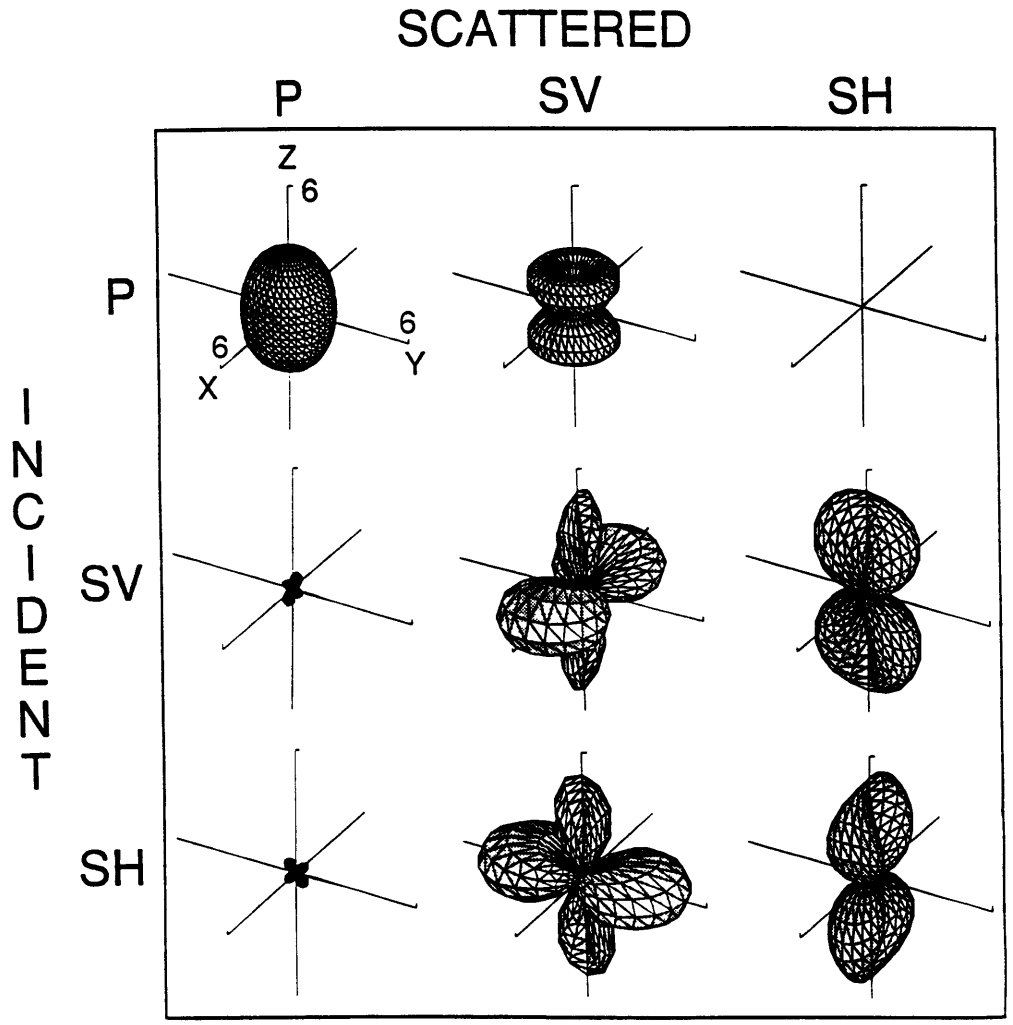

Figure 3-4: Radiation patterns for vertical incidence ($\phi_0 = \theta_0 = 0$) on the isotropic scattering region with randomly oriented cracks. All plots in this figure are plotted at the same scale, with the range of axes shown in the upper left pattern. Perturbations to the Lamé parameters used to generate these patterns are given in Table 3.1, and the multiplicative factor $A\delta V\omega^2$ was set to 1×10^{10}, an arbitrary scaling factor for plotting. Incident wave type is indicated on the left, and the scattered wave is shown across the top of the figure.

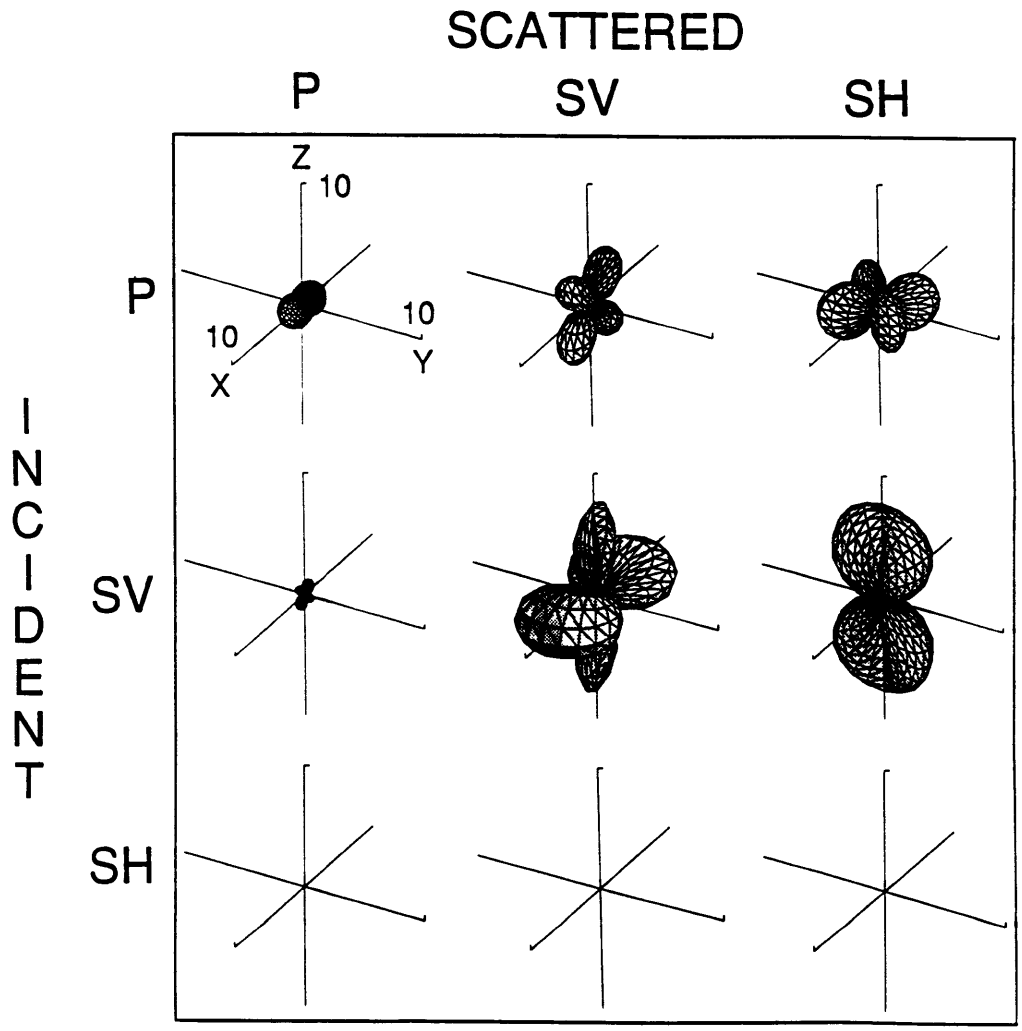

Figure 3-5: Radiation patterns for vertical incidence ($\phi_0 = \theta_0 = 0$) on the anisotropic scattering volume with aligned cracks. The format is the same as for Figure 3-4.

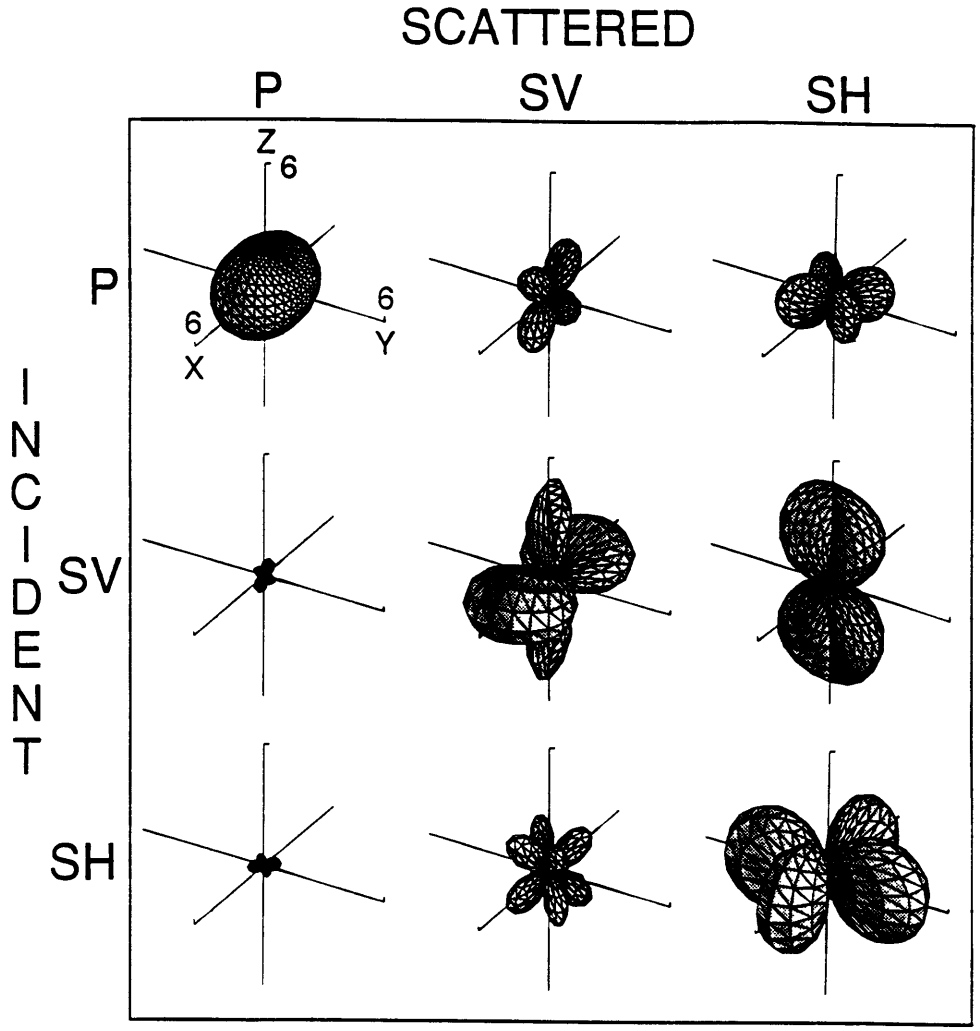

Figure 3-6: Radiation patterns for horizontal incidence along the x axis ($\theta_0 = 90°, \phi_0 = 0$) on the isotropic scattering region. The format is the same as for Figure 3-4.

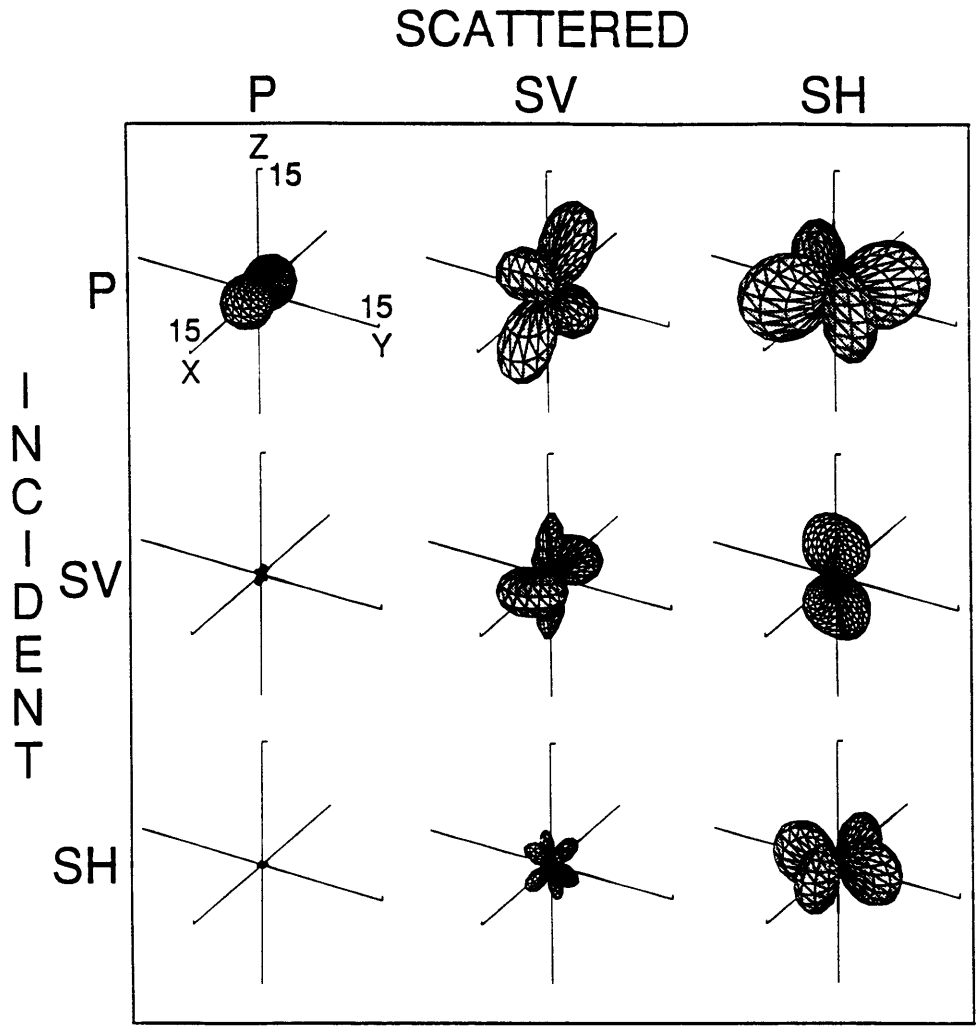

Figure 3-7: Radiation patterns for horizontal incidence perpendicular to the cracks ($\theta_0 = 90°, \phi_0 = 0$) on the anisotropic fractured region. The format is the same as for Figure 3-4.

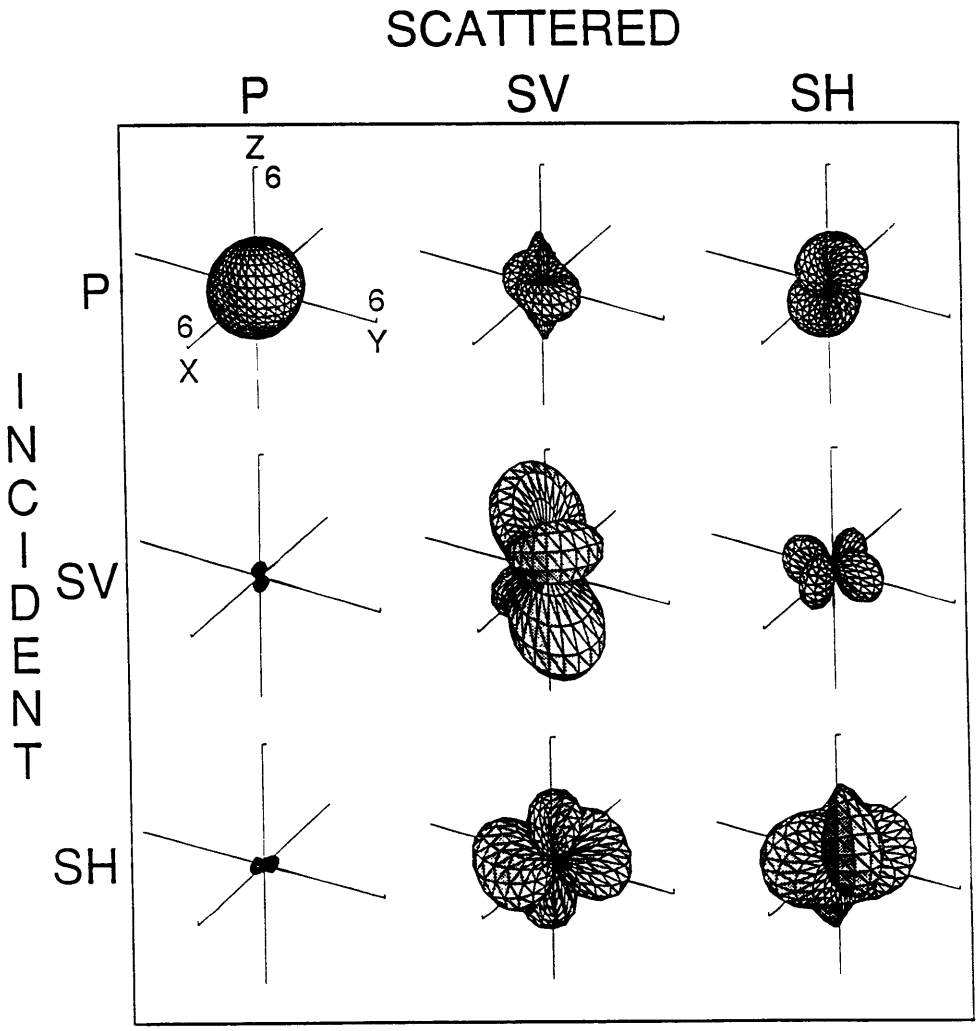

Figure 3-8: Radiation patterns for incidence with $\theta_0 = 45°$, $\phi_0 = 45°$ on the isotropic, randomly oriented crack volume. The format is the same as in Figure 3-4.

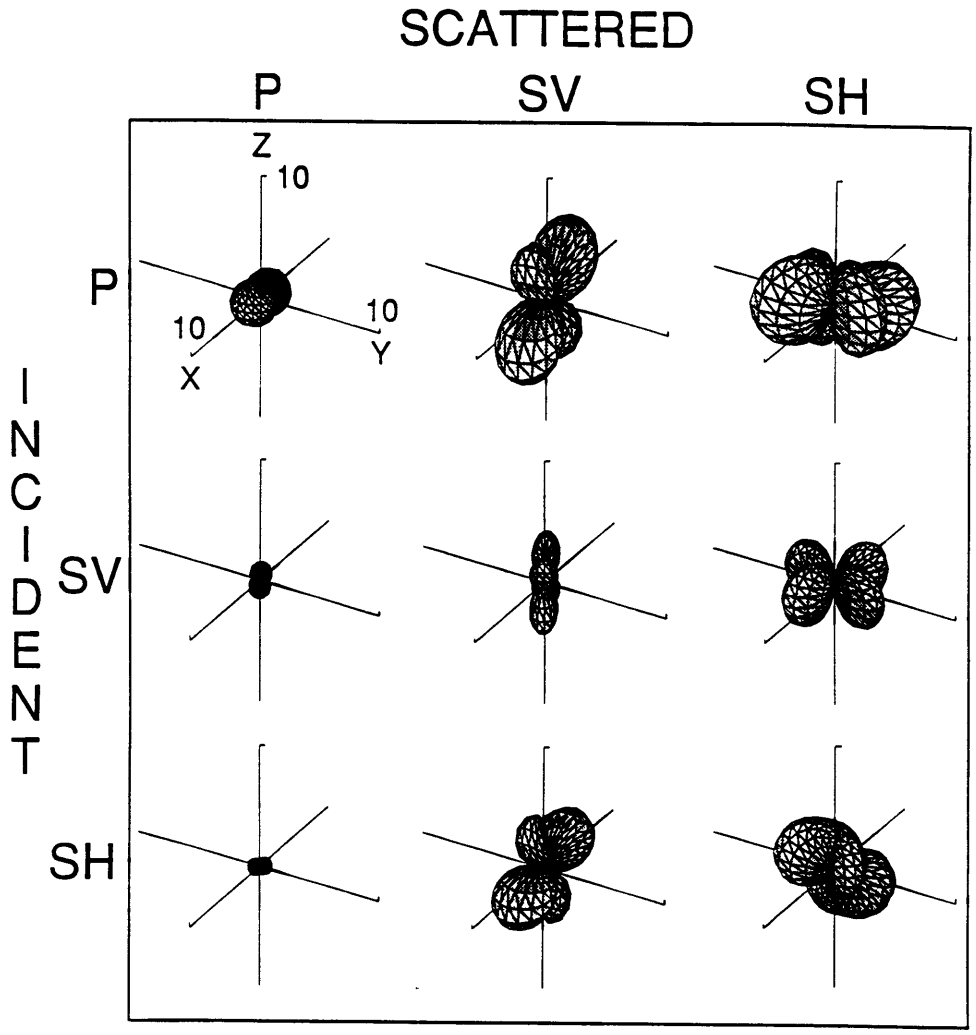

Figure 3-9: Radiation patterns for incidence with $\theta_0 = 45°, \phi_0 = 45°$ on the anisotropic volume. The format is the same as Figure 3-4.

Chapter 4

Ray-Born Synthetic Seismograms for Anisotropic, Fractured Media

The trouble with the world is not that people know too little, but that they know so many things that ain't so.

–Mark Twain

4.1 Introduction

The modeling of seismic wave propagation to understand the effects of various earth structures on observations and, conversely, to infer rock properties from data is hindered by the complexity of geological materials. In many cases, the geologic structures of interest are small compared to the three-dimensional volume through which the waves are transmitted, leading to practical difficulties in implementation of numerical schemes such as finite differences. Wave propagation is also complicated in many cases by anisotropy, which may be an inherent anisotropy of the minerals or an effective anisotropy due to the presence of a stack of thin isotropic layers (Crampin, 1981). Either of these effects usually leads to a transversely isotropic medium with a vertical axis of symmetry. Another very important source of effective anisotropy in the

crust is the alignment of fractures in an otherwise isotropic and homogeneous layer, also leading to a transversely isotropic medium (Bamford and Nunn, 1979; Crampin, 1981; Crampin et al., 1986; Leary et al., 1987). Frequently the least principal stress is known through geological, seismological or borehole observations to be horizontal at depth (Zoback and Zoback, 1980; Jamison and Cook, 1980; Hickman et al., 1988; Evans et al., 1989), resulting in a vertical alignment of cracks. The resulting medium has a horizontal axis of symmetry.

There have been many analyses of the effects of fractured layers of the earth on synthetic seismograms or field data (Crampin, 1978; Crampin, 1981; Crampin and McGonigle, 1985; Leary and Henyey, 1985; Martin and Davis, 1987). Most of these studies have focused on the effects of shear wave splitting and the consequent anomalies in the polarization of observed shear wave data. These approaches are very successful in locations where the fractured, anisotropic region is sufficiently thick that the propagating quasi-shear waves can separate sufficiently in time that they may be resolved.

However, it is not realistic to suggest that the earth is everywhere uniformly fractured, and many practical problems require the location of relatively small fracture zones within the surrounding bedrock. Some important examples of such problems are the location of fractures for the development of geothermal fields (Leary and Henyey, 1985; Batini et al., 1985a; Batini et al., 1990), for nuclear waste disposal (Green and Mair, 1983; Carswell and Moon, 1985), or for other purposes (Juhlin et al., 1991). In these situations, the dimensions of the fracture zones are often not sufficiently thick that shear wave splitting will be detectable, even if the zone is anisotropic. Therefore, a different form of evidence for the fracturing must be sought in seismic data.

In order to achieve this objective, we apply a Ray-Born computation of synthetic seismograms to model the scattering of elastic waves by relatively small features in three-dimensional structures. This approach is similar to that of Beydoun and Mendes (1989), who outline a Ray-Born algorithm for migration or inversion

problems in three-dimensional, isotropic media with examples of application to two-dimensional problems. Two basic approximations are employed to compute the wavefields expected for relatively complicated media. First, ray theory is used to compute the Green's tensors for a background earth model. Because asymptotic ray theory is employed, this background reference model must be sufficiently smooth that the high frequency assumption is valid (Ben-Menahem and Beydoun, 1985). Ray tracing has the advantage of allowing the computation of Green's tensors for large, three-dimensional models with minimal computation time. The second step is to use the Born approximation to compute the elastic waves generated by perturbations to the reference model, a method which expresses the effects of the perturbations as secondary sources radiating energy as they are encountered by the wave propagating in the background medium (Gubernatis et al., 1978b; Wu and Aki, 1985). Application of this approximation is valid only for small, short wavelength features of an earth model. We show how the Ray-Born method can be extended to fully general anisotropic and inhomogeneous earth models using the high frequency Green's tensor for anisotropic background media (Ben-Menahem et al., 1990) and the expressions for the secondary source radiation by anisotropic perturbations developed in Chapter 3. We apply the method to three-dimensional isotropic earth models with anisotropic perturbations.

After describing the Ray-Born algorithm including a brief review of the Born approximation, we explore the question of the accuracy of the Born approximation in computing the scattered waves caused by varying degrees of heterogeneity. This is accomplished by comparing the Ray-Born results with the complete solution for waves scattered from an elastic sphere by an incident plane P-wave. Using the guidelines for application of the Ray-Born algorithm developed by this comparison, we next examine the wavefields generated by a thin but laterally extensive fracture zone in a hypothetical layered earth model in order to gain an understanding of the effects of both fracture orientation and of the fluid filling the fractures on seismic waves in

an ideal case. Lastly, we examine a set of VSP data from the Lardarello geothermal field in Italy, where an important objective in the course of exploitation of geothermal resources is the delineation of thin fracture zones several kilometers below ground. We present a fracture zone model which explains the observed data and discuss the implications of the results for determination of fracture alignment in the Lardarello field based on the synthetic results from our model.

4.2 Computation of the Born Scattered Field

4.2.1 The Born Integral Equation

The vector form of the source free equation of motion for an inhomogeneous medium is

$$\rho\ddot{\mathbf{u}} - \nabla \cdot \mathbf{T} = \mathbf{0}, \tag{4.1}$$

where ρ is density, $\mathbf{u}$ is the displacement vector, and $\mathbf{T}$ is the stress tensor (Ben-Menahem and Singh, 1981). Derivatives with respect to time are indicated by the dot symbols over the vector $\mathbf{u}$. Hooke's law relates the stress tensor and the strain tensor $\mathbf{E}$ through the fourth order elastic tensor $\mathbf{c}$:

$$\mathbf{T} = \mathbf{c} : \mathbf{E}. \tag{4.2}$$

The elastic tensor obeys the usual symmetry relationships

$$\begin{aligned} c_{ijkl} &= c_{klij} \\ &= c_{jikl} \\ &= c_{ijlk}, \end{aligned} \tag{4.3}$$

resulting in a total of 21 independent elastic constants.

The Born approximation to the scattered field generated by heterogeneous materials is obtained by considering perturbations of the elastic properties of a prescribed

background reference model:

$$\begin{aligned} \rho(\mathbf{x}) &= \rho^0(\mathbf{x}) + \delta\rho(\mathbf{x}) \\ c_{ijkl}(\mathbf{x}) &= c^0_{ijkl}(\mathbf{x}) + \delta c_{ijkl}(\mathbf{x}). \end{aligned} \tag{4.4}$$

Here the superscript ^{0} indicates a value of the known background model and $\mathbf{x}$ is the position vector. The values $\delta\rho(\mathbf{x})$ and $\delta c_{ijkl}(\mathbf{x})$ are the perturbations to the reference values $\rho^0(\mathbf{x})$ and $c^0_{ijkl}(\mathbf{x})$. Both the background and perturbation models are taken to be functions of location $\mathbf{x}$. Derivation of expressions for the scattered field proceeds by assuming that the displacement field in the total medium is also given by the sum of the field $\mathbf{u^0}(\mathbf{x})$ which would propagate in the background material and a scattered field $\delta\mathbf{u}(\mathbf{x})$:

$$\mathbf{u}(\mathbf{x},t) = \mathbf{u^0}(\mathbf{x},t) + \delta\mathbf{u}(\mathbf{x},t). \tag{4.5}$$

In Chapter 3, we show that substitution of equations (4.4) and (4.5) into the equation of motion (4.1), neglection second order terms, yields a solution for the scattered field

$$\delta\mathbf{u}(\mathbf{x},t) = \int dV(\mathbf{x}') \int dt' \;\; \mathbf{G}^0(\mathbf{x},t;\mathbf{x}',t') \cdot (\delta\rho\ddot{\mathbf{u}}^0(\mathbf{x}',t')) \tag{4.6}$$

$$\int dV(\mathbf{x}') \int dt' \;\; [\delta\mathbf{c}(\mathbf{x}',t') : \mathbf{E}^0(\mathbf{x}',t')] : [\nabla\tilde{\mathbf{G}}^0(\mathbf{x},t;\mathbf{x}',t')]. \tag{4.7}$$

This Born approximation provides an approximation to the scattered field in terms of the incident wavefield $\mathbf{u^0}(\mathbf{x},t)$ propagating in the background medium, as $\mathbf{E}^0(\mathbf{x}',t')$ is the strain associated with this displacement. $\mathbf{G}^0(\mathbf{x},t;\mathbf{x}',t')$ is the Green's tensor for the background earth model, yielding the disturbance at location $\mathbf{x}$ from a source applied at $\mathbf{x}'$. The perturbations to the material quantities act as secondary sources for displacement fields propagating in the reference model, where the product of density perturbation and acceleration vector yields a single force source vector at each point $\mathbf{x}'$ and time t'. Likewise, perturbations to the elastic tensor $\mathbf{c}$ result in double force source terms which are doubly contracted against $\mathbf{G}^0(\mathbf{x},t;\mathbf{x}',t')$. This moment tensor type source $\delta M_{ij} = \delta c_{ijkl} E_{kl}$ is more easily interpreted by writing it

in the following form, employing the standard Voigt notation as described in Chapter 3 (equations 3.3 through 3.11):

$$\begin{bmatrix} \delta M_{11} \\ \delta M_{22} \\ \delta M_{33} \\ \delta M_{23} \\ \delta M_{13} \\ \delta M_{12} \end{bmatrix} = \begin{bmatrix} \delta C_{11} & \delta C_{12} & \delta C_{13} & \delta C_{14} & \delta C_{15} & \delta C_{16} \\ & \delta C_{22} & \delta C_{23} & \delta C_{24} & \delta C_{25} & \delta C_{26} \\ & & \delta C_{33} & \delta C_{34} & \delta C_{35} & \delta C_{36} \\ & & & \delta C_{44} & \delta C_{45} & \delta C_{46} \\ & & & & \delta C_{55} & \delta C_{56} \\ & & & & & \delta C_{66} \end{bmatrix} \begin{bmatrix} \epsilon^0_{11} \\ \epsilon^0_{22} \\ \epsilon^0_{33} \\ 2\epsilon^0_{23} \\ 2\epsilon^0_{13} \\ 2\epsilon^0_{12} \end{bmatrix}. \quad (4.8)$$

4.2.2 Evaluation of the Integral

Using equation (4.7), the Born scattered field for prescribed perturbations $\delta\rho$ and δc_{ijkl} can be computed once the incident field $\mathbf{u}^0(\mathbf{x},t)$ and its associated strain $\mathbf{E}^0$ are known. The Green's tensor $\mathbf{G}^0(\mathbf{x},t;\mathbf{x}',t')$ is the fundamental quantity which must be obtained, as it can be used to compute these background fields as well as the displacements generated by the secondary sources on the right hand side of equation (4.7). Therefore, application of the integral solution requires first the knowledge of the Green's tensors for propagation in the background model and then an algorithm for the actual evaluation of the integral.

Following Beydoun and Mendes (1989), we proceed by discretizing the perturbed volume of the earth model (Figure 4-1). Each unit cell within the discretization is a rectangular prism with dimensions dx_1, dx_2, and dx_3. As long as the wavelength of the incident wave is much greater than the largest dimension dx_i, the scattering due to each individual elemental volume is equivalent to Rayleigh scattering, which reduces the integration over volume in equation (4.7) to a simple multiplication by the elemental volume $dV = dx_1 dx_2 dx_3$:

$$\delta\mathbf{u}(\mathbf{x},t) = \delta V \int dt' \ (\delta\mathbf{c}(\mathbf{0},t') : \mathbf{E}^0(\mathbf{0},t')) : \nabla\widetilde{\mathbf{G}}^0(\mathbf{x},t;\mathbf{0},t'). \quad (4.9)$$

Under the condition of Rayleigh scattering, each cell in the perturbed volume therefore acts as a point source located at the center of the cell, indicated by the dots in Figure 4-

1. The point source at each lattice point is equivalent to some combination of single or double forces as presented in equation (4.7). Evaluation of the integral is most easily accomplished by simply summing the contributions of each of the point sources within the scattering volume, which corresponds to the most elementary implementation of the definition of an integral as a Darboux sum (Budak and Fomin, 1983).

Application of this integration scheme then requires a knowledge of the Green's tensors corresponding to the wave propagation from the primary source to each elemental scattering volume, yielding the properties of each secondary point source, and also from the scattering volume to the receivers, which determines the scattered field from each point source. Ray methods provide a fast and flexible means for performing these calculations in general three-dimensional layered models. The principal requirement for ray solutions to be applicable is that the wavelength must be much less than the characteristic length scale of the background earth model (Ben-Menahem and Beydoun, 1985). For inhomogeneous and anisotropic media meeting this length scale requirement, the ray theoretical Green's tensor is given by (Ben-Menahem et al., 1990)

$$\mathbf{u}(\mathbf{x},t) = \frac{1}{4\pi[v(\mathbf{x}_0)]^2}\left[\frac{\rho(\mathbf{x}_0)v(\mathbf{x}_0)\widehat{J}(\mathbf{x}_0)}{\rho(\mathbf{x})v(\mathbf{x})\widehat{J}(\mathbf{x})}\right]^{1/2}[\mathbf{g}(\mathbf{x})\mathbf{g}(\mathbf{x}_0)]\,\delta(\tau(\mathbf{x}|\mathbf{x}_0)). \tag{4.10}$$

The source position is indicated by $\mathbf{x}_0$, $\mathbf{x}$ is the observation point, $v(\mathbf{x})$ is phase velocity, and $v(\mathbf{x})\widehat{J}(\mathbf{x})$ is the Jacobian of the transformation from Cartesian coordinates x_i to ray coordinates γ_j, where $\widehat{J}(\mathbf{x})$ is given by

$$\widehat{J}(\mathbf{x}) = \left|\frac{\partial \mathbf{x}}{\partial \gamma_1} \times \frac{\partial \mathbf{x}}{\partial \gamma_2}\right|. \tag{4.11}$$

The ray coordinates here are specified to be the two take-off angles of the ray at the source, the declination angle ψ and the azimuthal angle ϕ (Figure 4-2). It is important to realize that this Green's tensor contains only quantities obtained in the course of normal ray tracing algorithms. It contains the effects of geometrical spreading on amplitudes through the ratio of Jacobians $v(\mathbf{x}_0)\widehat{J}(\mathbf{x}_0)/v(\mathbf{x})\widehat{J}(\mathbf{x})$, as well as the material properties at the source and receiver points. The scalar amplitude multiplies

a dyad given by the outer product of the polarization vectors at the source and at the observation position, reproducing the usual reciprocity of elastic wave propagation in inhomogeneous media whereby exchange of source and receiver positions result in the equivalence (Ben-Menahem and Singh, 1981)

$$G_{ij}(\mathbf{x}, t; \mathbf{x}', t') = G_{ji}(\mathbf{x}', t'; \mathbf{x}, t). \tag{4.12}$$

This ray theoretical Green's tensor will not be able to model aspects of wave propagation such as caustics or shadow zones, a fundamental limitation of the high frequency approximation (Červený, 1985).

Given the general ray theoretical Green's tensor in equation (4.10), the Ray-Born method could be applied to general anisotropic media with anisotropic inhomogeneity. However, as a first step, in this paper we consider only an isotropic, inhomogeneous background model with anisotropic inclusions in order to develop an understanding of the effects of localized anisotropic regions on elastic wave propagation. This also allows the utilization of the elegant dynamic ray tracing (DRT) techniques in the ray-centered coordinates q_I with basis vectors $\mathbf{e}_I$ (Figure 4-2) (Červený, 1985). The DRT involves, in addition to the standard determination of ray path and travel time (kinematic ray tracing, KRT), the integration of eight additional ordinary differential equations to obtain the two by two matrices $\mathbf{Q}$ and $\mathbf{P}$. These components of these matrices can be expressed as

$$Q_{IJ} = \frac{\partial q_I}{\partial \gamma_J} \tag{4.13}$$

$$P_{IJ} = \frac{1}{v^2}\frac{dQ_{IJ}}{d\tau} \tag{4.14}$$

Here τ is the travel time along the ray, and $I, J = 1, 2$. The P_{IJ} are needed only to obtain Q_{IJ}.

The matrix $\mathbf{Q}$ is related to the curvature of the wavefront (Červený, 1985). Knowledge of the components of this matrix yields geometric spreading, which is proportional to $\det \mathbf{Q}$. $\mathbf{Q}$ is also used for the application of the paraxial method, which

allows extrapolation of travel time and polarization vectors from a central ray which has been obtained by integration to nearby observation points. This results in significant savings in computation time, as the two-point ray tracing is avoided. In an application such as the Ray-Born method where the incident wavefield must be known at a large number of points, this is an especially valuable feature. As these paraxial ray tracing procedures are discussed in many references, the standard aspects are summarized in Appendix F.

In addition to these more typical paraxial corrections, we also include a correction to the geometrical spreading amplitude factor which can be derived using geometrical arguments. The integration of both the KRT and DRT equations is dependent on the choice of initial values, but once these values are selected the integration of the ray equations governs all propagation effects along the ray path from the initial point, within the limitations of the validity of ray methods. As the initial conditions can be chosen along an initial wavefront as easily as from a source point, it follows that the additional geometrical spreading from the wavefront at central ray point $\mathbf{x}'$ and time $\tau(\mathbf{x}')$ to the wavefront at observation point $\mathbf{x}$ and time $\tau(\mathbf{x})+\Delta\tau$ is in a homogeneous, isotropic material equivalent to the distance between wavefronts $v\Delta\tau$. The total geometrical spreading is then

$$\det \mathbf{Q} + v\Delta\tau \tag{4.15}$$

In an inhomogeneous material, this correction will be less accurate, but since the paraxial corrections can only be applied a relatively short distance from the central ray anyway, it should not be a severe limitation, and application of this correction can be restricted to homogeneous regions of a model. It should also be noted that in this formulation, the changes in reflection and transmission coefficients with the variation in incidence angles on interfaces from the central ray to the ray which would actually intersect the observation point are not included. This also should not be a severe limitation except possibly near critical angles.

Another aspect of the DRT which proves very useful is that the partial derivatives

may be used in an iterative two-point ray tracing scheme for rays propagating from the source to fixed receiver locations. While this is not necessary for the calculation of synthetic seismograms, it is often desirable for the determination of accurate ray paths and will also yield more accurate results than straight application of the paraxial method. Once a ray is traced with an initial source point $\mathbf{x}$ and take-off angles γ_1^0 and γ_2^0, the γ_1 and γ_2 corresponding to the ray arriving at the desired observation point can be estimated through

$$\gamma_I \approx \gamma_I^0 + (Q^{-1})_{IJ} q_J \tag{4.16}$$

We apply this result to two steps in the Ray-Born procedure. First, for the computation of the background synthetic seismograms, we perform an iterative two-point ray tracing procedure where we shoot a fan of rays over some range of prescribed take-off angles, and, beginning with the closest ray to each receiver, repeatedly apply equation (4.16) until the ray arrives with some distance of the desired receiver point. For layered models, the ray arriving essentially at the receiver point can usually be determined in three or fewer iterations, providing a very rapid determination of ray paths for multiply reflected and transmitted rays. For more complicated models, the procedure may not converge well, in which case the straight paraxial method can be applied. The second application of equation (4.16) is in the computation of the Green's tensor. Since the dyad in equation (4.10) contains the polarization vector at both the source and receiver points, in order to compute the tensor using the paraxial method at the scattering lattice we employ (4.16) to correct the polarization at the start of the central ray to be approximately that of the ray joining the source point and scattering point (these corrections are specified in Appendix F). Červený et al. (1987) outline the conversion of the results for the polarization dyad in ray-centered coordinates to Cartesian coordinates. Both SH and SV waves are automatically included in this procedure applied in ray-centered coordinates.

The algorithm can be summarized as follows:

1. Synthetic seismograms are computed for the background model using the iter-

ative two-point ray tracing technique or the paraxial method. Green's tensors are computed and then the desired primary source type is applied to compute the background displacement field.

2. Green's tensor are computed for propagation from the primary source to each elemental volume in the scattering region. The Green's tensors are also computed for propagation from the scattering lattice to receivers. It is generally more convenient to do the ray tracing from receivers to the scattering volume and then apply the principle of reciprocity, transposing the Green's tensors (Ben-Menahem and Singh, 1981). Paraxial corrections are applied to rays passing near scattering points to minimize the amount of ray tracing necessary.

3. Perturbations to the material properties are specified, and the integration of equation (4.7) is performed by summing the contribution of each point source within the scattering lattice. The scattered field resulting from this calculation is then added to the primary field to produce the final synthetic seismograms.

An advantage of this method is that the Green's tensors may be saved prior to application of the primary source of the Born approximation. This makes possible rapid comparison of the effects of different primary sources or different material perturbations on the wavefields, as the ray tracing, the most time consuming part of the algorithm, need only be done once.

4.3 Comparison of Ray-Born Results to a Known Analytic Solution

The preceding Ray-Born algorithm is in principle very general and can be applied to a wide variety of three-dimensional earth models, both isotropic and anisotropic. As long as the ray tracing can be satisfactorily accomplished, the integral over volume of heterogeneity is simply computed by summation. However, prior to application

of the method to general problems, it is desirable to have some knowledge as to the accuracy and validity of the resulting synthetic seismograms. For this purpose, we compare the Ray-Born scattered field results for a spherical obstacle to the known solution in terms of spherical harmonics.

The scattered displacement field generated by a monochromatic plane wave incident on an isotropic, elastic sphere in an infinite homogeneous medium was obtained by Ying and Truell (1956). Derivation of this solution begins by expressing the components of displacement for a planar P-wave incident along the z axis

$$\begin{aligned} \mathbf{V}_i(x_3,t) &= \mathbf{v}_i(x_3,t)e^{i\omega t} \\ \mathbf{v}_i(x_3,t) &= \hat{x}_3 e^{-ik_i z} \end{aligned} \tag{4.17}$$

in terms of an expansion of a potential ψ_i in spherical harmonics:

$$\begin{aligned} \mathbf{u}_i &= -\nabla\psi_i \\ \psi_i &= \frac{1}{k_i}\sum_{m=0}^{\infty}(-i)^{m+1}(2m+1)j_m(k_i r)P_m(\cos\theta) \end{aligned} \tag{4.18}$$

In these expressions, $k_i = \omega\alpha$, where α is the compressional wave velocity in the infinite medium, j_m is the spherical Bessel function of the first kind, and P_m is the Legendre polynomial. Spherical coordinates r and θ are illustrated in Figure 4-3. The scattered displacements are given by

$$\begin{aligned} \mathbf{V}_s &= \mathbf{v}_s e^{i\omega t} \\ \mathbf{v}_s &= -\nabla\psi_s + \nabla\times\nabla\times(\hat{\mathbf{r}}r\Pi_s) \end{aligned} \tag{4.19}$$

where ψ_s and Π_s are the compressional and shear wave potentials respectively, with harmonic expansions

$$\begin{aligned} \psi_s &= \sum_{m=0}^{\infty} A_m h_m(k_i r)P_m(\cos\theta) \\ \Pi_s &= \sum_{m=0}^{\infty} B_m h_m(\kappa_i r)P_m(\cos\theta). \end{aligned} \tag{4.20}$$

Here h_m is the spherical Bessel function of the third kind, $\kappa_i = \omega\beta$ is the shear wave number, and A_m and B_m are the as yet unknown coefficients of the expansion. The displacement field inside the sphere is expressed in similar expansions, giving two more unknown coefficients C_m and D_m. Boundary conditions on continuity of stress and displacement are applied at the surface of the spherical obstacle, resulting in 4 simultaneous equations which must be solved for the coefficients in each term m in the expansions.

Since a general seismic signal is actually composed of contributions from multiple frequencies, we apply a discrete wavenumber algorithm to compute synthetic seismograms as follows. A range of discrete frequencies is specified, $f_i = \Delta f, 2\Delta f, 3\Delta f, ..., f_{Nyq}$, where $f_{Nyq} = 1/2\Delta t$ is the Nyquist frequency corresponding to the time domain sample interval Δt. Each frequency f_i corresponds to a wavenumber k_i. The boundary value problem is then solved at frequencies f_i for the coefficients A_m, B_m, C_m and D_m. At each frequency, the harmonic expansion is carried out to sufficiently high order m_n that coefficients A_{m_n}, B_{m_n}, C_{m_n} and D_{m_n} are negligible compared to A_0, B_0, C_0 and D_0. The Bessel functions of the first and second kinds of arbitrary order are computed using a Miller's algorithm appropriately modified for spherical Bessel functions (Press et al., 1988). Finally, after the scattered field r and θ components have been computed at each frequency, this impulse response is convolved with the spectrum of the incident plane wave signal through frequency domain multiplication, and an inverse FFT is applied in order to produce the time domain response. In this way, the full waveform elastic wave scattered field of the spherical obstacle can be computed for a general incident plane wave pulse.

A comparison of the Ray-Born and discrete wavenumber algorithm results was made using a spherical heterogeneity of radius $a = 0.5$ km surrounded by a ring of receivers at a distance of 40 km (Figure 4-4). This configuration of receivers allows a comparison of both forward (90°) and back scattering results (270°). The infinite medium velocities were $\alpha_0 = 4.5$ km/sec and $\beta_0 = 2.7$ km/sec, with density 2.67

g/cm^3, and velocities within the spherical region were set to $\alpha = 4.545$ km/s and $\beta = 2.727$ km/s, perturbations of 1%. Density was kept constant, so that only the elastic Lamé parameters were varied. For the Ray-Born calculations, a 10 by 10 by 20 lattice with spacings $dx_1 = dx_2 = 0.10$ km and $dx_3 = 0.05$ km was specified and located centered on the origin. A finer spacing in the z direction was used for accurate evaluation of the Ray-Born integral since this was the direction of the incident wave propagation and therefore also of the most rapid variation of the integrand. Amplitude and phase of the incident plane wave are constant in both x and y. The perturbations at all lattice points at a distance larger than 0.5 km were set to zero providing an approximation to the spherical inhomogeneity. For both methods, the source wavelet used was given by

$$s(t_i) = e^{-(\omega_0(t-t_0))^2/\gamma^2} \cos(\omega_0(t-t_0)), \tag{4.21}$$

where t_0 is the arrival time, $\omega_0 = 2\pi f_0$ contains the center frequency f_0, and γ is a free parameter which we set to three. The resulting radial component P-wave synthetic seismograms from the two methods for center frequencies of 0.25, 1, 2.5 and 5 Hz are compared in Figures 4-5 and 4-6. Analogous plots for the S-wave theta component are given in Figures 4-7 and 4-8. The important parameter for determination of the validity of the Born approximation is the ratio of wavelength to sphere diameter $\eta = k_i/d$. These frequencies we have examined, 0.25, 1, 2.5 and 5 Hz, provide ratios $\eta_p = 18$, 4.5, 1.8 and 0.9, respectively, for compressional waves. The corresponding values for shear waves are $\eta_s = 10.8$, 2.7, 1.08 and 0.39. Examination of the results for $\eta_p = 18$ (Figures 4-5A, 4-6A, 4-7A and 4-8A) shows that the two solutions are very similar, which is not surprising as this long wavelength reproduces the Rayleigh scattering result, where the forward (90°) and back scattering (270°) amplitudes are the same. A plot of the maximum amplitudes as a function of scattering direction shows that there is a systematic difference in the two results, with the Ray-Born amplitude about 15% to 20% less than the discrete wavenumber result (Figure 4-9). An error of approximately 2% results simply because the volume of the discretized

version of the sphere is 98% that of the true sphere. The rest of the variation is explained by the spherical harmonic solution P-wave impulse response and incident waveform spectra presented in Figure 4-10. Because the impulse response increases more rapidly with frequency than the amplitude of the incident wavelet decreases for this low frequency source wavelet, the maximum response after convolution is actually shifted to a slightly higher frequency. As the amplitude of Rayleigh scattering goes as ω^2, this increases the amplitude of the discrete wavenumber solution. This is not reflected in the Ray-Born solution, since it only includes the ω_0^2 specified for the center frequency of the incident wavelet.

As the incident center frequency increases to 1 Hz and the ratio η_p decreases to 4.5 (Figures 4-5B, 4-6B, 4-7B and 4-8B), the two methods compare about as well as for η_p, noting also the amplitude plot in Figure 4-9. Errors are less than 20% in all directions for the P-wave amplitudes and less than 10% for all back scattered energy. Decreasing the incident wavelength further, however, causes the results for the Ray-Born method to begin to degrade. We see that the spherical harmonic solution predicts that the back scattering amplitude at 270° will become approximately constant for shorter wavelengths though forward scattering amplitude increases significantly with frequency (Figures 4-5C, 4-6C). In one sense, the comparison of maximum amplitudes is not a strictly valid measure of equivalence for the higher frequency results in back scattering, since the discrete wavenumber results show that for $\eta_p = 0.9$ (5 Hz), both shear and compressional wave back scattering have the form of two reflections from the front and back of the sphere, while the Ray-Born method yields only a single wide pulse due to insufficient cancellation of back scattered waves. Therefore, comparing the amplitude of the single Ray-Born wavelet with the values for the two reflected arrivals from the discrete wavenumber results does not reflect the true mismatch of waveforms. It should also be noted that the same double reflection effect can be seen for the scattered shear waves at $\eta_p = 1.8$ (2.5 Hz) on the theta component plots. It is because of the shorter shear wavelength that this happens at the lower frequency

for shear waves.

It is worth noting, however, that the results for forward scattering at 90° from both solution methods still tend to compare relatively well at higher frequencies. Also encouraging is that both methods predict a much shorter pulse of higher apparent frequency for forward scattering than for back scattering and that the total width in time of energy at each observation point is the same. The Ray-Born method does succeed in matching the gross features of the wavefields, including achieving at least some of the general trends of amplitude variation with respect to both scattering direction and increasing frequency. Details of the reflections are missing from the Born approximation.

We computed the scattered fields using both methods for P and S-wave velocity perturbations of 10% and 50% as well as the 1% perturbation results shown here. The comparisons are essentially the same as these results, though the details of the complete waveform solution change slightly for the 50% velocity perturbation and these are not reproduced by the Ray-Born method, which has strictly linear behavior with respect to variation in elastic constants. The amplitude comparisons become only slightly worse as the velocity perturbations increase to 50% (Figure 4-11). The more significant failures of the Ray-Born solution are still caused by increasing frequency. Therefore, we conclude that a principal requirement for accurate solutions using the Ray-Born technique with the degrees of heterogeneity we considered is that the incident and scattered wavelengths must be 4 to 5 times larger than the length scale of the heterogeneity, a restriction which for the case above corresponds to frequencies less than or equal to 1 Hz. As the magnitude of the perturbations decreases, this requirement can be relaxed as the Born approximation will be more accurate for weaker heterogeneity. Conversely, for equal accuracy for larger perturbations, a somewhat larger ratio of wavelength to heterogeneity dimension must be imposed as the stronger velocity changes will reduce the accuracy of the Born approximation (Figures 4-9 and 4-11). Even when the wavelength ratio is larger than five, subtle

aspects of wave interaction with the heterogeneity can degrade results, as for the 0.25 Hz scattering for our spherical model, where the resonances of the sphere cause a shift of the principal response frequency.

Although density perturbations were not considered in the above examples, the restrictions on accuracy of the Ray-Born method should be the same as for elastic properties. Both types of perturbations occur in convolutional integrals over volume and time of the same form in equation 4.7. Therefore, the main factor which controls the accuracy of the Born approximation in is still the rapidity of variation of the incident wavefield with respect to the volume of the heterogeneity. The only difference is that for density, the particle acceleration multiplies the perturbation whereas the strain multiplies the elastic constant variation. Both accleration and strain will vary with the same incident wavelength.

4.4 Synthetic Seismograms from a Fracture Zone Model

Given the guidelines established in the comparisons with the complete solution for scattering by an elastic sphere, we next apply the method to a layered earth model containing a relatively thin but laterally extended zone of fracturing in the subsurface. Using the Ray-Born method, we can easily compare the expected seismic response of the model without the fractured region and with isotropic and anisotropic fracturing present. In addition, the effects of various crack filling materials on the back scattered displacement fields are tested.

The background earth model is presented in Figure 4-12. It consists of 3 layers overlying a half space. The source is located at a depth of 0.25 km in the top layer, which is 0.50 km thick, and receivers are located on the free surface at offsets from the source epicenter of 0 to 1.95 km at an interval of 0.05 km, yielding a total of 40 observation points. A simulated fracture zone is located in the third layer, and

it is shaped like a rectangular prism with dimensions of 0.315 km, 0.099 km and 0.018 km in the x, y and z directions, respectively. These axis directions are chosen such that the receiver array is contained within the $x - z$ plane (Figure 4-12). We applied a center frequency of 25 Hz for the source wavelet, and the lattice spacing was set to 0.009 km in all coordinate directions. The shear wavelength is 9.6 times the lattice spacing so that the Ray-Born results should be valid for back scattered waves. One end of this heterogeneity is located under the source point, and the region is centered under the receiver array in the y direction, the direction perpendicular to the receiver array. Though the background model is one-dimensional, the Ray-Born solution requires three-dimensional calculation of the Green's tensors due to the three-dimensional nature of the scattering lattice. This example allows the paraxial method to be used to full advantage, however, as rays need only be traced down the axis of the lattice in the $x - z$ plane and the paraxial corrections can be used to project the results out of this symmetry plane. Considerable computation time is saved, since the need to trace rays along multiple azimuths is eliminated.

To calculate the scattered field for an isotropically fractured inhomogeneity, we use the perturbations to the Lamé parameters given by the Hudson theory for the effective elastic moduli of a fractured medium (Hudson, 1980, 1981) (see Appendix A). The effective moduli are given in terms of an expansion to second order in crack density $\xi = na^3$, where n is the number density of cracks, and a is the radius of the penny-shaped cracks. We applied a crack density of 0.10, and assumed an aspect ratio of 0.005. For the first case, we consider cracks which are dry or, equivalently, gas-filled. The Lamé parameters for the unfractured layer and the fractured perturbations are presented in Table 4.1. Note that for the case of perturbations due only to fine cracks, that density variations are not important (Appendix E).

4.4.1 Isotropic, gas-filled fractures

In the calculations for the background field, we included P and S-waves leaving the source in both the upward and downward directions. The reflections from each interface were then modeled, including phases with a single mode conversion from P to S or S to P on reflection, as waves changing mode more than once are generally of very low amplitude. We first consider the effects of the fracture zone on the propagation of SH waves generated by a single force source oriented perpendicular to the receiver line (Figure 4-13). No compressional waves are emitted in the direction of the receiver array, and all shear signals have a horizontal polarization. Taking the dot product of all the Green's tensors with the source vector then yields a total of only six arrivals for this source on the transverse component, the shear to shear wave reflections from each interface, including the rays reflecting first from the free surface.

The calculated scattered field includes two S to S scattered waves, one leaving the source in the downward direction, the other reflecting from the free surface and subsequently traveling to the fractured zone (Figure 4-14). Like the case of reflection from a planar interface, the incident SH-waves also do not yield a scattered P-wave signal. The pulse broadens at farther offsets in Figure 4-14, which is plotted at a scale 2.5 times larger than the background field (Figure 4-13). This change in pulse shape is caused by the directivity of the volume source of elastic waves, the fractured zone. At near offsets, the energy from all points of the perturbed zone arrives more or less simultaneously, yielding a single large arrival. At the farther offsets, the length of the source becomes important and the difference in arrival times from the near and far ends of the fracture zone is observable. The slight peaks at the start and end of the pulse result from the concentration of energy from the two ends of the fracture zone and are somewhat analogous to stopping phases from the ends of a planar earthquake source (e.g., Bernard and Madariaga, 1984).

The total displacement field, the sum of the background field and the scattered field, shows clearly the presence of the fractured zone (Figure 4-15). Arrows in Fig-

ure 4-15 mark the arrival times of the two scattered signals on the zero offset trace, and they are clearly of comparable amplitude to the standard reflections from the nearby planar interfaces. The finite extent of the fracture zone can be inferred from the fact that the back scattered waves are only observed in the shorter offset receivers. These synthetic results show that even thin fractured regions can be detected with seismic experiments.

The effects of the isotropic perturbation on P-waves are examined by applying an explosion source to the Green's tensors. Figure 4-16 presents the resulting background displacement field, which now contains non-zero radial and vertical components. The largest disturbances on the vertical component are P-waves, with a pair of reflections from the first interface observed at 0.2 and 0.32 sec on the zero-offset trace, from the second interface at 0.52 and 0.65 sec, and from the third at 0.77 and 0.9 sec. In addition, some large amplitude shear arrivals are observed at larger offsets. The radial component is weaker at near source offsets since near vertical P-waves have minimal horizontal displacement and shear wave conversions also only become significant at larger offsets.

For the gas-filled fracture case, the perturbation to the Lamé parameter $\delta\lambda$ is about 5.5 times greater than the change in rigidity μ (Table 4.1), and so we can expect that the compressional wave scattering will be relatively significant, as a change in λ affects only P-wave scattering (Chapter 3). The total displacement fields for the explosion source are shown in Figure 4-17, where the arrival times of the principal scattered waves are marked. While the scattered shear waves are somewhat difficult to discern compared to the background displacements on the radial component synthetic seismograms, the scattered compressional waves are easily observed on the vertical component. These results and the example of the transverse component SH-waves show that both compressional and shear waves are of use in the detection of isotropic, gas-filled fracture zones.

4.4.2 Anisotropic, gas-filled fractures perpendicular to the receiver array

We next consider the case where the experimental configuration is exactly the same as above, except that within the fracture zone, all the fractures are vertical and aligned perpendicular to the receiver array. The perturbations to the elastic constants are again obtained from the theory presented by Hudson (1980) (see Appendix A). In this anisotropic case, the fractured zone is transversely isotropic with a horizontal axis of symmetry. The resulting perturbations to the elastic constants are given in Table 4.2. Note that $\delta C_{44} = 0$, which significantly affects the total displacement field due to the SH-wave source (Figure 4-18). Since the only incident strain component which is not vanishingly small is ϵ_{23}, and only perturbation in this symmetry system which influences scattering from an incident SH-wave is δC_{44}, the scattered field will be essentially zero (equation 4.8). Accordingly, in Figure 4-18, the scattered field is not visible.

In contrast, the scattering from incident compressional wave energy is affected to a much lesser degree (Figure 4-19). Here we see that though reduced in amplitude the P to P scattering is still detectable. This result is not unexpected, as the incident P-wave strain, mostly ϵ_{33}, will still interact with the perturbation δC_{33}. Though reduced from the isotropic equivalent $\delta\lambda + 2\delta\mu$, this perturbation is still large enough to generate energy on the vertical component seismograms. Note that there is some subtle evidence of the anisotropy in that the P to S converted scattered waves are slightly larger than the corresponding arrivals for the isotropic case, due to the larger value of δC_{55} compared to $\delta\mu$. Clearly, though, the change in total displacement fields is far more significant for the SH-wave source.

4.4.3 Anisotropic, gas-filled fractures parallel to the receiver array

In order to explore the effects of varying orientation of vertical fractures, we next compute the scattered fields for a model of the same experimental configuration with fractures aligned parallel to the receiver array. Perturbations to the elastic constants have the same values as in the previous anisotropic model, but are rearranged somewhat due to the rotation of the elastic tensor (Table 4.3). The polarization of incident SH-waves is now perpendicular to the fracture plane, and so there will be large scattered fields, as the incident ϵ_{23} strain now interacts with a non-zero perturbation (equation 4.8). These effects are seen in the total field synthetic seismograms for the horizontal point force source (Figure 4-20). Comparison to Figure 4-15 shows that the scattered field for this anisotropic model is even larger than the original results presented for the isotropic case. This again shows the sensitivity of shear waves to fracture alignment.

The corresponding insensitivity of compressional waves is displayed by Figure 4-21, the total displacement field synthetic seismograms for the explosion source. This figure is essentially indistinguishable from Figure 4-19, where the fractures are oriented perpendicular to the receiver line. As before, the strains from the incident P-waves are almost entirely ϵ_{33}, and as the rotation of the fractures does not affect δC_{33}, the scattered fields are the same.

4.4.4 Anisotropic, gas-filled fractures at 45 degrees to the receiver array

The two previous anisotropic models are special cases in that both contain fractures oriented such that incident SH-wave displacement is polarized in a symmetry direction of the anisotropic fracture zone. In the first case, fractures perpendicular to the array, the SH polarization is contained in the symmetry plane. In the second example, the

SH-wave is polarized parallel to the symmetry axis. If the fracture orientation is at some arbitrary angle to the receiver line, the resulting synthetic seismograms would be expected to be less simple. This effect is examined by considering a model where the fractures are oriented at 45° to the array. Perturbations to the elastic constants for this model are presented in Table 4.4.

The total displacement field from the horizontal point force source is presented in Figure 4-22. For the first time, the SH-wave source results in a significant radial component synthetic seismogram. In the isotropic case, the perturbations are such that $\delta C_{11} = \delta C_{22} = \delta C_{33} = \delta\lambda + \delta\mu$, $\delta C_{12} = \delta C_{13} = \delta C_{23} = \delta\lambda$, and $\delta C_{44} = \delta C_{55} = \delta C_{66}$ are the only non-zero perturbations. However, the perturbations for the 45° case clearly have other non-zero perturbations (Table 4.4), and, in addition, the equivalencies which hold in the isotropic model are not all true. The result is a complicated secondary source representation which yields both SH and SV energy from an incident SH-wave (equation 4.8). The vertical component synthetic seismograms are still essentially zero since the vertically propagating shear waves have almost no vertical components of displacement.

In contrast to these distinctive results for the shear waves, the explosion source and resulting compressional waves incident on the fracture zone still generate a non-unique result for the total displacement field (Figure 4-23). Since the rotation of the elastic tensor does not affect δC_{33} (Table 4.4), there is essentially no difference between Figure 4-23 and the other sets of seismograms for the explosion source and anisotropic fractures (Figures 4-19 and 4-21). It is clear that the information contained in the shear wave polarizations is likely the most useful evidence for the alignment direction of vertical fractures in fracture zones within the earth.

4.4.5 Isotropic, water-filled fractures

The preceding examples of scattered wavefields predicted for fracture zones which contain gas show some of the possible effects of fracture alignment on seismic ob-

servations. Additionally, we can consider the effect of changing the pore-filling fluid from the gas state to liquid. The effective elastic constants for the model in Figure 4-12 with randomly oriented, water-filled fractures are given in Table 4.5. The crack density was held at 0.10, as in the anisotropic and isotropic examples considered above. Comparison with Table 4.1 shows that the most significant difference in the perturbations is that $\delta\lambda$ is an order of magnitude smaller for the water-filled crack case. Since $\delta\lambda$ affects only P to P-wave scattering, the compressional waves should be more affected by this change in pore fluid than shear waves.

The total synthetic seismograms for the horizontal point force (Figure 4-24) are very similar to those in Figure 4-15 for the isotropic gas-filled model. However, the results for an explosion source are very different for the two isotropic fracture models (Figures 4-17 and 4-25). Figure 4-25 shows that as expected, the amplitude of the scattered P-waves is considerably decreased and cannot be detected on the scale plotted here. This is a classic case of "bright spot" behavior, a phenomenon used to distinguish gas and oil reservoirs (Ensley, 1984). In hydrocarbon exploration studies, it has been observed that the P-wave reflectivity of gas reservoirs is significantly greater than that for oil reservoirs though S-wave reflection amplitudes are similar. We have shown that the same type of behavior is to be expected for thin fractured zones.

4.5 Application to Field Data

The delineation of fracture zones is of great practical interest in the development of geothermal fields, as the permeability created by the fractures can control the fluid flow in the geothermal systems. In order to facilitate the development of the Lardarello geothermal field in Italy (Figure 4-26), an extensive geophysical study has been conducted for a number of years (Batini et al., 1983, 1985a, 1985b, 1985c, 1990). Recently, a VSP experiment was conducted in the Badia 1A well in the Lardarello

field in order to attempt to further delineate several possible fracture zones (Batini et al., 1990). Interpretation of the processed data from the VSP experiments and a number of other surface seismic surveys resulted in the suggestion that three reflected events from a subsurface feature below the depth of the well bottom and labeled the "H marker" were due to thin, laterally continuous fractured zones distributed over a depth range of approximately 0.200 km. This model is based on some regional seismic observations. We have used Ray-Born synthetic seismograms to test this *a priori* hypothesis and to develop a laterally varying model of fracture density in three fracture zones which accounts for these arrivals as observed from two VSP surveys.

4.5.1 Background Model

A local three-dimensional seismic survey allowed the development of a fairly detailed model of the principal geological layers in the Badia area. The principal geological features of the locality are two shallow layers consisting of various sedimentary units overlying a thicker zone of metamorphic rock. The L1 and L markers form the lower interfaces of the first and second sedimentary layers, respectively. P-wave velocities for the model are given in a cross-section in Figure 4-27, a section in the east-west direction which intersects the position of the Badia 1A well. Contour maps of the depths of the L1, L and H markers are presented in Figure 4-28, along with the positions of the Badia 1A well and the two locations for the Vibroseis source. One of the shot points is very close to the well and will be called the zero offset point, and the A shot point is 0.981 km north and slightly east of the well. These maps clearly demonstrate the three-dimensional nature of this modeling problem.

4.5.2 Data

Due to difficult drilling conditions, the Badia 1A well is highly deviated (Figure 4-29), so that only vertical geophone components have sufficiently high signal to noise ratio to analyze the comparatively weak scattered arrivals. Many of the vertical

component data traces were however extremely noisy after the first arrival, especially at shallower depths. Therefore, a subset of recorded data was used, with receiver positions indicated in Figure 4-29. Slightly different depth ranges are covered by the geophones from the zero and A offset experiments.

Data from both shot points are shown in Figure 4-30 where each trace is normalized to unit amplitude on the first arrival. The signal from the far offset VSP is somewhat noisier, since the first arrival prior to normalization is lower in amplitude due to a greater distance from source to receiver. Therefore, noise is amplified more in the normalization than with the zero-offset traces. For both data sets, however, the downgoing waves are clearly much stronger than any reflected arrivals, which are not visible in these sections. In order to bring out the upgoing reflected waves, we processed the data using a median filter (Hardage, 1983; Reiter, 1990). The moveout velocity on the filter was set to the opposite of the apparent velocity of the downgoing wave in order to enhance the reflected P-waves, and the filter was applied across 17 traces. After median filtering, the data were subsequently low-pass filtered with cutoff frequencies of 55 and 85 Hz for the zero and A offset data, respectively. Since the predominant signal strength is at 30 Hz, this should not significantly affect the results. The processed data are displayed in Figure 4-31, where the zero offset data are magnified by a factor of three compared to the A offset plot. The arrivals from the H marker are indicated on these plots. Considering the difference in gain factors applied to the upgoing data plots, it is clear that the signal observed from the A offset source is much stronger, suggesting a lateral difference in the properties of the H marker.

4.5.3 Modeling results

The geological model (Figure 4-28) clearly demonstrates the three-dimensional structure of the sedimentary and metamorphic layers in the Lardarello area. This significantly affects the ray tracing procedures which must illuminate the H marker to

calculate the scattered waves, as would be expected. To illustrate this problem, we show the ray paths for a fan of rays traced from both the zero and A offset source positions with azimuthal take-off angle in the north-south direction (Figure 4-32). The resulting ray paths for both source positions have large distortion in the east-west direction due to the L1 and L interfaces (Figure 4-28), whereas in a one-dimensional earth model, these rays would be entirely contained in a vertical plane. In particular, we see that for the A offset source the bending of the rays at these interfaces is so large that the rays exit the model before reaching the H marker depth. Therefore, computation of the Green's tensors for the incident wavefield in equation 4.7 requires that we trace fans of rays like those in Figure 4-32 over all azimuths. Approximately 2800 rays were traced from the two source positions. Although the ray tracing is simpler from the receivers to the H marker since the metamorphic layer is homogeneous, even more rays are required since the closer proximity of the receivers to the marker increases the range of take-off angles for the fans of rays over all azimuths. Almost 8000 rays were traced from each receiver to insure sufficient coverage of the H marker. These points regarding the three-dimensional nature of the wave propagation for this problem emphasize the value of the ray tracing approach, which is a practical and feasible method of solution. A more complete solution might in principle be obtained using a finite-difference method, but the required discretization of the three-dimensional model to adequately represent the different layers and the H marker would be prohibitively time consuming.

Since the scattered waveforms are stronger on the A offset data, we began by developing a model which would account for these data. A lattice was set up to conform to the map of the H horizon in Figure 4-28C, though due to limitations of computer storage, we limited the size of the lattice to 1.20 by 1.20 km. It is more efficient for this modeling of scattering by a thin sheet to actually restrict the lattice points to trace the depth of the sheet rather than specifying a regular three-dimensional Cartesian lattice which would have many zero valued nodes. For the

A shot point, the lattice ranged from 0.6 to 1.8 km in the east-west direction, the complete width of the map, but only from 0.5 to 1.7 km in the north-south direction. Similarly, the lattice for the zero offset source ranged from 0.8 to 2.0 in the north-south direction. Utilizing a discretization in the two horizontal directions of 0.020 km, this results in a three-dimensional lattice of 61 by 61 by 1 points mapping the H marker. Other forms of data analysis were unable to specify a thickness for the hypothetical fracture zones, though various estimates ranged from 0.010 to 0.060 km. We therefore set the thickness of the lattice to be 0.020 km. A source pulse for both the zero and A offsets was applied by choosing the waveform recorded as a first arrival on representative traces with good signal to noise ratio. Final synthetic seismograms should therefore be directly comparable to the field observations.

By trial and error forward modeling, it was determined that a model consisting of three fractured horizons could account for the observations. This was accomplished by temporarily neglecting amplitude effects and matching only the arrival times of the observed data. The depth and shape of the first of the zones, the H1 event, was left to conform to the map in Figure 4-28C, since it was obtained by the regional three-dimensional survey. The second and third zones, the H2 and H3 events, were defined to have the same lateral variation as shown in Figure 4-28C, but deeper by 0.090 and 0.170 km, respectively. Our analysis therefore confirms a total thickness of the H marker on the order of 0.200 km. It should be noted that the largest amplitudes of the scattered waves in Figure 4-31 correspond to the arrivals from the H2 and H3 horizons, in agreement with some other regional observations (Batini et al., 1990).

After using these initial stages of modeling to define the depths of the H1, H2 and H3 markers, we developed a model to account for the differing strengths of the recorded scattered waves from the two offsets by considering the regions imaged by the two experiments. In Figures 4-33 and 4-34, we present contour maps of the total travel time from source to lattice point on the H2 marker and back to receiver for two pairs of receivers at equivalent well positions. The dot in the interior of each plot

indicates the minimum time, which corresponds to the Fermat's principle true travel time for the reflected pulse. The contour interval for these plots was chosen so that each contour outlines a Fresnel zone. Sherriff and Geldart (1982) define the Fresnel zone such that the distance from source to scattering surface is a quarter wavelength larger for the outer edge of the zone than from the inner edge. Using the dominant frequency for these data of 30 Hz and the medium velocity of 5.1 km/sec, this distance corresponds to a travel time difference of 0.0083 sec. Since most of the effect of the scattering surface is from that region enclosed within the first Fresnel zone, these figures allow a simple determination of the region of the H2 marker observed in the two VSP experiments.

Comparison of Figures 4-33A and 4-34A for receivers at the shallow region of the data and Figures 4-33 and 4-34 from the deep portion shows that the A offset survey is imaging a region of the H marker several hundred meters further to the north than the zero offset shot point, though the imaging point for the deeper A offset receiver (Figure 4-34B) approaches that for the shallow zero offset receiver (Figure 4-33A). We developed a model assuming that the velocity variations at these markers are due to fracturing and that there must be some larger velocity perturbations towards the north, towards shot point A. After attempting several models, an isotropic model was developed which satisfactorily explains the data. The crack density in the H1 marker, which is weak in both data sets was set to 0.004 uniformly, whereas for the H2 and H3 markers, crack density was set to 0.14 north of the 1.4 km line, and 0.004 south of this border. Temperature and pressure conditions at the depth of the H marker are very uncertain, but other wells suggest that values of about 300°C and several hundred bar pressure are appropriate (Batini et al, 1983). Under these conditions, the bulk modulus of the pore filling fluid can probably be roughly estimated as 0.1 GPa (Anderson and Whitcomb, 1973). The resulting perturbations to Lamé parameters are shown in Table 4.6, and the synthetic seismograms, processed exactly as were the data, in Figure 4-35. In order to more clearly show the match with the observations,

we present in Figure 4-36 the result of subtracting the synthetic results from the observed data. The A offset synthetic removes a significant portion of the signal from the observed data (Figure 4-36B), and so we infer that our model adequately accounts for the seismic properties in the region imaged by the A source. The quality of the fit of the zero offset synthetic is less satisfactory, however, which is at least in part a consequence of the lower signal to noise ratio for the weak scattered wave in this data set. At least part of the signal, especially from traces 55 to 65, is still relatively well modeled.

Although some observations from other wells have suggested that vertical fractures are present in the H marker, the successful match of data and synthetic seismograms, particularly for the A offset data, suggests that a purely isotropic model can account for these seismic observations. The synthetic examples shown above for the explosion source clearly demonstrate that in any case a compressional wave experiment will not yield any information allowing a unique interpretation of the presence of vertical fractures, the only difference from the isotropic case being a weaker reflected wave. We did attempt to develop a model for the H marker using the elastic constant perturbations appropriate for vertical fractures, but even a crack density as high as 0.30 yielded a signal for the A offset synthetics which was far weaker than the observed data. This crack density is already so high that it likely violates the single scattering assumption used in the derivation of the expressions for the effective elastic constants, so we did not test any higher values. Instead, we interpret these results as suggesting that the principle source of the scattered seismic energy is an isotropic velocity change which may have some weak anisotropy superimposed due to vertical fractures. The available data does not allow any further conclusions, and, as shown in the synthetic examples, shear wave observations would be necessary to uniquely determine the presence of anisotropy due to vertical fractures.

4.6 Discussion and Conclusions

The Ray-Born method for the modeling of the effects of small, localized regions of inhomogeneity on seismograms is very general and can in principle be applied to fully anisotropic models. Limitations on the ray theoretical aspects of the algorithm result from the well known assumption of high frequency methods, namely, that the wavelength of the propagating signal must be much less than the scale length of the background earth model (Ben-Menahem and Beydoun, 1985). Comparisons of Ray-Born solutions with the complete, discrete wavenumber solution for the elastic wave scattering from a spherical inhomogeneity illustrate some of the limitations of the Born approximation. The principal restriction is also one of scale lengths. As the ratio of the propagating wavelength to the scale length of the inhomogeneity decreases below a value of about 5, the Born approximation fails to reproduce some significant features of the scattered waves. For the sphere, the missing features were the dual reflections from the front and back of the sphere in the back scattering direction (Figures 4-5, 4-6, 4-7 and 4-8). The Ray-Born solution predicted only a single, broad pulse.

With these limitations in mind, we applied the method to synthetic studies of a thin, laterally extended fracture zone in a simple layered earth model (Figure 4-12). These synthetic results clearly demonstrate that shear waves can be expected to provide very useful information on the alignment direction of vertical fractures, as the scattered wavefield varies significantly with the polarization direction of the incident shear wave. In particular, if the incident SH-wave is polarized at an angle to the fracture orientation, the scattered wavefield can have significant energy on the radial component. This effect, especially when combined with the variation of the observations with different incident polarizations, is not likely to be reproduced by any realistic isotropic inhomogeneity in similar earth models.

The synthetic models also show that compressional wave scattering has different utility. Though the P-waves are essentially insensitive to the orientation of vertical

fractures (Figures 4-19, 4-21 and 4-23), the amplitude of the scattered wavefield varies dramatically with pore fluid. Large reflected P-waves are to be expected for gas-filled fractures, while water-filled fractures will lead to minimal scattering. In contrast, shear wave scattering is almost unaffected by the fracture contents.

These guidelines aid in interpretation of the VSP data from the Badia 1A well in the Italian Lardarello geothermal field. We successfully developed an isotropic model of three fracture zones contributing to the seismic H marker, accounting for observed reflected waves from below the depth of the well. The model implies that fracture density increases northwards and that this would be a good direction for further exploratory drilling in development of the geothermal resources.

There are, however, several ambiguities in the modeling which cannot be removed due to limitations on the available data. For example, we cannot absolutely rule out the presence of aligned, vertical fractures in the H marker since P-wave scattering from a vertically fractured region shows no indication of fracture orientation. Comparison of synthetic models for isotropic and anisotropic fracture zones of equal crack density (Figures 4-17 and 4-19) shows that the amplitude of the observed P-waves should be reduced for the anisotropic model. The large scattered field in the A offset data was not reproducible with realistic crack densities, which does give an indirect evidence for non-vertical fractures in this region. An ambiguity in the Ray-Born modeling of fracture zones that enters here is that of the state of the pore fluids. We applied a value for bulk modulus of the fluid based on some values representative for the estimated *in situ* conditions. It is possible, however, that there is some error in the bulk modulus value. If it is significantly overestimated, the effects of the fractures will be more like those of the synthetic gas-filled fracture models with non-zero bulk modulus of pore fluid and P-wave scattering amplitudes will increase for a given crack density. This might make it possible to develop an anisotropic model accounting for the field data.

Another area of ambiguity is that of the equivalent effects of increased fracture

zone thickness and increased fracture density. Due to the linearity of the method and our representation of the scattering lattices as only a single unit cell in the vertical direction, a doubling of the thickness of the unit cell results in a doubling of the scattered wavefield (equation 4.9). The same effect results from a doubling of the perturbations to elastic constants. Our assumed value of 0.020 km for the thickness of the three fractured intervals H1, H2 and H2 is of the same order of size as other estimates (Batini et al., 1990), but could very well be off. At the same time, the successful modeling of the observed data, especially for source offset A, suggests that our model of the zones as a single lattice point in thickness is not far off and that the zones are not too thick.

It is possible that both isotropic heterogeneity and superimposed vertical fracturing are present. In this active geothermal area, ongoing hydrothermal processes will likely cause mineral alteration and the sealing of many fractures (Batini et al., 1983; Batini et al., 1985c). Under these conditions, the properties of the rock across the fractured regions could well be altered in such a way that a superposition of anisotropic fracturing and isotropic velocity variations is not so unrealistic. An increase in porosity due to pores of large aspect ratio would change density proportionately more the elastic properties and would lead to isotropic scattering of elastic waves. It does appear from the modeling of the P-wave data that the velocity variations are not entirely due to vertical fracturing in any case, and a completely isotropic model can explain the data. The only way to concretely determine the presence or absence of anisotropy would be to obtain high quality shear wave data from the same localities.

Similar conclusions regarding the information contained in seismic data were obtained by Stolt and Weglein (1985) in an analysis of multiparameter, linearized inversion methods. Due to the physics of wave propagation and limitations on observed quantities from experimental configurations, signal to noise ratio, and the deep exploration targets, it may only be possible to achieve some knowledge of the location in depth or time of heterogeneity. Increasingly ambitious goals under better conditions

or more elaborate experiments include: (1) the sign of the property changes in the heterogeneous zone, (2) the magnitude of the changes, (3) lateral variations of data amplitudes allowing more detailed analysis, (4) inference of multiple physical properties, and (5) true values of all earth properties. Clearly the last goal is only going to be achievable in extremely rare cases. The analysis of the properties of scattered wavefields from fractured zones shows that to achieve anything but the first two or three goals requires very good quality seismic data and must incorporate shear wave observations. Therefore, given that only compressional wave data of relatively low signal to noise ratio was available, the Ray-Born method allowed some very useful information on the positions both vertically and laterally of some changes in earth properties.

Our models of both synthetic and field data emphasize the utility of the Ray-Born method for modeling scattered wavefields in complicated three-dimensional geological structures. Although there is non-uniqueness in relating amplitude to fracture density and fracture zone thickness, the model for the Badia 1A data does do well in predicting the kinematic properties of the scattered waves. It should therefore give concrete and valuable information on the depths of the fracture zones. This type of information is of great utility in geothermal field development. Especially for large three-dimensional problems, the method is a comparatively rapid and efficient means of exploring the effects of different models of small scale heterogeneity within the earth. The results also clearly show the value of shear wave observations in detailed resolution of subsurface seismic properties, particularly for the resolution of anisotropy.

Parameter	Background Value (GPa)	Perturbation (GPa)
λ	21.49	-8.34
μ	11.86	-1.49

Table 4.1. Background Lamé parameters and perturbations for the fracture zone in the model in Figure 4-12 with randomly oriented, gas-filled fractures.

Parameter	Background Value (GPa)	Perturbation (GPa)
C_{11}	45.21	-18.6
$C_{22} = C_{33}$	45.21	-4.19
C_{23}	21.49	-4.19
$C_{13} = C_{12}$	21.49	-8.80
C_{44}	11.86	0.0
$C_{55} = C_{66}$	11.86	-2.29

Table 4.2. Background elastic constants and perturbations for the fracture zone in the model in Figure 4-12 with gas-filled vertical fractures oriented perpendicular to the receiver array. The parameters C_{11}, C_{22}, and C_{33} are all equivalent to $\lambda + 2\mu$ in an isotropic medium, while $C_{12} = C_{13} = C_{23} = \lambda$ and $C_{44} = C_{55} = C_{66} = \mu$.

Parameter	Background Value (GPa)	Perturbation (GPa)
$C_{11} = C_{33}$	45.21	-4.19
C_{22}	45.21	-18.6
C_{13}	21.49	-4.19
$C_{23} = C_{12}$	21.49	-8.80
C_{55}	11.86	0.0
$C_{44} = C_{66}$	11.86	-2.29

Table 4.3. Background elastic constants and perturbations for the fracture zone in the model in Figure 4-12 with gas-filled vertical fractures oriented parallel to the receiver array.

Parameter	Background Value (GPa)	Perturbation (GPa)
$C_{11} = C_{22}$	45.21	-12.4
C_{33}	45.21	-4.19
$C_{13} = C_{23}$	21.49	-6.50
C_{12}	21.49	-7.80
$C_{44} = C_{55}$	11.86	-1.15
C_{66}	11.86	-1.29
$C_{16} = C_{26}$	0.0	3.60
C_{36}	0.0	2.31
C_{45}	0.0	1.15

Table 4.4. Background elastic constants and perturbations for the fracture zone in the model in Figure 4-12 with gas-filled vertical fractures oriented at 45° to the receiver array. In an isotropic medium or in a transversely isotropic material in a coordinate system where one of the coordinate axes parallels the axis of symmetry, C_{16}, C_{26}, C_{36}, and C_{45} are all zero.

Parameter	Background Value (GPa)	Perturbation (GPa)
λ	21.49	-0.836
μ	11.86	-1.01

Table 4.5. Background elastic constants and perturbations for the fracture zone in the model in Figure 4-12 with randomly oriented, water-filled fractures.

Crack density	Parameter	Background Value (GPa)	Perturbation (GPa)
$\xi = 0.14$	λ	23.6	-3.33
	μ	23.6	-3.33
$\xi = 0.004$	λ	23.6	-0.10
	μ	23.6	-0.10

Table 4.6. Background Lamé parameters and perturbations for the fracture zone model for the Badia location H markers. The marker H1 marker was assigned a crack density of 0.004 throughout the model, whereas the computed synthetics applied a crack density of 0.14 to the H2 and H3 markers north of the 1.4 km latitudinal line (Figure 4-28).

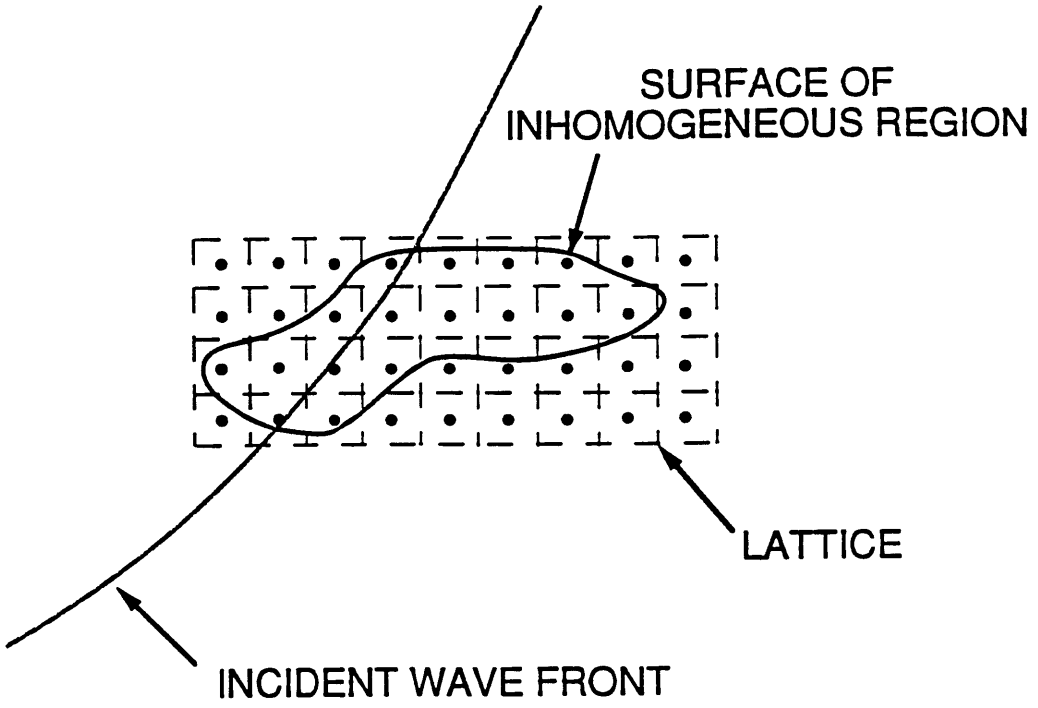

Figure 4-1: Discretization scheme for implementation of the Ray-Born algorithm. A two-dimensional example is shown for clarity, though the actual implementation includes three-dimensional scattering lattices and background models. All lattice points outside the boundary of the inhomogeneity are assigned zero perturbation values, while those points inside the boundary can be assigned non-zero perturbations to density or any of the elastic constants C_{IJ}. As the incident wavefront encounters a lattice point, that particular point becomes a secondary source.

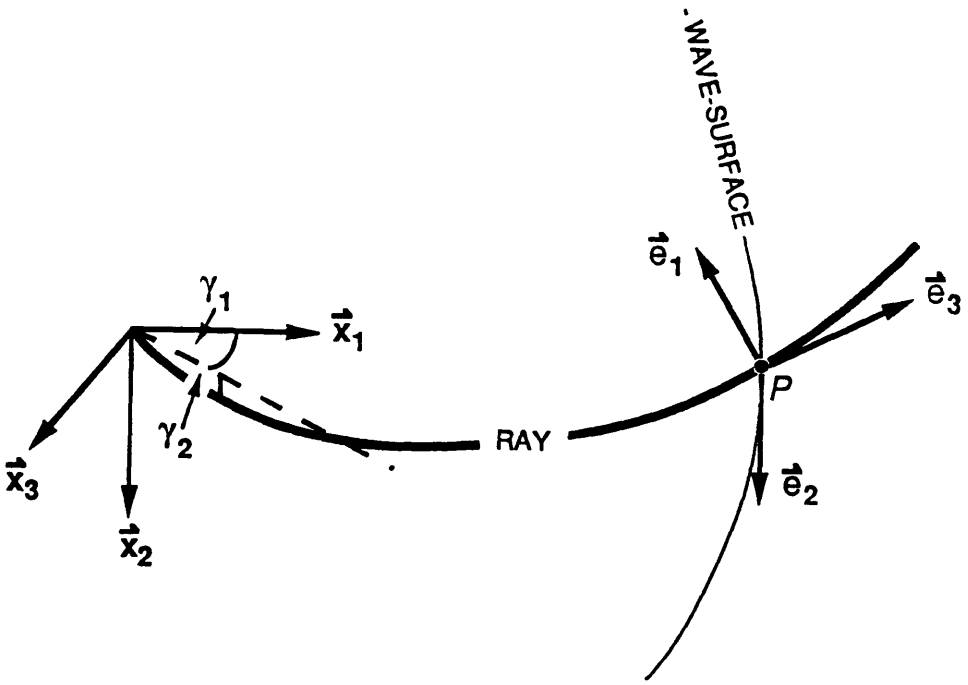

Figure 4-2: Diagrammatic illustration of the ray coordinates γ_1 and γ_2 and ray-centered coordinate basis vectors $\mathbf{e}_1$, $\mathbf{e}_2$, and $\mathbf{e}_3$. The ray coordinates correspond to the azimuthal and declination take-off angles, γ_1 and γ_2, respectively. At each point P on the ray, the two basis vectors $\mathbf{e}_1$ and $\mathbf{e}_2$ are located in the plane tangent to the wavefront, while the third vector $\mathbf{e}_3$ is tangent to the ray, forming a right-handed coordinate system valid in the vicinity of the ray (Červený, 1985).

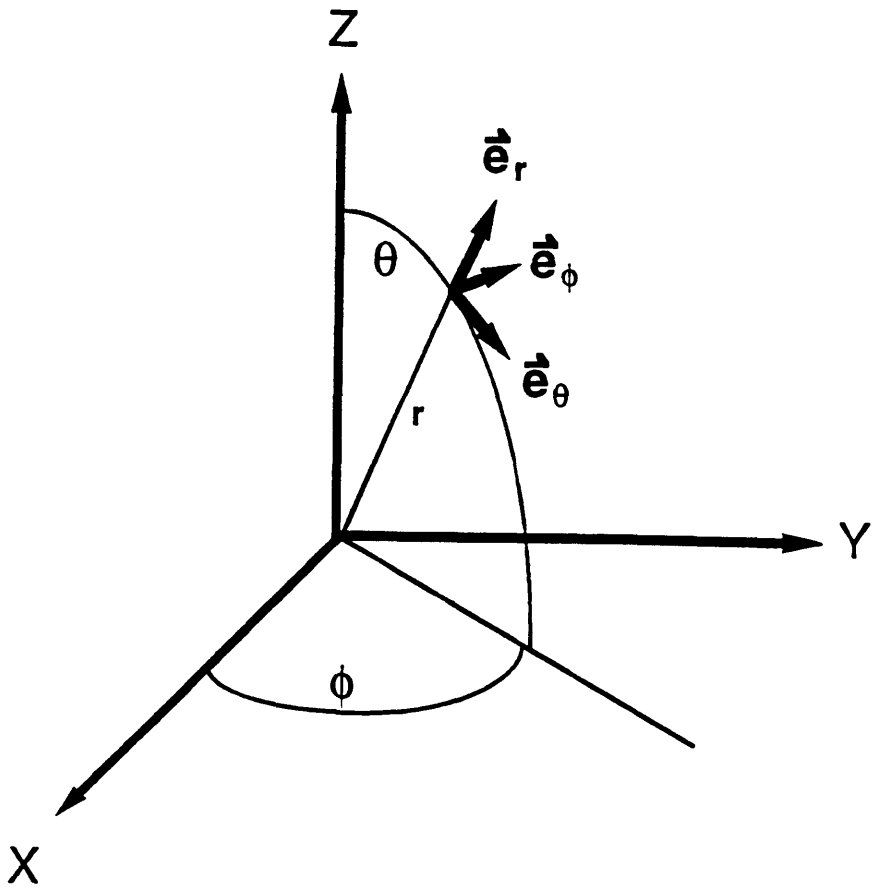

Figure 4-3: Spherical coordinate system. The scattered wavefields from the elastic sphere are calculated for receiver distances sufficiently distant that the P-wave displacement will be observed entirely on the radial component $\mathbf{e}_r$ and the S-wave will appear only on the $\mathbf{e}_\theta$ component. The shear wave has only a $\mathbf{e}_\theta$ component due to the symmetry of the problem for a plane P-wave incident along the z axis.

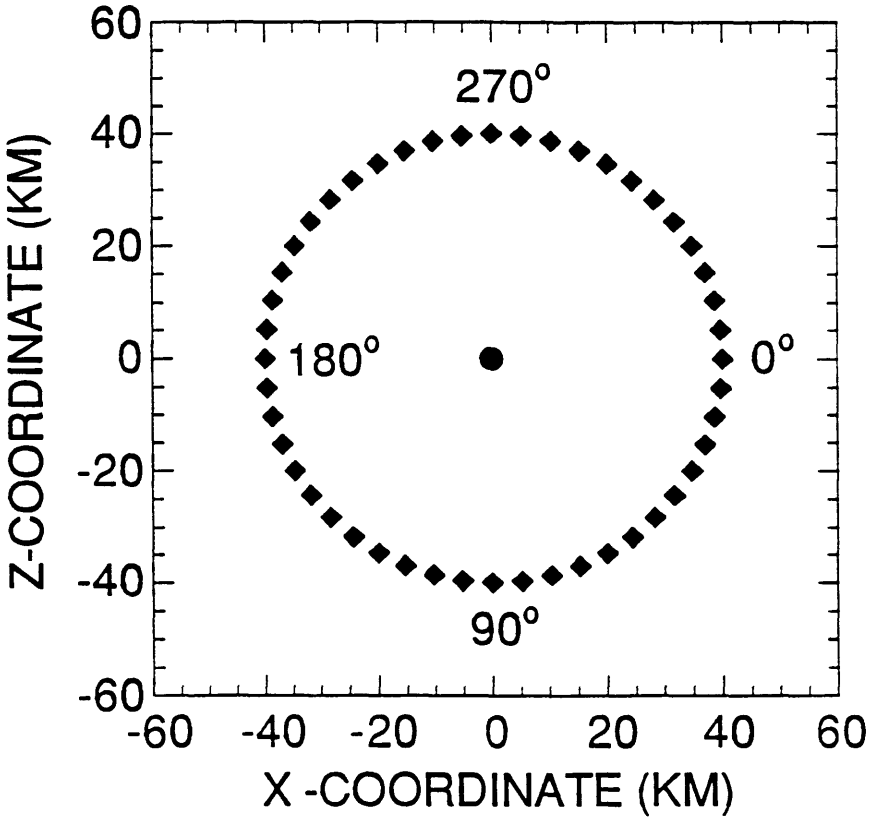

Figure 4-4: Receiver configuration for the computation of wavefields scattered from an elastic sphere. The sphere is located at the origin of the coordinate system and the incident plane P-wave is propagating in the downwards vertical direction so that the direction 90° corresponds to forward scattering, and 270° is the direction for back scattered waves. The angles given here are equal to the angular coordinate θ in Figure 4-3 minus 90° and are used for reference in the synthetic seismogram plots.

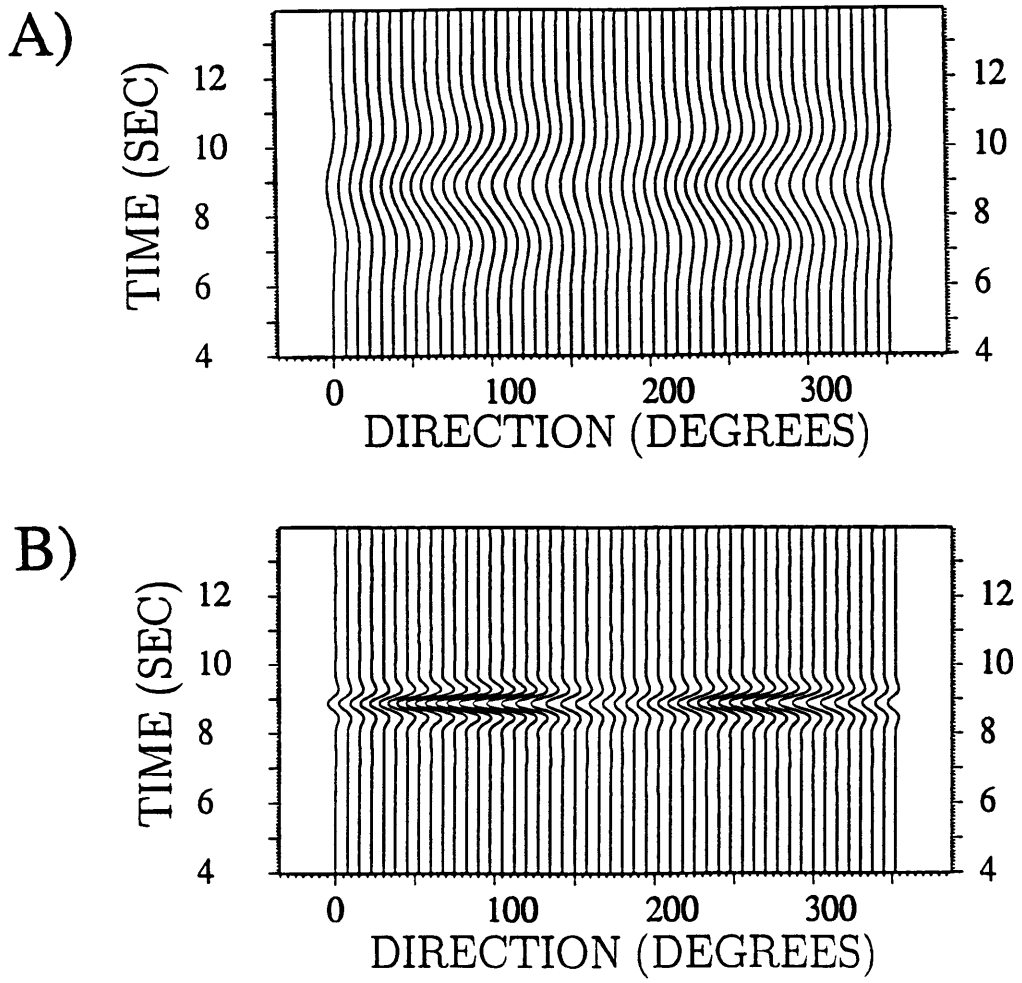

Figure 4-5: Ray-Born radial component synthetic seismograms for the scattering from a compressional plane wave vertically incident on a sphere showing scattered compressional waves. Since the amplitudes of the scattered waves increase dramatically with increasing frequency, the scale of the different plots was changed to allow the different waveforms to be observed. A) Ratio of compressional wavelength to sphere diameter $\eta_p = 18$, frequency $f = 0.25$ Hz. B) $\eta_p = 4.5$, $f = 1$ Hz. Plotting scale multiplied by 0.1 relative to the $\eta_p = 18$ plot.

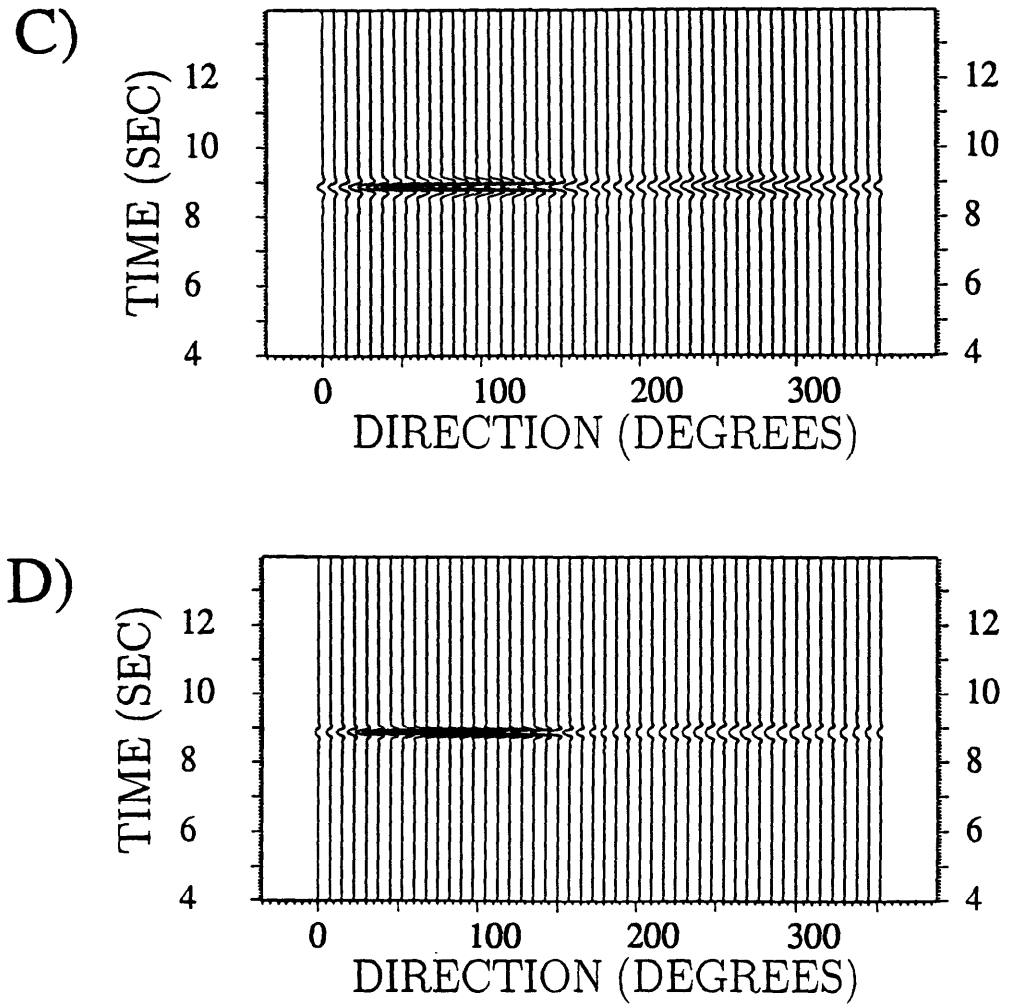

Figure 4-5: C) $\eta_p = 1.8, f = 2.5$ Hz. Plotting scale multiplied by 0.02 relative to the $\eta_p = 18$ plot. D) $\eta_p = 0.9, f = 5$ Hz. Plotting scale multiplied by 0.01 relative to the $\eta_p = 18$ plot.

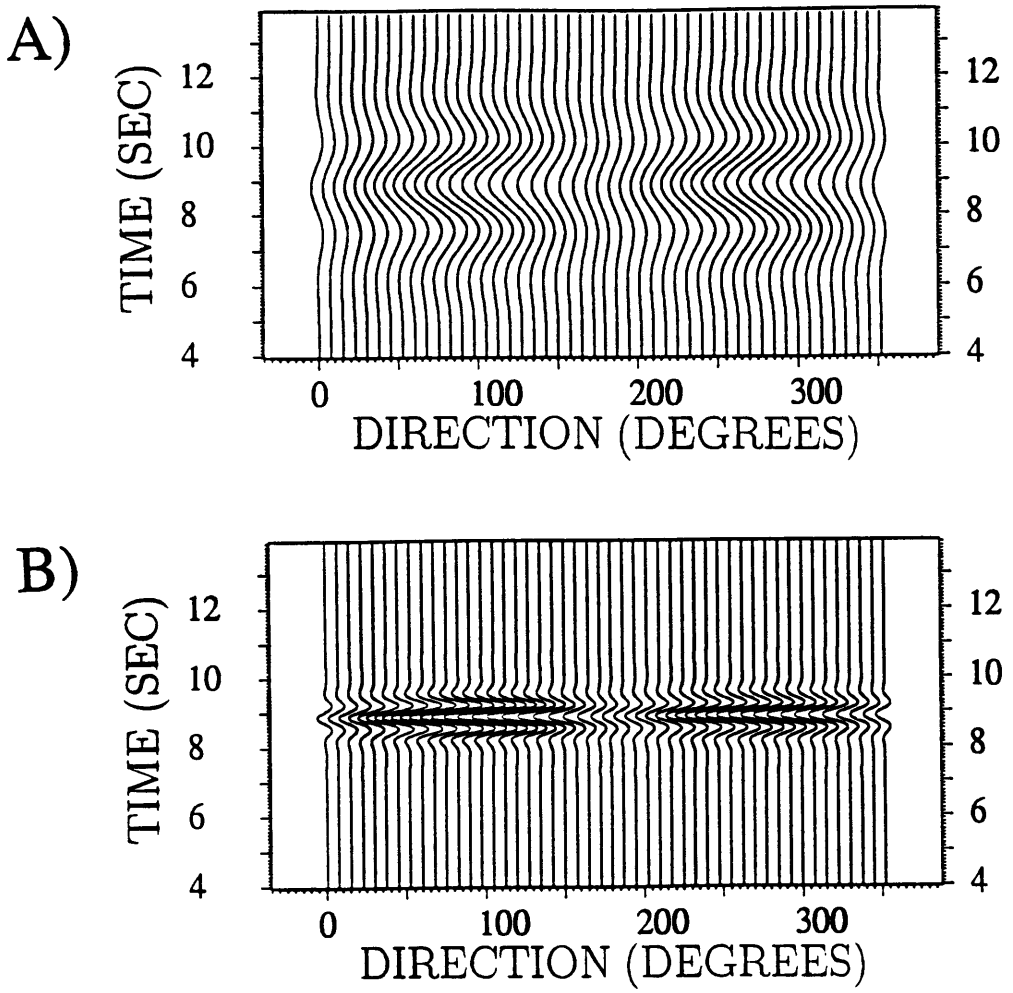

Figure 4-6: Discrete wavenumber radial component synthetic seismograms for the scattering from a compressional plane wave vertically incident on a sphere showing scattered compressional waves. All plot scales for a given frequency are the same as in Figure 4-5 so that waveforms may be directly compared for the Ray-Born and discrete wavenumber methods. A) Ratio of compressional wavelength to sphere diameter $\eta_p = 18$, frequency $f = 0.25$ Hz. B) $\eta_p = 4.5$, $f = 1$ Hz.

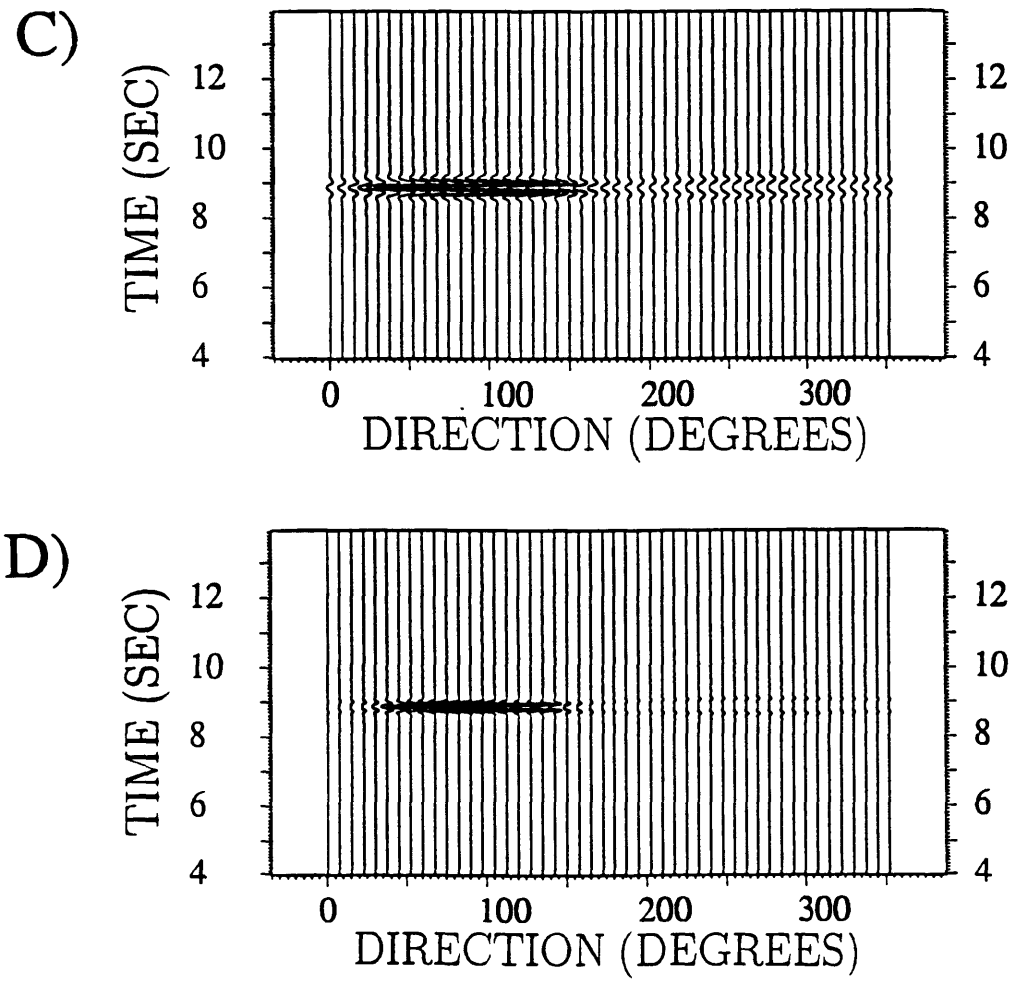

Figure 4-6: C) $\eta_p = 1.8, f = 2.5$ Hz. D) $\eta_p = 0.9, f = 5$ Hz.

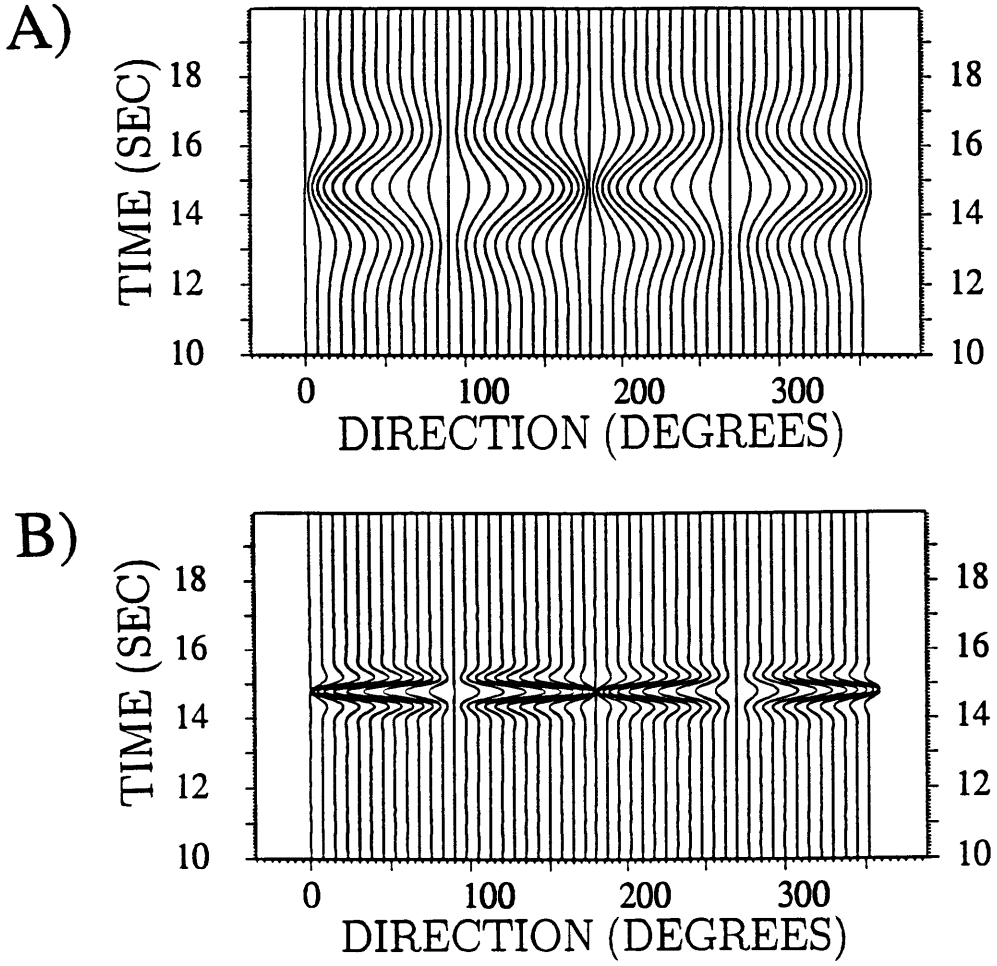

Figure 4-7: Ray-Born theta component synthetic seismograms for the scattering from a compressional plane wave vertically incident on a sphere showing scattered shear waves. All plot scales are the same as those applied in Figure 4-5, so that the waveforms from the Ray-Born and discrete wavenumber solutions may be directly compared for amplitudes for both shear and compressional wave scattering. A) Ratio of compressional wavelength to sphere diameter $\eta_p = 18$, frequency $f = 0.25$ Hz. B) $\eta_p = 4.5$, $f = 1$ Hz.

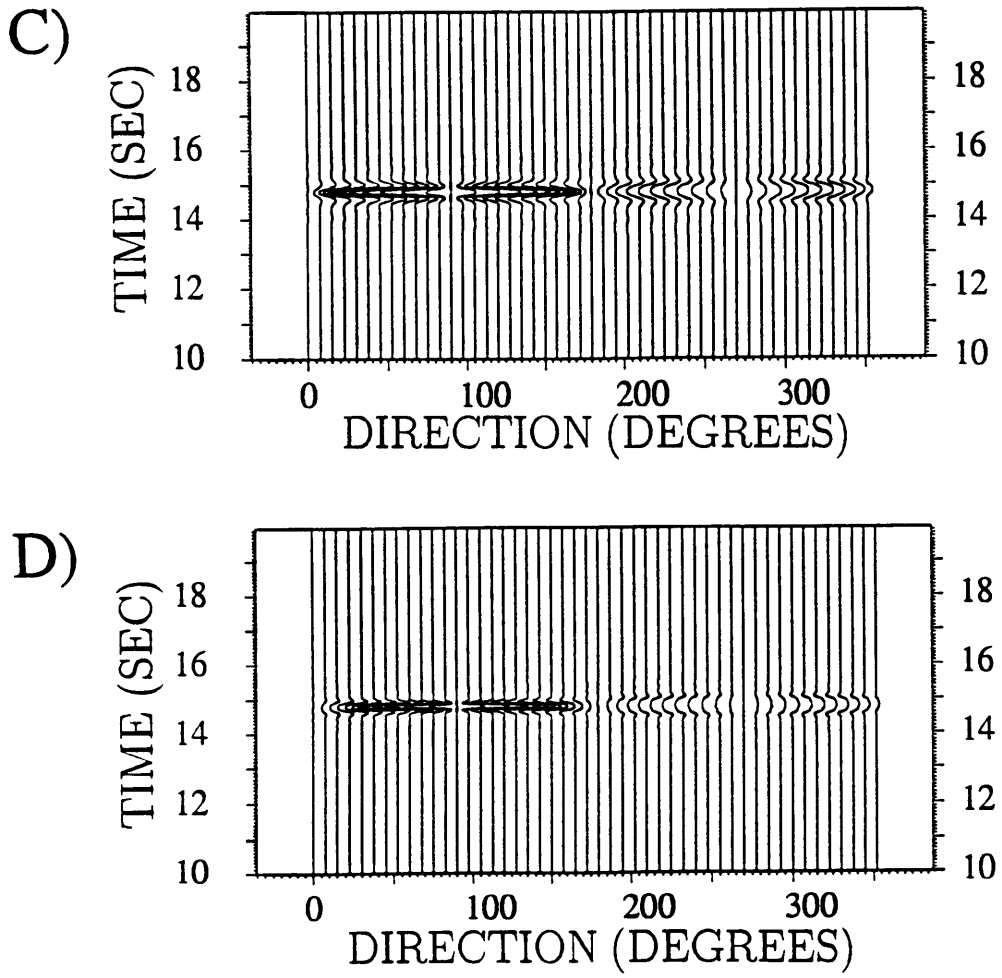

Figure 4-7: C) $\eta_p = 1.8, f = 2.5$ Hz. D) $\eta_p = 0.9, f = 5$ Hz.

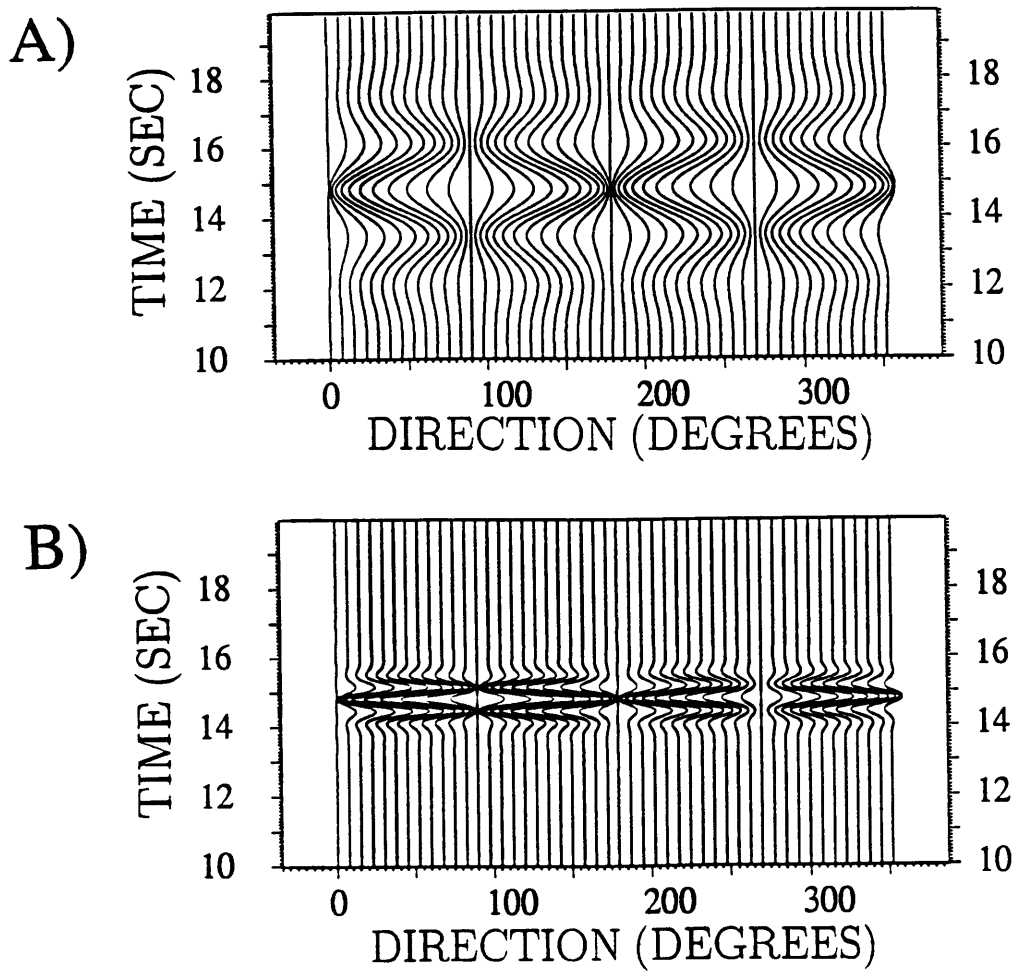

Figure 4-8: Discrete wavenumber theta component synthetic seismograms for the scattering from a compressional plane wave vertically incident on a sphere showing scattered shear waves. All plot scales for a given frequency are the same as in Figure 4-5 so that waveforms may be directly compared for the Ray-Born and discrete wavenumber methods and for shear and compressional wave scattering. A) Ratio of compressional wavelength to sphere diameter $\eta_p = 18$, frequency $f = 0.25$ Hz. B) $\eta_p = 4.5$, $f = 1$ Hz.

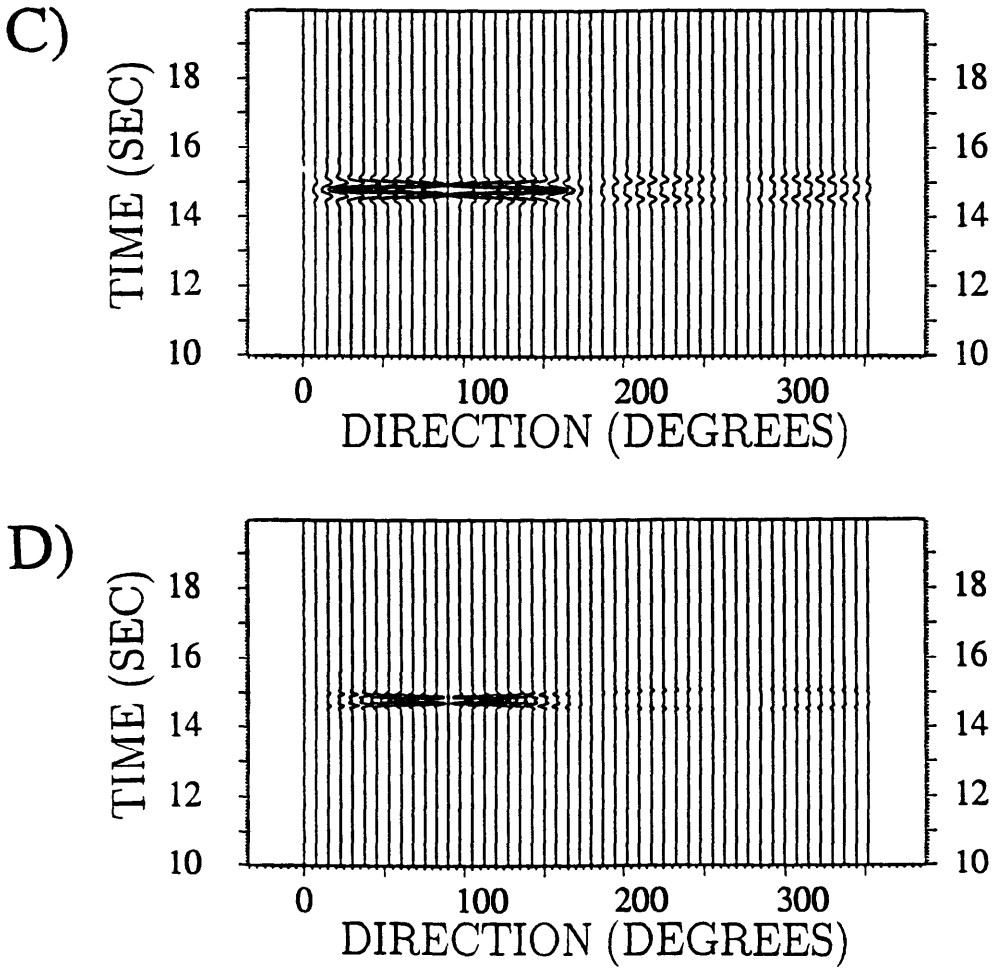

Figure 4-8: C) $\eta_p = 1.8, f = 2.5$ Hz. D) $\eta_p = 0.9, f = 5$ Hz.

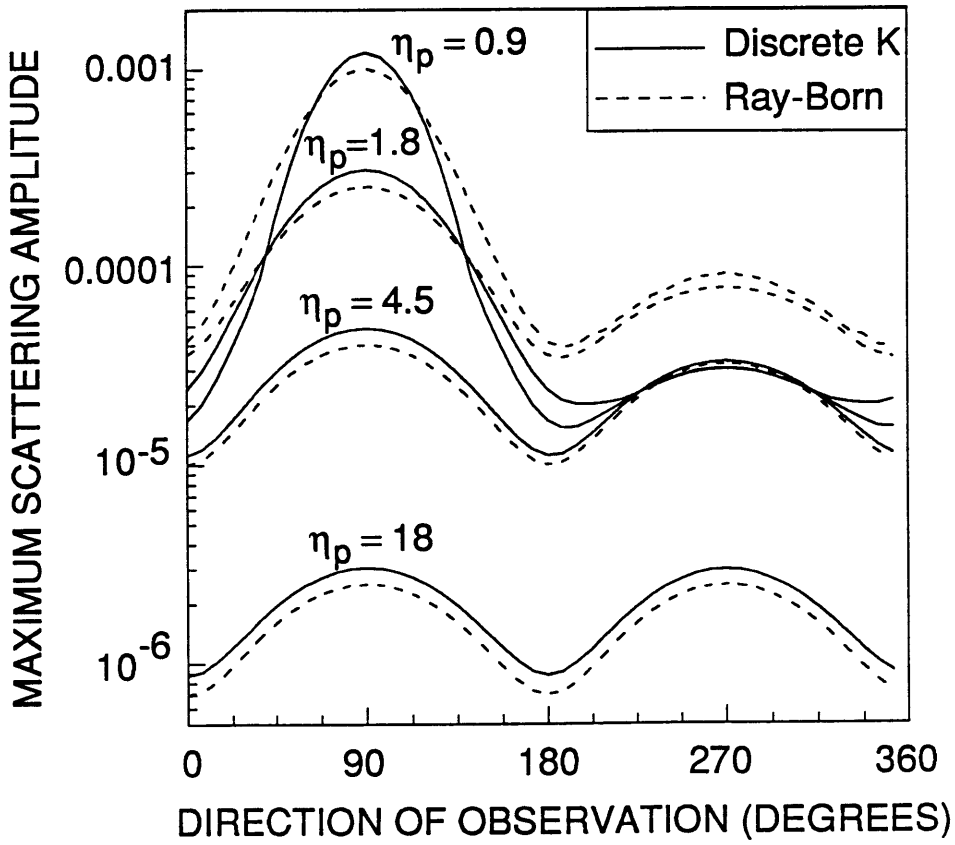

Figure 4-9: Comparison of the amplitudes of compressional waves scattered from the sphere with 1% velocity perturbations with different values of incident wavelength to sphere diameter ratio η_p indicated. Forward scattering is in the direction 90° and back scattering is at 270°.

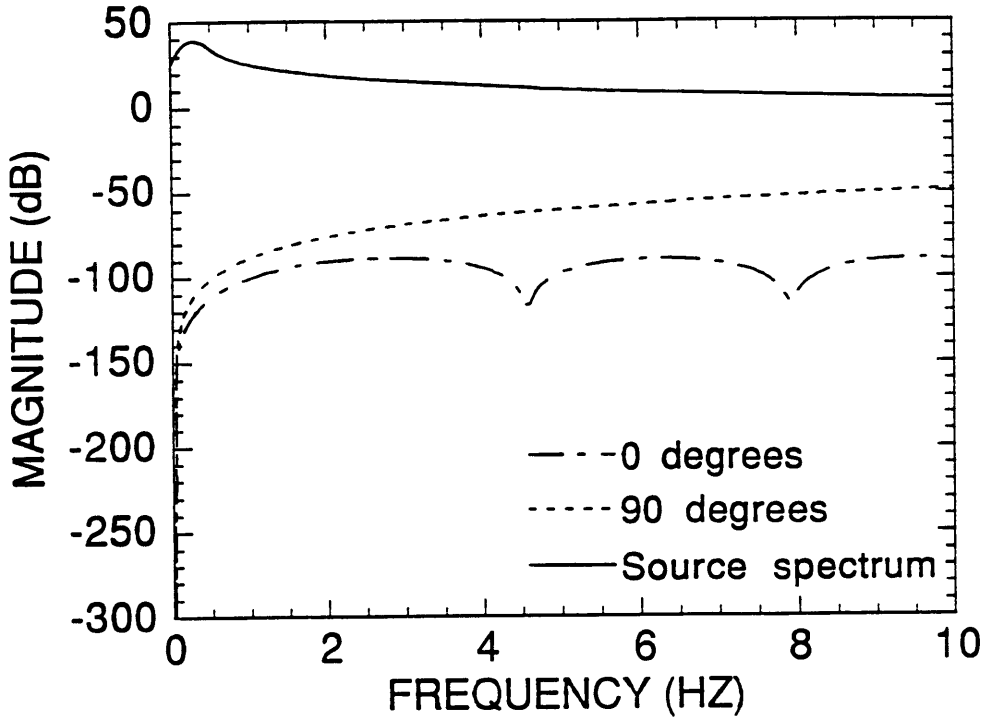

Figure 4-10: Comparison of the amplitude spectrum of the impulse response of the sphere and the amplitude spectrum of the incident wave at 0.25 Hz ($\eta_p = 18$). Dashed lines show impulse response spectra computed by the discrete wavenumber method for side scattering (0°) and forward scattering (90°) (Figure 4-4) . The solid line gives the impulse response of the incident wavelet. Convolution of the wavelet and impulse response, corresponding to multiplication of these frequency domain responses, yields the scattered waves. The rapid increase of the sphere impulse response with frequency near 0.25 Hz shifts the effective principal response frequency of the scattered waves to a slightly higher value. The result is a larger amplitude scattered wave than for simple Rayleigh scattering at 0.25 Hz due to the ω^2 dependence of the radiation patterns (see Appendix B).

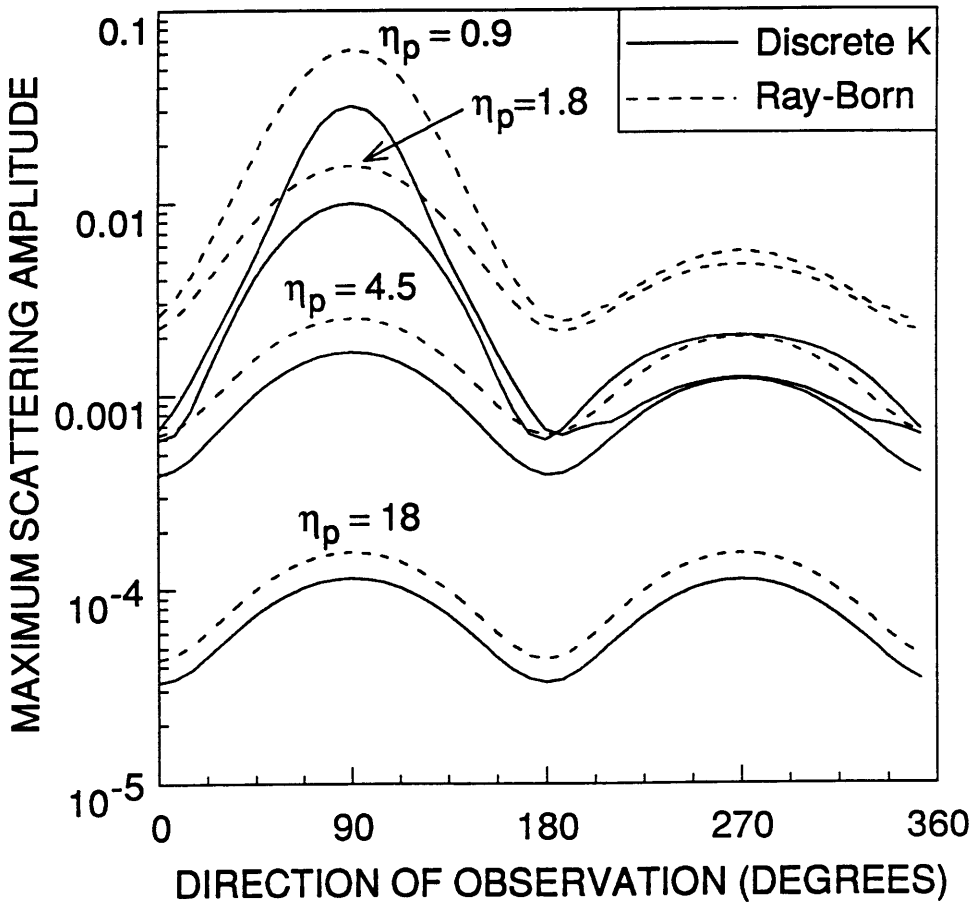

Figure 4-11: Comparison of the amplitudes of compressional waves scattered from the sphere with 50% velocity perturbations with different values of incident wavelength to sphere diameter ratio η_p indicated. Forward scattering is in the direction 90° and back scattering is at 270°.The error in the Ray-Born solution is only slightly worse than for the 1% inhomogeneity.

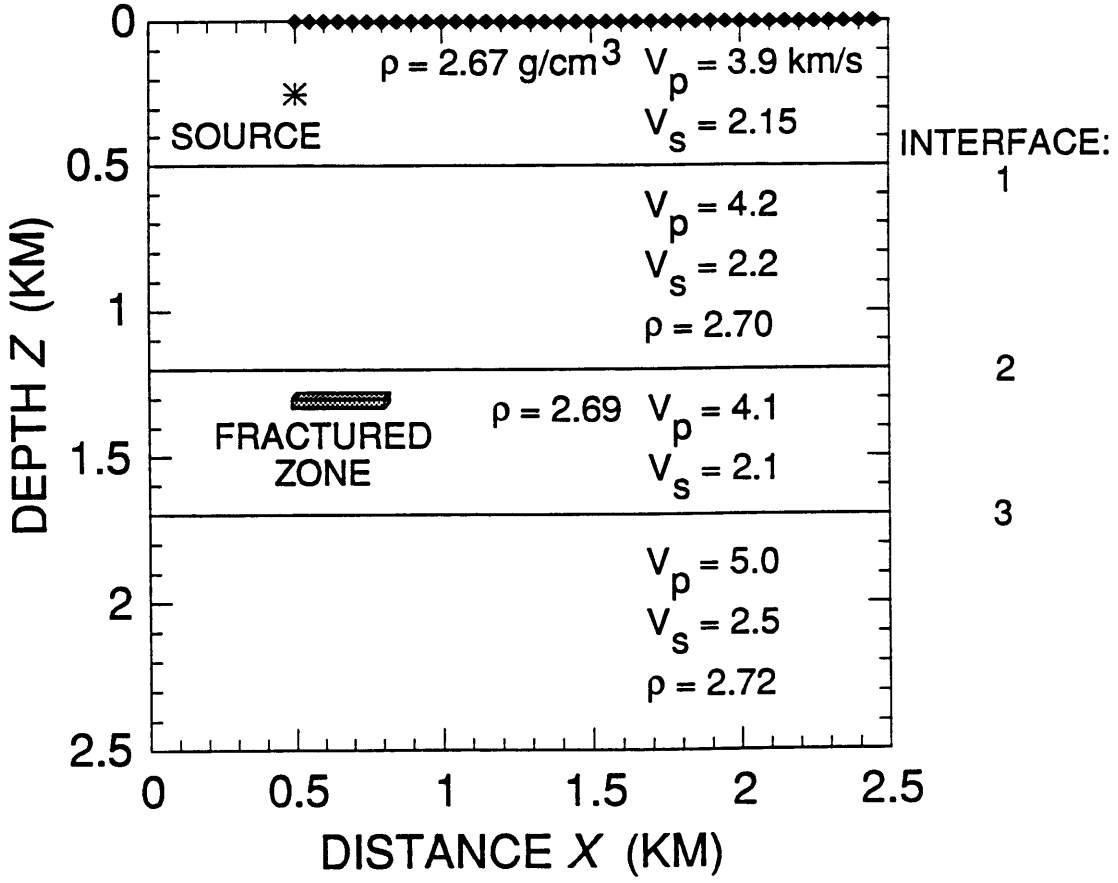

Figure 4-12: Background model used to calculate synthetic seismograms including the effect of a thin fracture zone. Receivers are indicated by the black diamond symbols, and the position of the source is shown. This model cross-section is contained in the $x - z$ plane, and the y axis is perpendicular to the figure.

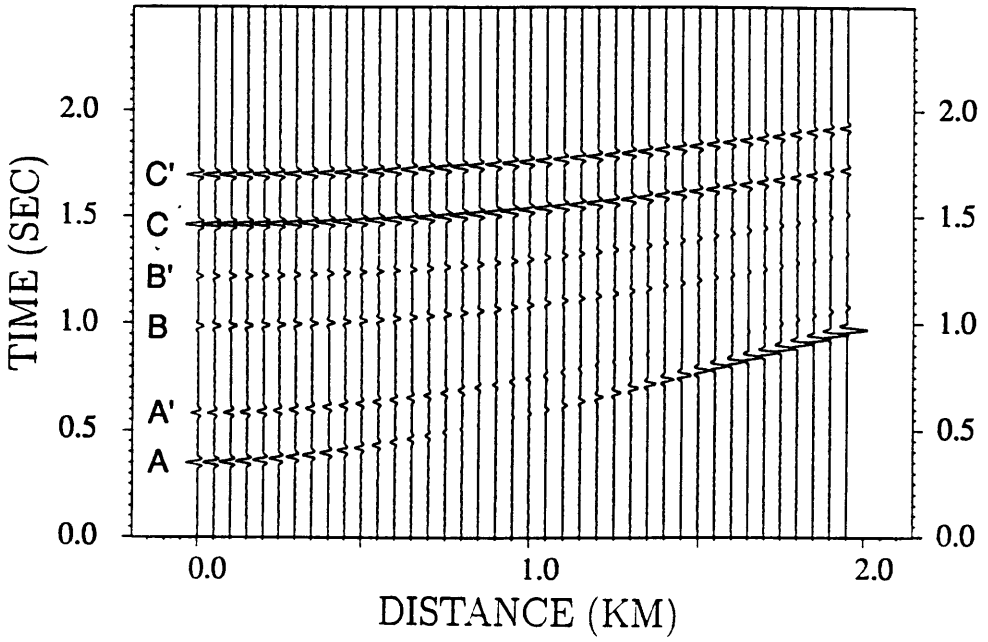

Figure 4-13: Transverse component background displacement field from a cross-line point source for the earth model shown in Figure 4-12. Since only SH-waves are radiated in this coordinate plane by the source vector, the radial and vertical component synthetic seismograms contain no signal. Main reflections are identified as follows (prime indicates free surface multiple): (A) S to S reflection from interface 1. (B) S to S reflection from interface 2. (C) S to S reflection from interface 3.

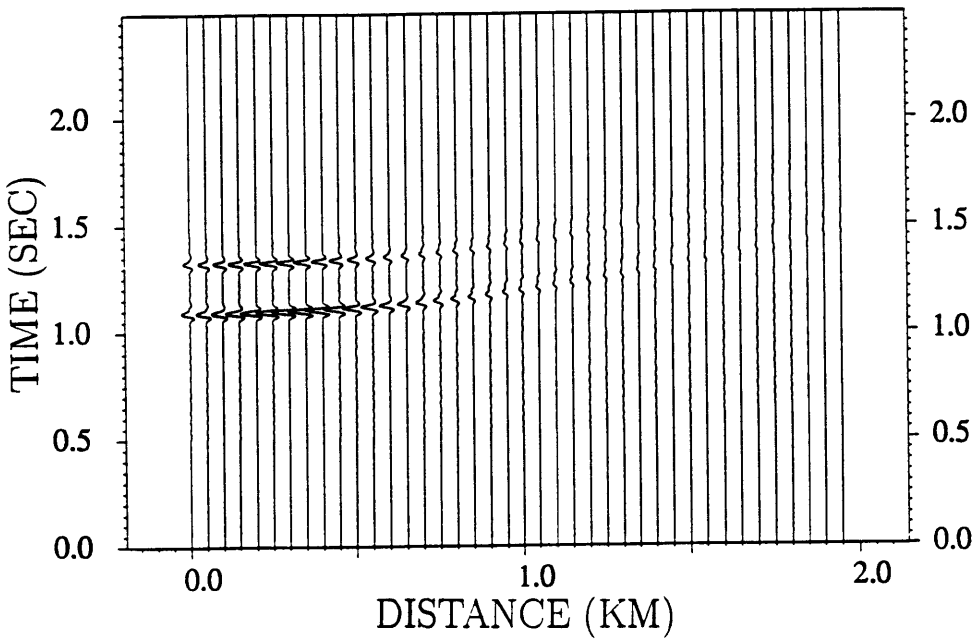

Figure 4-14: Transverse component scattered field from the cross-line source for the fracture zone containing isotropic, randomly oriented, and gas-filled fractures (Figure 4-12). These seismograms are plotted at a scale 2.5 times larger than Figure 4-13 to show the details of the scattered wave.

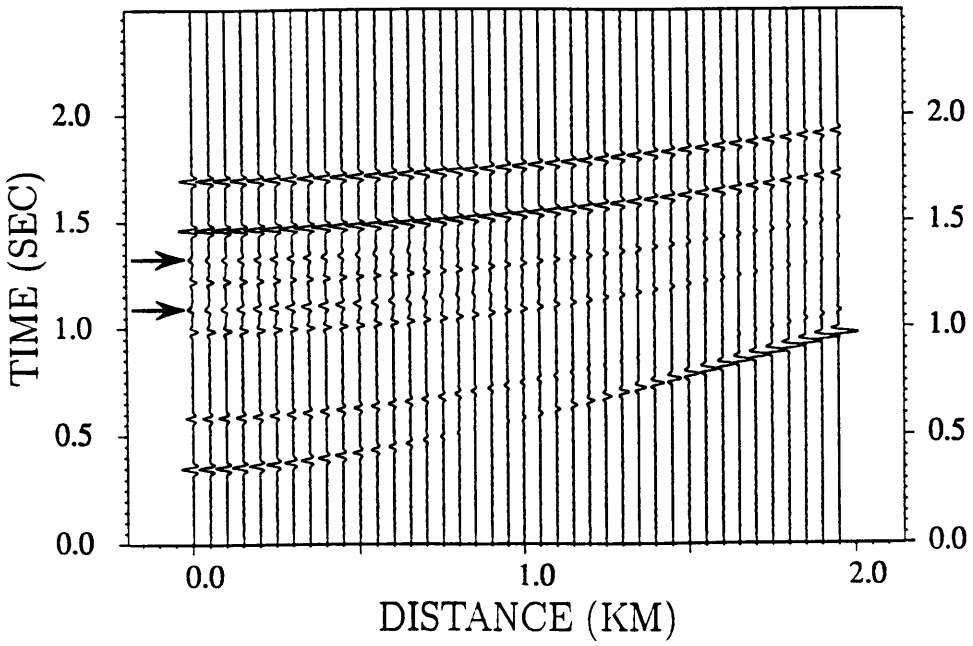

Figure 4-15: Transverse component total wavefield from the cross-line source for the fracture zone model in Figure 4-12 containing isotropic, randomly oriented, and gas-filled fractures. Arrows mark the positions of the scattered waves from the fracture zone, and main reflections from background model are identified in Figure 4-13.

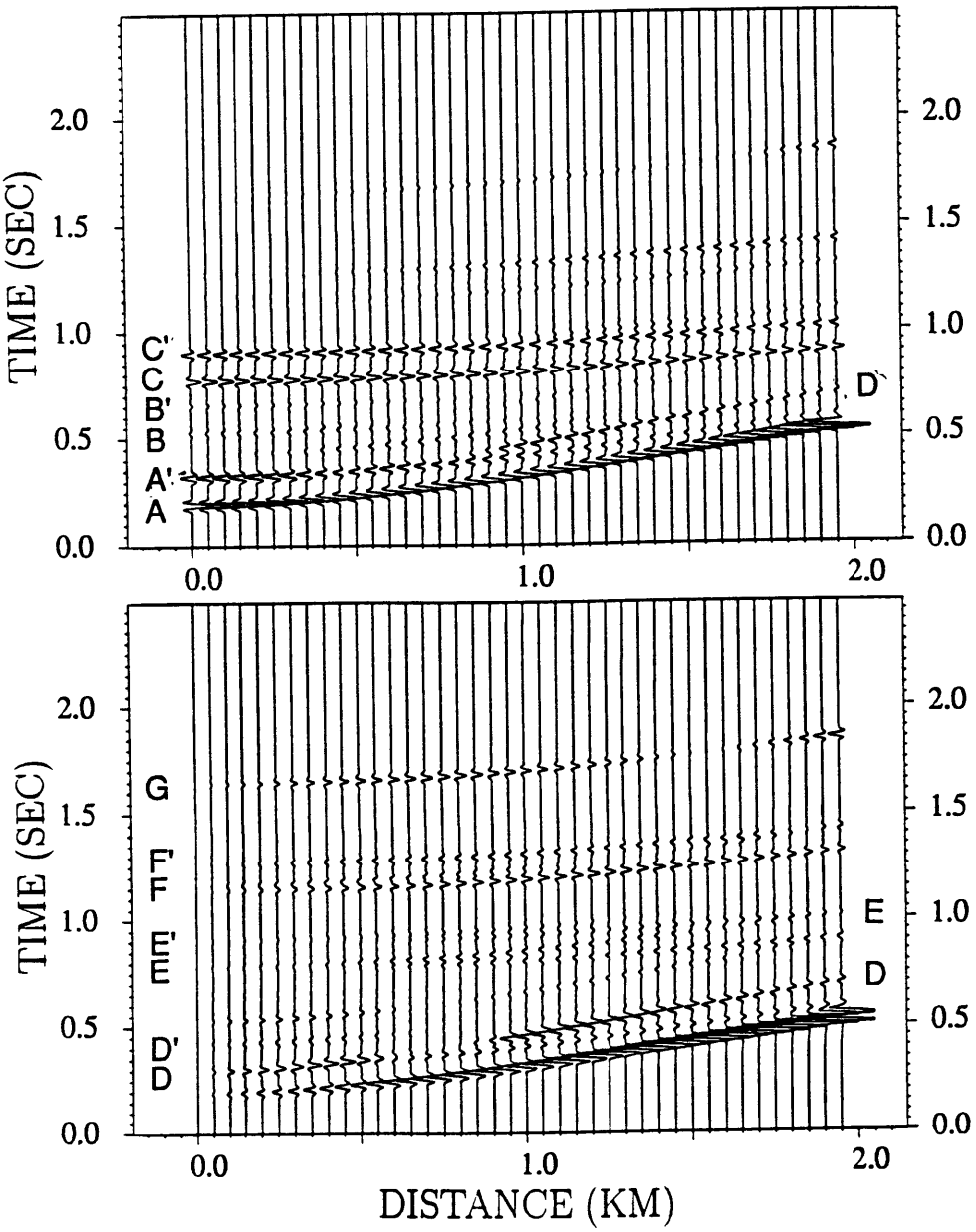

Figure 4-16: Vertical (above) and radial (below) component synthetic seismograms from an explosion source for the background model in Figure 4-12. The main reflections are identified as follows (prime indicates a free surface multiple): (A) P to P reflection from interface 1. (B) P to P reflection from interface 2. (C) P to P reflection from interface 3. (D) P to S reflection from interface 1. (E) P to S reflection from interface 2. (F) P to P reflection from interface 3. (G) P to S reflection at free surface, followed by S to S reflection at interface 3.

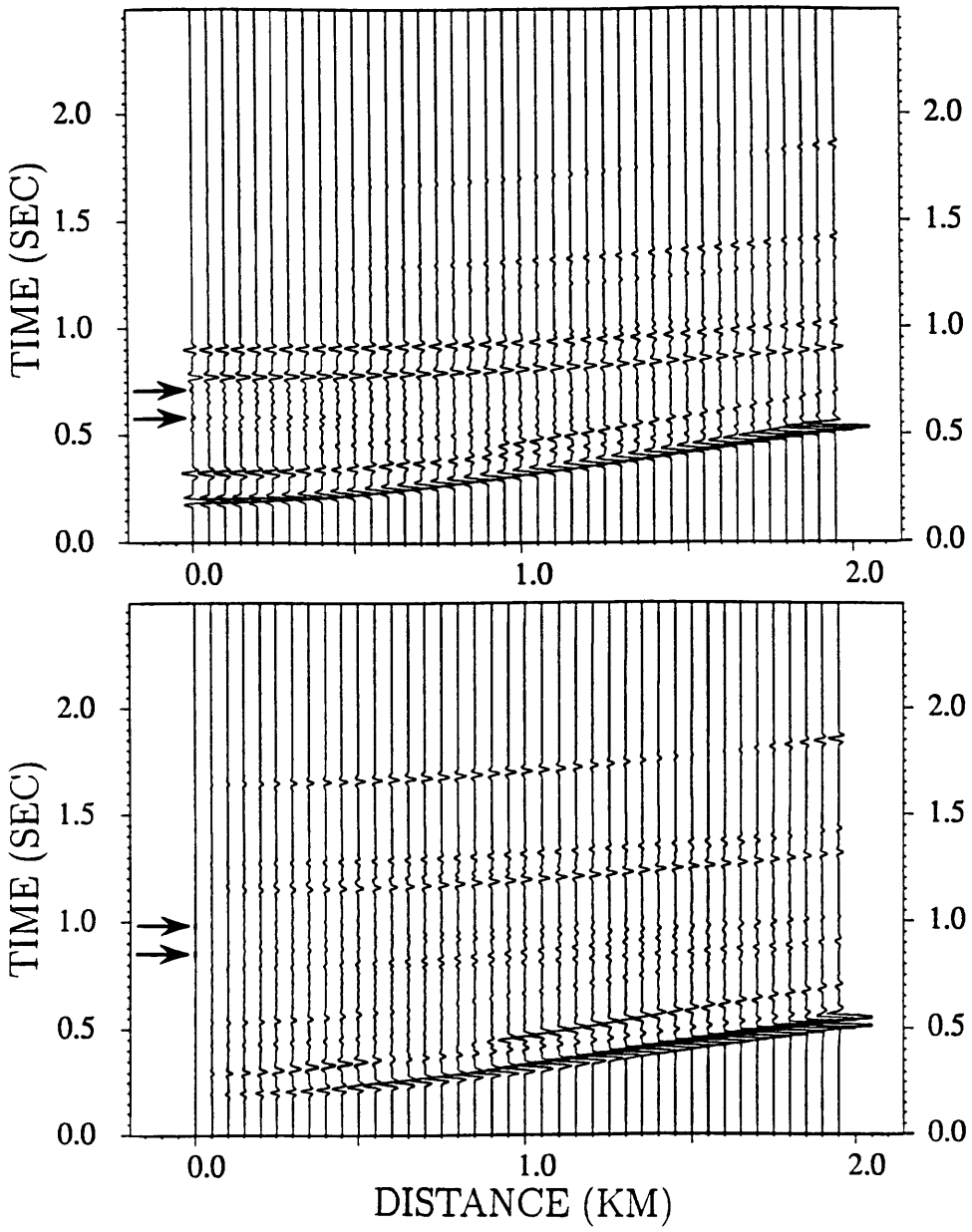

Figure 4-17: Vertical (above) and radial (below) component total wavefield synthetic seismograms from an explosion source for the fracture zone containing isotropic, randomly oriented and gas-filled cracks (Figure 4-12). Arrows mark the positions of scattered P-waves on the vertical component and scattered S-waves on the radial component.

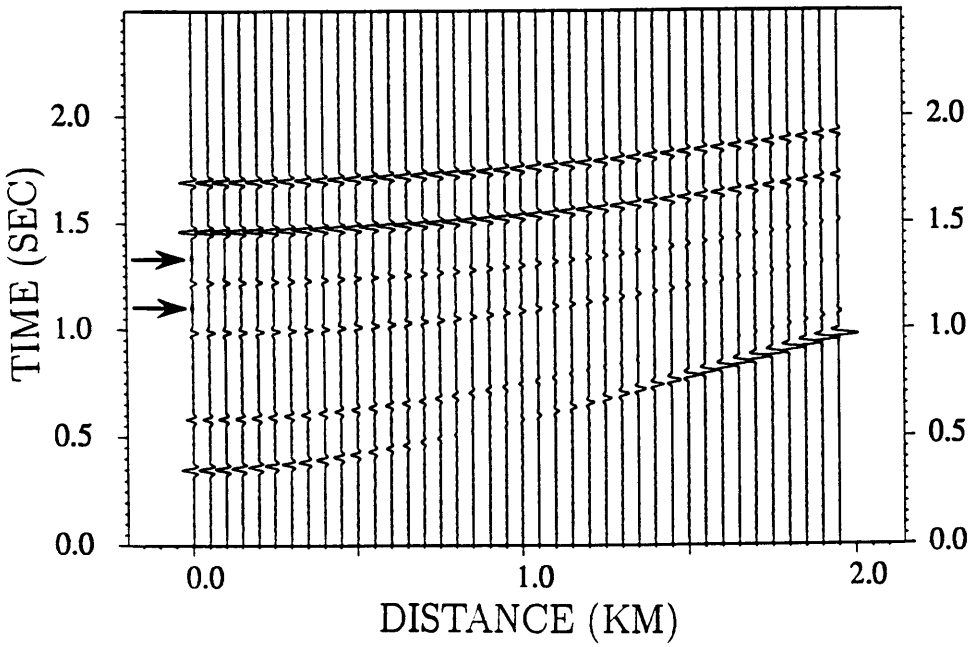

Figure 4-18: Transverse component total wavefield from the cross-line source for the fracture zone model in Figure 4-12 containing anisotropic vertical fractures oriented perpendicular to the receiver array. The fractures are gas-filled. Arrows mark the positions of the scattered waves from the fracture zone.

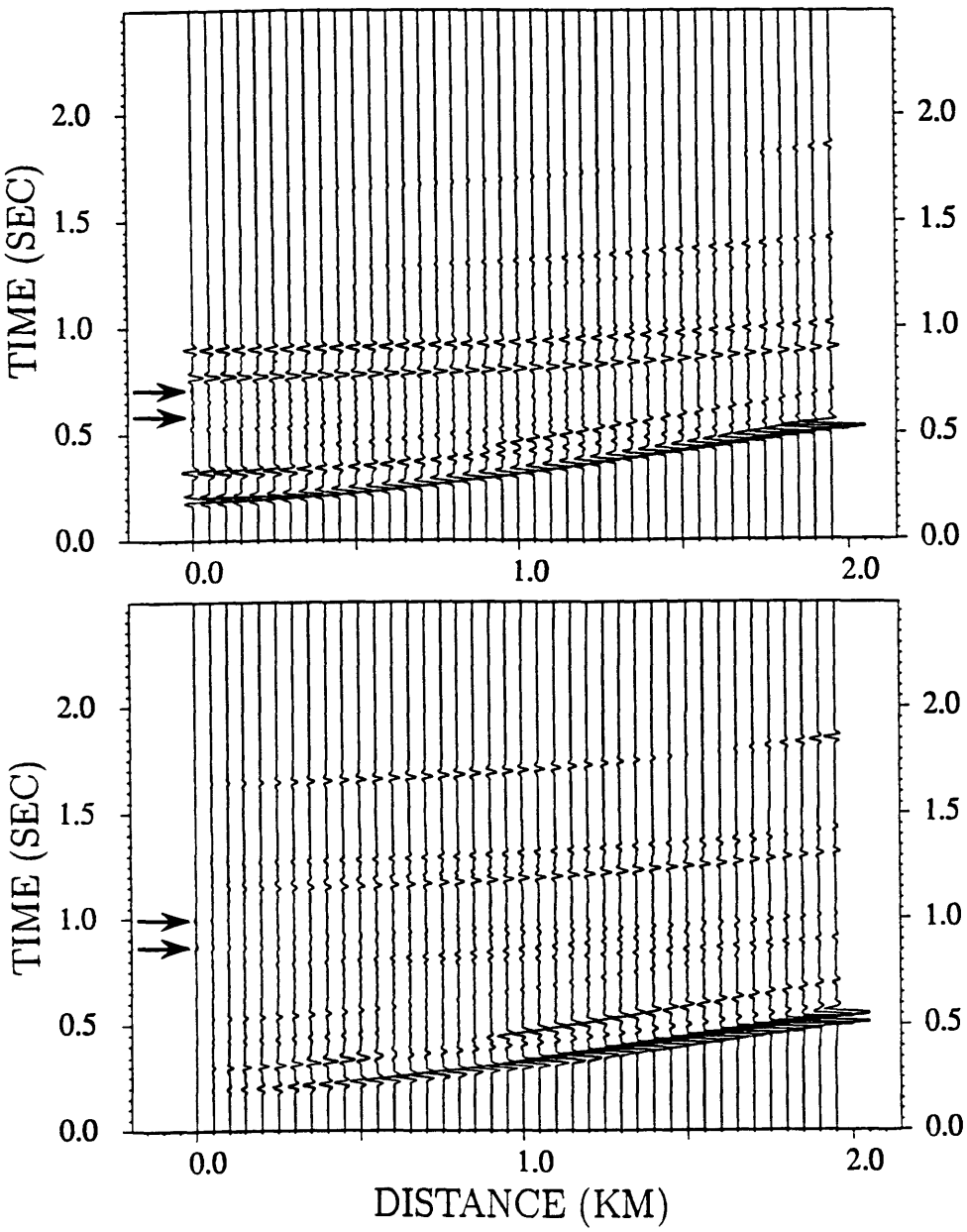

Figure 4-19: Vertical (above) and radial (below) component total wavefield synthetic seismograms from an explosion source for the fracture zone containing anisotropic vertical fractures oriented perpendicular to the receiver array. The fractures are gas-filled (Figure 4-12). Arrows mark the positions of scattered P-waves on the vertical component and scattered S-waves on the radial component.

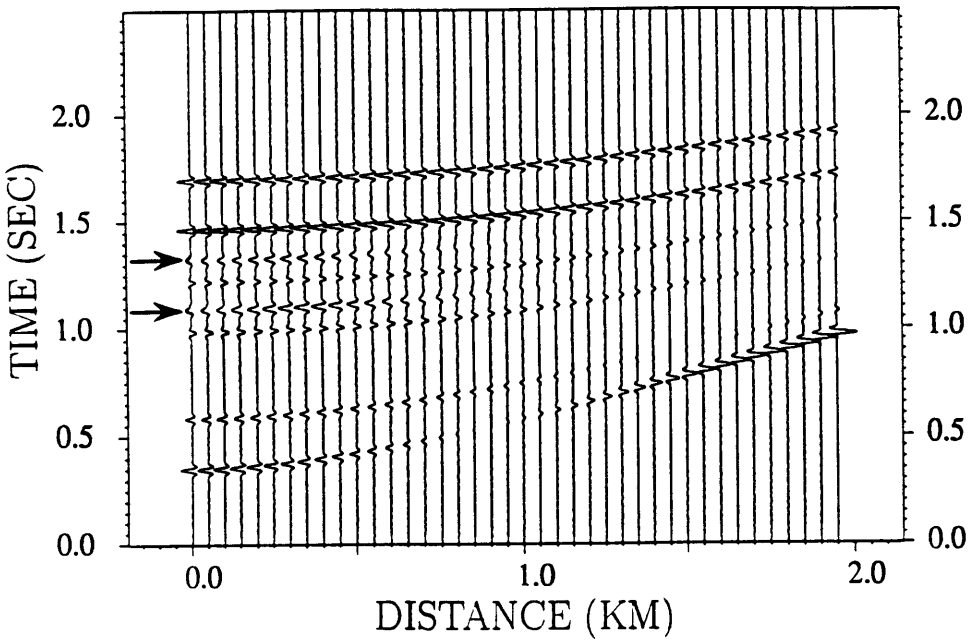

Figure 4-20: Transverse component total wavefield from the cross-line source for the fracture zone model in Figure 4-12 containing anisotropic vertical fractures oriented parallel to the receiver array. The fractures are gas-filled. Arrows mark the positions of the scattered waves from the fracture zone.

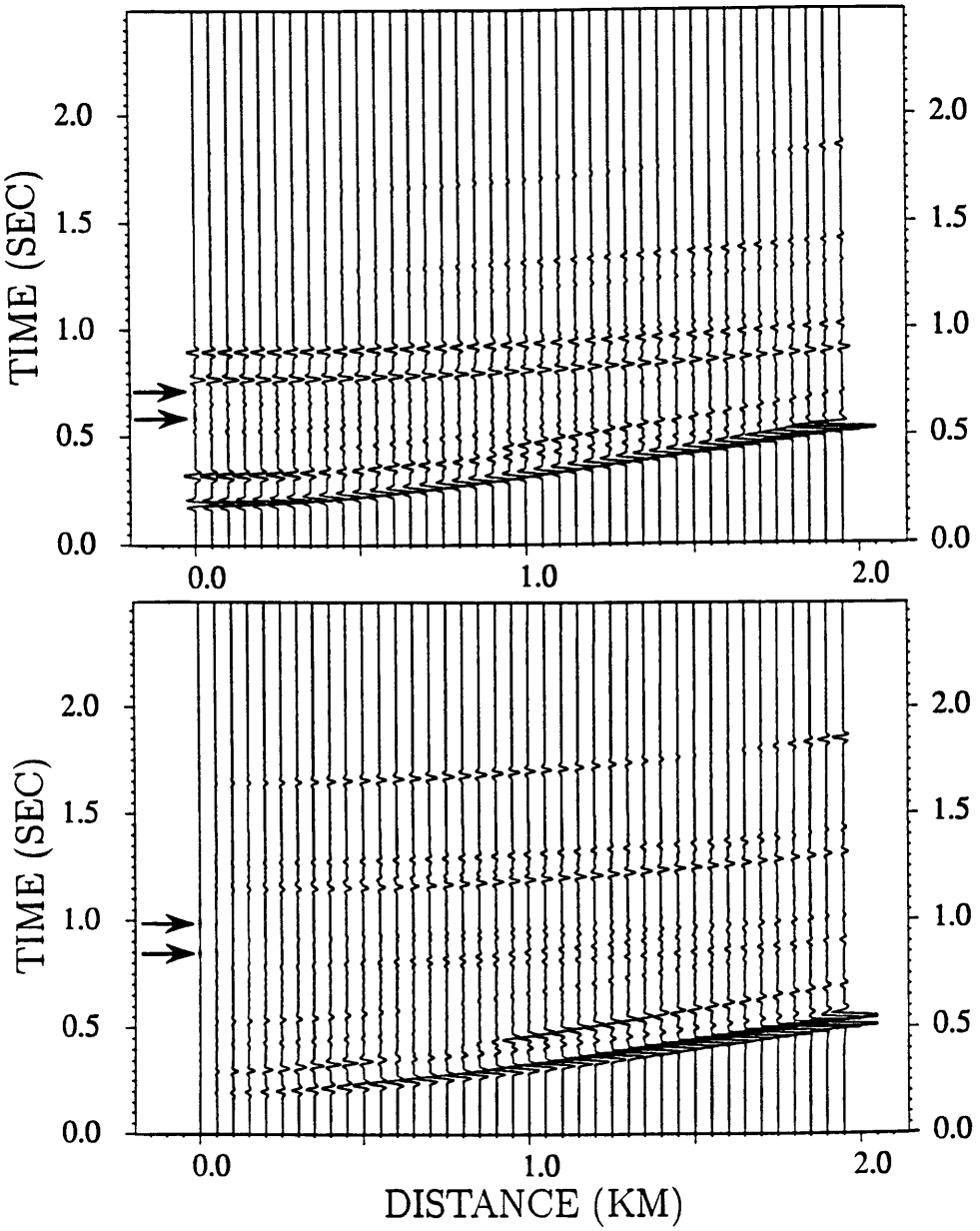

Figure 4-21: Vertical (above) and radial (below) component total wavefield synthetic seismograms from an explosion source for the fracture zone containing anisotropic vertical fractures oriented parallel to the receiver array. The fractures are gas-filled (Figure 4-12). Arrows mark the positions of scattered P-waves on the vertical component and scattered S-waves on the radial component.

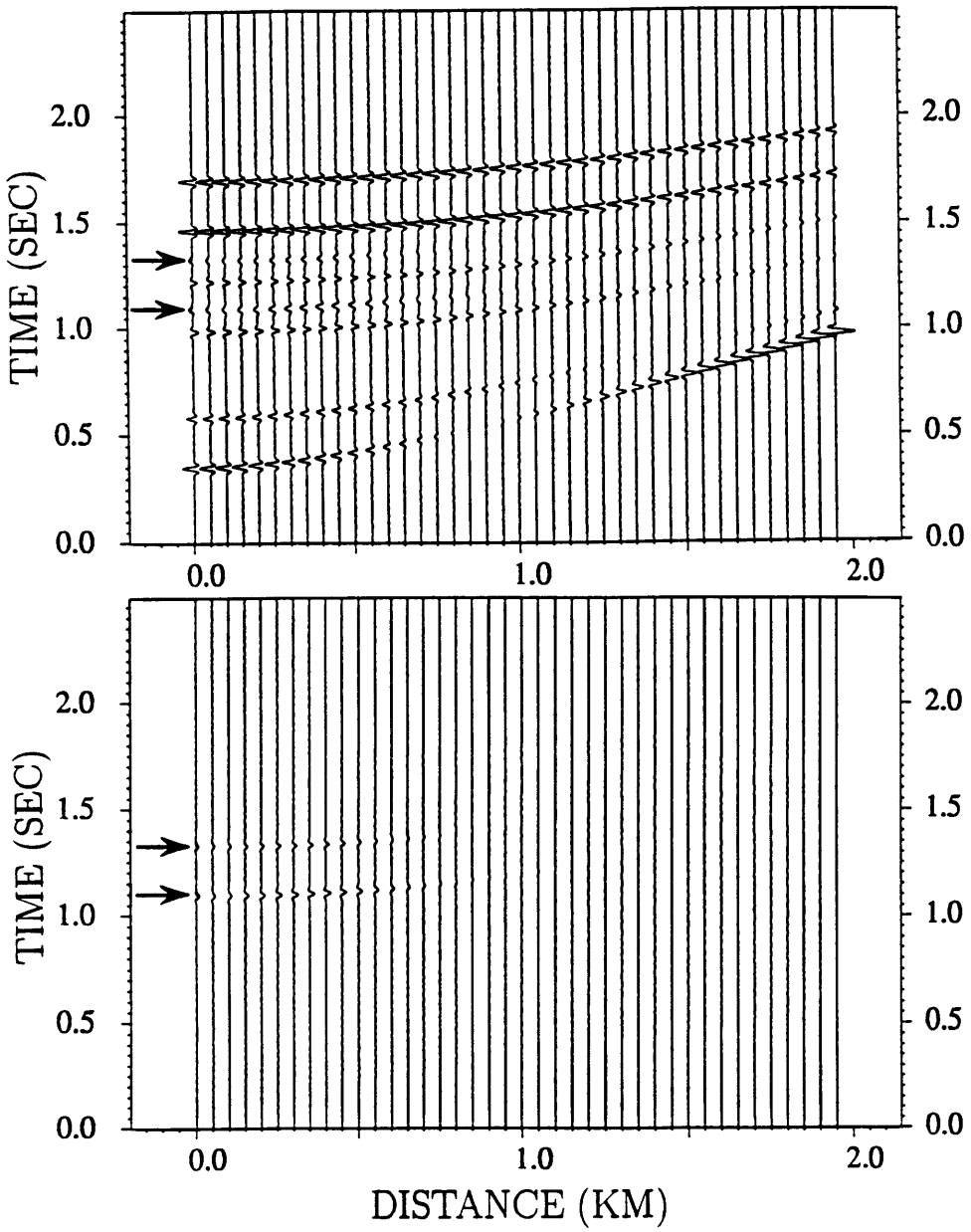

Figure 4-22: Transverse (above) and radial (below) component total wavefield from the cross-line source for the fracture zone model in Figure 4-12 containing anisotropic vertical fractures oriented 45° to the receiver array. The fractures are gas-filled. Arrows mark the positions of the scattered waves from the fracture zone.

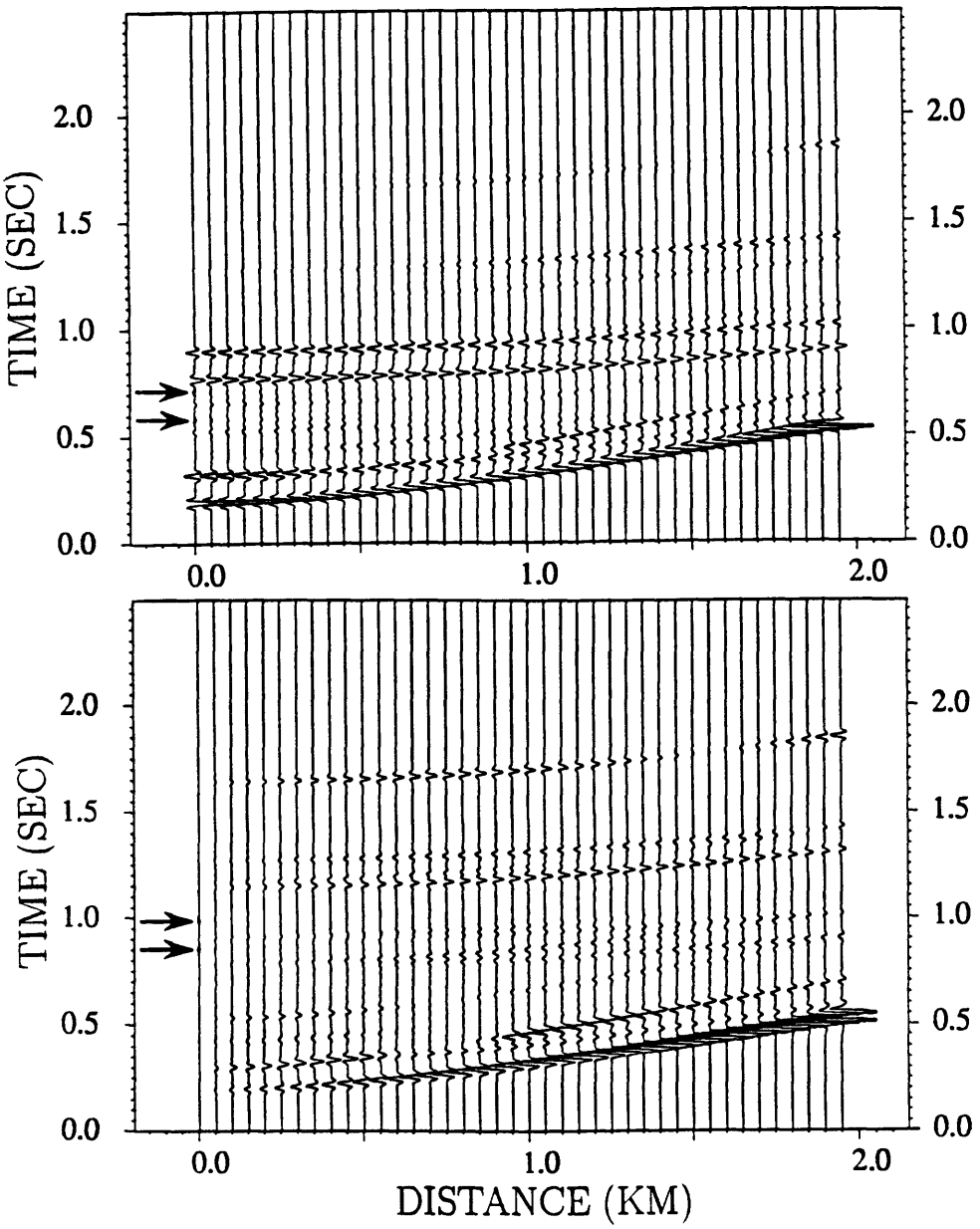

Figure 4-23: Vertical (above) and radial (below) component total wavefield synthetic seismograms from an explosion source for the fracture zone containing anisotropic vertical fractures oriented 45° to the receiver array. The fractures are gas-filled (Figure 4-12). Arrows mark the positions of scattered P-waves on the vertical component and scattered S-waves on the radial component.

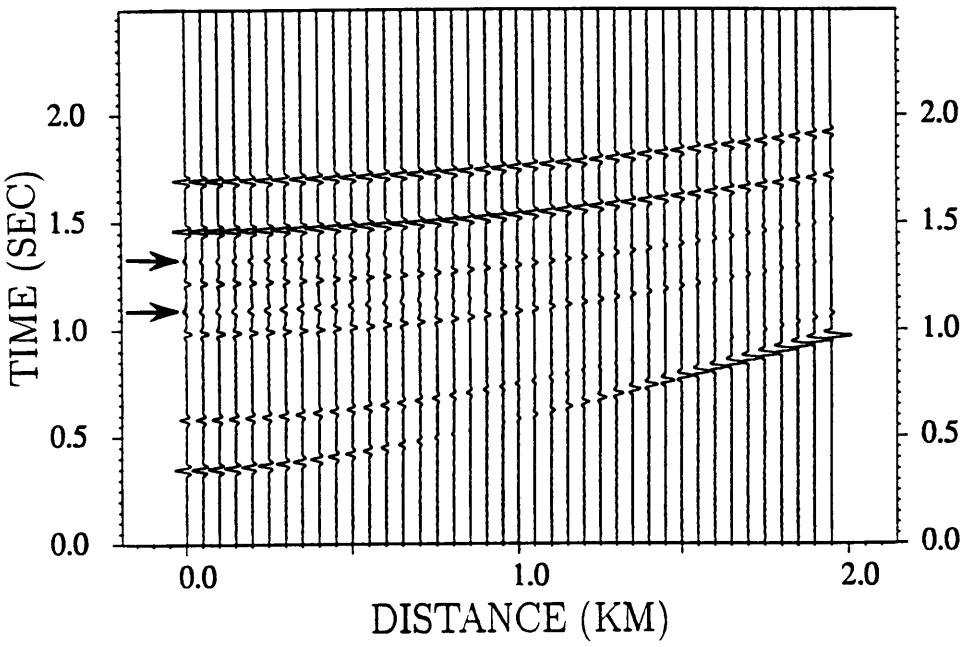

Figure 4-24: Transverse component total wavefield from the cross-line source for the fracture zone model in Figure 4-12 containing isotropic, randomly oriented and water-filled fractures. Arrows mark the positions of the scattered waves from the fracture zone.

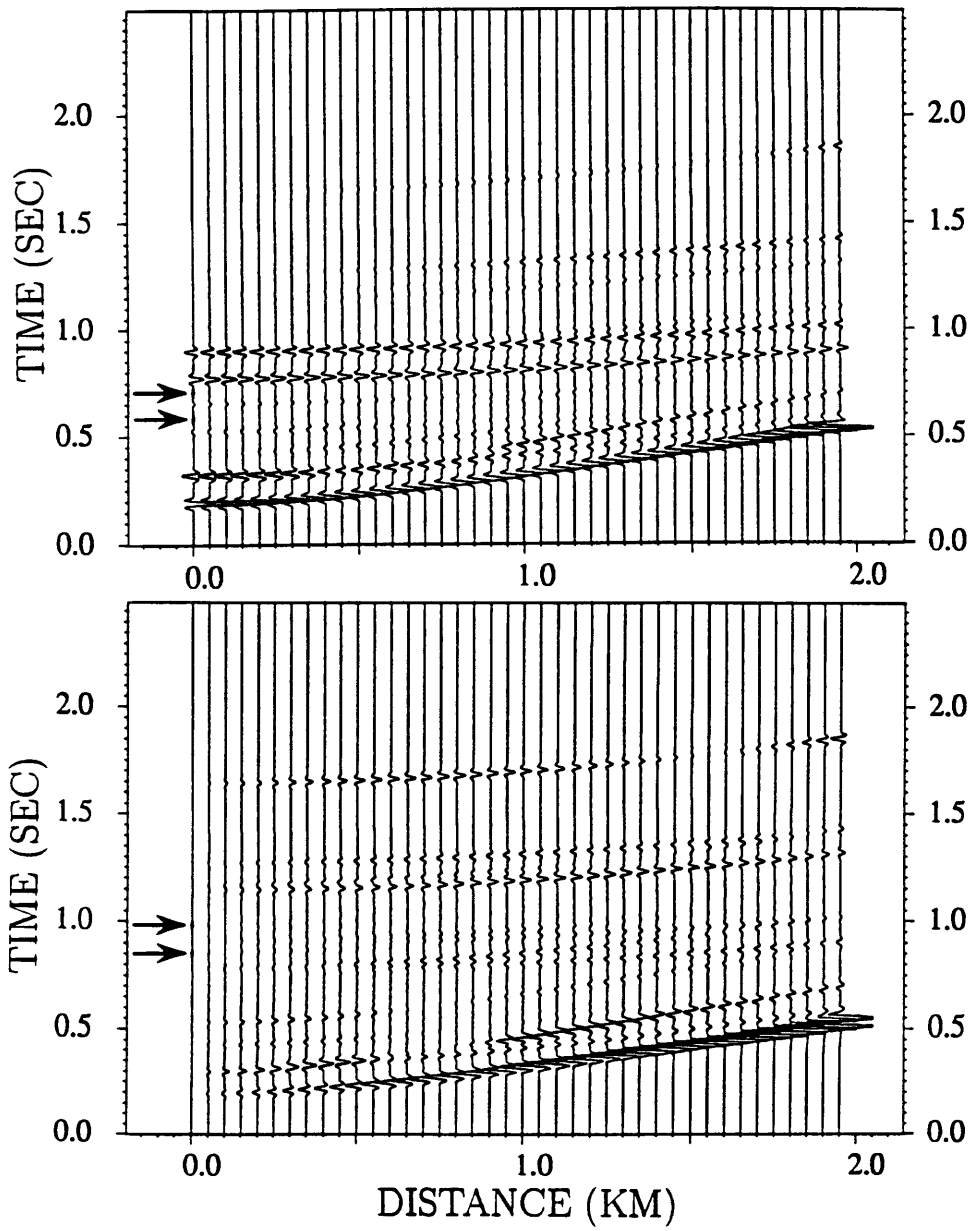

Figure 4-25: Vertical (above) and radial (below) component total wavefield synthetic seismograms from an explosion source for the fracture zone containing isotropic, randomly oriented and water-filled fractures. Arrows mark the positions of scattered P-waves on the vertical component and scattered S-waves on the radial component.

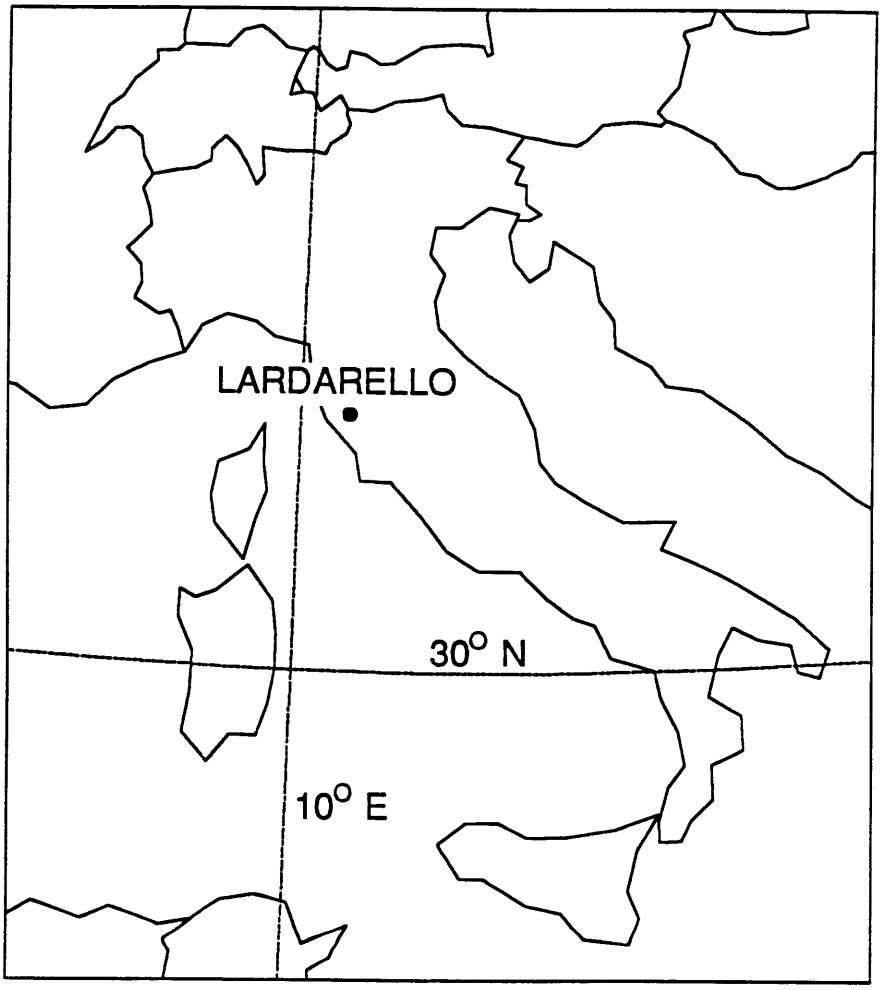

Figure 4-26: Map showing the location of the Lardarello geothermal field in Italy.

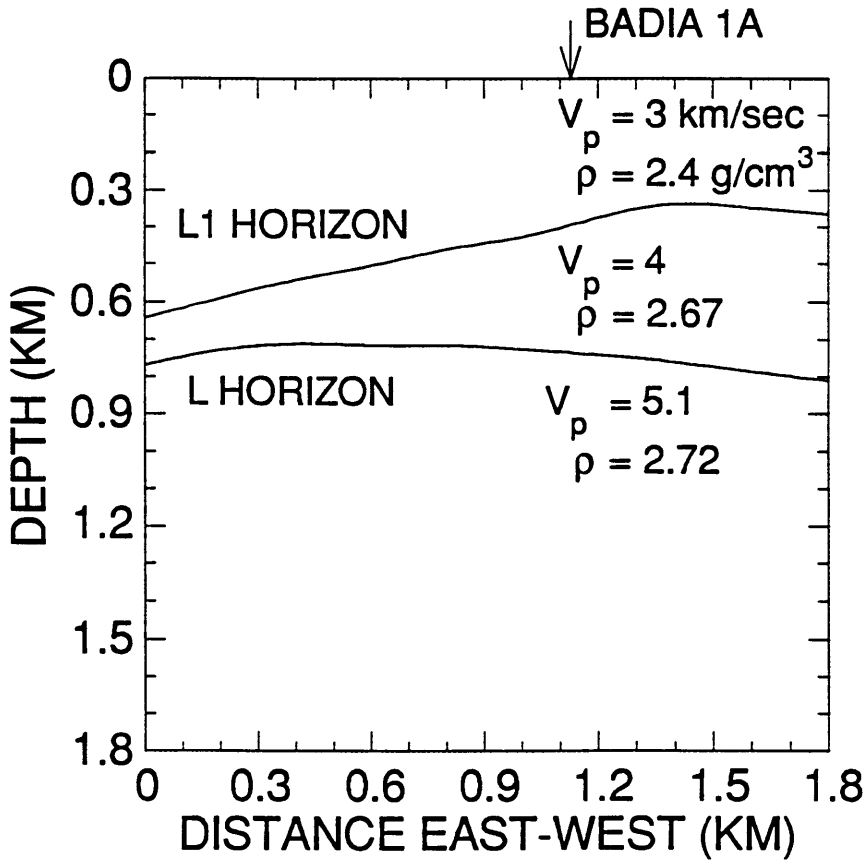

Figure 4-27: East-west cross-section of the background earth model used to compute the synthetic seismograms for the Badia 1A VSP data. Sedimentary units are present in both layers over the L horizon, while the rock below is metamorphic. The seismic properties of the metamorphic zone are relatively homogeneous so that it may be represented by a single velocity. Compressional wave velocities and densities are indicated in the figure, and shear wave velocities were chosen so that the V_p/V_s ratio was $\sqrt{3}$.

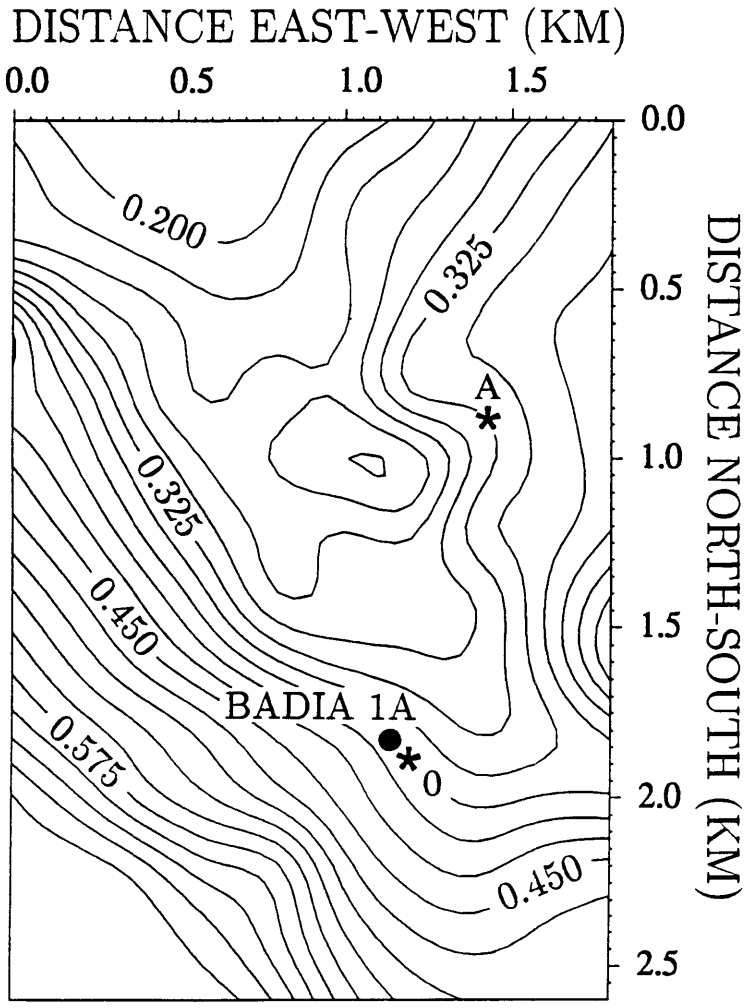

Figure 4-28: Contour maps of the three surfaces used in the modeling of the Badia 1A VSP data. The positions of the Badia 1A well, the zero offset source position (0) and A offset source position (A) are all indicated. A) L1 interface.

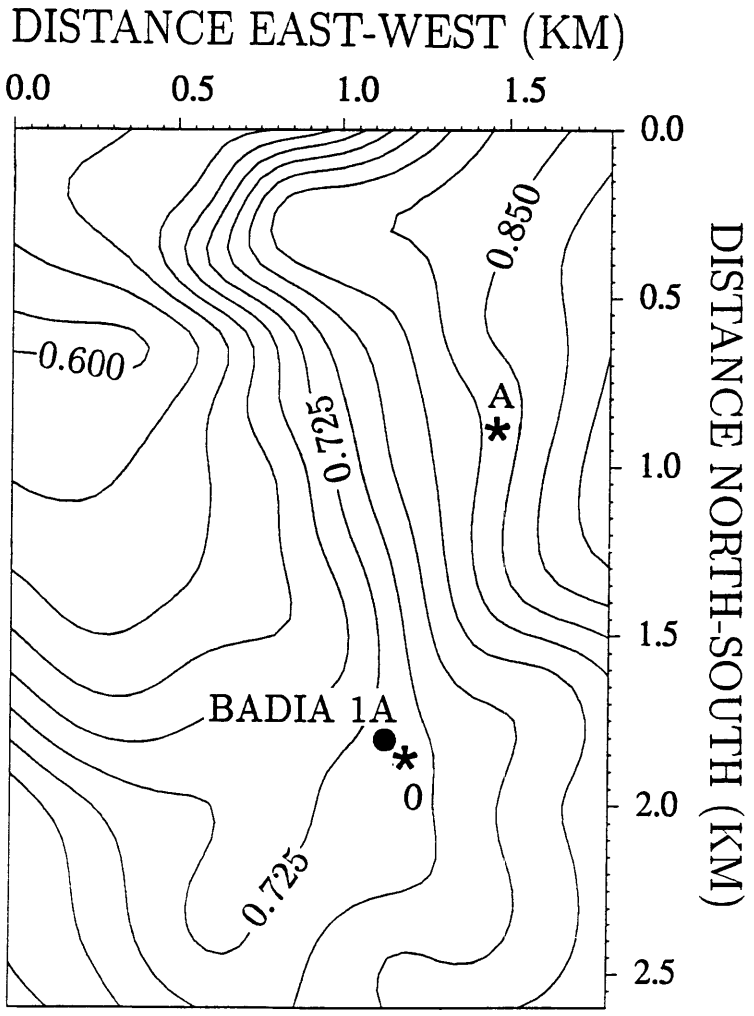

Figure 4-28: B) L interface.

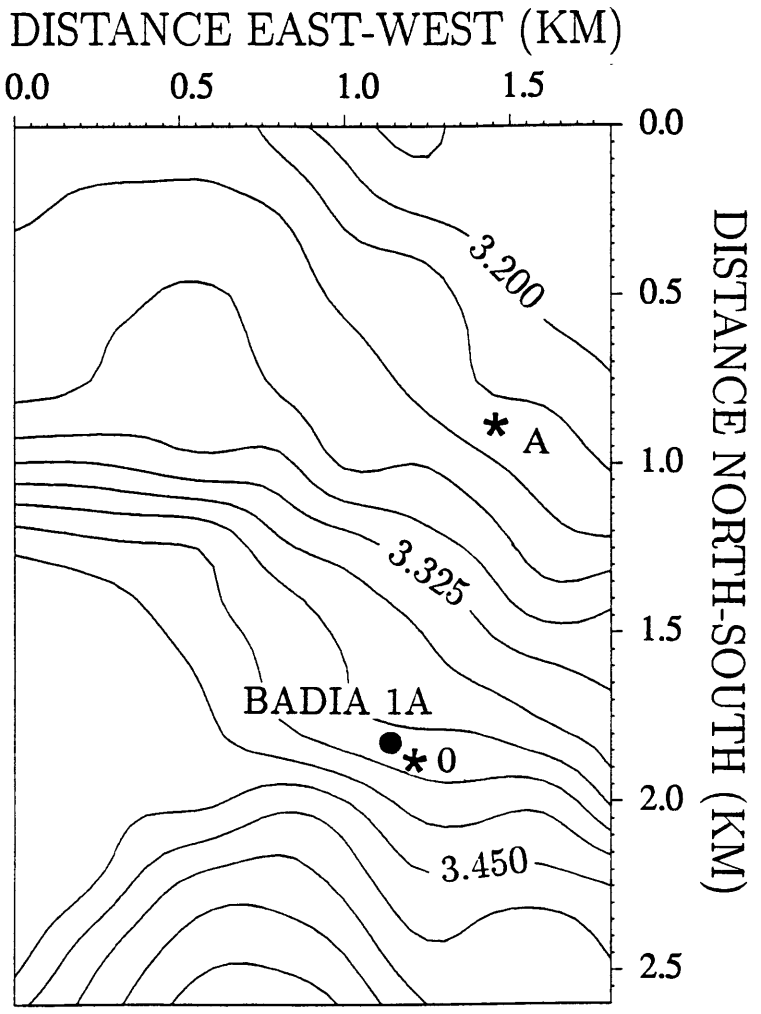

Figure 4-28: C) H marker.

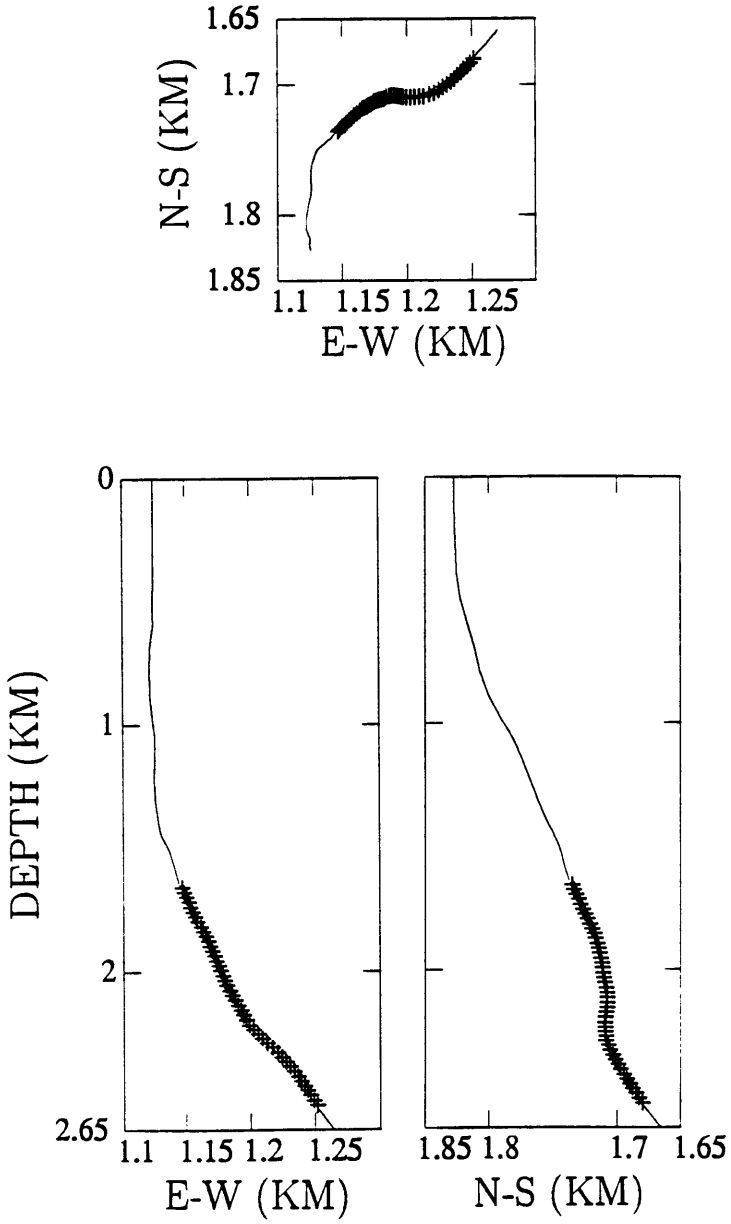

Figure 4-29: Positions of geophones and the deviated Badia 1A well. The geophones are plotted in all three coordinate planes. A) Geophone positions for the zero offset source.

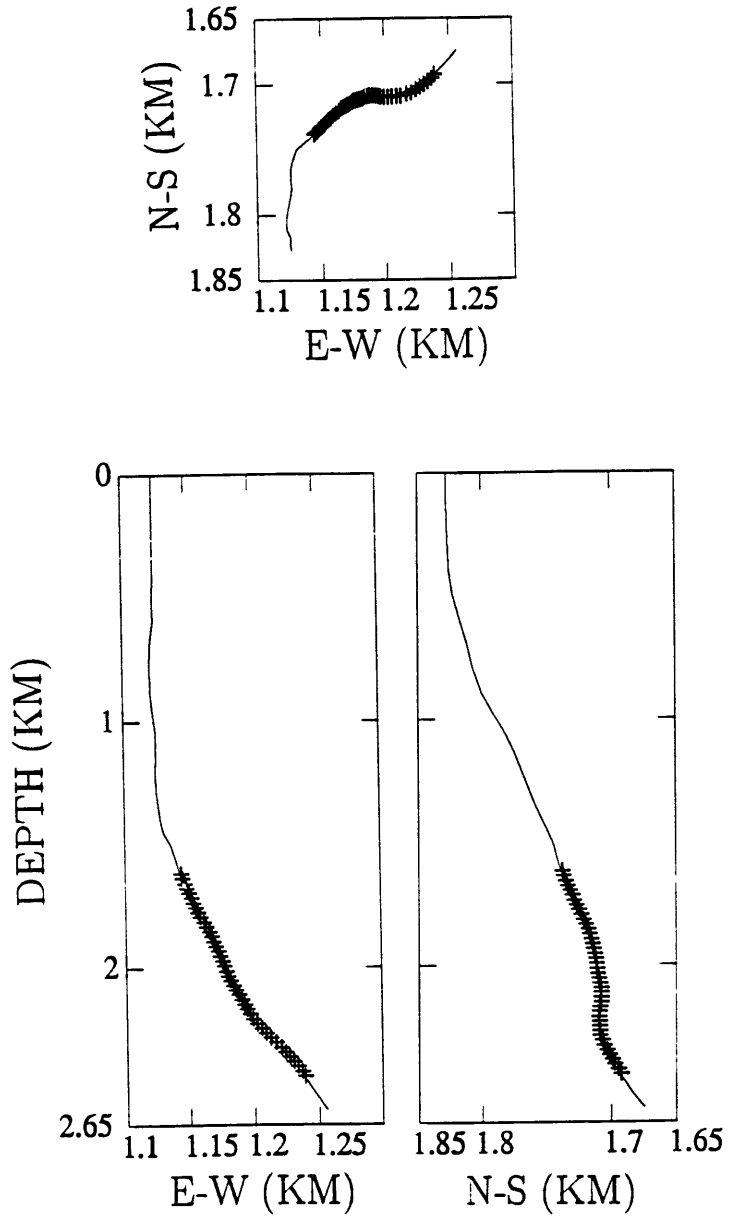

Figure 4-29: B) Geophone positions for the A offset source.

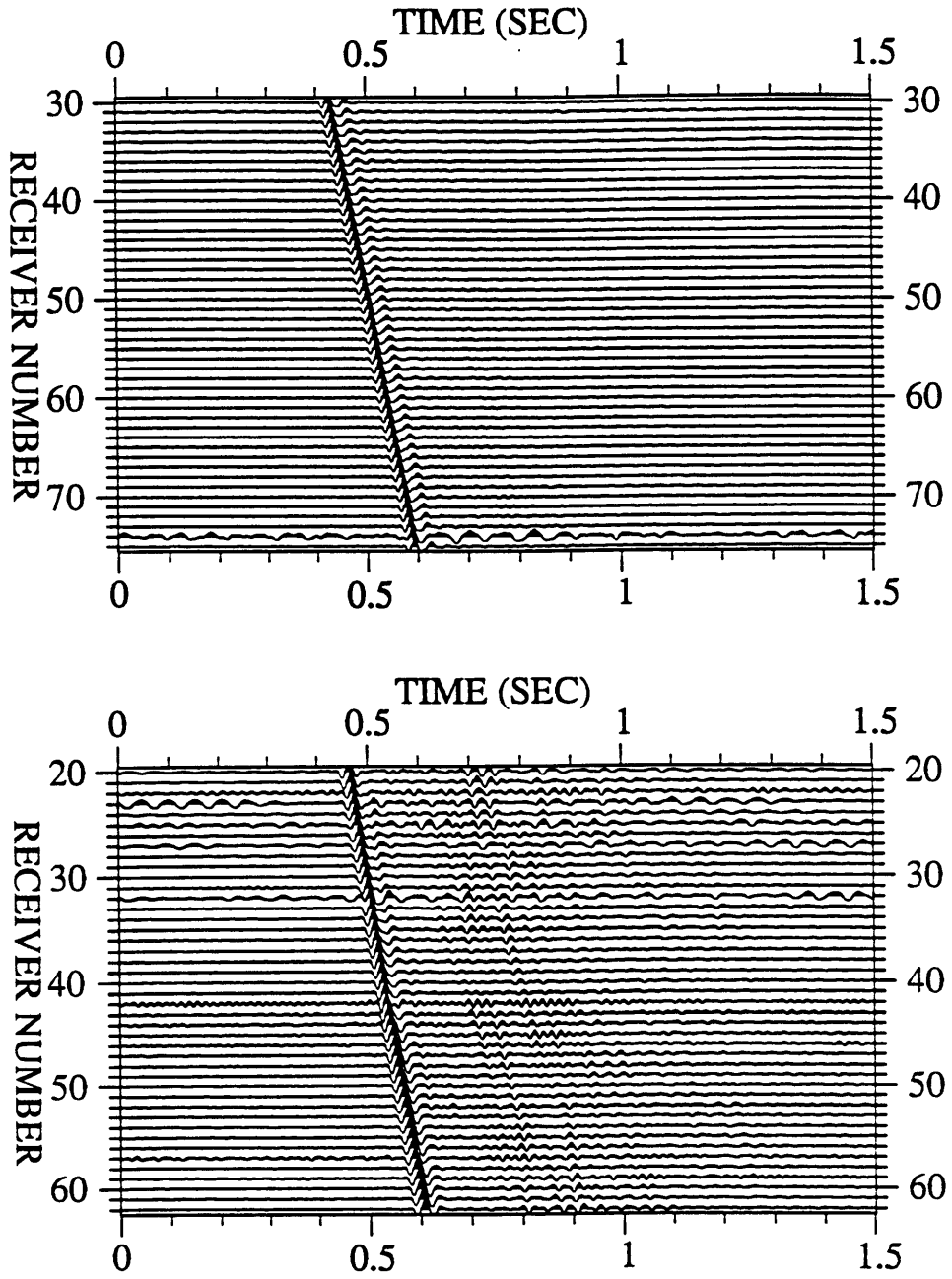

Figure 4-30: Trace normalized data from the zero offset source (above) and the A offset (below). The data were normalized so that the first arrival had unit amplitude.

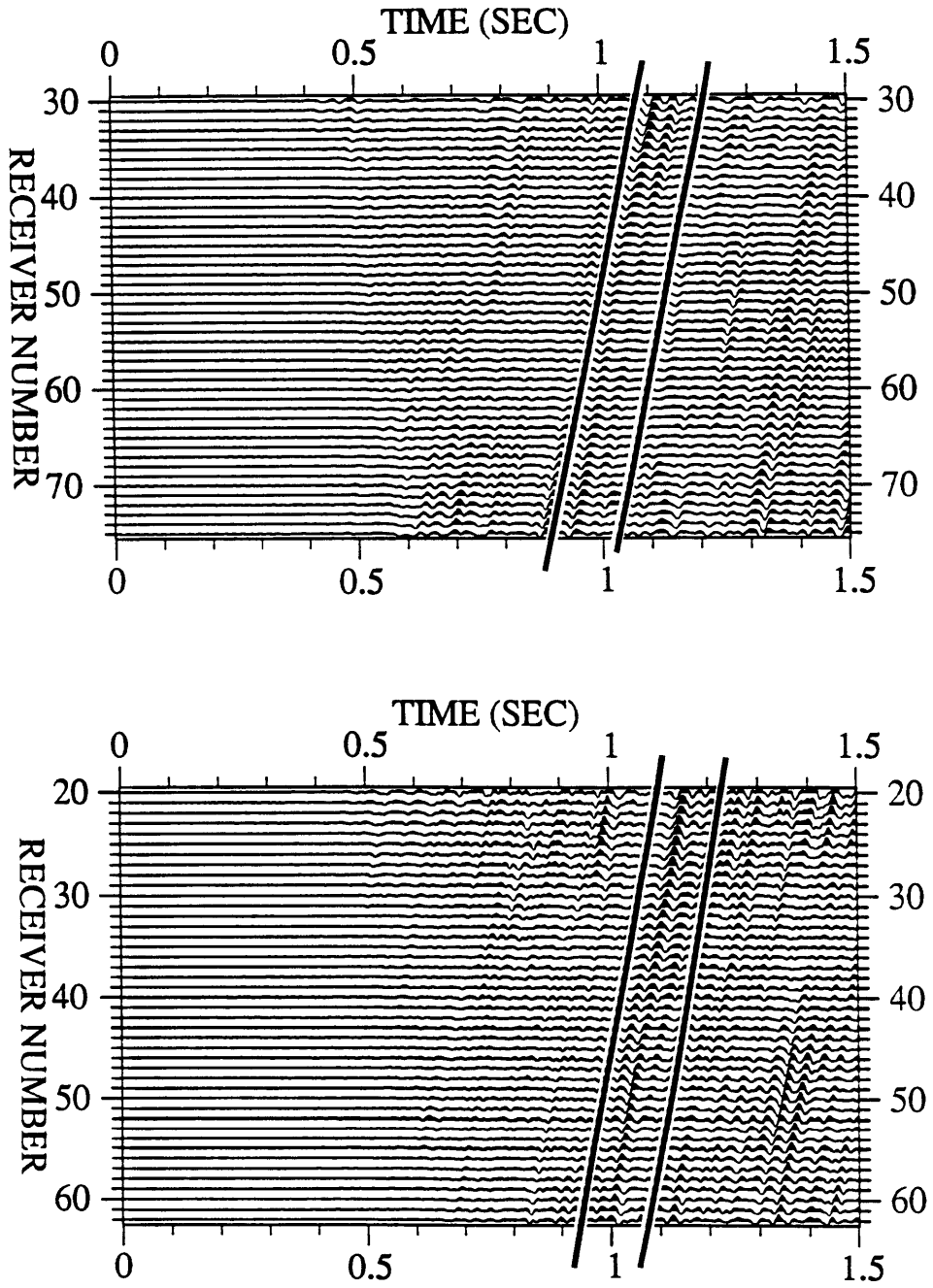

Figure 4-31: Upgoing wavefields for the zero offset source (above) and the A offset (below). The data from Figure 4-30 were median filtered, then low-pass filtered to obtain these sections. The signal from the H marker is found between the lines indicated on these plots. Note that the zero offset plot is scaled by a factor of three compared to the A offset seismograms, showing that the H marker event is much stronger in the A offset data.

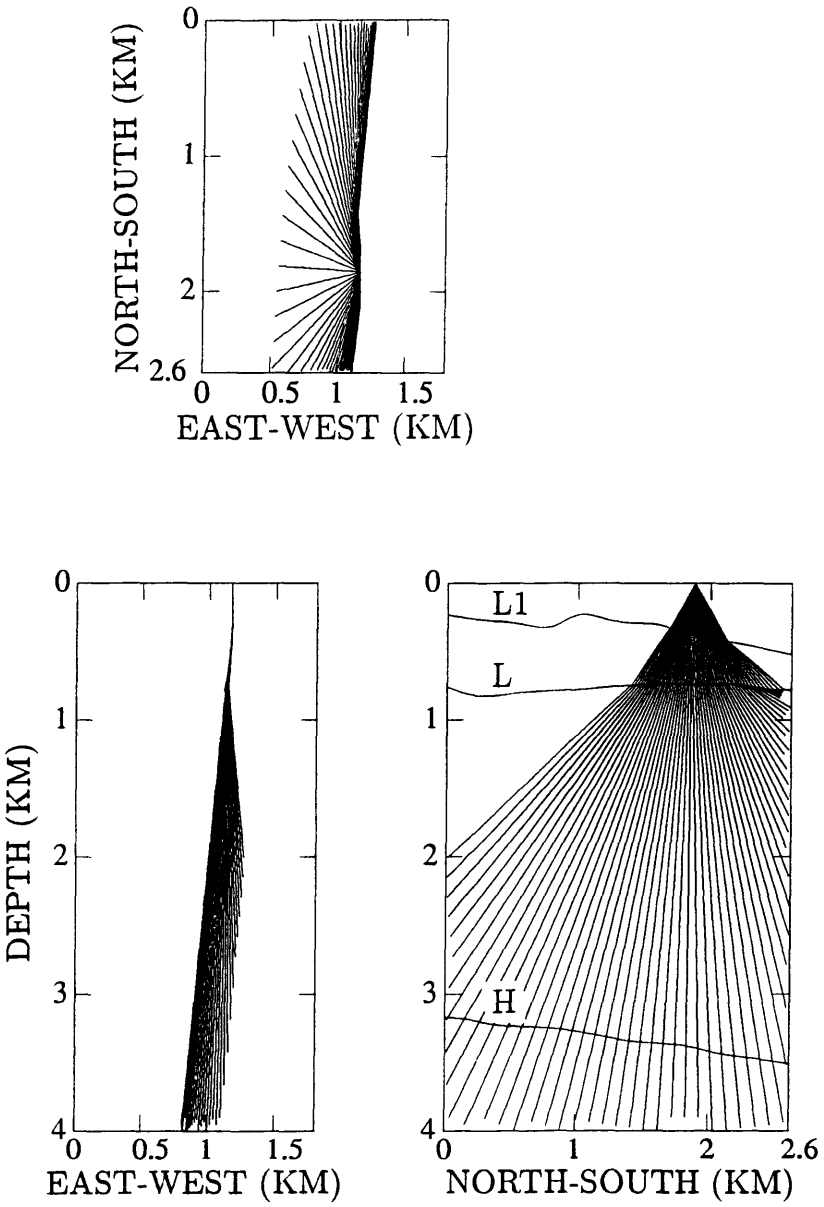

Figure 4-32: Ray paths for a fan of rays initially in the north-south vertical plane. All three coordinate planes are plotted, and the L1, L and H markers are shown in the appropriate north-south cross section. When the rays encounter the L1 and L horizon, the irregular interfaces bend the ray paths so that they have a strongly three-dimensional propagation showing the complexity of wave propagation in the Lardarello region. In a one-dimensional earth model, these rays would have no east-west components. To completely illuminate the H marker, similar fans of rays were traced over all azimuths from both source positions. A) Ray fan from the zero offset source.

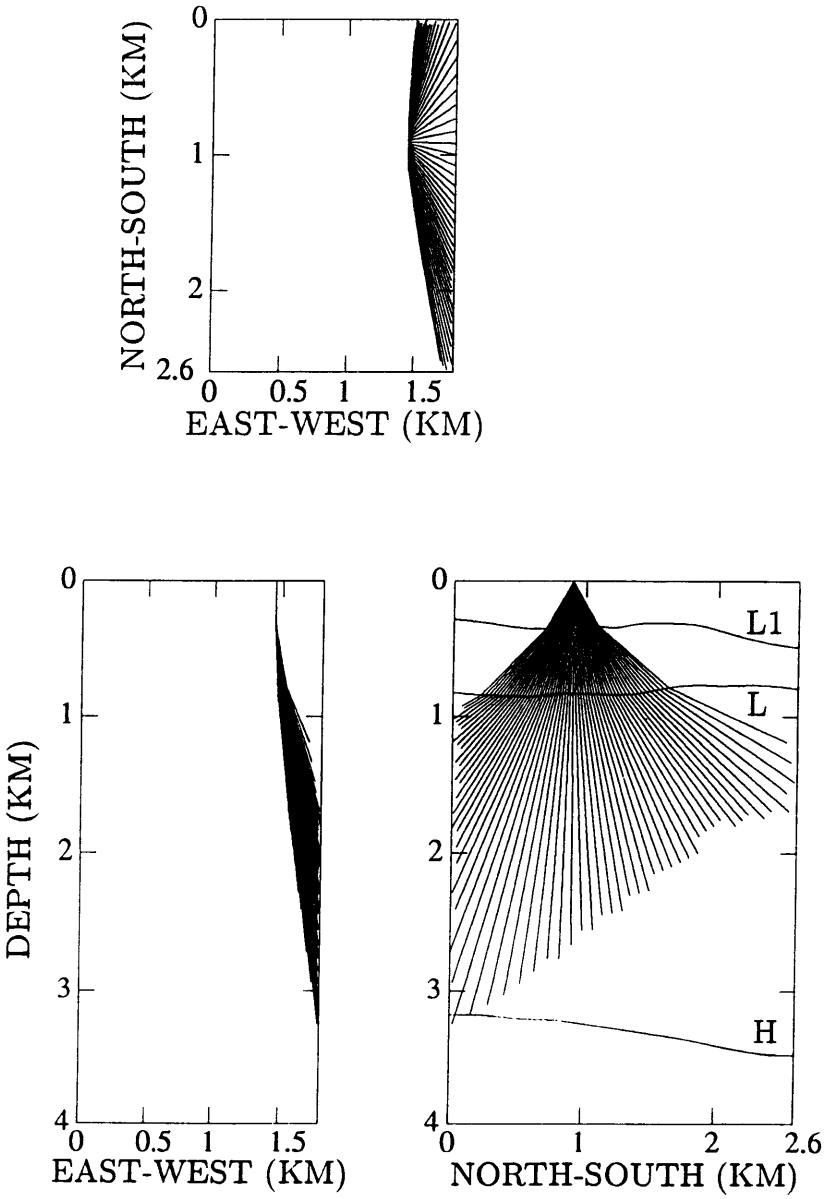

Figure 4-32: B) Ray fan from the A offset source.

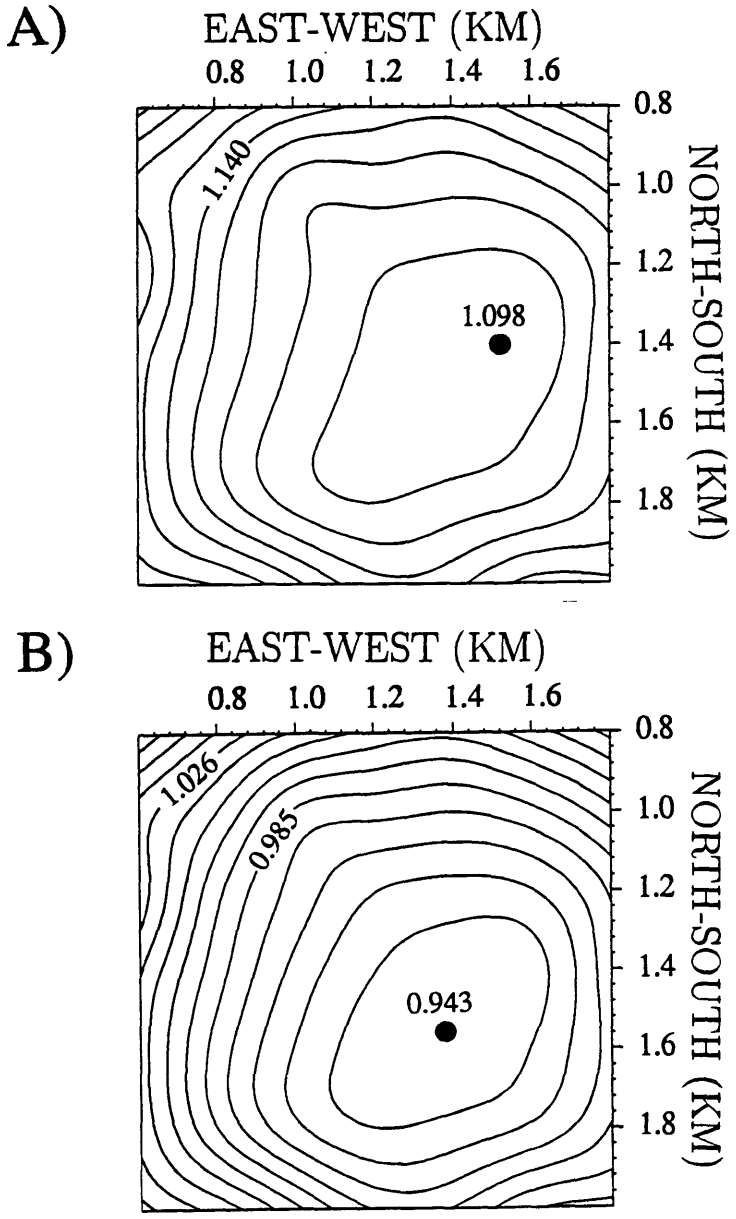

Figure 4-33: Contour plots of total travel time from the zero offset source to the H2 marker and then to the receiver. Each contour line bounds a Fresnel zone as described in the text. A) Total travel time for receiver 30. B) Total travel time for receiver 70.

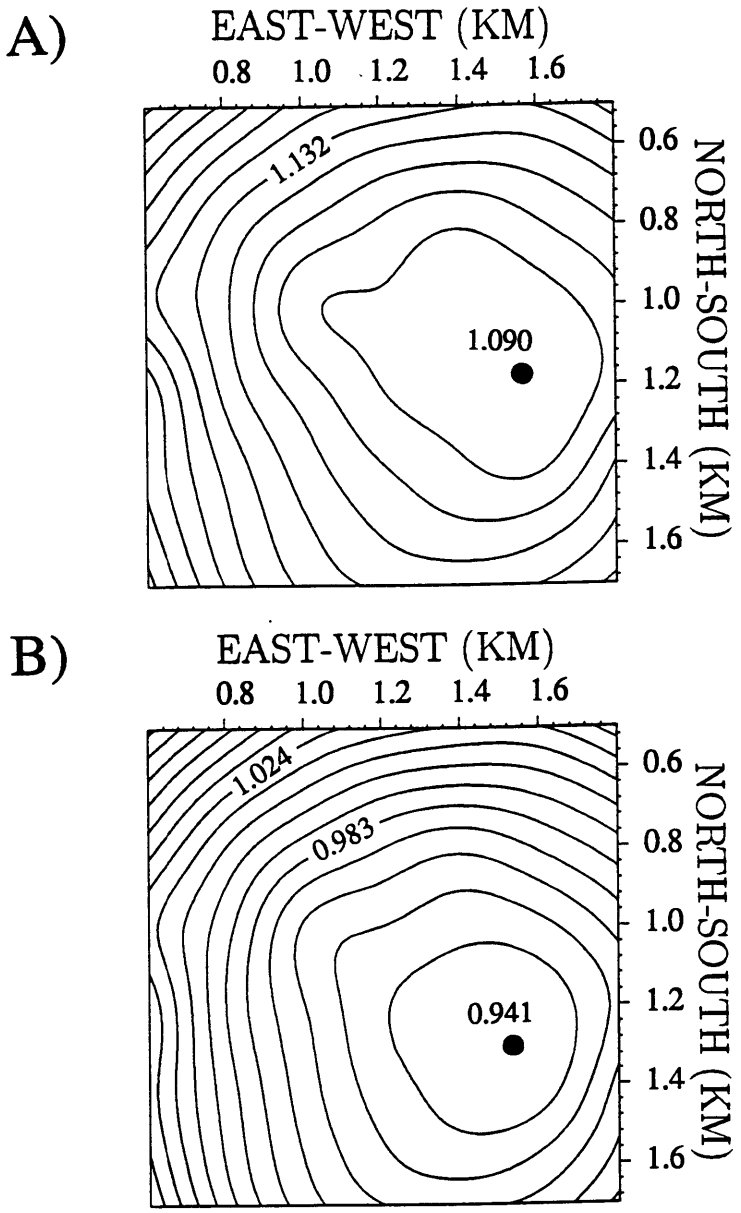

Figure 4-34: Contour plots of total travel time from the A offset source to the H2 marker and then to the receiver. Each contour line bounds a Fresnel zone as described in the text. A) Total travel time for receiver 22. B) Total travel time for receiver 62.

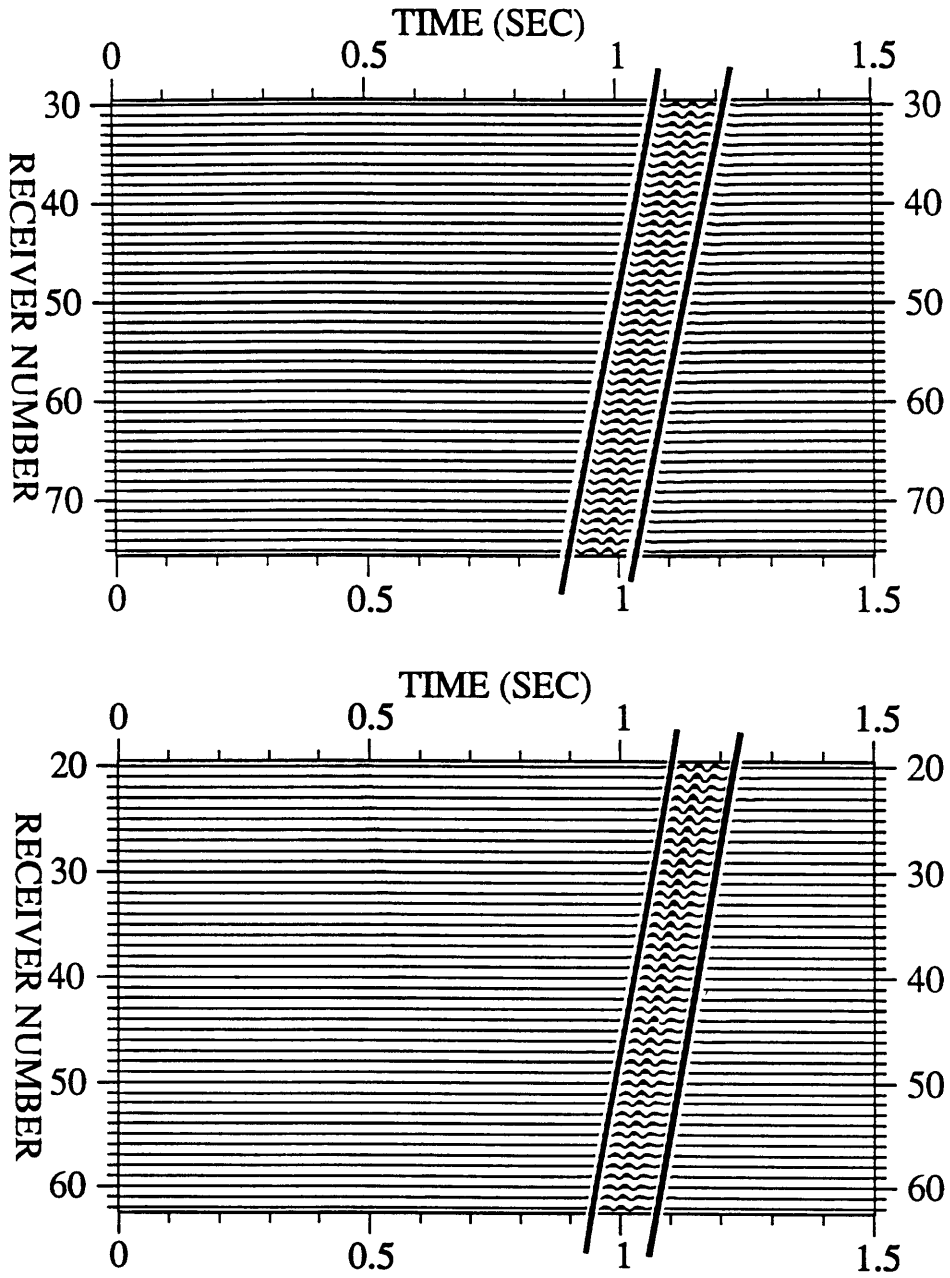

Figure 4-35: Synthetic seismograms for the H marker model described in the text. The results for both the zero offset source (above) and A offset (below) are shown. The arrival is marked as in the data in Figure 4-31. The downgoing wavefields were also ray-traced, allowing the synthetics results to be processed exactly as were the field data.

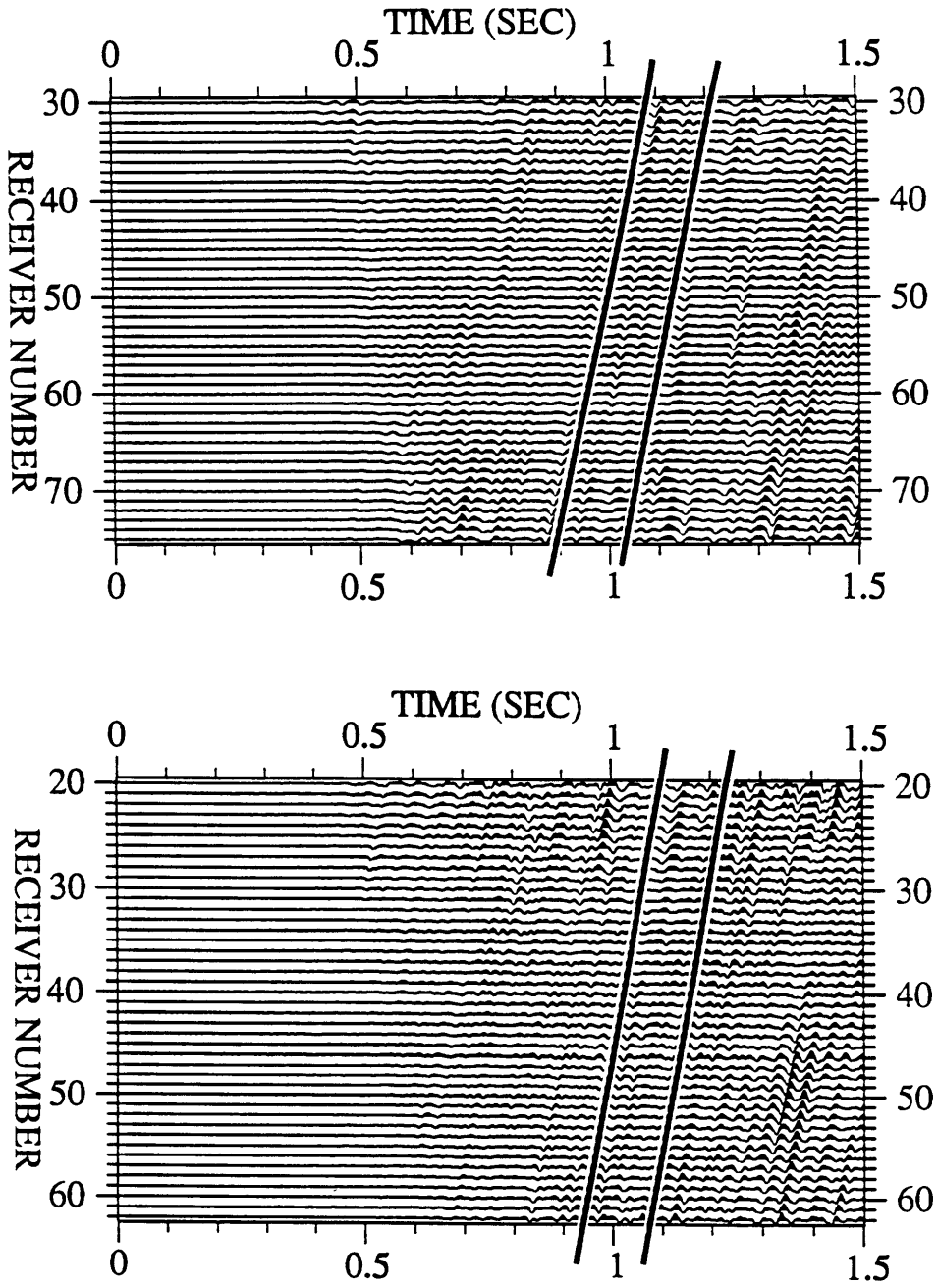

Figure 4-36: The result of subtracting the synthetic upgoing wavefields (Figure 4-35) from the processed data (Figure 4-33) for the zero offset data (above) and A offset data (below). Lines indicate the same time interval as in Figures 4-33 and 4-35.

Chapter 5

Summary and Conclusions

The further one pursues knowledge, the less one knows.

—Lao-tzu

In this thesis we have developed two basic theories of elastic wave interaction with anisotropic fractured media. The first approach was to include a distribution of fracture orientations in the calculation of effective elastic moduli, while the second advance was the application of elastic wave scattering theory to the study of localized zones of fracturing instead of homogeneous layers. Both approaches have specific advantages which allow more realistic representations of the fractured medium. The first method is an improvement in that it eliminates the oversimplification which represents the fractures as a set of perfectly parallel cracks. In contrast, our study of scattered waves still applied the simple model of crack orientation, instead allowing for a geometrically complex fracture zone which for many important research problems is an important step. At the same time, the results reveal certain ambiguities in the elastic behavior of an elastic material containing cracks which will be difficult to resolve using seismic observations.

In Chapter 2, for example, we developed an inversion for the parameters controlling the crack orientation distribution function in a uniaxially stressed rock sample which yields a unique value for crack density but a more ambiguous result for the

aspect ratio distribution. The forward model for crack orientations was obtained by consideration of the closure of penny-shaped cracks under uniaxial stress, which will depend on the orientation of the crack with respect to the applied stress axis. Assuming that the initial prestress distribution of cracks is isotropic, the stressed distribution of crack orientations can be expressed in generalized spherical harmonics. This in turn allows an evaluation of the effective elastic constants which appear govern the velocities in the rock. Inversions of velocity data from samples of Barre granite (Nur and Simmons, 1969) show that the crack density is uniquely and easily determined with results essentially the same as those obtained by Sayers (1988a, 1988b) using a curve fitting algorithm. However, our method also gave an estimate for α_m, the maximum value of the aspect ratio distribution included in the model of crack closure. This parameter is strongly dependent on the model aspect ratio distribution chosen and controls the details of the velocity variation with direction. An initial model for permeability variation in the stressed, anisotropic rock was also considered. This model showed some promise, but is also a simplification in its representation of the crack system for the purposes of fluid flow.

In Chapter 3 the emphasis of the thesis changed to the scattering of elastic waves from anisotropic inclusions. Substitution of perturbations of the elastic moduli and density into the elastic wave equation led to an expression of the scattered wavefield as a perturbation to the background wavefield which would propagate in the absence of the variations in material properties, the classic Born approximation. The effects of a perturbation to density are expressed as a single force secondary source, while a perturbation to any of the 21 independent elastic constants results in a moment tensor secondary source. We derived the radiation patterns for a point perturbation to any of the elastic constants, Rayleigh scattering, and these are summarized in Table D.1.

After this derivation, we examined the application of this scattering theory to a localized region of fracturing. This can be viewed as a canonical problem with a

solution that gives some good intuitive guidelines for developing an understanding of the elastic wave scattering from larger, more complex regions. In this case, the Hudson theory for fractured media provides some very natural values for the perturbations, as the effective elastic constants for a fractured material are expressed as a sum of the background Lamé parameters from the unfractured background medium and correction terms of first and second order in crack density. These correction terms were substituted into the equations for Rayleigh scattering radiation patterns, and resulting patterns were computed for various directions of plane wave incidence. Both isotropic and anisotropic fractured zones were considered. For P and S-wave incidence, the scattering from an isotropic region will have an equal amplitude distribution with respect to the direction of the incident wave. The results clearly demonstrate, however, that the scattering due to an incident shear wave contains the most information on aligned fractures, as the theory predicts that the amplitude of the scattered wavefields, both P and S, will vanish for an shear wave incident with polarization parallel to the plane of fracture orientation. Mathematically, this happens because for vertical fractures aligned perpendicular to the x axis, the Hudson theory predicts that the perturbation $\delta C_{44} = 0$. Since the strain due to a vertically propagating shear wave polarized in the y direction will not multiply any other perturbations in the expression for the Born secondary source (equation 3.11), the source terms are all zero, and no scattered field is generated. Physically, this can be understood as occurring because the particle displacement is entirely parallel to the fractures and is only minimally affected by a relatively thin zone of fracturing. Scattering from an incident plane compressional wave will also show variation with direction, but to a much lesser degree. It is important to remember that with the Born approximation, the vanishing of the scattering for shear waves incident on anisotropically fractured regions will not change as the fracture zone becomes larger. Even though Rayleigh scattering results will not apply, the secondary source term in the Born approximation is controlled by the strain due to the incident wave and will therefore always be

zero when the perturbations interacting with the strain component generated by the propagating wave are zero.

The application of the Born approximation to larger fractured regions is the basis of Chapter 4. A Ray-Born algorithm was applied to the computation of the scattered wavefields from arbitrary regions of inhomogeneity. We outlined the method for a fully anisotropic medium and presented applications to isotropic background media with anisotropic perturbations due to the presence of aligned fractures. Two fundamental restrictions are required in the use of the Ray-Born method resulting from the approximations involved. The first is due to the use of asymptotic ray methods for the calculation of Green's tensors representing seismic wave propagation in the background medium. This requires that this background be smooth relative to a wavelength. In contrast, the Born approximation imposes the constraint that the wavelength be much longer than the scale of the heterogeneity.

The practical meaning of "much longer" in the application of the Born approximation is generally not well understood (Beydoun and Mendes, 1989), and so we addressed this question before applying the algorithm to general models. By comparing the Ray-Born results to those of a full waveform solution obtained by a discrete wavenumber technique, we showed that results with about 15% accuracy in amplitude, often better, can be obtained as long as the wavelength is four to five times greater than the scale length of the perturbed region. The waveforms match fairly well also. For shorter wavelengths, the general trends of amplitude for forward scattering are predicted by both methods, but the Ray-Born results for the back scattered waves show two important failures. First, the amplitude continues to increase with increasing frequency of the incident wave, and, second, the Ray-Born method obtains only a single scattered pulse. In contrast, the full waveform approach shows that the true solution should reach a constant amplitude with two independent reflected waves from the front and back of the sphere.

Using these guidelines, we apply the Ray-Born computations to a layered earth

model containing a thin but laterally extensive fracture zone. The notions of shear wave scattering from anisotropic zones developed in Chapter 3 are confirmed here, as the reflected arrivals for shear wave incidence show a strong dependency on orientation of the polarization with respect to the fractures. Even for the larger, continuous fracture zone, no scattered shear waves are predicted when the incident wave is polarized parallel to the fractures. In contrast, we also confirm that the reflected waves due to an incident P-wave show almost no variation for different directions of observation since the incident wave is almost vertical in all cases. The use of compressional waves may be for the inference of the properties of the crack-filling material, as P-wave scattering from liquid-filled cracks is vanishingly small compared to scattering from gas-filled cracks.

The last application of the Ray-Born method is to the modeling of data from a VSP survey at the Badia 1A well in the Lardarello geothermal field. This location contains several fracture zones which are of importance for development of the geothermal resources. We presented a completely isotropic model for three fracture zones closely spaced in depth which was able to adequately match the observed scattered waves from below the depth of the well, even though some other well observations suggest the presence of vertical fractures. It was impossible to develop an anisotropic fracture model which could generate scattered signals as strong as those present in the VSP data set. Through the analysis of Fresnel zones for the scattering of waves from the fracture zones, we infer that the density of fracturing should increase significantly to the north of the Badia 1A well site.

5.1 Implications for Fracture Analysis with Seismic Data

The results from the two basic approaches to fracture modeling applied in this thesis allow some conclusions in regard to the practical analysis of fractured regions

through seismic exploration. An estimate of fracture orientations should be possible using different techniques. We can model the effects of aligned fractures on seismic velocities for a simple model of parallel cracks using the Hudson (1980, 1981) theory or for a more complex model allowing for a distribution of orientations by averaging the Hudson results over orientation. Chapter 2 shows that it is possible to invert for parameters describing this distribution from velocity measurements. Fracture orientation for regions sufficiently small that velocities cannot be practically estimated can be determined from the properties of scattered shear waves. Therefore, it seems reasonable to conclude that either velocity or reflected wave information can provide useful constraints on the orientation of subsurface fractures, as well as the more commonly applied polarization analyses (e.g., Crampin et al., 1986).

On the other hand, inference of a more detailed description of the crack shapes and sizes may be an elusive goal. This information, while not a strong influence on seismic properties, is probably very important in controlling rock properties such as permeability and conductivity. The results from Chapter 2 imply that even in the well controlled laboratory setting we could not obtain a unique description of the crack aspect ratio distribution. Mavko and Nur (1978) showed that it is possible to develop a crack model with a tapered crack shape which gives exactly the same results for elastic properties as the more commonly applied penny-shaped crack models (O'Connell and Budiansky, 1974; Kuster and Toksöz, 1974; Hudson, 1980). Schoenberg and Douma (1988) examined the extreme case of parallel joints of infinite extent and determined that a joint model can produce the same elastic behavior as a crack model. Details of cracks in real rocks may sometimes lead to an underestimate of crack density, as the complicated nature of crack surfaces will have asperities and other features which tend to prop open parts of cracks. This will reduce the compliance of an individual crack from the idealized model of a simple ellipsoidal void. Therefore, we must conclude that a detailed picture of the fractures beyond orientation in the subsurface will be difficult to obtain without *a priori* geologic knowledge which can,

for example, eliminate a joint model from consideration.

The implications of the results of Chapters 3 and 4 for the design of field experiments are important. Modeling of the waves reflected from a thin fracture zone shows that P-wave data will yield almost no information on anisotropic fracture alignment, which curtails the conclusions possible from the analysis of the Badia 1A VSP data. Therefore, if seismic data are to be used to attempt to locate and study fracture zones in the subsurface, the experiment should include the best quality shear wave data possible. In addition, a single source polarization will not be sufficient, as it is the variation of scattering with polarization direction relative to fracture orientation which signals the presence of aligned fractures. The ideal experiment would include at least two source polarizations. If it is of importance to make an estimate of the fluid filling the cracks, then comparison of P and S-wave scattering amplitudes will be of use, due to the sensitivity of P-wave scattering to pore contents. A large reflection observed on the shear wave data which is small or absent from compressional wave data suggests a liquid filled fracture or porous zone. Likewise, equal amplitude P and S-wave events indicate that the pore filling fluid is probably a gas.

5.2 Future Work

Wave propagation in fractured media is a complex problem for many reasons. The existence of aligned cracks alone introduces an effective anisotropy which significantly complicates data analysis relative to more ordinary isotropic materials. We have shown that even zones of anisotropy due to fracturing which are too thin to generate shear-wave splitting can generate shear wave reflections which could not be recorded in a purely isotropic medium. Research involving wave propagation must take into account such phenomena in order to begin to develop methods for interpreting the structure of the medium.

The first step which can be accomplished using existing ray-tracing algorithms is

the application of the Ray-Born method of Chapter 4 to anisotropic background media. At least in principle, this can be done using ray tracing techniques for anisotropic media (e.g., Gibson et al., 1991), though the effects of shear wave singularities and the accompanying numerical difficulties in ray tracing will make the problem more difficult. In addition, the numerical code will have to include the possibility of three types of incident waves as well three scattered waves. This extension will allow the inclusion of transversely isotropic media above or below the fractured zone such as is commonly found in sedimentary regions, and it will be possible to examine the effects of varying intensities of fracturing by taking a uniformly fractured medium as the background model. Perturbations to this background will allow an examination of the waves reflected from a zone of more or less intense fracturing.

The far more difficult problem is to develop a means of relating a more complex and realistic description of crack geometry to effective elastic properties. Cracks in rocks clearly are not penny-shaped and often intersect in complex patterns. While the theories developed to date can account for general trends in elastic behavior, it would be advantageous to have a theory which allows a unique relationship of crack shapes to elasticity. Unfortunately, the theoretical results discussed above suggest that this is not a likely development.

This thesis has demonstrated some distinct advances in the understanding of wave propagation in fractured media, however. We have shown the possibility of inverting for fracture orientations from velocity data, and have introduced an method for computing elastic wave scattering including the effects of localized anisotropic regions. In addition, we suggested a way to relate information on fracture orientation to directional variations of permeability. These methods allow the remote delineation of fractured regions in the subsurface along with the estimation of some important properties of the fracture zones, and future adaptations will allow the consideration of models of even greater complexity and realism.

Appendix A

Effective Elastic Constants for Fractured Media

Hudson (1980, 1981) presented a theory for the effective moduli of a homogeneous, isotropic medium containing cracks by considering the scattering from ellipsoidal inclusions with the assumption that the incident wavelength is much longer the the size of the ellipsoids and that there is only a dilute concentration of cracks, thereby deriving a single scattering approximation. In addition, it was assumed that the cracks were of low aspect ratio. In other words the cracks are "penny-shaped", with two equal semi-axes being much larger than the third. When the cracks are parallel, the resulting composite material is transversely isotropic with an axis of symmetry perpendicular to the crack orientation. If the cracks are vertical and perpendicular to the x axis, the following expressions for the effective constants may be written (Crampin, 1984):

$$\mathbf{C} \cong \mathbf{C^0} \tag{A.1}$$

$$- \frac{\xi}{\mu} \begin{bmatrix} (\lambda_0+2\mu_0)^2 U_{11} & \lambda_0(\lambda_0+2\mu_0)U_{11} & \lambda_0(\lambda_0+2\mu_0)U_{11} & & & & \\ \lambda_0(\lambda_0+2\mu_0)U_{11} & \lambda_0^2 U_{11} & \lambda_0^2 U_{11} & & & & \\ \lambda_0(\lambda_0+2\mu_0)U_{11} & \lambda_0^2 U_{11} & \lambda_0^2 U_{11} & & & & \\ & & & 0 & & & \\ & & & & \mu_0^2 U_{33} & & \\ & & & & & \mu_0^2 U_{33} & \end{bmatrix}$$

$$+ \frac{\xi^2}{15} \begin{bmatrix} (\lambda_0+2\mu_0)qU_{11}^2 & \lambda_0 qU_{11}^2 & \lambda_0 qU_{11}^2 & & & & \\ \lambda_0 qU_{11}^2 & \frac{\lambda_0^2 qU_{11}^2}{\lambda_0+2\mu_0} & \frac{\lambda_0^2 qU_{11}^2}{\lambda_0+2\mu_0} & & & & \\ \lambda_0 qU_{11}^2 & \frac{\lambda_0^2 qU_{11}^2}{\lambda_0+2\mu_0} & \frac{\lambda_0^2 qU_{11}^2}{\lambda_0+2\mu_0} & & & & \\ & & & 0 & & & \\ & & & & XU_{33}^2 & & \\ & & & & & XU_{33}^2 & \end{bmatrix},$$

where

$$\begin{aligned} q &= 15\frac{\lambda_0^2}{\mu_0^2} + 28\frac{\lambda_0}{\mu_0} + 28 \\ X &= 2\mu_0 \frac{3\lambda_0 + 8\mu_0}{\lambda_0 + 2\mu_0}. \end{aligned}$$

Here λ_0 and μ_0 are the the Lamé parameters of the unfractured background medium, and ξ is the crack density na^3. In this expression n is the number density of cracks and a is the radius of the cracks.

The parameters U_{11} and U_{33} are related to the Lamé parameters of the material filling the cracks. For cracks filled with a material with Lamé parameters λ_1 and μ_1 low compared to those of the matrix medium, they are given by

$$\begin{aligned} U_{11} &= \frac{4}{3}\frac{\lambda_0+2\mu_0}{\lambda_0+\mu_0}\frac{1}{1+K} \\ U_{33} &= \frac{16}{3}\frac{\lambda_0+2\mu_0}{3\lambda_0+4\mu_0}\frac{1}{1+M} \end{aligned} \tag{A.2}$$

$$
\begin{aligned}
K &= \frac{\kappa_1 + 4/3\mu_1}{\pi\alpha\mu_0}\frac{\lambda_0 + 2\mu_0}{\lambda_0 + \mu_0} \\
M &= \frac{4\mu_1}{\pi\alpha\mu_0}\frac{\lambda_0 + 2\mu_0}{3\lambda_0 + 4\mu_0} \\
\kappa_1 &= \lambda_1 + \mu_1.
\end{aligned}
$$

In these expressions, α is the aspect ratio of the cracks, the ratio of the small semi-axis to large semi-axis. As K and M both vanish when the stiffnesses of the crack-filling material go to zero, the aspect ratio will have no effect on the effective elastic constants for cracks which are empty or filled with a material with very low bulk modulus, such as a low pressure gas.

In this configuration, with the x axis serving as the symmetry axis, the three elastic waves are not simply categorizable in terms of polarizations. However, the phase velocities in a given direction can be determined using Christoffel's equation in the form (Musgrave, 1970)

$$
\begin{aligned}
(\Gamma_{jk} - V^2\delta_{jk})g_k = 0, \qquad \text{(A.3)} \\
\Gamma_{jk} = \frac{C_{ijkl}}{\rho}n_i n_l.
\end{aligned}
$$

The n_i are the components of the unit vector $\widehat{N}$ in the desired direction for the phase velocity vector, and the summation convention is applied. There are in general three different eigenvalues V^2 corresponding to the squared phase velocity for two quasi-shear waves and the quasi-compressional wave. This equation also yields the polarizations $\mathbf{g}$, the eigenvectors, of the three waves. When the symmetry axis of a transversely isotropic medium is vertical, the three waves are a true SH wave, a quasi-SV wave and a quasi-P wave. The latter two waves have polarizations which are contained in a vertical plane, but are not exactly the same is a true SV or P-wave in an isotropic medium. Phase velocity expressions for waves in the transversely isotropic medium are given in Chapter 2 (equations 2.10 to 2.12).

Hudson (1980, 1981) also extended these relationships to media with a purely random distribution of cracks, an isotropic effective medium. In this case the Lamé

parameters of the composite material are

$$\begin{aligned}\mu &\cong \mu_0 + \mu_0[-\xi\frac{2}{15}(3U_{33}+2U_{11}) + \xi^2\left(\frac{2}{15}\right)^3\left(\frac{3\lambda_0+8\mu_0}{\lambda_0+\mu_0}\right)(3U_{33}+2U_{11})^2] \quad \text{(A.4)}\\ &= \mu_0 + \delta\mu\end{aligned}$$

$$\begin{aligned}\lambda &\cong \lambda_0 - \xi\left[\frac{(3\lambda_0+2\mu_0)^2}{9\mu_0} + \frac{2}{3}\frac{2\mu_0}{15}(3U_{33}+2U_{11})\right]\\ &\quad + \xi^2\left[\frac{(3\lambda_0+2\mu_0)^4}{81\mu_0^2(\lambda_0+2\mu_0)}U_{11}^2 - \frac{2}{3}\mu_0\left(\frac{2}{15}\right)^3\frac{3\lambda_0+8\mu_0}{\lambda_0+2\mu_0}(3U_{33}+2U_{11})^2\right] \quad \text{(A.5)}\\ &= \lambda_0 + \delta\lambda.\end{aligned}$$

As for the anisotropic example, this is an expansion to second order in crack density.

Other theories for the effective moduli of both anisotropic and isotropic materials with cracks have been presented. For example, Nishizawa (1982) presented an interative numerical scheme for the evaluation of the effective properties of an anisotropically fractured medium which in principle can incorporate fairly high crack densities and aspect ratios ranging from very flat, ellipsoidal cracks to spherical pores. This approach is an extension and improvement of the results of Anderson et al. (1974). Douma (1988) examined and compared the two approaches and showed that the Nishizawa (1982) and Hudson (1980, 1981) methods give similar results for aspect ratios up to 0.30, assuming a crack density of 0.05. This suggests that the Hudson (1980, 1981) theory gives a good representation of the elastic behavior of the model of a homogeneous, isotropic matrix containing aligned, ellipsoidal cracks. In regard to the isotropic material with randomly aligned cracks, some disparity apparently exists between the numerous results which have been published. While most of the results agree to first order in crack density (e.g., Toksöz et al., 1976; Chatterjee et al., 1978; O'Connell and Budiansky, 1974; Hudson, 1980), the results for the second order term differ. These differences are not easily reconciled and depend on large part on the statistical assumptions built into the models (Hudson, 1980).

Appendix B

Derivations of Radiation Patterns for Rayleigh Scattering

In Chapter 3 the derivation of the most general expression for Rayleigh scattering due to an anisotropic obstacle was presented (equation (3.12)). Here we present the derivations of explicit equations for the radiation patterns for a perturbation to an example of each of the five general categories of elastic constants from section 3.2.2 using the spherical coordinate expressions presented in Appendix C. Patterns for all 21 independent constants are summarized in Appendix D.

B.1 Single dipole

Equation (3.11) shows that a perturbation to δC_{11} results in a moment tensor source with a single dipole oriented along the $x-$axis:

$$\delta \mathbf{M} = \begin{bmatrix} \delta C_{11}\epsilon_{11}^0 & 0 & 0 \\ 0 & 0 & 0 \\ 0 & 0 & 0 \end{bmatrix}. \tag{B.1}$$

We consider an incident compressional plane wave with displacement given by

$$\mathbf{u}^0(\mathbf{x},t) = A\mathbf{p}e^{i(\omega t - \mathbf{k}_\alpha \cdot \mathbf{x})} \tag{B.2}$$

$$\begin{aligned}
\mathbf{p} &= \sin\theta_0\cos\phi_0\mathbf{e_x} + \sin\theta_0\sin\phi_0\mathbf{e_y} + \cos\theta_0\mathbf{e_z} \\
\mathbf{k}_\alpha &= \frac{\omega}{\alpha}\mathbf{p}
\end{aligned}$$

The two angles θ_0 and ϕ_0 are the two spherical coordinate angles (Figure 3-2). Utilizing equation (3.12) for the far-field displacement and equation (B.1) for the δM_{11} gives the scattered field vector:

$$\begin{aligned}
\delta\mathbf{u}(\mathbf{x},t) &= \delta V\delta C_{11}\epsilon^0_{11}(\mathbf{0},0)[G^0_{11,1}\mathbf{e_x} + G^0_{21,1}\mathbf{e_y} + G^0_{31,1}\mathbf{e_z}] \\
&= \delta V\delta C_{11}\epsilon^0_{11}[\partial_1(\mathbf{G^0}\cdot\mathbf{e_x})].
\end{aligned}$$

Here $\mathbf{G}^0$ without subscripts indicates the Green's tensor. The strain $\epsilon^0_{11} = u^0_{1,1}$ due to the incident wave is

$$\begin{aligned}
u^0_{1,1} &= -ik_\alpha A\sin^2\theta_0\cos^2\phi_0 e^{i\psi_\alpha} \qquad \text{(B.3)} \\
\psi_\alpha &= \omega t - \mathbf{k}_\alpha\cdot\mathbf{x} \\
k_\alpha &= |\mathbf{k}_\alpha|
\end{aligned}$$

Spherical coordinates provide a natural reference frame for expressing the radiation patterns for a source at the origin, since the radiated compressional waves will only have a radial component $\mathbf{e_r}$ of displacement, vertically polarized shear waves (SV) will only have a θ component e_θ, and horizontally polarized shear waves (SH) only have a ϕ component e_ϕ (Figure 3-2). Substituting for $\partial_1(\mathbf{G^0}\cdot\mathbf{e_x})$ in spherical coordinates (Appendix C), we derive the following scattered displacement field for the incident compressional wave:

$$\delta\mathbf{u}^P(\mathbf{x},t) = \delta V\delta C_{11}(-ik_\alpha A\sin^2\theta_0\cos^2\theta_0)\mathbf{s} \qquad \text{(B.4)}$$

$$\begin{aligned}
\mathbf{s} &= \mathbf{e_r}\sin^2\theta\cos^2\phi\left(\frac{-ik_\alpha e^{i\psi_\alpha}}{4\pi\alpha^2\rho r}\right) + \mathbf{e_\theta}\sin\theta\cos\theta\cos^2\phi\left(\frac{-ik_\beta e^{i\psi_\beta}}{4\pi\beta^2\rho r}\right) \\
&\quad -\mathbf{e_\phi}\sin\theta\cos\phi\sin\phi\left(\frac{-ik_\beta e^{i\psi_\beta}}{4\pi\beta^2\rho r}\right) \\
\psi_\beta &= \omega t - \mathbf{k}_\beta\cdot\mathbf{x} \\
\mathbf{k}_\beta &= \frac{\omega}{\beta}\mathbf{p} \\
k_\beta &= |\mathbf{k}_\beta|.
\end{aligned}$$

The individual components may be written

$$\begin{aligned}
\delta u_r^P(\mathbf{x},t) &= -(\delta V \delta C_{11} A \sin^2\theta_0 \cos^2\phi_0)\frac{\omega^2}{4\pi\rho\alpha^4}\frac{e^{i(\omega t - r/\alpha)}}{r}\sin^2\theta\cos^2\phi \\
\delta u_\theta^P(\mathbf{x},t) &= -(\delta V \delta C_{11} A \sin^2\theta_0 \cos^2\phi_0)\frac{\omega^2}{4\pi\rho\alpha\beta^3}\frac{e^{i(\omega t - r/\beta)}}{r}\sin\theta\cos\theta\cos^2\phi \quad \text{(B.5)} \\
\delta u_\phi^P(\mathbf{x},t) &= +(\delta V \delta C_{11} A \sin^2\theta_0 \cos^2\phi_0)\frac{\omega^2}{4\pi\rho\alpha\beta^3}\frac{e^{i(\omega t - r/\beta)}}{r}\sin\theta\cos\phi\sin\phi
\end{aligned}$$

The P, SV and SH fields are given by δu_r, δu_θ and δu_ϕ, respectively. No scattered field is generated for incidence in the $y-z$ plane.

The polarization of an incident SV-wave is defined to be in the $\mathbf{e}_\theta$ direction (Figure 3-2) for a given wave normal direction $\mathbf{p}$. The displacement associated with this plane wave is

$$\begin{aligned}
\mathbf{u^0}(\mathbf{x},t) &= A\mathbf{p^{SV}}e^{i(\omega t - \mathbf{k}_\beta\cdot\mathbf{x})} \quad \text{(B.6)} \\
\mathbf{p^{SV}} &= \mathbf{e_x}\cos\theta_0\cos\phi_0 + \mathbf{e_y}\cos\theta_0\sin\theta_0 - \mathbf{e_z}\sin\theta_0.
\end{aligned}$$

The vector $\mathbf{p^{SV}}$ giving the direction of shear displacement is the unit vector $\mathbf{e}_\theta$ expressed in Cartesian coordinates (Ben-Menahem and Singh, 1981). For this wave the incident strain $u^0_{1,1}$ associated with the moment tensor source is

$$u^0_{1,1} = -ik_\beta A \sin\theta_0\cos\theta_0\cos^2\phi_0 e^{i\psi_\beta}, \quad \text{(B.7)}$$

and the components of the scattered field are

$$\begin{aligned}
\delta u_r^{SV}(\mathbf{x},t) &= -(\delta V \delta C_{11} A \sin\theta_0\cos\theta_0\cos^2\phi_0)\frac{\omega^2}{4\pi\rho\beta\alpha^3}\frac{e^{i(\omega t - r/\alpha)}}{r}\sin^2\theta\cos^2\phi \\
\delta u_\theta^{SV}(\mathbf{x},t) &= -(\delta V \delta C_{11} A \sin\theta_0\cos\theta_0\cos^2\phi_0)\frac{\omega^2}{4\pi\rho\beta^4}\frac{e^{i(\omega t - r/\beta)}}{r}\sin\theta\cos\theta\cos^2\phi \quad \text{(B.8)} \\
\delta u_\phi^{SV}(\mathbf{x},t) &= +(\delta V \delta C_{11} A \sin\theta_0\cos\theta_0\cos^2\phi_0)\frac{\omega^2}{4\pi\rho\beta^4}\frac{e^{i(\omega t - r/\beta)}}{r}\sin\theta\cos\phi\sin\phi.
\end{aligned}$$

Therefore, we see that the P and SV incident waves have the same directional variation of the radiation pattern, though the dependence on incidence angle is different. The scattered field vanishes for incidence in the $x-y$ and $y-z$ planes. In addition, the

quantities multiplying the angular terms are different. For $\theta_0 = \pi/4$, the scattered amplitudes due to an incident SV wave are larger by a factor of α/β due to the different weighting coefficients.

Finally, we can consider the scattering due to the δC_{11} perturbation in the case of an incident SH wave. Define the incident polarization to be in the direction of $\mathbf{e}_\phi$ (Ben-Menahem and Singh, 1981):

$$\begin{aligned} \mathbf{u^0}(\mathbf{x},t) &= A\mathbf{p^{SH}} e^{i(\omega t - \mathbf{k}_\beta \cdot \mathbf{x})} \\ \mathbf{p^{SH}} &= -\sin\phi_0 \mathbf{e_x} + \cos\phi_0 \mathbf{e_y}. \end{aligned} \tag{B.9}$$

The strain component for this wave is

$$u^0_{1,1} = +ik_\beta A \sin\theta_0 \sin\phi_0 \cos\phi_0 e^{i\psi_\beta}, \tag{B.10}$$

and the scattered waves are

$$\begin{aligned} \delta u_r^{SH}(\mathbf{x},t) &= +(\delta V \delta C_{11} A \sin\theta_0 \cos\phi_0 \sin\phi_0) \frac{\omega^2}{4\pi\rho\beta\alpha^3} \frac{e^{i(\omega t - r/\alpha)}}{r} \sin^2\theta \cos^2\phi \\ \delta u_\theta^{SH}(\mathbf{x},t) &= +(\delta V \delta C_{11} A \sin\theta_0 \cos\phi_0 \sin\phi_0) \frac{\omega^2}{4\pi\rho\beta^4} \frac{e^{i(\omega t - r/\beta)}}{r} \sin\theta \cos\theta \cos^2\phi \\ \delta u_\phi^{SH}(\mathbf{x},t) &= -(\delta V \delta C_{11} A \sin\theta_0 \cos\phi_0 \sin\phi_0) \frac{\omega^2}{4\pi\rho\beta^4} \frac{e^{i(\omega t - r/\beta)}}{r} \sin\theta \cos\phi \sin\phi. \end{aligned} \tag{B.11}$$

The relative amplitude of scattering due to SH incidence will be similar to that due to an incident SV wave. There is no scattering predicted for an incident wave in either the $x-z$ or $y-z$ planes. In these cases, $u^0_{1,1} = 0$, and so the moment tensor is also identically zero.

B.2 Two dipoles

As an example of this category of elastic constant scattering, we consider a perturbation to δC_{13}. Again applying equation (3.9), the moment tensor source is

$$\delta\mathbf{M} = \begin{bmatrix} \delta C_{13}\epsilon^0_{33} & 0 & 0 \\ 0 & 0 & 0 \\ 0 & 0 & \delta C_{13}\epsilon^0_{11} \end{bmatrix}. \tag{B.12}$$

The total scattered field will be that due to a superposition of two dipoles, one oriented along the $x-$axis, the other along the $z-$axis, proportional to the ϵ^0_{33} and ϵ^0_{11} components of the strain tensor, respectively.

The general expression for the scattered field in this case can be written

$$\delta\mathbf{u}(\mathbf{x},t) = \delta V \delta C_{13}[\epsilon^0_{33}(\mathbf{0},0)(\partial_1(\mathbf{G^0}\cdot\mathbf{e_x})) + \epsilon^0_{11}(\mathbf{0},0)(\partial_3(\mathbf{G^0}\cdot\mathbf{e_z}))]. \tag{B.13}$$

Considering first the incident compressional plane wave, and applying the displacements given by equation (B.2), the strain components in the source are

$$\begin{aligned} u^0_{1,1} &= -ik_\alpha A \sin^2\theta_0 \cos^2\phi_0 e^{i\psi_\alpha} \\ u^0_{3,3} &= -ik_\alpha A \cos^2\theta_0 e^{i\psi_\alpha} \end{aligned} \tag{B.14}$$

Using these expressions in the equation for the scattered field and again applying spherical far-field equivalents for $\partial_1(\mathbf{G^0}\cdot\mathbf{e_x})$ and $\partial_3(\mathbf{G^0}\cdot\mathbf{e_z})$ (Appendix C) yields

$$\begin{aligned} \delta u^P_r(\mathbf{x},t) &= -(\delta V\delta C_{13}A)\frac{\omega^2}{4\pi\rho\alpha^4}\frac{e^{i(\omega t - r/\alpha)}}{r} \\ &\quad \times [\cos^2\theta_0 \sin^2\theta\cos^2\phi + \sin^2\theta_0\cos^2\phi_0\cos^2\theta] \\ \delta u^P_\theta(\mathbf{x},t) &= -(\delta V\delta C_{13}A)\frac{\omega^2}{4\pi\rho\alpha\beta^3}\frac{e^{i(\omega t - r/\beta)}}{r} \\ &\quad \times [\cos^2\theta_0 \sin\theta\cos\theta\cos^2\phi - \sin^2\theta_0\cos^2\phi_0\sin\theta\cos\theta] \\ \delta u^P_\phi(\mathbf{x},t) &= +(\delta V\delta C_{13}A)\frac{\omega^2}{4\pi\rho\alpha\beta^3}\frac{e^{i(\omega t - r/\beta)}}{r}[\cos^2\theta_0\sin\theta\cos\phi\sin\phi]. \end{aligned} \tag{B.15}$$

Next examining the SV wave incident displacement, given in equation (B.6), the appropriate strains are

$$\begin{aligned} u^0_{1,1} &= -ik_\beta A \sin\theta_0\cos\theta_0\cos^2\phi_0 e^{i\psi_\beta} \\ u^0_{3,3} &= +ik_\beta A \sin\theta_0\cos\theta_0 e^{i\psi_\beta}. \end{aligned} \tag{B.16}$$

Substituted into equation (B.13), the resulting scattering in spherical coordinates is

$$\begin{aligned} \delta u^{SV}_r(\mathbf{x},t) &= -(\delta V\delta C_{13}A)\frac{\omega^2}{4\pi\rho\beta\alpha^3}\frac{e^{i(\omega t - r/\alpha)}}{r} \\ &\quad \times \sin\theta_0\cos\theta_0[-\sin^2\theta\cos^2\phi + \cos^2\phi_0\cos^2\theta] \end{aligned}$$

$$\begin{aligned}
\delta u_\theta^{SV}(\mathbf{x},t) &= -(\delta V \delta C_{13} A)\frac{\omega^2}{4\pi\rho\beta^4}\frac{e^{i(\omega t - r/\beta)}}{r} \\
&\quad \sin\theta_0 \cos\theta_0 \sin\theta \cos\theta[-\cos^2\phi - \cos^2\phi_0] \qquad \text{(B.17)} \\
\delta u_\phi^{SV}(\mathbf{x},t) &= +(\delta V \delta C_{13} A)\frac{\omega^2}{4\pi\rho\beta^4}\frac{e^{i(\omega t - r/\beta)}}{r}\sin\theta_0\cos\theta_0[\sin\theta\cos\phi\sin\phi].
\end{aligned}$$

The SH incident wave has the displacement given in equation (B.9), and the resulting strains are

$$\begin{aligned}
u^0_{1,1} &= +ik_\beta A \sin\theta_0 \sin\phi_0 \cos\phi_0 e^{i\psi_\beta} \\
u^0_{3,3} &= 0. \qquad \text{(B.18)}
\end{aligned}$$

Since the $u^0_{3,3}$ strain is identically zero, the scattering takes a simpler form than for incident P or SV waves and includes only a δM_{33} dipole source:

$$\begin{aligned}
\delta u_r^{SH}(\mathbf{x},t) &= +(\delta V \delta C_{13} A)\frac{\omega^2}{4\pi\rho\beta\alpha^3}\frac{e^{i(\omega t - r/\alpha)}}{r}[\sin\theta_0\cos\phi_0\sin\phi_0\cos^2\theta] \\
\delta u_\theta^{SH}(\mathbf{x},t) &= -(\delta V \delta C_{13} A)\frac{\omega^2}{4\pi\rho\beta^4}\frac{e^{i(\omega t - r/\beta)}}{r}[\sin\theta_0\cos\phi_0\sin\phi_0\sin\theta\cos\theta] \qquad \text{(B.19)} \\
\delta u_\phi^{SH}(\mathbf{x},t) &= 0.
\end{aligned}$$

Therefore, there is no SH to SH scattering for a perturbation to δC_{13}, and an SH wave will pass by the obstacle generating no scattering.

B.3 Double couple

An example of a perturbation leading to one double couple radiation pattern is δC_{66}. In this case, the moment tensor is

$$\delta\mathbf{M} = \begin{bmatrix} 0 & 2\epsilon^0_{12}\delta C_{66} & 0 \\ 2\epsilon^0_{12}\delta C_{66} & 0 & 0 \\ 0 & 0 & 0 \end{bmatrix}, \qquad \text{(B.20)}$$

and the scattered field is given by

$$\delta\mathbf{u}(\mathbf{x},t) = \delta V \delta C_{12}(u^0_{1,2} + u^0_{2,1})[\partial_2(\mathbf{G^0}\cdot\mathbf{e_x} + \partial_1(\mathbf{G^0}\cdot\mathbf{e_y}]. \qquad \text{(B.21)}$$

For the incident compressional wave,

$$2\epsilon^0_{12} = u^0_{1,2} + u^0_{2,1} = -ik_\alpha \sin^2\theta_0 \sin 2\phi_0 A e^{i\psi_\alpha}, \tag{B.22}$$

and so the scattered field is

$$\begin{aligned}
\delta u^P_r(\mathbf{x},t) &= -(\delta V \delta C_{66} A)\frac{\omega^2}{4\pi\rho\alpha^4}\frac{e^{i(\omega t - r/\alpha)}}{r}[\sin^2\theta_0 \sin 2\phi_0 \sin^2\theta \sin 2\phi] \\
\delta u^P_\theta(\mathbf{x},t) &= -(\delta V \delta C_{66} A)\frac{\omega^2}{4\pi\rho\alpha\beta^3}\frac{e^{i(\omega t - r/\beta)}}{r}[\sin^2\theta_0 \sin 2\phi_0 \sin\theta\cos\theta \sin 2\phi] \\
\delta u^P_\phi(\mathbf{x},t) &= -(\delta V \delta C_{66} A)\frac{\omega^2}{4\pi\rho\alpha\beta^3}\frac{e^{i(\omega t - r/\beta)}}{r}[\sin^2\theta_0 \sin 2\phi_0 \sin\theta\cos 2\phi].
\end{aligned} \tag{B.23}$$

Note that no scattering is obtained when the incident signal propagates in either the $x-z$ or $y-z$ planes. In this case, the perturbation is undetectable.

If the incident wave is an SV-wave, the incident strain is

$$2\epsilon^0_{12} = -ik_\beta \sin\theta_0 \cos\theta_0 \sin 2\phi_0 A e^{i\psi_\beta}, \tag{B.24}$$

and the scattering is

$$\begin{aligned}
\delta u^{SV}_r(\mathbf{x},t) &= -(\delta V \delta C_{66} A)\frac{\omega^2}{4\pi\rho\beta\alpha^3}\frac{e^{i(\omega t - r/\alpha)}}{r}[\sin\theta_0\cos\theta_0 \sin 2\phi_0 \sin^2\theta \sin 2\phi] \\
\delta u^{SV}_\theta(\mathbf{x},t) &= -(\delta V \delta C_{66} A)\frac{\omega^2}{4\pi\rho\beta^4}\frac{e^{i(\omega t - r/\beta)}}{r} \\
&\quad \times [\sin\theta_0\cos\theta_0 \sin 2\phi_0 \sin\theta\cos\theta \sin 2\phi] \\
\delta u^{SV}_\phi(\mathbf{x},t) &= -(\delta V \delta C_{66} A)\frac{\omega^2}{4\pi\rho\beta^4}\frac{e^{i(\omega t - r/\beta)}}{r}[\sin\theta_0\cos\theta_0 \sin 2\phi_0 \sin\theta\cos 2\phi].
\end{aligned} \tag{B.25}$$

Again there is no scattering for the incident wave travelling in the $x-z$ or $y-z$ vertical planes, but the scattering is also absent for vertical and horizontal incident signals.

Finally, for incident SH-waves, we have

$$2\epsilon^0_{12} = -ik_\beta \sin\theta_0 \cos 2\phi_0 A e^{i\psi_\beta}. \tag{B.26}$$

The scattered waves are

$$\delta u^{SH}_r(\mathbf{x},t) = -(\delta V \delta C_{66} A)\frac{\omega^2}{4\pi\rho\beta\alpha^3}\frac{e^{i(\omega t - r/\alpha)}}{r}[\sin\theta_0\cos 2\phi_0 \sin^2\theta \sin 2\phi]$$

$$\delta u_\theta^{SH}(\mathbf{x},t) = -(\delta V \delta C_{66} A)\frac{\omega^2}{4\pi\rho\beta^4}\frac{e^{i(\omega t - r/\beta)}}{r}[\sin\theta_0 \cos 2\phi_0 \sin\theta \cos\theta \sin 2\phi] \quad \text{(B.27)}$$

$$\delta u_\phi^{SH}(\mathbf{x},t) = -(\delta V \delta C_{66} A)\frac{\omega^2}{4\pi\rho\beta^4}\frac{e^{i(\omega t - r/\beta)}}{r}[\sin\theta_0 \cos 2\phi_0 \sin\theta \cos 2\phi].$$

For the incident SH-wave, the δC_{66} perturbation causes no scattering for vertical incidence, and for incident waves propagating in the vertical planes at $\theta_0 = \pi/4$ and $\theta_0 = 3\pi/4$. In both of these cases, the ϵ_{12}^0 strain associated with the SH-wave vanishes.

B.4 Double couple and a dipole

The radiation pattern equivalent to that of superposition of a dipole and a double couple is generated by a perturbation to δC_{14}. For this perturbation, the dipole is oriented along the x-axis, and the double couple moment tensor elements are $\delta M_{23} = \delta M_{32}$:

$$\delta\mathbf{M} = \begin{bmatrix} 2\epsilon_{23}^0 \delta C_{14} & 0 & 0 \\ 0 & 0 & \epsilon_{11}^0 \delta C_{14} \\ 0 & \epsilon_{11}^0 \delta C_{14} & 0 \end{bmatrix}, \quad \text{(B.28)}$$

and the general scattered field is given by

$$\delta\mathbf{u}(\mathbf{x},t) = \delta V \delta C_{14}[(u_{2,3}^0 + u_{3,2}^0)\partial_1(\mathbf{G^0}\cdot\mathbf{e_x}) + (u_{1,1}^0)(\partial_2(\mathbf{G^0}\cdot\mathbf{e_z}) + \partial_3(\mathbf{G^0}\cdot\mathbf{e_y}))]. \quad \text{(B.29)}$$

For the incident compressional wave, the strain components of interest are

$$\begin{aligned} \epsilon_{11}^0 &= -ik_\alpha \sin^2\theta_0 \cos^2\phi_0 A e^{i\psi_\alpha} \\ 2\epsilon_{23}^0 &= -ik_\alpha \sin 2\theta_0 \sin\phi_0 A e^{i\psi_\alpha}, \end{aligned} \quad \text{(B.30)}$$

and the scattered field is

$$\begin{aligned} \delta u_r^P(\mathbf{x},t) &= -(\delta V \delta C_{14} A)\frac{\omega^2}{4\pi\rho\alpha^4}\frac{e^{i(\omega t - r/\alpha)}}{r} \\ &\quad \times [\sin^2\theta_0 \cos^2\phi_0 \sin 2\theta \sin\phi + \sin 2\theta_0 \sin\phi_0 \sin^2\theta \cos^2\phi] \\ \delta u_\theta^P(\mathbf{x},t) &= -(\delta V \delta C_{14} A)\frac{\omega^2}{4\pi\rho\alpha\beta^3}\frac{e^{i(\omega t - r/\beta)}}{r} \end{aligned}$$

$$\times [\sin^2\theta_0 \cos^2\phi_0 \cos 2\theta \sin\phi + \sin 2\theta_0 \sin\phi_0 \sin\theta \cos\theta \cos^2\phi] \quad \text{(B.31)}$$

$$\delta u_\phi^P(\mathbf{x},t) = -(\delta V \delta C_{14} A)\frac{\omega^2}{4\pi\rho\alpha\beta^3}\frac{e^{i(\omega t - r/\beta)}}{r}$$
$$\times [\sin^2\theta_0 \cos^2\phi_0 \cos\theta \cos\phi - \sin 2\theta_0 \sin\phi_0 \sin\theta \sin\phi \cos\phi].$$

Because of the superposition of a dipole and a double couple source, the dependence of the radiation pattern on the incidence direction is more complicated than for the δC_{66} perturbation, and there are no vertical planes of incidence for which no scattering is generated. However, the vertically incident plane wave will not generate any scattered fields.

For an incident SV-wave, the strains are

$$\epsilon_{11}^0 = -ik_\beta \cos\theta_0 \sin\theta_0 \cos^2\phi_0 A e^{i\psi_\beta}$$
$$2\epsilon_{23}^0 = -ik_\beta \cos 2\theta_0 \sin\phi_0 A e^{i\psi_\beta}, \quad \text{(B.32)}$$

and the scattered fields are

$$\delta u_r^{SV}(\mathbf{x},t) = -(\delta V \delta C_{14} A)\frac{\omega^2}{4\pi\rho\beta\alpha^3}\frac{e^{i(\omega t - r/\alpha)}}{r}$$
$$\times [\sin\theta_0 \cos\theta_0 \cos^2\phi_0 \sin 2\theta \sin\phi + \cos 2\theta_0 \sin\phi_0 \sin^2\theta \cos^2\phi]$$
$$\delta u_\theta^{SV}(\mathbf{x},t) = -(\delta V \delta C_{14} A)\frac{\omega^2}{4\pi\rho\beta^4}\frac{e^{i(\omega t - r/\beta)}}{r}$$
$$\times [\sin\theta_0 \cos\theta_0 \cos^2\phi_0 \cos 2\theta \sin\phi$$
$$+ \cos 2\theta_0 \sin\phi_0 \sin\theta \cos\theta \cos^2\phi] \quad \text{(B.33)}$$
$$\delta u_\phi^{SV}(\mathbf{x},t) = -(\delta V \delta C_{14} A)\frac{\omega^2}{4\pi\rho\beta^4}\frac{e^{i(\omega t - r/\beta)}}{r}$$
$$\times [\sin\theta_0 \cos\theta_0 \cos^2\phi_0 \cos\theta \cos\phi$$
$$- \cos 2\theta_0 \sin\phi_0 \sin\theta \sin\phi \cos\phi].$$

In this case, there is no set of incidence directions for which scattering is absent, since the ϵ_{11}^0 and ϵ_{23}^0 strain tensor components do not vanish in the same directions.

Lastly, the appropriate strains associated with an SH-wave are

$$\epsilon_{11}^0 = +ik_\beta \sin\theta_0 \sin\phi_0 \cos\phi_0 A e^{i\psi_\beta}$$
$$2\epsilon_{23}^0 = -ik_\beta \cos\theta_0 \cos\phi_0 A e^{i\psi_\beta}, \quad \text{(B.34)}$$

and the scattered displacement fields are given by

$$\begin{aligned}
\delta u_r^{SH}(\mathbf{x},t) &= -(\delta V \delta C_{14} A)\frac{\omega^2}{4\pi\rho\beta\alpha^3}\frac{e^{i(\omega t - r/\alpha)}}{r} \\
&\quad \times [-\sin\theta_0 \sin\phi_0 \cos\phi_0 \sin 2\theta \sin\phi + \cos\theta_0 \cos\phi_0 \sin^2\theta \cos^2\phi] \\
\delta u_\theta^{SH}(\mathbf{x},t) &= -(\delta V \delta C_{14} A)\frac{\omega^2}{4\pi\rho\beta^4}\frac{e^{i(\omega t - r/\beta)}}{r} \\
&\quad \times [-\sin\theta_0 \sin\phi_0 \cos\phi_0 \cos 2\theta \sin\phi \\
&\quad + \cos\theta_0 \cos\phi_0 \sin\theta \cos\theta \cos^2\phi] \qquad \text{(B.35)} \\
\delta u_\phi^{SH}(\mathbf{x},t) &= -(\delta V \delta C_{14} A)\frac{\omega^2}{4\pi\rho\beta^4}\frac{e^{i(\omega t - r/\beta)}}{r} \\
&\quad \times [-\sin\theta_0 \sin\phi_0 \cos\phi_0 \cos\phi \cos\theta - \cos\theta_0 \cos\phi_0 \sin\theta \sin\phi \cos\phi].
\end{aligned}$$

In this case, there is no scattering when the incident SH-wave travels in the $y-z$ vertical plane, where $\epsilon_{11}^0 = \epsilon_{23}^0 = 0$.

B.5 Two double couples.

As an example of this final category of scattering source representations, we consider the perturbation to δC_{45}. The moment tensor for this perturbation is

$$\delta\mathbf{M} = \begin{bmatrix} 0 & 0 & \delta V \delta C_{45} 2\epsilon_{23}^0 \\ 0 & 0 & \delta V \delta C_{45} 2\epsilon_{13}^0 \\ \delta V \delta C_{45} 2\epsilon_{23}^0 & \delta V \delta C_{45} 2\epsilon_{13}^0 & 0 \end{bmatrix}. \qquad \text{(B.36)}$$

Here we write the general scattered field as

$$\begin{aligned}
\delta\mathbf{u}(\mathbf{x},t) &= \delta V \delta C_{45}[(u_{2,3}^0 + u_{3,2}^0)(\partial_1(\mathbf{G^0}\cdot\mathbf{e_z}) + \\
&\quad \partial_3(\mathbf{G^0}\cdot\mathbf{e_x})) + (u_{1,3}^0 + u_{3,1}^0)(\partial_2(\mathbf{G^0}\cdot\mathbf{e_z}) + \partial_3(\mathbf{G^0}\cdot\mathbf{e_y}))]. \qquad \text{(B.37)}
\end{aligned}$$

The strain components induced by an incident compressional wave are

$$\begin{aligned}
2\epsilon_{13}^0 &= -ik_\alpha \sin 2\theta_0 \cos\phi_0 A e^{i\psi_\alpha} \\
2\epsilon_{23}^0 &= -ik_\alpha \sin 2\theta_0 \sin\theta_0 A e^{i\psi_\alpha}, \qquad \text{(B.38)}
\end{aligned}$$

and the scattered displacements are

$$\begin{aligned}
\delta u_r^P(\mathbf{x},t) &= -(\delta V \delta C_{45} A)\frac{\omega^2}{4\pi\rho\alpha^4}\frac{e^{i(\omega t - r/\alpha)}}{r}(\sin 2\theta_0 \sin 2\theta)[\sin(\phi+\phi_0)] \\
\delta u_\theta^P(\mathbf{x},t) &= -(\delta V \delta C_{45} A)\frac{\omega^2}{4\pi\rho\alpha\beta^3}\frac{e^{i(\omega t - r/\beta)}}{r}\sin 2\theta_0 \cos 2\theta[\sin(\phi+\phi_0)] \\
\delta u_\phi^P(\mathbf{x},t) &= -(\delta V \delta C_{45} A)\frac{\omega^2}{4\pi\rho\alpha\beta^3}\frac{e^{i(\omega t - r/\beta)}}{r}\sin 2\theta_0 \cos\theta[\cos(\phi+\phi_0)].
\end{aligned} \tag{B.39}$$

All scattered fields vanish for both vertical and horizontal incidence in this case.

SV-wave incidence yields the following strain components:

$$\begin{aligned}
2\epsilon_{13}^0 &= -ik_\beta \cos 2\theta_0 \cos\phi_0 A e^{i\psi_\beta} \\
2\epsilon_{23}^0 &= -ik_\beta \cos 2\theta_0 \sin\phi_0 A e^{i\psi_\beta}.
\end{aligned} \tag{B.40}$$

The displacements generated by the SV-wave are

$$\begin{aligned}
\delta u_r^{SV}(\mathbf{x},t) &= -(\delta V \delta C_{45} A)\frac{\omega^2}{4\pi\rho\beta\alpha^3}\frac{e^{i(\omega t - r/\alpha)}}{r}\cos 2\theta_0 \sin 2\theta[\sin(\phi+\phi_0)] \\
\delta u_\theta^{SV}(\mathbf{x},t) &= -(\delta V \delta C_{45} A)\frac{\omega^2}{4\pi\rho\beta^4}\frac{e^{i(\omega t - r/\beta)}}{r}\cos 2\theta_0 \cos 2\theta[\sin(\phi+\phi_0)] \\
\delta u_\phi^{SV}(\mathbf{x},t) &= -(\delta V \delta C_{45} A)\frac{\omega^2}{4\pi\rho\beta^4}\frac{e^{i(\omega t - r/\beta)}}{r}\cos 2\theta_0 \cos\theta[\cos(\phi+\phi_0)].
\end{aligned} \tag{B.41}$$

In this case, the scattered fields vanish when the incident wave propagates $\theta_0 = \pi/4$ or $\theta_0 = 3\pi/4$.

Considering next the SH-wave incidence, we have for the incident strains

$$\begin{aligned}
2\epsilon_{13}^0 &= +ik_\beta \cos\theta_0 \sin\phi_0 A e^{i\psi_\beta} \\
2\epsilon_{23}^0 &= -ik_\beta \cos\theta_0 \cos\phi_0 A e^{i\psi_\beta}.
\end{aligned} \tag{B.42}$$

The scattered displacement fields are

$$\begin{aligned}
\delta u_r^{SH}(\mathbf{x},t) &= -(\delta V \delta C_{45} A)\frac{\omega^2}{4\pi\rho\beta\alpha^3}\frac{e^{i(\omega t - r/\alpha)}}{r}\cos\theta_0 \sin 2\theta[\cos(\phi+\phi_0)] \\
\delta u_\theta^{SH}(\mathbf{x},t) &= -(\delta V \delta C_{45} A)\frac{\omega^2}{4\pi\rho\beta^4}\frac{e^{i(\omega t - r/\beta)}}{r}\cos\theta_0 \cos 2\theta[\cos(\phi+\phi_0)] \\
\delta u_\phi^{SH}(\mathbf{x},t) &= -(\delta V \delta C_{45} A)\frac{\omega^2}{4\pi\rho\beta^4}\frac{e^{i(\omega t - r/\beta)}}{r}\cos\theta_0 \cos\theta[-\sin(\phi+\phi_0)].
\end{aligned} \tag{B.43}$$

In this case, the scattered fields vanish for a horizontally incident wave.

Appendix C

Spherical Coordinates in the Development of Radiation Pattern Equations

Spherical coordinates allow a relatively straightforward expression of the components of the scattered field in a given direction. Utilizing the spherical coordinate system shown in Figure 3-1 and expressing the Cartesian components in terms of spherical coordinates (Ben-Menahem and Singh, 1981), the following relationships can be derived. They provide far-field approximations which can be used in the derivation of the radiation patterns given in the text and Appendix D. This approach was also employed by Ben-Menahem and Gibson (1990) to consider the special case of a transversely isotropic inclusion with a vertical axis of symmetry.

$$\begin{aligned} \frac{\partial}{\partial x} &= \sin\theta\cos\phi\frac{\partial}{\partial r} \\ \frac{\partial}{\partial y} &= \sin\theta\sin\phi\frac{\partial}{\partial r} \\ \frac{\partial}{\partial z} &= \cos\theta\frac{\partial}{\partial r} \end{aligned} \tag{C.1}$$

Expressing the Cartesian basis vectors in spherical coordinates yields also

$$\begin{aligned}
\mathbf{e_x}\frac{\partial}{\partial x} &= [\mathbf{e_r}\sin^2\theta\cos^2\phi + \mathbf{e}_\theta\sin\theta\cos\theta\cos^2\phi - \mathbf{e}_\phi\sin\theta\cos\phi\sin\phi]\frac{\partial}{\partial r}\,, \\
\mathbf{e_y}\frac{\partial}{\partial y} &= [\mathbf{e_r}\sin^2\theta\sin^2\phi + \mathbf{e}_\theta\sin\theta\cos\theta\sin^2\phi + \mathbf{e}_\phi\sin\theta\cos\phi\sin\phi]\frac{\partial}{\partial r}\,, \\
\vec{e}_z\frac{\partial}{\partial z} &= [\mathbf{e_r}\cos^2\theta - \mathbf{e}_\theta\sin\theta\cos\theta]\frac{\partial}{\partial r}\,, \\
\vec{e}_x\frac{\partial}{\partial y} + \vec{e}_y\frac{\partial}{\partial x} &= [\mathbf{e_r}\sin 2\phi\sin\theta + \mathbf{e}_\theta\sin 2\phi\cos\theta + \mathbf{e}_\phi\cos 2\phi]\sin\theta\frac{\partial}{\partial r}\,, \\
\vec{e}_y\frac{\partial}{\partial z} + \vec{e}_z\frac{\partial}{\partial y} &= [\mathbf{e_r}\sin 2\theta\sin\phi + \mathbf{e}_\theta\cos 2\theta\sin\phi + \mathbf{e}_\phi\cos\theta\cos\phi]\frac{\partial}{\partial r}\,, \\
\vec{e}_z\frac{\partial}{\partial x} + \vec{e}_x\frac{\partial}{\partial z} &= [\mathbf{e_r}\sin 2\theta\cos\phi + \mathbf{e}_\theta\cos 2\theta\cos\phi - \mathbf{e}_\phi\cos\theta\sin\phi]\frac{\partial}{\partial r}\,,
\end{aligned} \tag{C.2}$$

In deriving the radiation patterns for the scattered displacement fields, expressions such as

$$\frac{\partial \mathbf{G}\cdot\mathbf{e_x}}{\partial x}, \tag{C.3}$$

for example, occur. Using the far-field Green's tensor

$$\mathbf{G} = \frac{e^{-ik_\alpha r}}{4\pi\alpha^2\rho r}\mathbf{e_r}\mathbf{e_r} + \frac{e^{-ik_\beta r}}{4\pi\alpha^2\rho r}(\mathbf{e}_\theta\mathbf{e}_\theta + \mathbf{e}_\phi\mathbf{e}_\phi) \tag{C.4}$$

and equations (C.2), these partial derivatives may be written as

$$\frac{\partial \mathbf{G}\cdot\mathbf{e_x}}{\partial x} = [\mathbf{e_r}\sin^2\theta\cos^2\phi + \mathbf{e}_\theta\sin\theta\cos\theta\cos^2\phi - \mathbf{e}_\phi\sin\theta\cos\phi\sin\phi]\frac{\partial \mathbf{G}}{\partial r}. \tag{C.5}$$

This approach allows all radiation patterns to be written in a straightforward manner.

Appendix D

Radiation Patterns for Perturbations to the Elastic Constants

The components of the scattered displacement field due to a perturbation to any one of the 21 elastic coefficients δC_{IJ} can be derived using the techniques described in the text and Appendix B and expressed in the following form for an incident compressional plane wave:

$$\begin{aligned} \delta u_r(\mathbf{x},t) &= -(\delta V \delta C_{IJ} A)\frac{\omega^2}{4\pi\rho\alpha}\frac{e^{i(\omega t - r/\alpha)}}{r}E_r^P \\ \delta u_\theta(\mathbf{x},t) &= -(\delta V \delta C_{IJ} A)\frac{\omega^2}{4\pi\rho\beta}\frac{e^{i(\omega t - r/\beta)}}{r}E_\theta^P \\ \delta u_\phi(\mathbf{x},t) &= -(\delta V \delta C_{IJ} A)\frac{\omega^2}{4\pi\rho\beta}\frac{e^{i(\omega t - r/\beta)}}{r}E_\phi^P. \end{aligned} \tag{D.1}$$

Here δV is the volume of the perturbed region, δC_{IJ} is the elastic constant perturbation, and A is the amplitude of the incident wave. Material properties of the background medium are P and S-wave velocities α and β, respectively, and density ρ. The *scattering coefficients* E_r^P, E_θ^P and E_ϕ^P are functions of the angular coordinates θ, ϕ, θ_0 and ϕ_0 defining the direction of propagation of the scattered and incident waves, as

well as the P and S-wave velocities of the background material. The scattered fields for an incident SV-wave have the same form as those given in equation (D.1), with scattering coefficients indicated by E_r^{SV}, E_θ^{SV} and E_ϕ^{SV}. For an incident SH-wave, the superscript is replaced by SH.

The scattering coefficients for the different elastic constants are given in Table D.1 in the form of a 3 by 3 matrix for each constant. In the matrices, a row corresponds to an incident wave type (P, SV, or SH), and a column corrsponds to a scattered wave type. An interesting type of "antisymmetry" is apparent in the scattering coefficient matrices where the off-diagonal ij element of each matrix has the same form as the ji element with the roles of the incidence and scattering direction angles reversed. For example, for δC_{11}, the P to SV coefficient is

$$E_\theta^P = \frac{1}{\alpha\beta^2} \sin^2\theta_0 \cos^2\phi_0 \sin\theta \cos\theta \cos^2\phi, \tag{D.2}$$

and the SV to P coefficient is

$$E_r^{SV} = \frac{1}{\beta\alpha^2} \sin\theta_0 \cos\theta_0 \cos^2\phi_0 \sin^2\theta \cos^2\phi. \tag{D.3}$$

Note that in the fraction preceding the angular terms, $\alpha\beta^2$ is replaced by $\beta\alpha^2$, another aspect of the "antisymmetry".

TABLE D.1. SCATTERING COEFFICIENTS FOR THE ELASTIC CONSTANTS.

	INCIDENT WAVE	SCATTERED WAVE		
		P	SV	SH
δC_{11}	P	$\frac{1}{\alpha^3}\sin^2\theta_0\cos^2\phi_0\sin^2\theta\cos^2\phi$	$\frac{1}{\alpha\beta^2}\sin^2\theta_0\cos^2\phi_0\sin\theta\cos\theta\cos^2\phi$	$\frac{1}{\alpha\beta^2}\sin^2\theta_0\cos^2\phi_0\sin\theta\sin\phi\cos\phi$
	SV	$\frac{1}{\beta\alpha^2}\sin\theta_0\cos\theta_0\cos^2\phi_0\sin^2\theta\cos^2\phi$	$\frac{1}{\beta^3}\sin\theta_0\cos\theta_0\cos^2\phi_0\sin\theta\cos\theta\cos^2\phi$	$\frac{1}{\beta^3}\sin\theta_0\cos\theta_0\cos^2\phi_0\sin\theta\sin\phi\cos\phi$
	SH	$\frac{1}{\beta\alpha^2}\sin\theta_0\sin\phi_0\cos\phi_0\sin^2\theta\cos^2\phi$	$\frac{1}{\beta^3}\sin\theta_0\sin\phi_0\cos\phi_0\sin\theta\cos\theta\cos^2\phi$	$\frac{1}{\beta^3}\sin\theta_0\sin\phi_0\cos\phi_0\sin\theta\sin\phi\cos\phi$
δC_{22}	P	$\frac{1}{\alpha^3}\sin^2\theta_0\sin^2\phi_0\sin^2\theta\sin^2\phi$	$\frac{1}{\alpha\beta^2}\sin^2\theta_0\sin^2\phi_0\sin\theta\cos\theta\sin^2\phi$	$\frac{1}{\alpha\beta^2}\sin^2\theta_0\sin^2\phi_0\sin\theta\sin\phi\cos\phi$
	SV	$\frac{1}{\beta\alpha^2}\sin\theta_0\cos\theta_0\sin^2\phi_0\sin^2\theta\sin^2\phi$	$\frac{1}{\beta^3}\sin\theta_0\cos\theta_0\sin^2\phi_0\sin\theta\cos\theta\sin^2\phi$	$\frac{1}{\beta^3}\sin\theta_0\cos\theta_0\sin^2\phi_0\sin\theta\sin\phi\cos\phi$
	SH	$\frac{1}{\beta\alpha^2}\sin\theta_0\sin\phi_0\cos\phi_0\sin^2\theta\sin^2\phi$	$\frac{1}{\beta^3}\sin\theta_0\sin\phi_0\cos\phi_0\sin\theta\cos\theta\sin^2\phi$	$\frac{1}{\beta^3}\sin\theta_0\sin\phi_0\cos\phi_0\sin\theta\sin\phi\cos\phi$
δC_{33}	P	$\frac{1}{\alpha^3}\cos^2\theta_0\cos^2\theta$	$-\frac{1}{\alpha\beta^2}\cos^2\theta_0\sin\theta\cos\theta$	0
	SV	$-\frac{1}{\beta\alpha^2}\sin\theta_0\cos\theta_0\cos^2\theta$	$\frac{1}{\beta^3}\sin\theta_0\cos\theta_0\sin\theta\cos\theta$	0
	SH	0	0	0

δC_{44}	P	$\frac{1}{\alpha^3}\sin 2\theta_0 \sin\phi_0 \sin 2\theta \sin\phi$	$\frac{1}{\alpha\beta^2}\sin 2\theta_0 \sin\phi_0 \cos 2\theta \sin\phi$	$\frac{1}{\alpha\beta^2}\sin 2\theta_0 \sin\phi_0 \cos\theta \cos\phi$
	SV	$\frac{1}{\beta\alpha^2}\cos 2\theta_0 \sin\phi_0 \sin 2\theta \sin\phi$	$\frac{1}{\beta^3}\cos 2\theta_0 \sin\phi_0 \cos 2\theta \sin\phi$	$\frac{1}{\beta^3}\cos 2\theta_0 \sin\phi_0 \cos\theta \cos\phi$
	SH	$\frac{1}{\beta\alpha^2}\cos\theta_0 \cos\phi_0 \sin 2\theta \sin\phi$	$\frac{1}{\beta^3}\cos\theta_0 \cos\phi_0 \cos 2\theta \sin\phi$	$\frac{1}{\beta^3}\cos\theta_0 \cos\phi_0 \cos\theta \cos\phi$
δC_{55}	P	$\frac{1}{\alpha^3}\sin 2\theta_0 \cos\phi_0 \sin 2\theta \cos\phi$	$\frac{1}{\alpha\beta^2}\sin 2\theta_0 \cos\phi_0 \cos 2\theta \cos\phi$	$\frac{1}{\alpha\beta^2}\sin 2\theta_0 \cos\phi_0 \cos\theta \sin\phi$
	SV	$\frac{1}{\beta\alpha^2}\cos 2\theta_0 \cos\phi_0 \sin 2\theta \cos\phi$	$\frac{1}{\beta^3}\cos 2\theta_0 \cos\phi_0 \cos 2\theta \cos\phi$	$\frac{1}{\beta^3}\cos 2\theta_0 \cos\phi_0 \cos\theta \sin\phi$
	SH	$\frac{1}{\beta\alpha^2}\cos\theta_0 \sin\phi_0 \sin 2\theta \cos\phi$	$\frac{1}{\beta^3}\cos\theta_0 \sin\phi_0 \cos 2\theta \cos\phi$	$\frac{1}{\beta^3}\cos\theta_0 \sin\phi_0 \cos\theta \sin\phi$
δC_{66}	P	$\frac{1}{\alpha^3}\sin^2\theta_0 \sin 2\phi_0 \sin^2\theta \sin 2\phi$	$\frac{1}{\alpha\beta^2}\sin^2\theta_0 \sin 2\phi_0 \sin\theta \cos\theta \sin 2\phi$	$\frac{1}{\alpha\beta^2}\sin^2\theta_0 \sin 2\phi_0 \sin\theta \cos 2\phi$
	SV	$\frac{1}{\beta\alpha^2}\sin\theta_0 \cos\theta_0 \sin 2\phi_0 \sin^2\theta \sin 2\phi$	$\frac{1}{\beta^3}\sin\theta_0 \cos\theta_0 \sin 2\phi_0 \sin\theta \cos\theta \sin 2\phi$	$\frac{1}{\beta^3}\sin\theta_0 \cos\theta_0 \sin 2\phi_0 \sin\theta \cos 2\phi$
	SH	$\frac{1}{\beta\alpha^2}\sin\theta_0 \cos 2\phi_0 \sin^2\theta \sin 2\phi$	$\frac{1}{\beta^3}\sin\theta_0 \cos 2\phi_0 \sin\theta \cos\theta \sin 2\phi$	$\frac{1}{\beta^3}\sin\theta_0 \cos 2\phi_0 \sin\theta \cos 2\phi$

δC_{12}	P	$\frac{1}{\alpha^3}\sin^2\theta_0\sin^2\theta$ $\cdot[\sin^2\phi_0\cos^2\phi+\cos^2\phi_0\sin^2\phi]$	$\frac{1}{\alpha\beta^2}\sin^2\theta_0\sin\theta\cos\theta$ $\cdot[\sin^2\phi_0\cos^2\phi+\cos^2\phi_0\sin^2\phi]$	$\frac{1}{\alpha\beta^2}\sin^2\theta_0\cos 2\phi_0\sin\theta\sin\phi\cos\phi$
	SV	$\frac{1}{\beta\alpha^2}\sin\theta_0\cos\theta_0\sin^2\theta$ $\cdot[\sin^2\phi_0\cos^2\phi+\cos^2\phi_0\sin^2\phi]$	$\frac{1}{\beta^3}\sin\theta_0\cos\theta_0\sin\theta\cos\theta$ $\cdot[\sin^2\phi_0\cos^2\phi+\cos^2\phi_0\sin^2\phi]$	$\frac{1}{\beta^3}\sin\theta_0\cos\theta_0\cos 2\phi_0\sin\theta\sin\phi\cos\phi$
	SH	$\frac{1}{\beta\alpha^2}\sin\theta_0\sin\phi_0\cos\phi_0\sin^2\theta\cos 2\phi$	$\frac{1}{\beta^3}\sin\theta_0\sin\phi_0\cos\phi_0\sin\theta\cos\theta\cos 2\phi$	$-\frac{1}{\beta^3}\sin\theta_0\sin\phi_0\cos\phi_0\sin\theta\sin 2\phi$
δC_{13}	P	$\frac{1}{\alpha^3}[\cos^2\theta_0\sin^2\theta\cos^2\phi$ $+\sin^2\theta_0\cos^2\phi_0\cos^2\theta]$	$\frac{1}{\alpha\beta^2}\sin\theta\cos\theta[\cos^2\theta_0\cos^2\phi$ $-\sin^2\theta_0\cos^2\phi_0]$	$-\frac{1}{\alpha\beta^2}\cos^2\theta_0\sin\theta\sin\phi\cos\phi$
	SV	$\frac{1}{\beta\alpha^2}\sin\theta_0\cos\theta_0$ $\cdot[\cos^2\phi_0\cos^2\theta-\sin^2\theta\cos^2\phi]$	$-\frac{1}{\beta^3}\sin\theta_0\cos\theta_0\sin\theta\cos\theta$ $[\cos^2\phi+\cos^2\phi_0]$	$\frac{1}{\beta^3}\sin\theta_0\cos\theta_0\sin\theta\sin\phi\cos\phi$
	SH	$-\frac{1}{\beta\alpha^2}\sin\theta_0\sin\phi_0\cos\phi_0\cos^2\theta$	$\frac{1}{\beta^3}\sin\theta_0\sin\phi_0\cos\phi_0\sin\theta\cos\theta$	0
δC_{23}	P	$\frac{1}{\alpha^3}[\cos^2\theta_0\sin^2\theta\sin^2\phi$ $+\sin^2\theta_0\sin^2\phi_0\cos^2\theta]$	$\frac{1}{\alpha\beta^2}[\cos^2\theta_0\sin\theta\cos\theta\sin^2\phi$ $-\sin^2\theta_0\sin^2\phi_0\sin\theta\cos\theta]$	$\frac{1}{\alpha\beta^2}\cos^2\theta_0\sin\theta\sin\phi\cos\phi$
	SV	$\frac{1}{\beta\alpha^2}[-\sin\theta_0\cos\theta_0\sin^2\theta\sin^2\phi$ $+\sin\theta_0\cos\theta_0\sin^2\phi_0\cos^2\theta]$	$-\frac{1}{\beta^3}\sin\theta_0\cos\theta_0\sin\theta\cos\theta$ $[\sin^2\phi+\sin^2\phi_0\ ]$	$-\frac{1}{\beta^3}\sin\theta_0\cos\theta_0\sin\theta\sin\phi\cos\phi$
	SH	$\frac{1}{\beta\alpha^2}\sin\theta_0\sin\phi_0\cos\phi_0\cos^2\theta$	$-\frac{1}{\beta^3}\sin\theta_0\sin\phi_0\cos\phi_0\sin\theta\cos\theta$	0

δC_{14}	P	$\frac{1}{\alpha^3}[\sin^2\theta_0\cos^2\phi_0\sin 2\theta\sin\phi$ $+\sin 2\theta_0\sin\phi_0\sin^2\theta\cos^2\phi]$	$\frac{1}{\alpha\beta^2}[\sin^2\theta_0\cos^2\phi_0\cos 2\theta\sin\phi+$ $\sin 2\theta_0\sin\phi_0\sin\theta\cos\theta\cos^2\phi]$	$\frac{1}{\alpha\beta^2}[\sin^2\theta_0\cos^2\phi_0\cos\theta\cos\phi-$ $\sin 2\theta_0\sin\phi_0\sin\theta\sin\phi\cos\phi]$
	SV	$\frac{1}{\beta\alpha^2}[\sin\theta_0\cos\theta_0\cos^2\phi_0\sin 2\theta\sin\phi$ $+\cos 2\theta_0\sin\phi_0\sin^2\theta\cos^2\phi]$	$\frac{1}{\beta^3}[\sin\theta_0\cos\theta_0\cos^2\phi_0\cos 2\theta\sin\phi$ $+\cos 2\theta_0\sin\phi_0\sin\theta\cos\theta\cos^2\phi]$	$\frac{1}{\beta^3}[\sin\theta_0\cos\theta_0\cos^2\phi_0\cos\theta\cos\phi$ $-\cos 2\theta_0\sin\phi_0\sin\theta\sin\phi\cos\phi]$
	SH	$\frac{1}{\beta\alpha^2}[-\sin\theta_0\sin\phi_0\cos\phi_0\sin 2\theta\sin\phi$ $+\cos\theta_0\cos\phi_0\sin^2\theta\cos^2\phi]$	$\frac{1}{\beta^3}[-\sin\theta_0\sin\phi_0\cos\phi_0\cos 2\theta\sin\phi$ $+\cos\theta_0\cos\phi_0\sin\theta\cos\theta\cos^2\phi]$	$-\frac{1}{\beta^3}[\sin\theta_0\sin\phi_0\cos\phi_0\cos\theta\cos\phi$ $+\cos\theta_0\cos\phi_0\sin\theta\sin\phi\cos\phi]$
δC_{15}	P	$\frac{1}{\alpha^3}[\sin^2\theta_0\cos^2\phi_0\sin 2\theta\cos\phi$ $+\sin 2\theta_0\cos\phi_0\sin^2\theta\cos^2\phi]$	$\frac{1}{\alpha\beta^2}[\sin^2\theta_0\cos^2\phi_0\cos 2\theta\cos\phi$ $+\sin 2\theta_0\cos\phi_0\sin\theta\cos\theta\cos^2\phi]$	$-\frac{1}{\alpha\beta^2}[\sin^2\theta_0\cos^2\phi_0\cos\theta\sin\phi$ $\sin 2\theta_0\cos\phi_0\sin\theta\sin\phi\cos\phi]$
	SV	$\frac{1}{\beta\alpha^2}[\sin\theta_0\cos\theta_0\cos^2\phi_0\sin 2\theta\cos\phi$ $+\cos 2\theta_0\cos\phi_0\sin^2\theta\cos^2\phi]$	$\frac{1}{\beta^3}[\sin\theta_0\cos\theta_0\cos^2\phi_0\cos 2\theta\cos\phi$ $+\cos 2\theta_0\cos\phi_0\sin\theta\cos\theta\cos^2\phi]$	$-\frac{1}{\beta^3}[\sin\theta_0\cos\theta_0\cos^2\phi_0\cos\theta\sin\phi$ $+\cos 2\theta_0\cos\phi_0\sin\theta\sin\phi\cos\phi]$
	SH	$-\frac{1}{\beta\alpha^2}[\sin\theta_0\sin\phi_0\cos\phi_0\sin 2\theta\cos\phi$ $+\cos\theta_0\sin\phi_0\sin^2\theta\cos^2\phi]$	$-\frac{1}{\beta^3}[\sin\theta_0\sin\phi_0\cos\phi_0\cos 2\theta\cos\phi$ $+\cos\theta_0\sin\phi_0\sin\theta\cos\theta\cos^2\phi]$	$\frac{1}{\beta^3}[\sin\theta_0\sin\phi_0\cos\phi_0\cos\theta\sin\phi$ $+\cos\theta_0\sin\phi_0\sin\theta\sin\phi\cos\phi]$
δC_{16}	P	$\frac{1}{\alpha^3}\sin^2\theta_0\sin^2\theta$ $\cdot[\cos^2\phi_0\sin 2\phi+\sin 2\phi_0\cos^2\phi]$	$\frac{1}{\alpha\beta^2}\sin^2\theta_0\sin\theta\cos\theta$ $\cdot[\cos^2\phi_0\sin 2\phi+\sin 2\phi_0\cos^2\phi]$	$\frac{1}{\alpha\beta^2}\sin^2\theta_0\sin\theta$ $\cdot[\cos^2\phi_0\cos 2\phi-\sin 2\phi_0\sin\phi\cos\phi]$
	SV	$\frac{1}{\beta\alpha^2}\sin\theta_0\cos\theta_0\sin^2\theta$ $\cdot[\cos^2\phi_0\sin 2\phi+\sin 2\phi_0\cos^2\phi]$	$\frac{1}{\beta^3}\sin\theta_0\cos\theta_0\sin\theta\cos\theta$ $\cdot[\cos^2\phi_0\sin 2\phi+\sin 2\phi_0\cos^2\phi]$	$\frac{1}{\beta^3}\sin\theta_0\cos\theta_0\sin\theta$ $\cdot[\cos^2\phi_0\cos 2\phi-\sin 2\phi_0\sin\phi\cos\phi]$
	SH	$\frac{1}{\beta\alpha^2}\sin\theta_0\sin^2\theta[\cos 2\phi_0\cos^2\phi$ $-\sin\phi_0\cos\phi_0\sin 2\phi]$	$\frac{1}{\beta^3}\sin\theta_0\sin\theta\cos\theta[\cos 2\phi_0\cos^2\phi$ $-\sin\phi_0\cos\phi_0\sin 2\phi]$	$-\frac{1}{\beta^3}\sin\theta_0\sin\theta[\sin\phi_0\cos\phi_0\cos 2\phi$ $+\cos 2\phi_0\sin\phi\cos\phi]$

δC_{24}	P	$\frac{1}{\alpha^3}\sin\phi_0\sin\phi[\sin 2\theta_0\sin^2\theta\sin\phi + \sin^2\theta_0\sin\phi_0\sin 2\theta]$	$\frac{1}{\alpha\beta^2}\sin\phi_0\sin\phi[\sin 2\theta_0\sin\theta\cos\theta\sin\phi + \sin^2\theta_0\sin\phi_0\cos 2\theta]$	$\frac{1}{\alpha\beta^2}\sin\phi_0\cos\phi[\sin 2\theta_0\sin\theta\sin\phi + \sin^2\theta_0\sin\phi_0\cos\theta]$
	SV	$\frac{1}{\beta\alpha^2}\sin\phi_0\sin\phi[\cos 2\theta_0\sin^2\theta\sin\phi + \sin\theta_0\cos\theta_0\sin\phi_0\sin 2\theta]$	$\frac{1}{\beta^3}\sin\phi_0\sin\phi[\cos 2\theta_0\sin\theta\cos\theta\sin\phi + \sin\theta_0\cos\theta_0\sin\phi_0\cos 2\theta]$	$\frac{1}{\beta^3}\sin\phi_0\cos\phi[\cos 2\theta_0\sin\theta\sin\phi + \sin\theta_0\cos\theta_0\sin\phi_0\cos\theta]$
	SH	$\frac{1}{\beta\alpha^2}\cos\phi_0\sin\phi[\cos\theta_0\sin^2\theta\sin\phi + \sin\theta_0\sin\phi_0\sin 2\theta]$	$\frac{1}{\beta^3}\cos\phi_0\sin\phi[\cos\theta_0\sin\theta\cos\theta\sin\phi + \sin\theta_0\sin\phi_0\cos 2\theta]$	$\frac{1}{\beta^3}\cos\phi_0\cos\phi[\cos\theta_0\sin\theta\sin\phi + \sin\theta_0\sin\phi_0\cos\theta]$
δC_{25}	P	$\frac{1}{\alpha^3}[\sin 2\theta_0\cos\phi_0\sin^2\theta\sin^2\phi + \sin^2\theta_0\sin^2\phi_0\sin 2\theta\cos\phi]$	$\frac{1}{\alpha\beta^2}[\sin 2\theta_0\cos\phi_0\sin\theta\cos\theta\sin^2\phi + \sin^2\theta_0\sin^2\phi_0\cos 2\theta\cos\phi]$	$\frac{1}{\alpha\beta^2}\sin\phi[\sin 2\theta_0\cos\phi_0\cos\phi - \sin^2\theta_0\sin^2\phi_0\cos\theta]$
	SV	$\frac{1}{\beta\alpha^2}[\cos 2\theta_0\cos\phi_0\sin^2\theta\sin^2\phi + \sin\theta_0\cos\theta_0\sin^2\phi_0\sin 2\theta\cos\phi]$	$\frac{1}{\beta^3}[\cos 2\theta_0\cos\phi_0\sin\theta\cos\theta\sin^2\phi + \sin\theta_0\cos\theta_0\sin^2\phi_0\cos 2\theta\cos\phi]$	$\frac{1}{\beta^3}\sin\phi[\cos 2\theta_0\cos\phi_0\sin\theta\cos\phi - \sin\theta_0\cos\theta_0\sin^2\phi_0\cos\theta]$
	SH	$\frac{1}{\beta\alpha^2}\sin\phi_0[-\cos\theta_0\sin^2\theta\sin^2\phi + \sin\theta_0\cos\phi_0\sin 2\theta\cos\phi]$	$\frac{1}{\beta^3}\sin\phi_0[-\cos\theta_0\sin\theta\cos\theta\sin^2\phi + \sin\theta_0\cos\phi_0\cos 2\theta\cos\phi]$	$-\frac{1}{\beta^3}\sin\phi_0\sin\phi[-\cos\theta_0\sin\theta\cos\phi + \sin\theta_0\cos\phi_0\cos\theta]$
δC_{26}	P	$\frac{1}{\alpha^3}\sin^2\theta_0\sin^2\theta[\sin^2\phi_0\sin 2\phi + \sin 2\phi_0\sin^2\phi]$	$\frac{1}{\alpha\beta^2}\sin^2\theta_0\sin\theta\cos\theta[\sin^2\phi_0\sin 2\phi + \sin 2\phi_0\sin^2\phi]$	$\frac{1}{\alpha\beta^2}\sin^2\theta_0\sin\theta[\sin^2\phi_0\cos 2\phi + \sin 2\phi_0\sin\phi\cos\phi]$
	SV	$\frac{1}{\beta\alpha^2}\sin\theta_0\cos\theta_0\sin^2\theta[\sin^2\phi_0\sin 2\phi + \sin 2\phi_0\sin^2\phi]$	$\frac{1}{\beta^3}\sin\theta_0\cos\theta_0\sin\theta\cos\theta[\sin^2\phi_0\sin 2\phi + \sin 2\phi_0\sin^2\phi]$	$\frac{1}{\beta^3}\sin\theta_0\cos\theta_0\sin\theta[\sin^2\phi_0\cos 2\phi + \sin 2\phi_0\sin\phi\cos\phi]$
	SH	$\frac{1}{\beta\alpha^2}\sin\theta_0\sin^2\theta[\sin\phi_0\cos\phi_0\sin 2\phi + \cos 2\phi_0\sin^2\phi]$	$\frac{1}{\beta^3}\sin\theta_0\sin\theta\cos\theta[\sin\phi_0\cos\phi_0\sin 2\phi + \cos 2\phi_0\sin^2\phi]$	$\frac{1}{\beta^3}\sin\theta_0\sin\theta[\sin\phi_0\cos\phi_0\cos 2\phi + \cos 2\phi_0\sin\phi\cos\phi]$

δC_{34}	P	$\frac{1}{\alpha^3}[\cos^2\theta_0 \sin 2\theta \sin\phi + \sin 2\theta_0 \sin\phi_0 \cos^2\theta]$	$\frac{1}{\alpha\beta^2}[\cos^2\theta_0 \cos 2\theta \sin\phi - \sin 2\theta_0 \sin\phi_0 \sin\theta \cos\theta]$	$\frac{1}{\alpha\beta^2}[\cos^2\theta_0 \cos\theta \cos\phi]$
	SV	$\frac{1}{\beta\alpha^2}[-\sin\theta_0 \cos\theta_0 \sin 2\theta \sin\phi + \cos 2\theta_0 \sin\phi_0 \cos^2\theta]$	$-\frac{1}{\beta^3}[\sin\theta_0 \cos\theta_0 \cos 2\theta \sin\phi + \cos 2\theta_0 \sin\phi_0 \sin\theta \cos\theta]$	$-\frac{1}{\beta^3}[\sin\theta_0 \cos\theta_0 \cos\theta \cos\phi]$
	SH	$\frac{1}{\beta\alpha^2}[\cos\theta_0 \cos\phi_0 \cos^2\theta]$	$\frac{1}{\beta^3}[-\cos\theta_0 \cos\phi_0 \sin\theta \cos\theta]$	0
δC_{35}	P	$\frac{1}{\alpha^3}[\cos^2\theta_0 \sin 2\theta \cos\phi + \sin 2\theta_0 \cos\phi_0 \cos^2\theta]$	$\frac{1}{\alpha\beta^2}[\cos^2\theta_0 \cos 2\theta \cos\phi - \sin 2\theta_0 \cos\phi_0 \sin\theta \cos\theta]$	$\frac{1}{\alpha\beta^2}[-\cos^2\theta_0 \cos\theta \sin\phi]$
	SV	$\frac{1}{\beta\alpha^2}[-\sin\theta_0 \cos\theta_0 \sin 2\theta \cos\phi + \cos 2\theta_0 \cos\phi_0 \cos^2\theta]$	$-\frac{1}{\beta^3}[\sin\theta_0 \cos\theta_0 \cos 2\theta \cos\phi + \cos 2\theta_0 \cos\phi_0 \sin\theta \cos\theta]$	$\frac{1}{\beta^3}[\sin\theta_0 \cos\theta_0 \cos\theta \sin\phi]$
	SH	$\frac{1}{\beta\alpha^2}[-\cos\theta_0 \sin\phi_0 \cos^2\theta]$	$\frac{1}{\beta^3}[\cos\theta_0 \sin\phi_0 \sin\theta \cos\theta]$	0
δC_{36}	P	$\frac{1}{\alpha^3}[\cos^2\theta_0 \sin^2\theta \sin 2\phi + \sin^2\theta_0 \sin 2\phi_0 \cos^2\theta]$	$\frac{1}{\alpha\beta^2}\sin\theta \cos\theta[\cos^2\theta_0 \sin 2\phi - \sin^2\theta_0 \sin 2\phi_0]$	$\frac{1}{\alpha\beta^2}[\cos^2\theta_0 \sin\theta \cos 2\phi]$
	SV	$\frac{1}{\beta\alpha^2}\sin\theta_0 \cos\theta_0[-\sin^2\theta \sin 2\phi + \sin 2\phi_0 \cos^2\theta]$	$-\frac{1}{\beta^3}\sin\theta_0 \cos\theta_0 \sin\theta \cos\theta [\sin 2\phi + \sin 2\phi_0]$	$-\frac{1}{\beta^3}[\sin\theta_0 \cos\theta_0 \sin\theta \cos 2\phi]$
	SH	$\frac{1}{\beta\alpha^2}[\sin\theta_0 \cos 2\phi_0 \cos^2\theta]$	$-\frac{1}{\beta^3}[\sin\theta_0 \cos 2\phi_0 \sin\theta \cos\theta]$	0

δC_{45}	P	$\frac{1}{\alpha^3}\sin 2\theta_0 \sin 2\theta[\sin(\phi_0+\phi)]$	$\frac{1}{\alpha\beta^2}\sin 2\theta_0 \cos 2\theta[\sin(\phi_0+\phi)]$	$\frac{1}{\alpha\beta^2}\sin 2\theta_0 \cos\theta[\cos(\phi_0+\phi)]$
	SV	$\frac{1}{\beta\alpha^2}\cos 2\theta_0 \sin 2\theta[\sin(\phi_0+\phi)]$	$\frac{1}{\beta^3}\cos 2\theta_0 \cos 2\theta[\sin(\phi_0+\phi)]$	$\frac{1}{\beta^3}\cos 2\theta_0 \cos\theta[\cos(\phi_0+\phi)]$
	SH	$\frac{1}{\beta\alpha^2}\cos\theta_0 \sin 2\theta[\cos(\phi_0+\phi)]$	$\frac{1}{\beta^3}\cos\theta_0 \cos 2\theta[\cos(\phi_0+\phi)]$	$\frac{1}{\beta^3}\cos\theta_0 \cos\theta[-\sin(\phi_0+\phi)]$
δC_{46}	P	$\frac{1}{\alpha^3}[\sin^2\theta_0 \sin 2\phi_0 \sin 2\theta \sin\phi + \sin 2\theta_0 \sin\phi_0 \sin^2\theta \sin 2\phi]$	$\frac{1}{\alpha\beta^2}[\sin^2\theta_0 \sin 2\phi_0 \cos 2\theta \sin\phi + \sin 2\theta_0 \sin\phi_0 \sin\theta \cos\theta \sin 2\phi]$	$\frac{1}{\alpha\beta^2}[\sin^2\theta_0 \sin 2\phi_0 \cos\theta \cos\phi + \sin 2\theta_0 \sin\phi_0 \sin\theta \cos 2\phi]$
	SV	$\frac{1}{\beta\alpha^2}[\sin\theta_0 \cos\theta_0 \sin 2\phi_0 \sin 2\theta \sin\phi + \cos 2\theta_0 \sin\phi_0 \sin^2\theta \sin 2\phi]$	$\frac{1}{\beta^3}[\sin\theta_0 \cos\theta_0 \sin 2\phi_0 \cos 2\theta \sin\phi + \cos 2\theta_0 \sin\phi_0 \sin\theta \cos\theta \sin 2\phi]$	$\frac{1}{\beta^3}[\sin\theta_0 \cos\theta_0 \sin 2\phi_0 \cos\theta \cos\phi + \cos 2\theta_0 \sin\phi_0 \sin\theta \cos 2\phi]$
	SH	$\frac{1}{\beta\alpha^2}[\sin\theta_0 \cos 2\phi_0 \sin 2\theta \sin\phi + \cos\theta_0 \cos\phi_0 \sin^2\theta \sin 2\phi]$	$\frac{1}{\beta^3}[\sin\theta_0 \cos 2\phi_0 \cos 2\theta \sin\phi + \cos\theta_0 \cos\phi_0 \sin\theta \cos\theta \sin 2\phi]$	$\frac{1}{\beta^3}[\sin\theta_0 \cos 2\phi_0 \cos\theta \sin\phi + \cos\theta_0 \cos\phi_0 \sin\theta \cos 2\phi]$
δC_{56}	P	$\frac{1}{\alpha^3}[\sin^2\theta_0 \sin 2\phi_0 \sin 2\theta \cos\phi + \sin 2\theta_0 \cos\phi_0 \sin^2\theta \sin 2\phi]$	$\frac{1}{\alpha\beta^2}[\sin^2\theta_0 \sin 2\phi_0 \cos 2\theta \cos\phi + \sin 2\theta_0 \cos\phi_0 \sin\theta \cos\theta \sin 2\phi]$	$\frac{1}{\alpha\beta^2}[-\sin^2\theta_0 \sin 2\phi_0 \cos\theta \sin\phi + \sin 2\theta_0 \cos\phi_0 \sin\theta \cos 2\phi]$
	SV	$\frac{1}{\beta\alpha^2}[\sin\theta_0 \cos\theta_0 \sin 2\phi_0 \sin 2\theta \cos\phi + \cos 2\theta_0 \cos\phi_0 \sin^2\theta \sin 2\phi]$	$\frac{1}{\beta^3}[\sin\theta_0 \cos\theta_0 \sin 2\phi_0 \cos 2\theta \cos\phi + \cos 2\theta_0 \cos\phi_0 \sin\theta \cos\theta \sin 2\phi]$	$\frac{1}{\beta^3}[-\sin\theta_0 \cos\theta_0 \sin 2\phi_0 \cos\theta \sin\phi + \cos 2\theta_0 \cos\phi_0 \sin\theta \cos 2\phi]$
	SH	$\frac{1}{\beta\alpha^2}[\sin\theta_0 \cos 2\phi_0 \sin 2\theta \cos\phi - \cos\theta_0 \sin\phi_0 \sin^2\theta \sin 2\phi]$	$\frac{1}{\beta^3}[\sin\theta_0 \cos 2\phi_0 \cos 2\theta \cos\phi - \cos\theta_0 \sin\phi_0 \sin\theta \cos\theta \sin 2\phi]$	$-\frac{1}{\beta^3}[\sin\theta_0 \cos 2\phi_0 \cos\theta \cos\phi + \cos\theta_0 \sin\phi_0 \sin\theta \cos 2\phi]$

Appendix E

Density Contributions to Scattering by Fractured Volumes

In principle, the contribution to scattering radiation patterns of density changes due to fracturing will add to and change the results derived considering only the perturbations to elastic constants. However, the amplitude of scattering due to density fluctuations is sufficiently small compared to that created by changes in the elastic properties that it may be neglected. This can be shown by direct comparison of the maximum amplitudes of the scattered fields.

The size of the density perturbation is based on the total volume of voids within the rock. Since the cracks are modeled as oblate spheroids, the volume of an individual crack is $4\pi a^2 h/3$, where a and h are the radius and half-width of the crack. Given the aspect ratio

$$\gamma = \frac{h}{a} \tag{E.1}$$

of the crack, the volume can also be expressed as

$$v_1 = \frac{4}{3}\pi a^3 \gamma \tag{E.2}$$

Therefore, the total volume of porosity within a unit volume sample of the rock is

$$v = \frac{4}{3}\pi \gamma \epsilon \tag{E.3}$$

where crack density $\epsilon = na^3$, and n is the number density of cracks. When the cracks are empty, the density perturbation is negative, and is given by multiplying the above volume of crack space by the density of unfractured rock. Using the crack density 0.05 and rock density 2.70 g/cm^3 considered in the text, this perturbation is -8.48×10^{-5} g/cm^3 for $\alpha = 10^{-4}$. This value of aspect ratio is typical of that used to model changes in elastic properties of rocks using this crack model under pressures typical of the upper crust (e.g., Gibson and Toksöz, 1990; Cheng and Toksöz, 1979; Feves and Simmons, 1976).

Considering the forms of equations (3.21) through (3.24), the maximum amplitudes of the various radiation patterns are the same except for the factors presented in Table E.1. Expressing all quantities in units of kilograms, kilometers and seconds, and using the density perturbation derived above and isotropic elastic parameter perturbations in Table 3.1, the maximum amplitudes of the radiation patterns for each of the incident and scattered wave fields are presented in Table E.2. It is clear that the scattered displacement field due to the density change is always at least 3 orders of magnitude smaller than that due to the perturbations to the Lamé parameters λ and μ. Therefore, the effects of density can be neglected to assess the principal effects in the scattered fields due to the presence of the randomly oriented cracks. Since the perturbations to the various elastic constants, except δC_{44}, are of the same order of magnitude as those to the isotropic parameters (Table 3.1), the same conclusions will hold for the aligned crack volume. The exception to this conclusion is for the case of a shear wave polarized *parallel* to the crack plane. Since the effects of the elastic constants will vanish in this case, the scattering due to density variations will dominate. It must be remembered, however, that the scattered field generated by a shear wave polarized *perpendicular* to the crack plane will still reflect the magnitude of δC_{55}, which is non-zero, and will be several orders of magnitude larger than the scattering in the former case. This shows that the change in the scattered displacement field with variation of the polarization of an incident shear wave will still be

very significant.

This analysis is based on the assumption that the variations in elastic properties are caused only by the small aspect ratio cracks modeled by the Hudson (1980, 1981) theory. In some geological examples, it is possible that the heterogeneous zone will include an increase in porosity due to more equidimensional pores as well as the fine cracks. If this is true, then the overall pore volume will become much larger, and density changes will become more important and will mask the effects of the elastic constant perturbations to some extent since density causes significant back scattering (e.g., Wu and Aki, 1985b). However, as is shown in the examples of radiation patterns presented in the text, the variations in radiation with incident shear wave polarization should still be observable and will yield observations that cannot occur in the isotropic case.

INCIDENT WAVE	SCATTERED WAVE	PERTURBED PARAMETER		
		$\delta\rho$	$\delta\lambda$	$\delta\mu$
P	P	$\frac{\delta\rho}{\alpha^2}$	$\frac{\delta\lambda}{\alpha^4}$	$\frac{2\delta\mu}{\alpha^4}$
P	S	$\frac{\delta\rho}{\beta^2}$		$\frac{2\delta\mu}{\alpha\beta^3}$
S	S	$\frac{\delta\rho}{\beta^2}$		$\frac{2\delta\mu}{\beta^4}$
S	P	$\frac{\delta\rho}{\alpha^2}$		$\frac{2\delta\mu}{\alpha^3\beta}$

Table E.1. Unique terms in radiation patterns expressions controlling maximum amplitude of scattered wave fields for a perturbation to one of the isotropic parameters.

INCIDENT WAVE	SCATTERED WAVE	PERTURBED PARAMETER		
		$\delta\rho$	$\delta\lambda$	$\delta\mu$
P	P	1.51×10^6	7.53×10^9	2.71×10^9
P	S	5.29×10^6		1.78×10^{10}
S	S	5.29×10^6		1.67×10^{10}
S	P	1.51×10^6		5.07×10^9

Table E.2. Numerical values for the maximum amplitude factors in Table E.1 using parameter values given in the text.

Appendix F

Overview of Dynamic Ray Tracing

The ray method is a high frequency asymptotic approach to the calculation of synthetic seismograms (Karal and Keller, 1959; Červený *et al.* 1977; Ben-Menahem and Beydoun, 1985). A rapid, flexible computation of the asymptotic wavefield results from the high frequency assumption applied to the wave equation, though the resulting equations are not able to model such features as diffraction or caustics. Indeed, the high frequency assumption requires that the medium be smooth compared to the seismic wavelength for the solution to be valid (Ben-Menahem and Beydoun, 1985). The two principal parts of the ray tracing procedure are computation of travel times and computation of amplitudes, the kinematic and dynamic ray tracing problems, respectively. In order to facilitate computation of the wavefield at a specific receiver point, we apply the paraxial method. We briefly describe the better known aspects of these procedures below.

Substitution of the ray series solution

$$u_k(x_i,t) = e^{-i\omega(t-\tau(x_i))} \sum_{n=0}^{\infty} (-i\omega)^{-n} u_k^{(n)}(x_i) \qquad \text{(F.1)}$$

into the equation of motion (4.1) yields the transport equation, and ultimately two sets of ordinary differential equations of the following form for the characteristics of

the eikonal equation (Červený et al., 1977; Červený, 1985):

$$\begin{aligned} \frac{dx_i}{d\tau} &= \sigma_{1i} \\ \frac{dp_i}{d\tau} &= \sigma_{2i}. \end{aligned} \tag{F.2}$$

The forms of the right hand sides σ_{1i} and σ_{2i} are given in many references for both isotropic (Červený, 1985) and anisotropic media (Červený, 1972). These six simultaneous equations are then integrated to obtain the ray path and travel time of the wave corresponding to the particular ray, solving the KRT problem.

The effect of geometrical spreading on amplitudes of the waves is obtained from the DRT. Explicit analytic formulae for the partial derivatives $\partial x_i/\partial \gamma_j$ can be obtained both for isotropic (Červenýet al., 1974) and anisotropic media (Gajewski and Pšenčik, 1990), yielding an additional twelve simultaneous equations which must be integrated along the ray path. Alternatively, the partial derivatives may estimated numerically by tracing additional *auxiliary rays* with take-off angles slightly perturbed from those of the original *central ray* where the geometrical spreading value is desired. For an accurate, stable solution through this finite difference technique, in general four auxiliary rays must be traced corresponding to perturbations of $\pm\phi$ and $\pm\psi$.

For the special case of an isotropic earth model, the introduction of ray-centered coordinates q_i allows considerable simplification of the computation of the geometrical spreading (Červený, 1985) (Figure 4-2). The three basis vectors of the ray-centered coordinate system at a general point P along the ray are the unit vector $\mathbf{t}$ tangent to the ray, and two additional unit vectors contained in the plane perpendicular to the ray at the point P. The tangent vector $\mathbf{t}$ is always known, since its components are simply (vp_1, vp_2, vp_3), and simple and numerically inexpensive procedures for obtaining the two vectors $\mathbf{e_1}$ and $\mathbf{e_2}$ are discussed by several authors (e.g., Červený, 1985; Červený and Hron, 1980; Pšenčik, 1979). This coordinate system is clearly only regular in the vicinity of the ray, since the curvature of the ray will lead to the intersection of coordinate planes at some distance from the ray.

Expressing the eikonal equation in ray-centered coordinates, Červený (1985) shows that the Jacobian $\hat{J}(\tau)$ is given by the determinate of the second order matrix $\mathbf{Q}$

$$Q_{IJ} = \frac{\partial q_I}{\partial \gamma_J} \tag{F.3}$$

Subscripts given by upper case letters range in value from 1 to 2. Four simultaneous differential equations are integrated to determine the different components of the matrix $\mathbf{Q}$, and these in turn depend on the matrix $\mathbf{P}$:

$$\mathbf{P} = \frac{1}{v^2}\frac{d\mathbf{Q}}{d\tau}. \tag{F.4}$$

Therefore, a total of eight differential equations are integrated to determine the geometrical spreading, as compared to the twelve which must be utilized when Cartesian coordinates are employed. In addition to the reduction of the overall number of equations, the forms of the right hand sides of the equations are somewhat simpler and thereby reduce computational complexities.

In application of ray methods to any wave propagation problem, one of the principal difficulties lies in determining the take-off angles of the ray connecting a given source and observation point, two-point ray tracing. In anisotropic media, difficulties arise because the ray and the corresponding slowness vector, the quantity actually specified to initiate ray tracing, have significantly different directions which in general can not be identified prior to ray tracing. In isotropic media, the effects of model geometry lead to similar difficulties. For the Ray-Born method, where rays are needed from the true receiver positions to all scattering points in the lattice, application of a two-point ray tracing algorithm would be very difficult and time consuming. We circumvent this difficulty by utilizing paraxial ray tracing techniques. This approach takes information from the central ray, which serves as an axis, and projects it using quantities obtained by the DRT to nearby observation points (Červený, 1985; Červený et al., 1984; Beydoun and Keho, 1987). In particular, the travel time at points near the ray is obtained by expanding the time τ on the ray in a Taylor series,

retaining terms up to second order:

$$\begin{aligned} \tau(\mathbf{x}) &= \tau(\mathbf{x}') + (\mathbf{x}-\mathbf{x}')\cdot\mathbf{p} + \frac{1}{2}(\mathbf{x}-\mathbf{x}')^{\mathbf{T}}\mathbf{N}(\mathbf{x}')(\mathbf{x}-\mathbf{x}') \qquad \text{(F.5)} \\ N_{ij}(\mathbf{x}') &= \left.\frac{\partial^2\tau}{\partial x_i \partial x_j}\right|_{\mathbf{x}'} \end{aligned}$$

The components of the slowness vector $\mathbf{p}(\mathbf{x}')$ are as usual $p_i = \partial\tau/\partial x_i$, $\mathbf{x}'$ is a point on the central ray, and $\mathbf{x}$ is the desired observation point. The matrix $\mathbf{N}$ is evaluated in Cartesian coordinates by rewriting it as

$$N_{ij}(\mathbf{x}') = \frac{\partial p_i}{\partial \gamma_k}\frac{\partial \gamma_k}{\partial x_j}. \qquad \text{(F.6)}$$

The same paraxial correction to travel time can be utilized in ray-centered coordinates by introducing the transformation matrix $\mathbf{H}$ from the ray-centered coordinate system to Cartesian coordinates with components (Červený, 1985)

$$H_{ij} = \frac{\partial x_i}{\partial q_j}. \qquad \text{(F.7)}$$

As each column of this matrix corresponds to one of the basis vectors $\mathbf{t}$, $\mathbf{e_1}$ and $\mathbf{e_2}$ of the ray-centered coordinates, this matrix is always known during the DRT procedure. The paraxial travel time then takes the form

$$\tau(\mathbf{x}) = \tau(\mathbf{x}') + (\mathbf{x}-\mathbf{x}')\cdot\mathbf{p} + \frac{1}{2}(\mathbf{x}-\mathbf{x}')^{\mathbf{T}}\mathbf{H}(\mathbf{x}')\mathbf{M}(\mathbf{x}')\mathbf{H}^{\mathbf{T}}(\mathbf{x}')(\mathbf{x}-\mathbf{x}'). \qquad \text{(F.8)}$$

The partial derivative matrix $\mathbf{M}$ is

$$\begin{aligned} \mathbf{M} &= \begin{bmatrix} \widehat{M}_{11} & \widehat{M}_{12} & -\frac{1}{v^2}\frac{\partial v}{\partial q_1} \\ \widehat{M}_{21} & \widehat{M}_{22} & -\frac{1}{v^2}\frac{\partial v}{\partial q_2} \\ -\frac{1}{v^2}\frac{\partial v}{\partial q_1} & -\frac{1}{v^2}\frac{\partial v}{\partial q_2} & -\frac{1}{v^2}\frac{\partial v}{\partial q_3} \end{bmatrix} \qquad \text{(F.9)} \\ \widehat{\mathbf{M}} &= \mathbf{P}\mathbf{Q}^{-1}. \end{aligned}$$

The knowledge of wavefront curvature can also be used to correct polarization vectors as well. For an isotropic medium, the compressional wave polarization is always in the direction of the wavefront normal, which is also parallel to the slowness vector.

Therefore, a straightforward correction for compressional waves is (Gajewski and Pšenčik, 1987)

$$t_i(\mathbf{x}) = \mathbf{t}(\mathbf{x}')v(x'_j) \cdot N_{ik}(x'_j)(x_k - x'_k), \tag{F.10}$$

Corrections for the shear polarization vectors are also available (Červený et al., 1984):

$$g_{Ii}(\mathbf{x}) = e_{Ii}(x'_j) - N_{kl}(x'_j) \cdot v(x'_j) \cdot p_i(x'_j) \cdot e_{Ik}(x'_j) \cdot (x_l - x'_l). \tag{F.11}$$

REFERENCES

Aki, K., Analysis of the seismic coda of local earthquakes as scattered waves, *J. Geophys. Res.*, *74*, 615–631, 1969.

Aki, K., Scattering and attenuation of shear waves in the lithosphere, *J. Geophys. Res.*, *85*, 6496–6504, 1980.

Aki, K. and B. Chouet, Origin of coda waves: source, attenuation, and scattering effects, *J. Geophys. Res.*, *80*, 3322–3342, 1975.

Aki, K. and P. G. Richards, *Quantitative seismology*, W.H. Freeman and Co., 1980.

Anderson, D.A.and J.H. Whitcomb, The dilatancy-diffusion model of earthquake prediction, in *Proceedings of the Conference on Tectonic Problems of the San Andreas Fault System,* edited by R.L. Kovach and A. Nur, Stanford University Press, Palo Alto, Calif., 417–426, 1973.

Anderson, D.A., B. Minster, and D. Cole, The effect of oriented cracks on seismic velocities, *J. Geophys. Res.*, *79*, 4011–4015, 1974.

Andersson, J., and B. Dverstorp, Conditional simulations of fluid flow in three-dimensional networks of discrete fractures, *Water Resour. Res.*, *23*, 1876–1886, 1987.

Bachman, R.T., Acoustic anisotropy in marine sediments and sedimentary rocks, *J. Geophys. Res.*, *84*, 113–119, 1979.

Bachman, R.T., Elastic anisotropy in marine sedimentary rocks, *J. Geophys. Res.*, *88*, 539–545, 1983.

Backus, G. and M. Mulcahy, Moment tensors and other phenomenological descriptions of seismic sources–I. Continuous displacements, *Geophys. J. R. astr. Soc.*, *46*, 341–361, 1977a.

Backus, G. and M. Mulcahy, Moment tensors and other phenomenological descriptions of seismic sources–I. Discontinuous displacements, *Geophys. J. R. astr. Soc.*, *47*, 301–329, 1977b.

Bamford, D. and K.R. Nunn, In situ seismic measurements of crack anisotropy in the Carboniferous limestone of Northwest England, *Geophys. Prosp.*, *27*, 322–338, 1979.

Banik, N.C., Velocity anisotropy of shales and depth estimation in the North Sea basin, *Geophys.*, *49*, 1411-1419, 1984.

Batini, F., G. Bertini, G. Gianelli, E. Pandeli, and M. Puxeddu, Deep structure of the Lardarello field: contribution from recent geophysical and geological data, *Mem. Soc. Geol. It.*, *25*, 219–235, 1983.

Batini, F., A. Duprat and R. Nicolich, Contribution of seismic reflection to the study of geothermal reservoirs in Tuscany (Italy), *Geothermal Resources Council Transactions*, *9*, 245–252, 1985a.

Batini, F., R. Celati, V. Cigni, P. Squarci, G. Stefani and L. Taffi, Development of deep exploration in the geothermal areas of Tuscany, Italy, *1985 International Symposium on Geothermal Energy, Kailua-Kona, Hawaii, Intl vol.*, 303–309, 1985b.

Batini, F., G. Bertini, G. Gianelli, E. Pandeli, M. Puxeddu, and I.M. Villa, Deep struc-

ture, age and evolution of the Lardarello-Travale geothermal field, *Geothermal Resources Council Transactions*, *9*, Part I, 1985c.

Batini, F., G. Omnes, and P. Renoux, Proc. of International Geothermal Research Conference, Hawaii, 1990.

Batzle, M.L., G. Simmons, and R.W. Siegried, Microcrack closure in rocks under stress: Direct observation, *J. Geophys. Res.*, *85*, 7072–7090, 1980.

Ben-Menahem, A. and W. Beydoun, Range of validity of seismic ray and beam methods in general inhomogeneous media–I. General theory, *Geophys. J. R. astr. Soc.*, *82*, 207–234, 1985.

Ben-Menahem, A. and R.L. Gibson, Jr., Scattering of elastic waves by localized anisotropic inclusions, *J. Acoust. Soc. Amer.*, *87*, 2300–2309, 1990.

Ben-Menahem, A., R.L. Gibson, Jr., and A.G. Sena, Green's tensor and radiation patterns of point sources in general anisotropic inhomogeneous elastic media, submitted to *Geophys. J. Inter.*.

Ben-Menahem, A. and S.J. Singh, *Seismic waves and sources*, Springer-Verlag, New York, 1981.

Berge, P.A., S. Mallick, G.J. Fryer, N. Barstow, J.A. Carter, G.H. Sutton and J.I. Ewing, *In situ* measurement of transverse isotropy in shallow-water marine sediments, *Geophys. J. Int.*, *104*, 241–254, 1991.

Bernabe, Y., Pore volume and transport properties changes during pressure cycling of several

crystalline rocks, *Mech. Mater.*, *5*, 235–249, 1986.

Bernard, P. and R. Madariaga, High-frequency seismic radiation from a buried circular fault, *Geophys. J. R. astr. Soc.*, *78*, 1–17, 1984.

Beydoun, W.B. and T. Keho, The paraxial ray method, *Geophys.*, *52*, 1639–1653, 1987.

Beydoun, W.B. and M. Mendes, Elastic ray-Born l_2-migration/inversion, *Geophys. J.*, *97*, 151–160, 1989.

Bond, L.J., C. Chaloner, S.J. Wormley, S.P. Neal and J.H. Rose, Recent advances in Born inversion (weak scatterers), in *Review of Progress in Quantitative Nondestructive Evaluation*, ed. D.O. Thompson and D.E. Chimenti, Plenum Press, New York, 1988.

Booth, D.C. and S. Crampin, The anisotropic reflectivity technique: theory, *Geophys. J.R. astr. Soc.*, *72*, 755–766, 1983.

Booth, D.C., S. Crampin, J.H. Lovell, and J.M. Chiu, Temporal changes in shear wave splitting during an earthquake swarm in Arkansas, *J. Geophys. Res.*, *95*, 11151–11164, 1990.

Boyse, W.E. and J.B. Keller, Inverse elastic scattering in three dimensions, *J. Acoust. Soc. Am.*, *79*, 215–218, 1986.

Brace, W.F., J.B. Walsh and W.T. Frangos, Permeability of granite under high pressure, *J. Geophys. Res*, *73*, 2225–2236, 1968.

Brown, S.R., and C.H. Scholz, Closure of random elastic surfaces in contact, *J. Geophys. Res.*, *90*, 5531–5545, 1985.

Brown, S.R., Fluid flow through rock joints: the effect of surface roughness, *J. Geophys. Res.*, *92*, 1337–1347, 1987.

Budak, B.M. and S.V. Fomin, *Multiple integrals, field theory and series*, Mir Publications, Moscow, 1983.

Carswell, A. and W.M. Moon, Application of multioffset vertical seismic profiling in fracture mapping, *Geophys.*, *54*, 737–746, 1989.

Červený, V., Seismic rays and ray intensities in inhomogeneous anisotropic media, *Geophys. J. R. astr. Soc.*, *29*, 1–13, 1972.

Červený, V., The application of ray tracing to the propagation of shear waves in complex media, in *Seismic shear waves, Part A: Theory*, edited by G.P. Dohr, in *Handbook of geophysical exploration*, Section 1: Seismic exploration, *15A*, edited by K. Helbig and S Treitel, Geophysical Press, 1985.

Červený, V., J. Langer, and I. Pšenčik, Computation of geometrical spreading of seismic body waves in laterally inhomogeneous media with curved interfaces, *Geophys. J.R. astr. Soc.*, *38*, 9–19, 1974.

Červený, V., I.A. Molotkov, and I. Pšenčik, *Ray methods in seismology*, University Karlova, 1977.

Červený, V. and F. Hron, The ray series method and dynamic ray tracing system for three-dimensional inhomogeneous media, *Bull. Seis. Soc. Amer.*, *70*, 47–77, 1980.

Červený, V., L. Klimeš and I. Pšenčik, Paraxial ray approximation in the computation of

seismic wavefields, in inhomogeneous media, *Geophys. J. R. astr. Soc.*, *79*, 89–104, 1984.

Červený, V., J. Pleinerová, L. Klimeš, and I. Pšenčik, *Geophys. J. R. astr. Soc.*, *88*, 43–79, 1987.

Chatterjee, A.K., A.K. Mal, and L. Knopoff, Elastic moduli of two-component systems, *J. Geophys. Res.*, *83*, 1785–1792, 1978. See also the discussion in *J. Geophys. Res.*, *84*, 5687–5690, 1979.

Cheng, C.H., and M.N. Toksöz, Inversion of seismic velocities for the pore aspect ratio spectrum of a rock, *J. Geophys. Res.*, *84*, 7533–7543, 1979.

Chernov, L.A., *Wave propagation in a random medium*, McGraw-Hill Book Company, Inc., New York, 1960.

Christensen, N.I., and D.L. Szymanski, Origin of reflections from the Brevard fault zone, *J. Geophys. Res.*, *93*, 1087–1102, 1988.

Chroston, P.N. and M.D. Max, Seismic anisotropy in mylonites: an example from the Mannin Thrust zone, southwest Connemara, Ireland, *Tectonophysics*, *148*, 29–39, 1988.

Clayton, R.W. and R.H. Stolt, A Born-WKBJ inversion method for acoustic reflection data, *Geophys.*, *46*, 1559–1567, 1981.

Cohen, J.K., F.G. Hagin, and N. Bleistein, Three-dimensional Born inversion with an arbitrary reference, *Geophys.*, *51*, 1552–1558, 1986.

Crampin, S., Seismic wave propagation through a cracked solid: polarization as a possible dilatancy diagnostic, *Geophys. J. R. astr. Soc.*, *53*, 467–496, 1978.

Crampin, S., A review of wave motion in anisotropic and cracked elastic media, *Wave Motion*, *3*, 343–391, 1981.

Crampin, S., Effective anisotropic elastic constants for wave propagation through cracked solids, *Geophys. J. R. astr. Soc.*, *76*, 135–145, 1984.

Crampin, S. and R. McGonigle, The variation of delays in stress-induced anisotropic polarization anomalies, *Geophys. J. R. astr. Soc.*, *64*, 115–131, 1985.

Crampin, S., R. Evans, and S.B. Uçer, Analysis of records of local earthquakes: the Turkish Dilatancy Projects (TDP1 and TDP2), *Geophys. J. R. astr. Soc.*, *83*, 1–16, 1985.

Crampin, S., R. McGonigle and M. Ando, Extensive-dilatancy anisotropy beneath Mt. Hood, Oregon and the effect of aspect ratio on seismic velocities through aligned cracks, *J. Geophys. Res.*, *91*, 12703–12710, 1986.

Dainty, A., A scattering model to explain seismic Q observations in the lithosphere between 1 and 30 Hz, *Geophys. Res. Lett.*, *8*, 1126–1128, 1981.

Dainty, A. and M. N. Toksöz, Elastic wave propagation in a highly scattering medium–a diffusion approach, *J. Geophys.*, *43*, 375–388, 1977.

Douman, J., The effect of aspect ratio on crack-induced anisotropy, *Geophys. Prosp.*, *36*, 614–632, 1988.

Doyen, P.M., Crack geometry in igneous rocks: A maximum entropy inversion of elastic and transport properties, *J. Geophys. Res.*, *92*, 8169–8181, 1987.

Ensley, Comparison of P and S wave seismic data: a new method for detecting gas reservoirs,

Geophys., *49*, 1420–1431, 1984.

Evans, K.F., T. Engelder, and R.A. Plumb, Appalachian stress study, 1. A detailed description of in situ stress variations in Devonian shales of the Appalachian Plateau, *J. Geophys. Res.*, *94*, 7129–7154, 1989.

Feves, M., and G. Simmons, Effects of stress on cracks in Westerly granite, *Bull. Seismol. Soc. Am.*, *66*, 1755–1765, 1976.

Gajewski, D. and I. Pšenčik, Computation of high-frequency seismic wavefields in 3-D laterally inhomogeneous anisotropic media, *Geophys. J. R. astr. Soc.*, *91*, 383–411, 1987.

Gajeswki, D. and I. Pšenčik, Vertical seismic profile synthetics by dynamic ray tracing in laterally varying anisotropic structures, *J. Geophys. Res.*, *95*, 11301–11315, 1990.

Ganji, A.F., Variation of whole and fracture porous rock permeability with confining pressure, *Int. J. Rock Mech. Min. Sci. Geomech. Abstr.*, *15*, 249–257, 1978.

Gao, L.S., L.C. Lee, N.N. Biswas, and K. Aki, Comparison of the effects between single and multiple scattering on coda waves for local earthquakes, *Bull. Seis. Soc. Amer.*, *73*, 377–389, 1983a.

Gao, L.S., N.N. Biswas, L.C. Lee, and K. Aki, Effects of multiple scattering on coda waves in three-dimensional medium, *PAGEOPH*, *121*, 3–15, 1983b.

Gibson, Jr., R.L., A.G. Sena, and M.N. Toksöz, Paraxial ray tracing in 3-d inhomogeneous, anisotropic media, *Geophys. Prosp.*, *39*, 473–504, 1991.

Gilbert, G.K., Report on the geology of the Henry Mountains: U.S. Geographical and Geo-

logical Survey of the Rocky Mountain Region (Powell), U.S. Department of the Interior, Washington, 1880.

Green, A.G. and J. A. Mair, Subhorizontal fractures in a granitic pluton: their detection and implications for radioactive waste disposal, *Geophys.*, *48*, 1428–1449, 1983.

Gubernatis, J.E., E. Domany, and J.A. Krumhansl, Formal aspects of the theory of the scattering of ultrasound by flaws in elastic materials, *J. Appl. Phys.*, *48*, 2804–2811, 1977a.

Gubernatis, J.E., E. Domany, J.A. Krumhansl, R.M. Thompson, The Born approximation in the theory of the scattering of elastic waves by flaws, *J. Appl. Phys.*, *48*, 2812–2819, 1977b.

Gubernatis, J.E., J.A. Krumhansl, R.M. Thompson, Interpretation of elastic-wave scattering theory for analysis and design of flaw-characterization experiments: The long-wavelength limit, *J. Appl. Phys.*, *50*, 3338–3345, 1979.

Hadley, K., Comparison of calculated and observed crack densities and seismic velocities in Westerly granite, *J. Geophys. Res.*, *81*, 3484–3494, 1976.

Hardage, B.A., *Vertical seismic profiling. Part A: Principles*, Geophysical Press, London, 1983.

Hatton, L., M.H. Worthington, and J. Makin, *Seismic Data Processing*, Blackwell Scientific, Boston, Mass., 1986.

Hearmon, R.F.S., *An Introduction to Applied Anisotropic Elasticity*, Oxford University Press,

New York, 1961.

Helbig, K., Transverse isotropy in exploration seismics, *Geophys. J.R. astr. Soc.*, *76*, 79–88, 1984.

Hess, H., Seismic anisotropy of the uppermost mantel under oceans, *Nature*, *203*, 629–631, 1964.

Hickman, S.H., M.D. Zoback, and J.H. Healy, Continuation of a deep borehole stress measurement profile near the San Andreas Fault, 1. Hydraulic fracturing stress measurements at Hi Vista, Mojave Desert, California, *J. Geophys. Res.*, *93*, 15183–15195, 1988.

Hudson, J.A., Scattered waves in the coda of *P*, *J. Geophycs.*, *43*, 359–374, 1977.

Hudson, J.A., Overall properties of a cracked solid, *Math. Proc. Camb. Phil. Soc.*, *88*, 371–384, 1980.

Hudson, J.A., Wave speeds and attenuation of elastic waves in material containing cracks, *Geophys. J. R. astr. Soc.*, *64*, 133–150, 1981.

Hudson, J.A. and J.R. Heritage, The use of the Born approximation in seismic scattering problems, *Geophys. J. R. astr. Soc.*, *66*, 221–240, 1981.

Hurich, C.A., S.B. Smithson, D.M. Fountain, and M.C. Humphreys, Seismic evidence of mylonite reflectivity and deep structure in the Kettle Dome metamorphic core complex, Washington, *Geology*, *13*, 577–580, 1985.

Iannaccone, G. and A. Deschamps, Evidence of shear-wave anisotropy in the upper crust of Central Italy, *Bull. Seis. Soc. Amer.*, *79*, 1905–1912, 1989.

Jamison, D.B. and N.G.W. Cook, Note on measured values for the state of stress in the Earth's crust, *J. Geophys. Res.*, *85*, 1833–1838, 1980.

Jones, L.E.A. and H.F. Wang, Ultrasonic velocities in Cretaceous shales from the Williston Basin, *Geophys.*, *46*, 288–297, 1981.

Juhlin, C., J. Lindgren, and G. Collini, Interpretation of seismic reflection and borehole data from Precambrian rocks in the Dala Sandstone area, central Sweden, *First Break*, *9*, 24–36, 1991.

Kaarsberg, E.A., Elastic studies of isotropic and anisotropic rock samples, *Trans. Am. Inst. Min. Metallurg. Eng.*, *241*, 470–475, 1968.

Kanashima, S., H. Ito, and M. Sugihara, Shear-wave splitting observed above small earthquakes in a geothermal area of Japan, *Geophys. J.*, *94*, 399–411, 1988.

Kanashima, S., H. Ito, and M. Sugihara, Shear wave polarization anisotropy observed in a rift zone in Japan, *Tectonophysics*, *157*, 281–300, 1989.

Karal, Jr., F.C. and J.B. Keller, Elastic wave propagation in homogeneous and inhomogeneous media, *Journal of the Acoustical Society of America*, *31*, 694–705, 1959.

Kennet, B.L.N., *Seismic wave propagation in stratified media*, Cambridge University Press, Cambridge, 1983.

Kerner, C. B. Dyer and M. Worthington, Wave propagation in a vertical transversely isotropic medium: field experiment and model study, *Geophys. J.R. astr. Soc.*, *97*, 295–309, 1989.

Kohn, W. and J.R. Rice, Scattering of long-wavelength elastic waves from localized defects

in solids, *J. Appl. Phys.*, *50*, 3346–3353, 1979.

Kuo, B.-Y., D.W. Forsyth, and M. Wysession, Lateral heterogeneity and azimuthal anisotropy in the North Atlantic from SS-S differential travel times, *J. Geophys. Res.*, *92*, 6421–6436, 1987.

Kuster, G.T., and M.N. Toksöz, Velocity and attenuation of seismic waves in two-phase media, I, Theoretical formulations, *Geophysics*, *39*, 607–618, 1974.

Leary, P.C. Basement rock fracture structure from Cajon Pass, CA and Siljan Ring, Sweden, borehole geophysical logs, paper presented at 60th Annual Meeting, Soc. of Explor. Geophys., San Francisco, 1990.

Leary, P.C. and T.L. Henyey, Anisotropy and fracture zones about a geothermal well from P-wave velocity profiles, *Geophys.*, *50*, 25–36, 1985.

Leary, P.C., Y.-G. Li and K. Aki, Observation and modeling of fault-zone fracture seismic anisotropy–I. P, SV, SH travel times, *Geophysical Journal of the Royal Astronomical Society*, *91*, 461–484, 1987.

Leary, P.C., S. Crampin, and T.V. McEvilly, Seismic fracture anisotropy in the earth's crust: an overview, *J. Geophys. Res.*, *95*, 11105-11114, 1990.

Liu, E., S. Crampin, and D. C. Booth, Shear-wave splitting in cross-hole surveys: Modeling, *Geophys.*, *54*, 57–65, 1989.

Lo, T.W., K.B. Coyner, and M.N. Toksöz, Experimental determination of elastic anisotropy of Berea sandstone, Chicopee shale, and Chelmsford granite, *Geophysics*, *51*, 164–171,

1986.

Long, J.C.S., and P.A. Witherspoon, The relationship of the degree of interconnection to permeability in fracture networks, *J. Geophys. Res.*, *90*, 3087–3098, 1985.

Long, J.C.S., P. Gilmour, and P.A. Witherspoon, A model for steady fluid flow in three-dimensional networks of disc-shaped fractures, *Water Resour. Res.*, *21*, 1105-1115, 1985.

Mandal, B. and M.N. Toksöz, Computation of complete waveforms in general anisotropic media–results from an explosion source in an anisotropic medium, *Geophys. J. Int.*, *103*, 33–45, 1990.

Martin, M.A., and T.L. Davis, Shear-wave birefringence: a new tool for evaluating fractured reservoirs, *Leading Edge*, *6*, 22–28, 1987.

Mavko, G.M., and A. Nur, The effect of nonelliptical cracks on the compressibility of rocks, *J. Geophys. Res.*, *83*, 4459–4468, 1978.

Miles, J.W., Scattering of elastic waves by small inhomogeneities, *Geophys.*, *25*, 642–648, 1960.

Morris, P.R., Averaging fourth-rank tensors with weight functions, *J. Appl. Phys.*, *40*, 447–448, 1969.

Musgrave, M.P.J., *Crystal Acoustics*, Holden-Day, San Francisco, 1970.

Nishizawa, O., Seismic velocity anisotropy in a medium containing oriented cracks–transversely isotropic case, *J. Phys. Earth*, *30*, 331–347, 1982.

Nur, A., Effects of stress on velocity anisotropy in rocks with cracks, *J. Geophys. Res.*, *76*,

2022–2034, 1971.

Nur, A., and G. Simmons, Stress-induced velocity anisotropy in rock: an experimental study, *J. Geophys. Res.*, *27*, 6667–6674, 1969.

O'Connell, R.J. and B. Budiansky, Seismic velocities in dry and saturated cracked solids, *J. Geophys. Res.*, *79*, 5412–5426, 1974.

Peacock, S., S. Crampin, D.C. Booth and J.B. Fletcher, Shear wave splitting in the Anza seismic gap, Southern California: temporal variations as possible precursors, *J. Geophys. Res.*, *93*, 3339–3356, 1988.

Podio, A.L., A.R. Gregory, and M.E. Gray, Dynamic properties of dry and water-saturated Green River shale under stress, *Soc. Petr. Eng. J.*, *8*, 389–404, 1968.

Press, W.H., B.P. Flannery, S.A. Teukolsky, and W.T. Vetterling, *Numerical recipes in C: the art of scientific computing*, Cambridge University Press, Cambridge, 1988.

Pšenčik, I., Ray amplitudes in inhomogeneous media with curved interfaces, *J. Geophys.*, *45*, 381–390, 1979.

Raitt, R.W., G.G. Shor, and G.B. Morris, Velocity anisotropy of the mantle near Hawaii, *Trans. Amer. Geophys. Union*, *49*, 296, 1968.

Rayleigh, J.W.S., *The theory of sound, Volume Two*, Dover Publications, New York, 1945.

Reiter, E.C., Imaging of large offset ocean bottom seismic data, Ph.D. thesis, Massachusetts Institute of Technology, 1991.

Roberston, J.D. and D. Corrigan, Radiation patterns of a shear-wave vibrator in near-surface

shale, *Geophys.*, *48*, 19–26.

Savage, M.K., W.A. Peppin, and U.R. Vetter, Shear wave velocity and stress direction in and near Long Valley Caldera, California, 1979–1988, *J. Geophys. Res.*, *95*, 11165–11178, 1990.

Sayers, C.M., Angular dependent ultrasonic wave velocities in aggregates of hexagonal crystals, *Ultrasonics*, *24*, 289–291, 1986.

Sayers, C.M., Inversion of ultrasonic wave velocity measurements to obtain the microcrack orientation distribution function in rocks, *Ultrasonics*, *26*, 73–77, 1988*a*.

Sayers, C.M., Stress-induced ultrasonic wave velocity anisotropy in fractured rock, *Ultrasonics*, *26*, 311–317, 1988*b*.

Schoenberg, M. and J. Douma, Elastic wave propagation in media with parallel fractures and aligned cracks, *Geophys. Prosp.*, *36*, 571–590.

Sheriff, R.E. and L.P. Geldart, *Exploration Seismology, Volume 1, History, theory & data acquisition*, Cambridge University Press, Cambridge, 1982.

Shih, X.R. and R.P. Meyer, Observation of shear wave splitting from natural events: south moat of Long Valley Caldera, California, June 29 to August 12, 1982, *J. Geophys. Res.*, *95*, 11179–11198, 1990.

Siegfried, R., and G. Simmons, Characterization of oriented cracks with differential strain analysis, *J. Geophys. Res.*, *83*, 1269–1278, 1978.

Snow, D.T., Anisotropic permeability of fractured media, *Water Resour. Res.*, *5*, 1273–1289,

1969.

Sprunt, E. and W.F. Brace, Direct observation of microcavities in crystalline rocks, *Int. J. Rock Mech. Min. Sci.*, *11*, 139–150, 1974.

Stephen, R.A., Seismic anisotropy observed in upper oceanic crust, *Geophys. Res. Lett.*, *8*, 865–868, 1981.

Stephen, R.A., Seismic anisotropy in the upper oceanic crust, *Journal of Geophysical Research*, *66*, 3487–3496, 1985.

Stolt, R.H. and A.B. Weglein, Migration and inversion of seismic data, *Geophys.*, *50*, 2458–2472, 1985.

Tarantola, A., A strategy for nonlinear elastic inversion of seismic reflection data, *Geophysics, 51,* 1893–1903, 1986.

Tarantola, A., *Inverse Problem Theory*, Elsevier, Amsterdam, 1987.

Thomsen, L., Weak elastic anisotropy, *Geophys.*, *51*, 1954–1966, 1986.

Toksöz, M.N., C.H. Cheng, and A. Timur, Velocities of seismic waves in porous rocks, *Geophysics*, *41*, 621–645, 1976.

Toksöz, M.N., A.M. Dainty, E. Reiter, and R.-S. Wu, A model for attenuation and scattering in the earth's crust, in *Scattering and attenuation of seismic waves, Part I*, edited by K. Aki and R.-S. Wu, pp. 81–100, Birkhäuser Verlag, Basel, 1988.

Tsang, Y.W., and P.A. Witherspoon, Hydromechanical behavior of a deformable rock fracture subject to normal stress, *J. Geophys. Res.*, *86*, 9287–9298, 1981.

Tsang, Y.W., and P.A. Witherspoon, The dependence of fracture mechanical and fluid flow properties on fracture roughness and sample size, *J. Geophys. Res.*, *88*, 2359–2366, 1983.

Walsh, J.B., The effects of cracks on the uniaxial elastic compression of rocks, *J. Geophys. Res.*, *70*, 399–411, 1965.

Walsh, J.B. and M.A. Grosenbaugh, A new model for analyzing the effect of fractures on compressibility, *J. Geophys. Res.*, *84*, 3532–3536, 1979.

Wang, C.-Y., D.A. Okaya, C. Ruppert, G.A. Davis, T.S. Guo, Z.-Q. Zhong, and H.-R. Wenk, Seismic reflectivity of the Whipple Mountain shear zone in southern California, *J. Geophys. Res.*, *94*, 2989–3005, 1989.

White, J.E., L. Martineau-Nicoletis, and C. Monash, Measured anisotropy in Pierre Shale, *Gephys. Prosp.*, *31*, 709–725, 1983.

White, R.S. and R.B. Whitmarsh, An investigation of seismic anisotropy due to cracks in the upper oceanic crust at 45°N, Mid-Atlantic Ridge, *Geophys. J.R. astr. Soc.*, *79*, 439–467, 1984.

Wong, T.-F., J.T. Fredrich, and G.D. Gwanmesia, Crack aperture statistics and pore space fractal geometry of Westerly granite and Rutland quartzite: Implications for an elastic contact model of rock compressibility, *J. Geophys. Res.*, *94*, 10267–10278, 1989.

Winterstein, D.R., Anisotropy effects in P-wave and SH-wave stacking velocities contain information on lithology. *Geophysics*, *51*, 661–672, 1986.

Wu, R.-S. and K. Aki, Elastic wave scattering by a random medium and the small-scale

inhomogeneities in the lithosphere, *J. Geophys. Res.*, *90*, 10261–10273, 1985a.

Wu, R.-S. and K. Aki, Scattering characteristics of elastic waves by an elastic heterogeneity, *Geophys.*, *50*, 585–595, 1985b.

Ying, C.F. and R. Truell, Scattering of a plane longitudinal wave by a spherical obstacle in an isotropically elastic solid, *J. Appl. Phys.*, *27*, 1086–1097, 1956.

Zhao, X. and M.N. Toksöz, Characterizing surface roughness from pressure-joint closure measurements using inversion procedure, submitted to *Geophys. Res. Lett.*, 1991a.

Zhao, X. and M. N. Toksöz, Modeling fluid flow in heterogeneous and anisotropic porous media, *Full Waveform Acoustic Logging Consortium Annual Report*, Earth Resources Laboratory, Massachusetts Institute of Technology, Cambridge, Massachusetts, 245–269, 1991b.

Zoback, M.D., and J.D. Byerlee, The effect of microcrack dilatancy on the permeability of Westerly granite, *J. Geophys. Res.*, *80*, 752–755, 1975.

Zoback, M.L. and M. Zoback, State of stress in the conterminous United States, *J. Geophys. Res.*, *85*, 6113–6156, 1980.